TU Delft

Delft University of Technology

Characterizing the transport patterns and climate effects of aviation emissions using a novel Lagrangian tagging method

Maruhashi, J.

DOI
10.4233/uuid:177577f9-d99c-4d57-a7a2-5142cce8c03d

Publication date
2025

Document Version
Final published version

Citation (APA)
Maruhashi, J. (2025). *Characterizing the transport patterns and climate effects of aviation emissions using a novel Lagrangian tagging method*. [Dissertation (TU Delft), Delft University of Technology]. https://doi.org/10.4233/uuid:177577f9-d99c-4d57-a7a2-5142cce8c03d

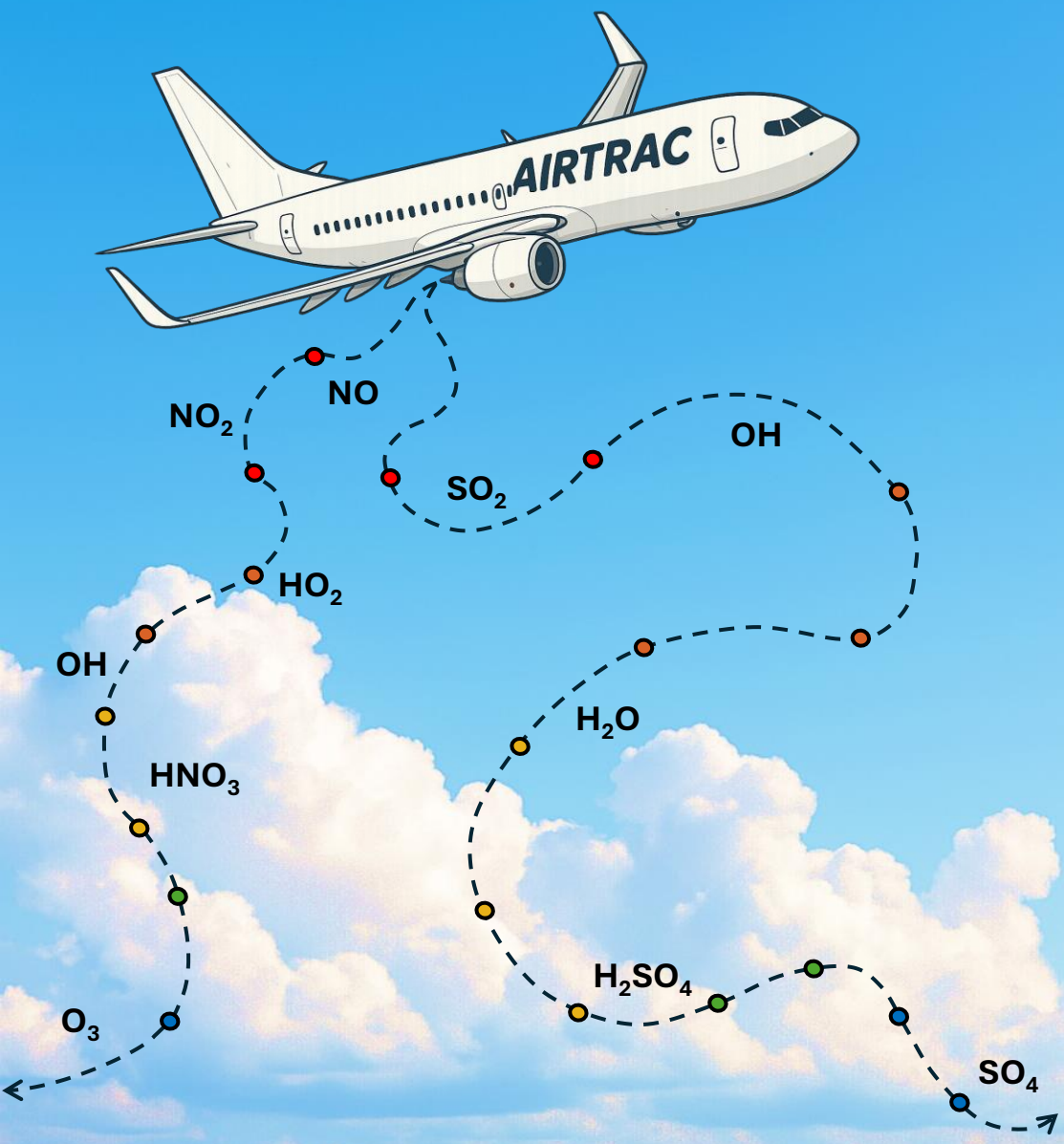
Important note
To cite this publication, please use the final published version (if applicable).
Please check the document version above.

Copyright
Other than for strictly personal use, it is not permitted to download, forward or distribute the text or part of it, without the consent of the author(s) and/or copyright holder(s), unless the work is under an open content license such as Creative Commons.

Takedown policy
Please contact us and provide details if you believe this document breaches copyrights.
We will remove access to the work immediately and investigate your claim.

This work is downloaded from Delft University of Technology.
For technical reasons the number of authors shown on this cover page is limited to a maximum of 10.

CHARACTERIZING THE TRANSPORT PATTERNS AND CLIMATE EFFECTS OF AVIATION EMISSIONS USING A NOVEL LAGRANGIAN TAGGING METHOD



JIN MARUHASHI

Characterizing the transport patterns and climate effects of aviation emissions using a novel Lagrangian tagging method

Characterizing the transport patterns and climate effects of aviation emissions using a novel Lagrangian tagging method

Dissertation

for the purpose of obtaining the degree of doctor
at Delft University of Technology,
by the authority of the Rector Magnificus prof. dr. ir. T.H.J.J. van der Hagen,
chair of the Board for Doctorates,
to be defended publicly on (Tuesday) 27 May 2025 at 10:00 o'clock

by

Jin MARUHASHI

Master of Science in Aerospace Engineering,
Instituto Superior Tecnico, Lisbon, Portugal.

Master of Science in Finance,
Nova University of Lisbon, Lisbon, Portugal.

born in Brasília, Brazil.

This dissertation has been approved by the promotors.

Composition of the doctoral committee:

Rector Magnificus,	Chairperson
Prof. dr. V. Grewe,	Delft University of Technology, German Aerospace Center (DLR), promotor
Dr. I.C. Dedoussi,	Delft University of Technology, University of Cambridge, promotor
Independent members:	
Prof. dr. H.W.J. Russchenberg,	Delft University of Technology
Prof. dr. L.L.A. Vermeersen,	Delft University of Technology
Prof. dr. J. Quaas,	Leipzig University
Prof. dr. C. Kiemle,	Technical University of Munich, German Aerospce Center (DLR)
Dr. F. Glassmeier,	Delft University of Technology







The present dissertation is part of the research produced by the EU-funded ACACIA (Advancing the Science for Aviation and Climate)[1] project, which has been funded under Grant Agreement no. 875036. Computational resources have been provided by the Dutch SURF Cooperative under grants EINF-441, EINF-2734 and EINF-10575.

Keywords: aviation emissions, climate effects, long-range transport, Lagrangian modeling, aerosols, nitrogen oxides, sulfates, tagging

Printed by: Proefschriftspecialist

Front & Back: Visualization of aircraft emission trajectories of primary and secondary pollutants.

Copyright © 2024 by J. Maruhashi

ISBN 978-94-93431-53-9

An electronic version of this dissertation is available at
http://repository.tudelft.nl/.

[1] https://www.acacia-project.eu/.

If I have seen further than others, it is by standing upon the shoulders of giants.

Isaac Newton

CONTENTS

Summary xi

Samenvatting xiii

1 Introduction 1
- 1.1 Motivation . . . 1
- 1.2 Knowledge gaps . . . 6
- 1.3 Dissertation overview . . . 7
  - 1.3.1 Objectives . . . 7
  - 1.3.2 Structure . . . 8

2 Background 11
- 2.1 The atmosphere . . . 12
  - 2.1.1 Vertical structure . . . 12
  - 2.1.2 Earth's radiation budget . . . 15
  - 2.1.3 Atmospheric circulation . . . 19
  - 2.1.4 Atmospheric chemistry . . . 24
- 2.2 Fundamentals of aerosols . . . 31
  - 2.2.1 Aerosol properties . . . 31
  - 2.2.2 Aerosol mechanics . . . 32
  - 2.2.3 Aerosol microphysical processes . . . 36
- 2.3 Aviation: climate effects and transport of emitted species . . . 38
  - 2.3.1 Aviation climate effects . . . 38
  - 2.3.2 Transport of aviation-emitted pollutants . . . 43

3 Modeling framework 47
- 3.1 An introduction to atmospheric modeling . . . 48
  - 3.1.1 Calculation methods . . . 48
- 3.2 The EMAC model . . . 50
- 3.3 Relevant submodels . . . 51
  - 3.3.1 AIRTRAC . . . 51
  - 3.3.2 TAGGING . . . 55
  - 3.3.3 MADE3 . . . 56
  - 3.3.4 DDEP and SEDI . . . 61
  - 3.3.5 SCAV . . . 62
  - 3.3.6 ATTILA and LGTMIX . . . 63

4 A multi-method comparison of the altitudinal sensitivity of aviation NO_x-O_3 climate effects 65
4.1 Introduction . . . 66
4.2 Methodology . . . 67
4.2.1 EMAC model configuration . . . 67
4.2.2 NO_x emissions . . . 67
4.2.3 Eulerian simulations . . . 68
4.2.4 Lagrangian simulations . . . 71
4.2.5 Method comparison metrics . . . 71
4.3 Results and discussion . . . 73
4.3.1 Comparison of O_3 production between methods . . . 73
4.3.2 Altitudinal variation of O_3 production efficiencies . . . 75
4.3.3 Altitudinal variation of short-term RF from aviation NO_x-O_3 interactions . . . 77
4.4 Summary and conclusions . . . 79
4.5 Acknowledgments . . . 80
4.6 Data availability statement . . . 80
4.7 Funding . . . 80

5 Analysis of global transport patterns of aviation NO_x and their link to atmospheric O_3 81
5.1 Introduction . . . 82
5.2 Methodology . . . 84
5.2.1 The modeling setup . . . 84
5.2.2 NO_x emission locations . . . 85
5.2.3 Source-receptor analysis . . . 86
5.2.4 Trajectory clustering . . . 87
5.2.5 The rate of descent $\dot{H}$ . . . 91
5.3 Results . . . 91
5.3.1 Seasonality and meteorological conditions as drivers of NO_x transport and chemistry . . . 92
5.4 Profiles of clustered trajectories . . . 99
5.4.1 Profiles for January 2014 . . . 99
5.4.2 Profiles for July 2014 . . . 103
5.4.3 Spatial variation of radiative forcing . . . 105
5.5 Discussion . . . 108
5.6 Summary and conclusions . . . 112
5.7 Acknowledgments . . . 113
5.8 Data availability statement . . . 113

6 Development and application of a new Lagrangian SO_4 tagging method 115
6.1 Introduction . . . 116
6.2 Modeling framework . . . 120
6.2.1 The EMAC model setup . . . 121
6.2.2 SO_2 and H_2SO_4 emission points . . . 121

6.3 The new AIRTRAC 2.0 submodel . . . 121
6.3.1 Submodel infrastructure . . . 122
6.3.2 Tracking aviation SO_2 and H_2SO_4 emissions . . . 122
6.3.3 Aviation's contribution to SO_4 via nucleation and condensation of H_2SO_4 . . . 124
6.3.4 Aviation's contribution to SO_4 via particle coagulation, growth and aging . . . 125
6.3.5 Aviation-attributable SO_4 removal processes . . . 127
6.3.6 An overview of the tagging equations for aviation SO_4 . . . 128
6.4 ESA cloud satellite data . . . 130
6.5 Application and evaluation of AIRTRAC 2.0 . . . 131
6.5.1 Emitted species: SO_2 and H_2SO_4 . . . 131
6.5.2 Impact on sulfate: SO_4 ks and as modes . . . 135
6.5.3 Evaluation of AIRTRAC 2.0 . . . 138
6.6 Seasonal dependence of aviation sulfur species . . . 140
6.7 Extension to aerosol-cloud interactions . . . 141
6.8 Discussion . . . 143
6.8.1 Achievements . . . 143
6.8.2 Limitations . . . 144
6.8.3 Future research . . . 144
6.9 Summary and conclusions . . . 145
6.10 Data availability statement . . . 147

7 Contribution to climate-optimal routing 149
7.1 Climate change functions (CCFs) and climate-optimal routing . . . 150
7.2 Algorithmic CCFs (aCCFs) . . . 151
7.3 Probabilistic aCCFs (paCCFs) . . . 152
7.4 Limitations and further research . . . 153

8 Conclusions and outlook 157
8.1 Conclusions . . . 158
8.2 Outlook . . . 161

A Appendix A: full list of applied EMAC submodels 165

B Appendix B: coordinates of emission points in Lagrangian simulations 167

C Appendix C: supplementary information on the comparative analysis between climate impact calculation methods 169
C.1 Complete O_3 production efficiencies - January . . . 170
C.2 Complete O_3 production efficiencies - July . . . 171
C.3 Kernel density estimator (KDE) plots for all scenarios . . . 172
C.4 Mean radiative forcing for all scenarios . . . 173
C.5 Variation of Δ RF between Lagrangian and Eulerian tagging . . . 174
C.6 Small signal correction to the TAGGING submodel . . . 175

D Appendix D: supplementary information on the analysis of NO_x-O_3 transport patterns **177**
D.1 Vertical profiles of median air parcel trajectories . . . 178
D.2 Horizontal distributions of median air parcels . . . 180
D.3 Calculation of the optimal numbers . . . 182
D.4 EMAC wind fields . . . 183
D.5 Vertical transport of NO_x for emission points 8 and 14 of Fig. 5.9 . . . 184
D.6 Mean radiative forcing per cluster . . . 184

E Appendix E: supplementary information on the analysis of SO_4 aerosol transport patterns **185**
E.1 Determination of SO_2 and H_2SO_4 emission locations and amounts . . . 186
E.2 Mathematical formulations for the tagging of the MADE3 coagulation tendency . . . 188
E.3 Spatio-temporal evolution of aviation SO_2 . . . 197
E.4 Spatio-temporal evolution of aviation H_2SO_4 . . . 203
E.5 Spatio-temporal evolution of aviation SO_4ks . . . 209
E.6 Spatio-temporal evolution of aviation SO_4as . . . 216
E.7 Evaluation of AIRTRAC 2.0: January - March 2015 . . . 223
E.8 Sensitivity of SO_4 mixing ratio with LGTMIX mixing parameter d . . . 224

Bibliography **226**

Acknowledgments **253**

Curriculum Vitæ **255**

List of Publications **257**

SUMMARY

Aviation's rapid and resilient growth over the past decades highlights the urgent need to address aviation's negative environmental externalities, which encompass both chemical and acoustic emissions. These emissions pose substantial challenges to public health, wildlife, agriculture and the environment as a whole. The focus here is on the climate impacts of aviation, which are currently estimated to contribute between 3-5% of the total anthropogenic climate effect, driven by both CO_2 and non-CO_2 pollutants. Given the current trajectory of post-pandemic growth, this share could increase further, especially since aviation remains one of the most difficult sectors to fully decarbonize. Non-CO_2 forcers, such as water vapor (H_2O), nitrogen oxides (NO_x), contrails, and aerosols like soot and sulfate (SO_4), are the primary contributors, accounting for roughly two-thirds of aviation's total climate impact. Unlike CO_2, which has long atmospheric lifetimes, the climate effects induced by these forcers are strongly dependent on their trajectories throughout the atmosphere. Factors such as cruise altitude play a critical role in shaping their transport patterns, making it essential to study them to better understand and mitigate their climate effects.

The transport patterns of aviation-induced gaseous pollutants such as NO_x remain uncertain, and the role of aerosol transport—specifically sulfate (SO_4)—in altering the optical properties of clouds is even less understood. This dissertation advances and extends the Lagrangian tagging algorithm called AIRTRAC, which is integrated within the EMAC modeling framework. AIRTRAC improves our understanding of NO_x and, for the first time, of SO_4 transport by tracking key aerosol microphysical processes throughout the atmosphere. For NO_x, its short-term impact on ozone (O_3) production is examined, as this process is the dominant warming contributor to the net warming effect of aviation NO_x emissions. Four key contributions arising from this dissertation are highlighted.

Firstly, this work compares the performance of AIRTRAC with a higher-fidelity submodel on a global scale in Chapter 4. This comparison has generated one of the most comprehensive datasets currently available for estimating instantaneous radiative forcing (iRF) from short-term aviation-induced NO_x-O_3 interactions, covering five geographic regions, three representative cruise altitudes, and two distinct seasons. From this analysis, scaling factors ranging from 1.7 to 5.9 were derived to enhance AIRTRAC's accuracy. Furthermore, this chapter establishes that the difference between tagging and perturbation methods for aviation is systematic on a global scale, with tagging estimates averaging 80% larger than perturbation-based estimates.

Secondly, Chapter 5 introduces a novel method for efficiently grouping large numbers of air parcel trajectories using a neuroscience-based clustering algorithm. This innovative approach systematically identified the most likely transport patterns for each region. Strong downdrafts were discovered to rapidly transport NO_x to lower altitudes, where it is removed more quickly than along trajectories that remain longer at the emission altitude. Additionally, when NO_x is transported to cleaner regions, such as Aus-

tralasia, O_3 production can increase by nearly a factor of 3, depending on the season. Furthermore, Chapter 4 revealed a seasonal dependence on the effects of cruise altitude shifts in relation to NO_x-O_3 chemistry. For example, flying at higher altitudes in Eurasia during the summer can intensify warming effects by a factor of 2 compared to winter.

Thirdly, Chapter 6 introduces the first tagging scheme for aircraft SO_4 aerosols implemented within the EMAC modeling framework, representing one of the few existing schemes of its kind within the climate modeling community. This advancement enables the analysis of SO_4 aerosols arising from aviation-induced sulfur dioxide (SO_2) and sulfuric acid (H_2SO_4), tracing their movement from cruise altitude to the surface over a period of three months. The results indicate that SO_2 transport patterns and lifetimes are heavily influenced by atmospheric circulation, with seasonal variability playing a key role. For example, SO_2 has a median e-folding time of 22 days in January, dropping to 14 days in July as increased solar radiation boosts OH levels, accelerating SO_2 oxidation. The conversion of SO_2 into H_2SO_4 further drives a delayed increase in H_2SO_4 mixing ratios days after emission. This seasonal difference also impacts SO_4 production efficiencies, which rise significantly from winter to summer, increasing by 41% and 174% for the soluble Aitken and accumulation modes, respectively. Cloud satellite data from ESA's Cloud_cci project further highlights AIRTRAC's ability to predict when aviation SO_4 emissions at cruise altitudes are most likely to interact with low-level liquid clouds. These clouds are particularly abundant in the southern tropics (0°-30° S) at pressure altitudes below 800 hPa, with the largest cloud cover observed during the summer simulation period (July-September 2015). Aviation-emitted SO_4 in the Southern tropics is more likely to interact with these clouds compared to emissions in the northern mid-latitudes, as the former descends more rapidly to lower altitudes. In contrast, emitted SO_4 in the Northern mid-latitudes can linger near its release altitude for about a week, resulting in lower concentrations of SO_4 reaching lower altitudes, thus reducing the likelihood of aerosol-cloud interactions.

Lastly, the improved and expanded version of AIRTRAC has contributed to the development of a new generation of reduced-order surrogate models, known as the probabilistic algorithmic climate change functions (paCCFs). These models, characterized by their fast computational speeds, have the potential to support operational, technological and regulatory interventions, as discussed in Chapter 7. Furthermore, AIRTRAC could be integrated into climate-optimized aircraft design workflows to identify cruise altitudes that minimize climate impact. However, several steps remain to be addressed before these applications can be fully realized. AIRTRAC's estimates of SO_4 concentration changes must be converted into iRF changes and validated against the few existing SO_4 tagging models. This will yield a more accurate estimate of aviation's net climate impact.

SAMENVATTING

De snelle en veerkrachtige groei van de luchtvaart in de afgelopen decennia benadrukt de dringende noodzaak om de negatieve milieueffecten van de sector aan te pakken, waaronder zowel chemische als akoestische emissies. Deze emissies vormen aanzienlijke uitdagingen voor de volksgezondheid, natuur, landbouw en het milieu als geheel. De nadruk in dit onderzoek ligt op de klimaateffecten van de luchtvaart, die momenteel naar schatting bijdragen aan 3-5% van het totale antropogene klimaateffect, veroorzaakt door zowel CO_2- als niet-CO_2-verontreinigende stoffen. Gezien het huidige groeipad na de pandemie kan dit aandeel verder toenemen, vooral omdat de luchtvaart een van de moeilijkste sectoren blijft om volledig te decarboniseren. Niet-CO_2-forcerende stoffen, zoals waterdamp (H_2O), stikstofoxiden (NO_x), contrails en aerosolen zoals roet en sulfaat (SO_4), zijn de belangrijkste bijdragers en zijn verantwoordelijk voor ongeveer twee derde van de totale klimaatimpact van de luchtvaart. In tegenstelling tot CO_2, dat een lange atmosferische levensduur heeft, zijn de klimaateffecten van deze forcers sterk afhankelijk van hun trajecten door de atmosfeer. Factoren zoals kruishoogte spelen hierbij een cruciale rol, wat het essentieel maakt om deze transportpatronen te bestuderen om hun klimaateffecten beter te begrijpen en te beperken.

De transportpatronen van door de luchtvaart veroorzaakte verontreinigende stoffen, zoals NO_x, zijn onzeker, waarbij de rol van aerosoltransport—met name sulfaat (SO_4)—bij het beïnvloeden van de optische eigenschappen van wolken bijzonder onduidelijk blijft. Dit proefschrift verbetert en breidt het Lagrangiaanse tagging-algoritme genaamd AIRTRAC uit, dat is geïntegreerd in het EMAC-modelraamwerk. AIRTRAC vergroot ons begrip van NO_x en, voor het eerst, van SO_4-transport door hun belangrijkste chemische reacties in de atmosfeer te volgen. In het bijzonder wordt het kortetermijneffect van NO_x op de productie van ozon (O_3) onderzocht, aangezien dit proces de dominante opwarmende factor is van de netto opwarmeffecten van NO_x-emissies door de luchtvaart. Vier belangrijke bijdragen voortkomend uit dit proefschrift worden uitgelicht.

Ten eerste vergelijkt dit onderzoek de prestaties van AIRTRAC met een submodel met hogere resolutie op mondiale schaal in Hoofdstuk 4. Deze vergelijking heeft een van de meest uitgebreide datasets opgeleverd die momenteel beschikbaar zijn voor het schatten van de onmiddellijke stralingsforcering van kortetermijninteracties tussen door luchtvaart veroorzaakte NO_x- en O_3-interacties. Deze dataset bestrijkt vijf geografische regio's, drie representatieve kruishoogtes en twee seizoenen. Uit deze analyse zijn schaalfactoren van 1,7 tot 5,9 afgeleid om de nauwkeurigheid van AIRTRAC te vergroten. Verder wordt in dit hoofdstuk vastgesteld dat het verschil tussen tagging- en perturbatiemethoden voor de luchtvaart systematisch is op mondiale schaal, waarbij tagging-schattingen gemiddeld 80% hoger zijn dan schattingen op basis van perturbatie.

Ten tweede introduceert Hoofdstuk 5 een nieuwe methode voor het efficiënt groeperen van grote aantallen luchtparceltrajecten met behulp van een clustering-algoritme

uit de neurowetenschap. Deze innovatieve aanpak identificeerde systematisch de meest waarschijnlijke transportpatronen voor elke regio. Er werd ontdekt dat sterke neerwaartse luchtstromen NO_x snel naar lagere hoogtes kunnen transporteren, waar het sneller wordt verwijderd dan langs trajecten die langer op de emissiehoogte blijven. Bovendien kan de O_3-productie toenemen met bijna een factor van 3 wanneer NO_x naar schonere regio's wordt getransporteerd, zoals Australazië, afhankelijk van het seizoen. Verder onthulde Hoofdstuk 4 een seizoensafhankelijkheid van de effecten van veranderingen in kruishoogte met betrekking tot NO_x-O_3-chemie. Zo kan vliegen op grotere hoogtes in Eurazië tijdens de zomer de opwarmingseffecten verdubbelen in vergelijking met de winter.

Ten derde presenteert Hoofdstuk 6 het eerste tagging-schema voor SO_4-aerosolen binnen het EMAC-modelraamwerk, een van de weinige schema's die momenteel bestaat. Deze vooruitgang maakt een eerste analyse mogelijk van SO_4-aerosolen die voortkomen uit door de luchtvaart veroorzaakte zwaveldioxide (SO_2) en zwavelzuur (H_2SO_4), waarbij hun beweging van kruishoogte naar het oppervlak over een periode van drie maanden wordt gevolgd. Resultaten tonen aan dat transportpatronen en de levensduur van SO_2 sterk worden beïnvloed door atmosferische circulatie, met seizoensvariabiliteit als een belangrijke factor. Zo heeft SO_2 een mediane e-voudige tijd van 22 dagen in januari, die afneemt tot 14 dagen in juli door toegenomen zonnestraling die OH-concentraties verhoogt en de oxidatie van SO_2 versnelt. De omzetting van SO_2 naar H_2SO_4 leidt tot een vertraagde toename van de H_2SO_4-mengverhoudingen enkele dagen na emissie. Dit seizoensverschil beïnvloedt ook de productie-efficiëntie van SO_4, die aanzienlijk stijgt van winter naar zomer, met een toename van 41% en 174% voor respectievelijk de oplosbare Aitken- en accumulatiemodi. Satellietgegevens over wolken van ESA's Cloud_cci-project benadrukken bovendien AIRTRAC's vermogen om te voorspellen wanneer SO_4-emissies door de luchtvaart op kruishoogte het meest waarschijnlijk interageren met laaggelegen vloeibare wolken. Deze wolken zijn bijzonder overvloedig in de zuidelijke tropen (0°–30°Z) op drukhoogtes onder 800 hPa, met de grootste wolkendekking waargenomen tijdens de zomerperiode. SO_4-emissies in de zuidelijke tropen hebben een grotere kans om met deze wolken te interageren in vergelijking met emissies in de noordelijke middenbreedten, omdat de eerstgenoemde sneller naar lagere hoogtes daalt. Daarentegen blijven emissies in de noordelijke middenbreedten ongeveer een week op de emissiehoogte hangen, wat resulteert in lagere concentraties SO_4 op lagere hoogtes, waardoor de kans op aerosol-wolkeninteracties wordt verkleind.

Tot slot heeft de verbeterde en uitgebreide versie van AIRTRAC bijgedragen aan de ontwikkeling van een nieuwe generatie geavanceerde modellen, bekend als probabilistische algorithmische klimaateffectfuncties (paCCFs). Deze modellen, gekenmerkt door hun snelle rekensnelheid, hebben het potentieel om operationele, technologische en regelgevende interventies te ondersteunen, zoals besproken in Hoofdstuk 7. Bovendien kan AIRTRAC worden geïntegreerd in ontwerpen voor klimaat-geoptimaliseerde vliegtuigen om kruishoogtes te identificeren die de klimaatimpact minimaliseren. Voordat deze toepassingen volledig kunnen worden gerealiseerd, zijn er echter enkele stappen nodig. AIRTRAC's schattingen van SO_4-concentratieveranderingen moeten worden omgezet in iRF-veranderingen en gevalideerd worden tegen de weinige bestaande SO_4-taggingmodellen. Dit zal leiden tot een nauwkeurigere schatting van de netto klimaatimpact van de luchtvaart.

NOMENCLATURE

Acronyms

ACACIA	Advancing the Science for Aviation and Climate
ATR	Average Temperature Response
AVHRR-AM	Advanced Very High Resolution Radiometer ante meridiem
BDC	Brewer-Dobson Circulation
BMIL	Base-model Interface Layer
BML	Base-model Layer
CCF	Climate Change Functions
CCI	Climate Change Initiative
CCM	Climate-chemistry Model
CCN	Cloud Condensation Nuclei
CDNC	Cloud Droplet Number Concentration
CRM	Climate-response Model
CTM	Chemistry-transport Model
CTP	Cloud Top Pressure
DKRZ	Deutsches Klimarechenzentrum
ECHAM	European Centre for Medium-Range Weather Forecasts – Hamburg
EI	Emission Index
EMAC	ECHAM - MESSy Atmospheric Chemistry Model
ERF	Effective Radiative Forcing
ESA	European Space Agency
EU ETS	European Union Emissions Trading Scheme
EU	European Union
FSC	Fuel Sulfur Content

GCM	General Circulation Model
GHG	Greenhouse Gas
HEFA	Hydro-processed Esters and Fatty Acids
HSR	High-speed Rail
IAGOS	In-service Aircraft for a Global Observing System
IATA	International Air Transport Association
IPCC	Intergovernmental Panel on Climate Change
ISA	International Standard Atmosphere
ISCCP	International Satellite Cloud Climatology Project
ISSR	Ice Supersaturated Region
ITCZ	Inter-tropical convergence zone
KG	Knowledge Gap
LCF	Liquid Cloud Fraction
MESSy	Modular Earth Submodel System
MMR	Mass Mixing Ratio
NAFC	North Atlantic Flight Corridor
NOAA	National Oceanic and Atmospheric Administration
paCCFs	Probabilistic-algorithmic CCFs
PACE	Plankton, Aerosol, Cloud, ocean Ecosystem
RF	Radiative Forcing
RH	Relative Humidity
RPK	Revenue Passenger Kilometers
SAF	Sustainable Aviation Fuel
SMCL	Submodel Core Layer
SMIL	Submodel Interface Layer
SST	Sea Surface Temperature
TOA	Top of the Atmosphere
UTLS	Upper Troposphere/Lower Stratosphere

UV	Ultra-violet
VMR	Volume Mixing Ratio

Chemical species

$(NH_4)_2SO_4$	Ammonium sulphate
Ar	Argon
C_3H_6	Propene
C_6H_6	Benzene
$CaCO_3$	Calcium carbonate
CFCs	Chlorofluorocarbons
CH_3	Methyl radical
CH_3O_2	Methylperoxy radical
CH_4	Methane
Cl	Chloride
CO_2	Carbon dioxide
CO	Carbon monoxide
H_2O_2	Hydrogen peroxide
H_2O	Water vapor
H_2SO_3	Sulphurous acid
HCHO	Formaldehyde
HNO_3	Nitric acid
HO_2	Hydroperoxyl radical
N_2	Molecular nitrogen
N_2O	Nitrous oxide
NH_3	Ammonia
NH_4	Ammonium
NH_4HSO_4	Ammonium bisulphate
NMHC	Non-methane Hydrocarbons
NO_2	Nitrogen dioxide

NO_3	Nitrate
NO	Nitric oxide
NO_x	Nitrogen oxides
O_2	Molecular oxygen
O_3	Ozone
OH	Hydroxyl radical
PMO	Primary mode ozone
RO_2	Organic peroxy radical
SO_4	Sulphate
SWV	Stratospheric Water Vapor
UHC	Unburnt hydrocarbons
VOCs	Volatile organic compounds

1

INTRODUCTION

1.1. MOTIVATION

AVIATION is the safest and, in many cases, the fastest mode of transport, connecting distant regions of the world [1]. It plays a vital role in driving economic growth, promoting knowledge exchange, and strengthening diplomatic relations. The rapid and resilient growth of the industry in recent decades highlights its significant societal and economic influence [2]. Before the COVID-19 pandemic, commercial aviation experienced a steady annual growth rate of approximately 5-6% [3], according to the International Air Transport Association (IATA). The pandemic caused the sharpest decline in revenue passenger kilometers (RPK) in aviation history, but by early 2024, demand had already fully recovered, even surpassing 2019 levels by 5% (Fig. 1.1 illustrates the global demand for air travel, measured in RPK, from the start of 2019 through early 2024). This rapid recovery and sustained growth have the potential to exacerbate aviation's negative externalities, particularly those stemming from acoustic and chemical emissions. Aircraft noise, for example, is linked to high levels of annoyance and numerous health issues, including cardiovascular disease, hypertension, and anxiety [4–6]. Similarly, aviation gaseous and particulate emissions contribute to poor air quality, which is responsible for tens of thousands of premature deaths worldwide each year [7]. Moreover, aviation chemical emissions also disrupt Earth's radiation balance, contributing approximately 4- 5% of total anthropogenic global warming [8, 9]. Although this may seem modest compared to other sectors such as road transport, which accounts for around 11% of human-induced warming [9], if left unchecked, aviation's contribution could soon surpass that of other transport sectors for three key reasons:

1. The aforementioned aviation industry's rapid and resilient growth will continue to translate into annual expansion, even in the face of global political and health crises [2, 3].

2. Unlike other modes of transport, aircraft release pollutants at altitudes where certain climate effects are significantly amplified. For example, the efficiency of short-term ozone (O_3) production from nitrogen oxide (NO_x) emissions is between two

to four times higher in the upper troposphere/lower stratosphere (UTLS) compared to emissions from shipping [10, 11]. Furthermore, emissions at these higher altitudes facilitate the long-range transport of harmful chemical species, impacting air quality and climate in regions far removed from the initial emission source [12, 13].

3. Aviation is arguably the most difficult sector to decarbonize, as no single solution can effectively address all of its environmental externalities while maintaining the benefits it brings. Mitigation efforts often involve trade-offs, where reducing the impact of one climate forcer[1] may exacerbate another. Various mitigation strategies exist, but each comes with its own limitations and challenges, making it difficult to fully neutralize the sector's environmental footprint:

   - **Technical solutions** encompass design modifications to airframe and propulsion systems, including adaptations for hydrogen propulsion, which Airbus now anticipates introducing between 2040 and 2045 at the earliest for its ZEROe fleet [14, 15]—or aerodynamic enhancements, like drag-reducing "sharklets" on A320neo aircraft [16] and novel configurations like the "Flying-V," tested by the Delft University of Technology and KLM [17]. A significant drawback of these measures is the lengthy testing and implementation process [18]. Sustainable aviation fuels (SAFs) are also part of this category. Among the most advanced is HEFA (Hydro-processed Esters and Fatty Acids) SAF, which is produced from renewable lipids like plant oils and waste fats. While HEFA SAF reduces CO_2 emissions by approximately 30%, its cost is about 120% higher than that of conventional kerosene. Achieving a 90% emission reduction would require SAFs costing over four times as much as conventional kerosene at current production rates, significantly constraining the scalability required to supply the global aviation fleet [19].
   - **Market-based solutions** enforce emissions targets by creating economic incentives or imposing penalties for exceeding emission allowances. An example is the European Union Emissions Trading Scheme (EU ETS), which allocates transferable carbon dioxide (CO_2) emission permits to corporations like airlines. Companies exceeding their allowances face fines, while those under their limits can sell unused permits. Based on the Kyoto Protocol [20], aviation CO_2 impacts were incorporated into the scheme in 2008. More recently, as of December 2022, agreements will require airlines to also account for non-CO_2 effects [21]. While EU ETS is relatively simple and cost-effective compared to operational and technological measures, its effectiveness is questioned, as some firms may buy extra allowances, enabling continued pollution rather than reducing emissions [22].
   - **Operational solutions** focus on adjusting flight operations to reduce climate impact. Climate-optimal routing, for instance, aims to avoid climate-sensitive regions during flight trajectories, minimizing overall environmental effects. Implementing this requires accurately quantifying all climate forcers, from

[1] A factor that can change the energy balance of Earth's atmosphere.

well-understood CO_2 to the more uncertain aerosol indirect effects. This approach can leverage climate change functions (CCFs), which are four-dimensional representations (time, latitude, longitude, altitude) quantifying the climate impact of emissions [23]. These are then integrated into flight optimization tools to design routes, considering air traffic and performance constraints. The key challenge lies in the uncertainty surrounding aviation's net climate impact, particularly due to poorly understood forcers like aerosol indirect effects.

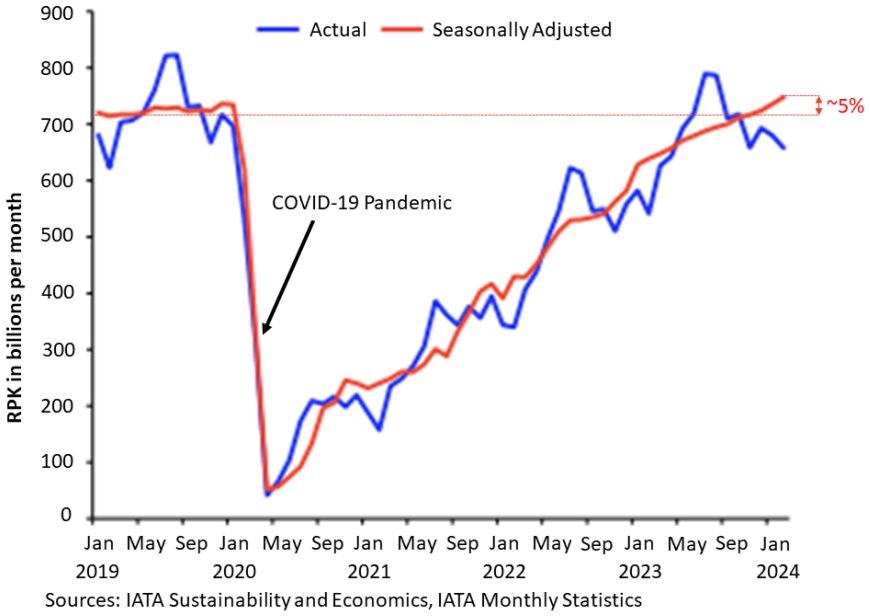


Figure 1.1: Monthly evolution of global air travel RPK, expressed in billions per month. Total RPK in February 2024 was 5.7% higher than the corresponding month in 2019. This marks the first full recovery of the aviation sector since the COVID-19 pandemic. Adapted figure and data from [24].

This dissertation focuses on some of the environmental impacts of aviation, which emanate from the complex interactions between aircraft-induced emissions and the atmosphere. Aircraft emissions include both CO_2 and non-CO_2 species, such as nitrogen oxides (NO_x), carbon monoxide (CO), water vapor (H_2O), soot and sulfur dioxide (SO_2). By altering the atmosphere's ability to reflect and absorb radiation, these pollutants can disrupt Earth's energy balance, which is determined by the difference between the incoming solar radiation and the outgoing terrestrial infrared radiation. Aircraft may destabilize this flow of energy by producing warming and cooling effects through direct greenhouse gas (GHG) emissions like H_2O, indirect alterations to GHG concentrations via NO_x-O_3 interactions, and through modifications to cloud lifetimes and reflective properties from aerosol-cloud interactions [25]. To assess the radiative imbalance from these emissions, two key metrics are typically employed: instantaneous radiative

forcing (iRF) and effective radiative forcing (ERF). Instantaneous RF represents the net change in radiative fluxes at either the top of the atmosphere (TOA) or the climatological tropopause, relative to preindustrial times (1850-1900). This metric is calculated by assuming fixed atmospheric and surface temperatures and is commonly used to quantify the direct effects of GHG emissions. However, it is limited in capturing the full scope of aerosol-cloud interactions. In contrast, ERF includes rapid adjustments in atmospheric conditions, such as changes in cloud cover, atmospheric water vapor concentrations, and the vertical temperature profile. Although slower feedbacks associated with atmospheric temperature changes are considered, surface conditions are typically kept constant in ERF calculations, so feedbacks dependent on changes in global mean surface temperature are not included [26]. Overall, ERF provides a more comprehensive representation of climate impacts, particularly for aerosols [26, 27].

The climate impact of CO_2 is considered the most well understood among all aviation-related climate forcers and is currently estimated to contribute approximately a third of the total net warming effect of aviation, as measured by ERF [27]. Carbon dioxide is a long-lived greenhouse gas that persists in the atmosphere for thousands of years. As a result, both past and present CO_2 emissions will continue to drive global warming for centuries to come [28]. The long atmospheric lifetimes of CO_2 also ensure that it becomes well mixed throughout the atmosphere, making the release location of emissions and their subsequent trajectories less significant for their climatic impact [29].

The remaining two-thirds of aviation's climate impact arises from non-CO_2 forcers, a term typically used to describe the collective effects of NO_x, H_2O, contrails, and aerosols such as soot and sulfate (SO_4). Unlike CO_2, these forcers have significantly shorter atmospheric lifetimes. Consequently, their transport pathways, seasonal variability, meteorological conditions, and background atmospheric composition play a crucial role in shaping their overall climate impact. The atmospheric trajectory of a pollutant becomes particularly relevant as it may determine whether a chemical species is rapidly removed at lower altitudes or remains at higher altitudes, thereby extending its lifetime and likely amplifying its climate influence.

Figure 1.2 presents the main climate forcers related to aviation, showing their mean ERF and RF values. Among these, CO_2 has a relatively narrow uncertainty interval, with its ERF estimated between 28 and 40 mW m^{-2} (mean of 34.3 mW m^{-2}). In contrast, aerosol-cloud interactions involving soot and sulfate remain poorly understood, with no established best estimates. This dissertation aims to address this gap for SO_4 by visualizing its transport pathways and examining seasonal variations in its atmospheric lifetime. Other pollutants like NO_x have complex interactions with greenhouse gases, contributing to short-term ozone (O_3) production while also leading to longer-term reductions in background O_3, methane (CH_4) and stratospheric water vapor (SWV). Another key focus of this research is the short-term warming effect of NO_x-induced O_3, as it constitutes the primary warming mechanism within the net NO_x effect and ranks as the second largest contributor to aviation-related warming. Its 90% ERF confidence interval ranges from 32 to 76 mW m^{-2}, with a mean of 49.3 mW m^{-2} [27].

The climate effects of aviation NO_x emissions exhibit significant spatial and temporal variability. Previous research has explored how these effects vary with cruise altitude [30, 31], geographic emission locations [32, 33], seasonal variations [34, 35], background NO_x

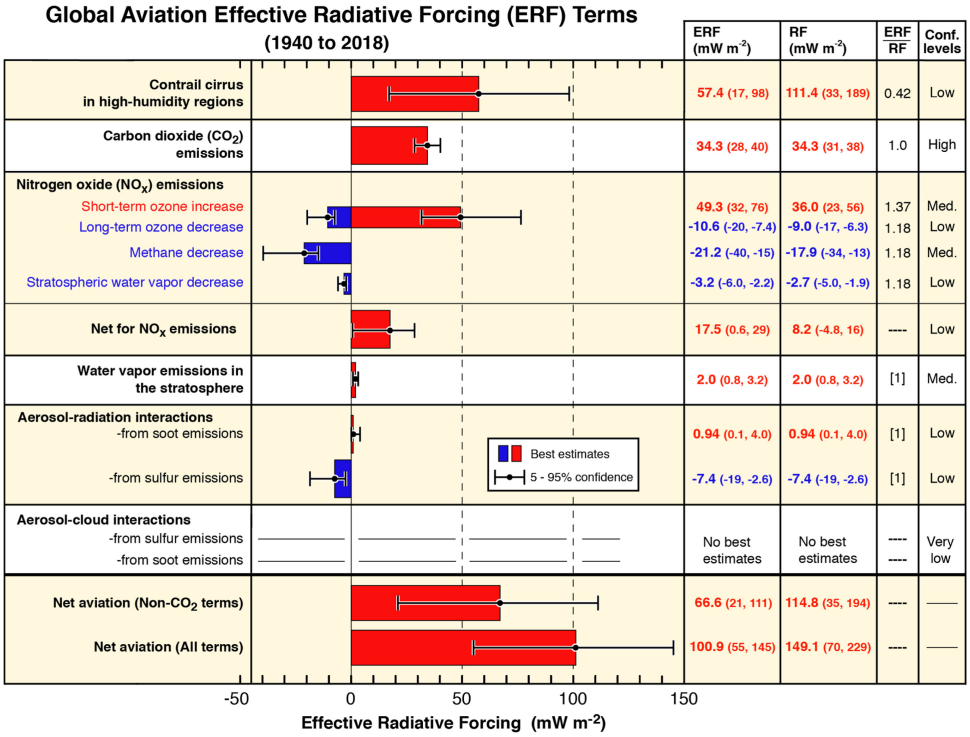


Figure 1.2: Overview of aviation climate forcers: the horizontal axis shows the effective radiative forcing (ERF) of each forcer in mW m^{-2} for the year 2018, with mean estimates and 90% confidence intervals presented in the ERF column. The ERF for CO_2 and CH_4 reflects cumulative global aviation emissions from 1940 to 2018, whereas the ERF for shorter-lived forcers considers only emissions from 2018. Radiative forcing (RF) values are also shown. Red color bars and font indicate warming effects, while blue represents cooling effects, with uncertainties represented by whiskers. Confidence levels indicate the current level of understanding for each forcer. Figure reproduced from [27].

concentrations [11], and meteorological conditions [36, 37]. The climate impact of NO_x emissions is particularly sensitive to solar radiation and background atmospheric conditions, as increased sunlight enhances O_3 production through reactions between atomic and molecular oxygen, while lower background NO_x levels may improve the efficiency of O_3 formation [32]. The transport pathways of emitted NO_x play a critical role in determining whether it reaches regions conducive to these processes, which makes an understanding of its atmospheric transport essential to predict its climate effects. However, most studies referenced above are limited by their focus on emission scenarios in which North American and European flight routes account for approximately 80% of global air traffic [31, 38–40]. As a result, these studies do not fully model the complete intercontinental journey of aviation NO_x and associated O_3, from its emission to its transport across the globe and its eventual removal from the atmosphere, which typically occurs within a few months. Moreover, most assessments of the climate impact of aviation, including those presented in Fig. 1.2, use the perturbation method, which is only effective

in quantifying the impact of a change in emissions. In contrast, the tagging approach offers an additive method that allows the attribution of a sector's contribution to a total quantity, which can be radiative forcing. Few studies have attempted to quantify the contribution of aviation using this tagging approach [11, 23, 31, 41].

Aerosol climate effects are typically categorized into direct and indirect effects. Direct effects influence Earth's energy balance by scattering and absorbing solar and thermal infrared radiation, depending on the aerosol's optical properties. Indirect effects, in contrast, involve aerosol-induced changes to cloud microphysical properties, such as cloud albedo and lifetime. Aviation-induced aerosols mainly include soot and SO_4. This dissertation focuses on SO_4 over soot due to past research findings [42] demonstrating the greater ability of sulfate aerosols to alter cloud properties. The substantial uncertainties surrounding indirect effects stem largely from the limited understanding of aerosol transport mechanisms, including their vertical transport, large-scale horizontal advection, and variations in microphysical processes along these pathways [43, 44].

Global three-dimensional climate-chemistry simulations, which are crucial for advancing our understanding of aviation climate effects, are computationally intensive and time-consuming. As a result, they cannot be routinely applied in operational contexts where multiple simulations would need to be completed within minutes for daily flight planning or for airlines to regularly assess their climate footprint. Currently available, more computationally efficient tools, such as AirClim [45] and algorithmic Climate Change Functions (aCCFs) [46], offer faster estimates, often within minutes. However, these tools have significant limitations that hinder their practical use in flight operations. AirClim, for example, provides only global mean estimates for CO_2 and non-CO_2 emissions, making it unsuitable for individual flight-level applications. However, aCCFs can be applied to specific flights, but they suffer from reduced accuracy and lack uncertainty quantification in their estimates. Consequently, there is a clear need for a tool that overcomes these limitations, offering more accurate flight-specific climate impact assessments with reliable uncertainty quantification for operational use.

1.2. KNOWLEDGE GAPS

Given the challenges outlined in mitigating and accurately quantifying aviation climate impacts, this dissertation aims to address the following key knowledge gaps (KG):

KG1. Transport phenomena are central to understanding the climate effects induced by aviation, yet few studies have conducted a complete trajectory analysis of aviation's emitted pollutants from the moment they are released until their removal from the atmosphere. A global assessment linking the transport patterns of such pollutants to their climate impact is therefore needed to fully understand the spatio-temporal variability of the climate impacts and contributions to atmospheric composition from aviation emissions.

KG2. A large number of previous studies have focused on quantifying aviation's climate impacts primarily along the more congested North Atlantic Flight Corridor (NAFC). With heterogeneous growth rates in flight traffic across the globe [47], a global quantification of regional sensitivities of climate forcers to factors like emission time, altitude and others is of high relevance to predict future climate impacts.

KG3. The estimates of aviation climate effects shown in Fig.1.2 reflect years of aviation climate research and compare forcers of varying time spans on a common scale. However, as a limitation, only the perturbation method was applied in their results, which when trying to quantify aviation's contribution is limited, as it may exclude or oppositely overcount contributions from other sectors [41]. Therefore, additional studies that extensively compare both methods are important for a more complete assessment of aviation climate effects.

KG4. Large uncertainties remain regarding aviation's non-CO_2 climate forcers. The most uncertain, according to Lee et al. [27], are aerosol-cloud interactions (i.e., aerosol indirect effects) with very few available estimates, especially for the tagging method. This uncertainty precludes an accurate estimate of aviation's net climate impact, making it unclear if the cooling from SO_4 interactions with clouds is sufficient to offset aviation's warming components. Furthermore, the uncertainty in SO_4 transport patterns is particularly critical to predict aerosol-cloud interactions, as accurate transport modeling is vital to understanding when and where they are more likely to occur.

KG5. Computationally efficient methods are rapidly becoming vital for sustainable decision-making. Time- and resource-intensive climate-chemistry simulations must be made more efficient not only to produce timely estimates of non-CO_2 forcers for airlines, but also to aid in the implementation of climate-optimized routing, which require daily recommendations of optimal routes.

1.3. DISSERTATION OVERVIEW

1.3.1. OBJECTIVES

This thesis aims to increase current knowledge of aviation climate impacts by expanding our understanding of the link between the transport of pollutants and their respective environmental impact. As referred to in section 1.2, it is mainly focused on studying the transport of two major chemical species: NO_x and SO_4. For NO_x, the global spatiotemporal dependence of short-term O_3 production is investigated, as this is the main component within the net NO_x effect that drives the warming effect. The thesis then focuses on the transport patterns of SO_4 particles and assesses which emission conditions (that is, location and season) maximize the concentrations of these aerosols so that they are more likely to reach lower-level liquid clouds and potentially alter their microphysical properties. For the specific purpose of analyzing the transport of both species, a reduced-order Lagrangian tagging submodel called AIRTRAC (Supplement of Grewe et al. [23]) was improved and further developed, which was originally conceived solely for the scrutiny of gaseous species. The specific objectives of this dissertation each address one or more of the KGs identified in Section 1.2 and are outlined as follows:

1. Understand the spatiotemporal dependence of aviation short-term NO_x-O_3 climate effects on emission altitude, region, and season of emission, as well as how transport patterns play a role. Addresses **KG1** and **KG2**.
2. Quantify the differences between the tagging and perturbation methods in the context of short-term aviation NO_x-O_3 chemistry. Derive correction factors for a

reduced-order Lagrangian tagging submodel (AIRTRAC) by comparing it to a high-fidelity tagging submodel to leverage its computational efficiency in sustainable decision-making. Addresses **KG3** and **KG5**.

3. Analyze how transport patterns influence SO_4 aerosol concentrations and identify conditions under which these aerosols are more likely to interact with low-level liquid clouds using the novel Lagrangian tagging submodel, AIRTRAC 2.0. Addresses **KG4**
4. Demonstrate how the datasets generated by AIRTRAC can power faster tools that can be trained to provide climate warming effects in a manner timely enough for climate-optimal routing. Addresses **KG5**

1.3.2. STRUCTURE

This dissertation comprises a total of eight chapters. Figure 1.3 provides a diagrammatic summary of its structure along with a brief explanation of the purpose of each chapter (Ch.) and the corresponding KGs it addresses.

Ch. 2 This chapter provides a theoretical overview of key concepts, including details on radiative forcing, NO_x-O_3 chemistry, and aerosol microphysics.

Ch. 3 An overview is provided of the climate-chemistry model EMAC, highlighting the model itself and detailing its most relevant submodels, a few of which have been further developed within this dissertation.

Ch. 4 This chapter compares the perturbation and tagging methods by calculating short-term O_3 production from aviation NO_x at various altitudes, regions and emission times. It validates the reduced-order AIRTRAC submodel against a high-fidelity tagging submodel, yielding correction factors and error estimates for AIRTRAC. Through this analysis, **KG2** is addressed by deriving regional sensitivities for NO_x-O_3 chemistry, while **KG3** is fulfilled by providing a detailed global comparison between the tagging and perturbation methods for aviation.

Ch. 5 The Lagrangian tagging capabilities of AIRTRAC are leveraged to provide a global characterization of transport pathways of aviation NO_x and O_3 along with an estimate of the warming in terms of RF, thereby addressing **KG1**.

Ch. 6 Chapter 6 presents the newly developed AIRTRAC 2.0 sub-model, which provides a Lagrangian tagging scheme for aviation-induced SO_4. An analysis of the transport patterns leading to the largest and smallest concentrations of the SO_4 aerosol is conducted. This addresses **KG4**.

Ch. 7 The dataset generated throughout this dissertation has been used to produce the probabilistic-algorithmic climate change functions (paCCFs), which provide, along with an estimate of the mean instantaneous RF, heteroskedastic confidence intervals for every emission scenario in a computationally efficient manner (addresses **KG5**).

Ch. 8 The concluding chapter provides a summary of the main contributions and provides suggestions for future research.

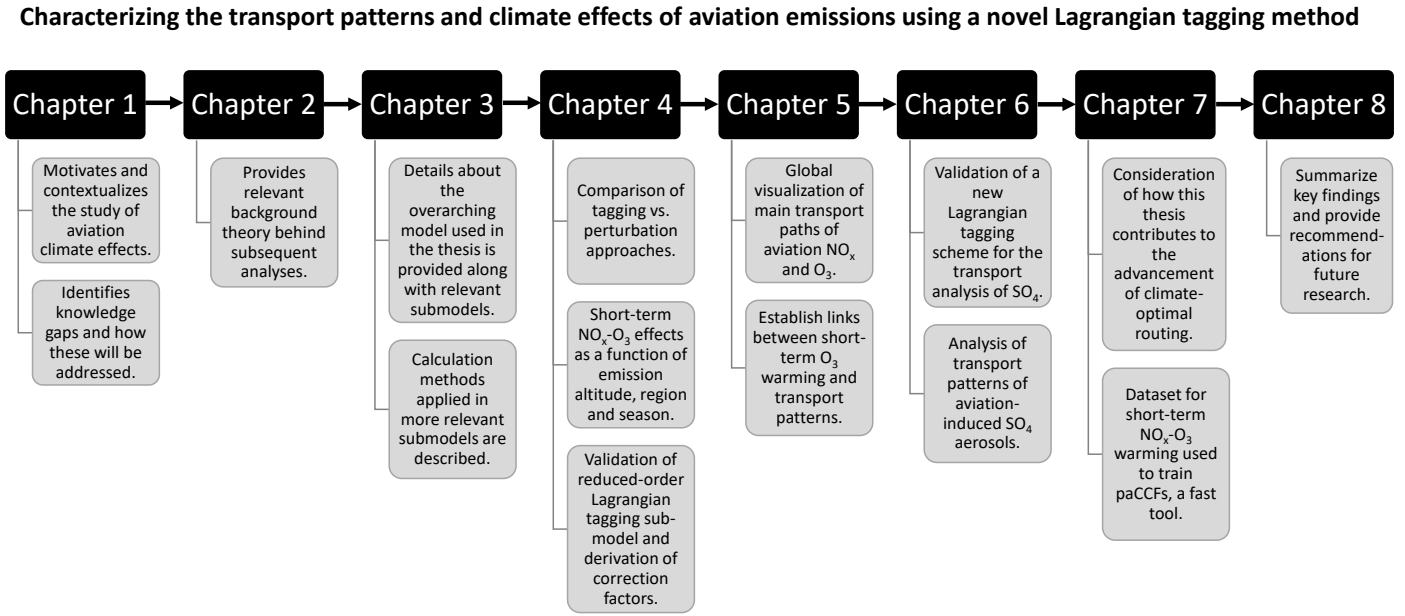


Figure 1.3: Structural overview of dissertation.

2

BACKGROUND

This chapter presents a theoretical overview of the foundational concepts central to this dissertation. Subsection 2.1 covers essential aspects of atmospheric science, including the planetary radiation budget, atmospheric dynamics, and chemistry. Subsection 2.2 delves into key principles of aerosol mechanics and microphysical processes. Finally, subsection 2.3 reviews the climate effects of subsonic aviation, along with current research on the transport pathways of aviation emissions.

2.1. THE ATMOSPHERE

THe atmosphere is a complex mixture of gases bound to Earth by gravity, with a total estimated mass of approximately 5.14×10^{18} kg, of which less than 1% or 1.25×10^{16} kg is water vapor, a quantity that varies seasonally [48]. In a dry state (excluding water vapor), the atmosphere consists primarily of molecular nitrogen (N_2, 78%) and oxygen (O_2, 21%), with the remaining 1% made up of trace gases, the most abundant of which is argon (Ar) [49]. However, certain trace gases, including H_2O, have a significant impact on the Earth's energy balance and are classified as direct greenhouse gases (GHGs), highlighted in red in Fig. 2.1. Human activities such as aviation, shipping, and agriculture alter the concentrations of these GHGs, directly contributing to global warming. This subchapter 2.1 explores essential concepts related to the structural, radiative, dynamic, and chemical characteristics of the atmosphere.

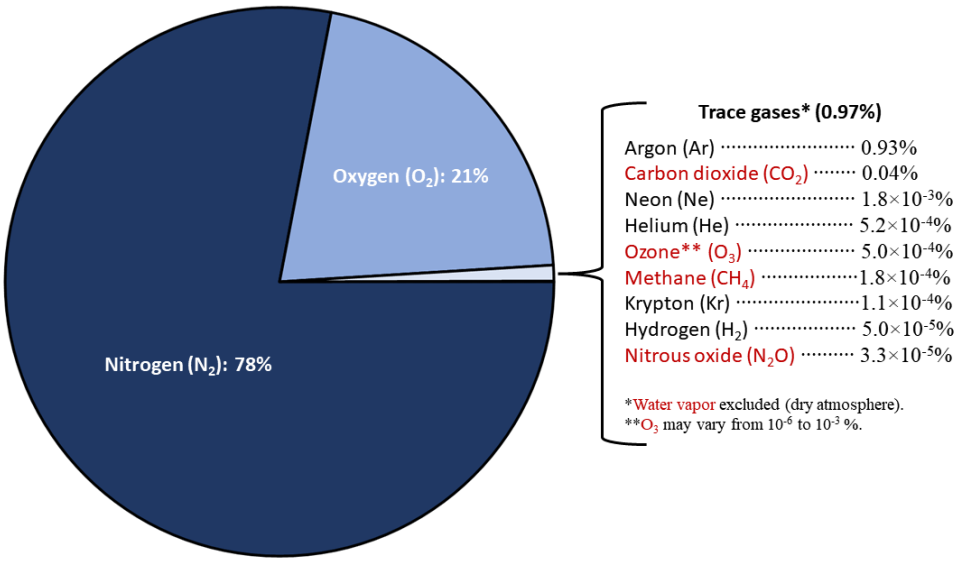


Figure 2.1: Pie chart illustrating the composition of the dry atmosphere. This figure has been constructed using data from [49]. The gases in red are the direct greenhouse gases.

2.1.1. VERTICAL STRUCTURE

The vertical structure of Earth's atmosphere is organized based on temperature profiles, resulting in the following layers: the troposphere, stratosphere, mesosphere, thermosphere, and exosphere. For aviation, the most relevant layers are the troposphere and stratosphere.

The lowermost layer, the troposphere, extends from Earth's surface to the tropopause, whose altitude varies by latitude and season, but is generally between 10 and 15 km [50]. This layer is highly unstable and turbulent due to warming from the Earth's surface, leading to frequent convective events, strong wind shear (especially near the tropopause [51]), and thunderstorms. The troposphere accounts for about 85% of the total mass of

the atmosphere. According to the International Standard Atmosphere (ISA), its temperature decreases linearly with altitude, with an average lapse rate of 6.5 K/km [49, 52].

Above the tropopause lies the stratosphere, extending up to the stratopause at approximately 50 km. Characterized by greater vertical stability, the stratosphere has a quasi-linear increase in temperature with altitude, reaching around 0°C at the stratopause. This temperature inversion is caused by absorption of ultraviolet (UV) radiation in the ozone (O_3) layer, which protects life on Earth from harmful UV rays. The stability in this layer results in longer residence times for pollutants deposited by aircraft [49, 50, 53]. A significant concern related to the resurgence of supersonic aviation is the potential for NO_x emissions at these altitudes to damage the protective O_3 layer [54].

In the mesosphere, which extends above the stratopause, temperatures again decrease with altitude, reaching the coldest point of the atmosphere at the mesopause (approximately 90-100 km), where temperatures can drop to nearly -90°C. Unlike the stratosphere, the mesosphere experiences more turbulence and vertical mixing and has lower O_3 levels. Its cooler temperatures are mainly due to the radiative cooling by CO_2 [49, 50].

Beyond the mesopause lies the thermosphere, where temperatures rise sharply due to UV absorption by N_2 and O_2. Above 100 km, the low air pressure means that atmospheric transport occurs primarily through molecular diffusion. The thermopause is then located between 250 and 500 km [49, 50].

Above 500 km is the exosphere, where satellites orbit and energetic gas molecules can reach escape velocity and enter space [49, 55]. With the exception of the exosphere, Fig. 2.2 [56] illustrates the vertical structure of the atmosphere and its temperature profile across each layer.

PRESSURE ALTITUDE

To describe vertical positions in the atmosphere, pressure altitudes (in hectopascals or hPa) are often used instead of geometric altitudes (in meters) for practicality. The altitudinal variation of pressure can be described by the hydrostatic approximation (Eq. 2.1), which is generally valid in the absence of extreme convective events. According to this approximation, the rate of change of atmospheric pressure p with respect to geometric altitude z depends on Earth's gravitational acceleration g (assumed constant given the relatively small scale height of the atmosphere compared to Earth's radius) and the density of air (ρ_{air}) as a function of z, as follows [49]:

$$\frac{\mathrm{d}p}{\mathrm{d}z} = -\rho_{\text{air}}(z) \cdot g. \tag{2.1}$$

Equation 2.1 can then be rewritten in terms of the pressure p by applying the ideal gas law, ergo replacing the air density with $\rho_{\text{air}} = \frac{p}{RT}$, where R is the specific gas constant for dry air and T is the air temperature. Integrating both sides from the surface to an altitude z then results in the following analytical expression for the pressure altitude (eventually leading to Eq. 2.2):

$$\frac{\mathrm{d}p}{p(z)} = -\frac{g}{RT(z)}\mathrm{d}z \xrightarrow{\text{Integrate}} [\ln p]\,|_{p(0)}^{p(z)} = -\int_0^z \frac{g}{RT(z)}\,dz.$$

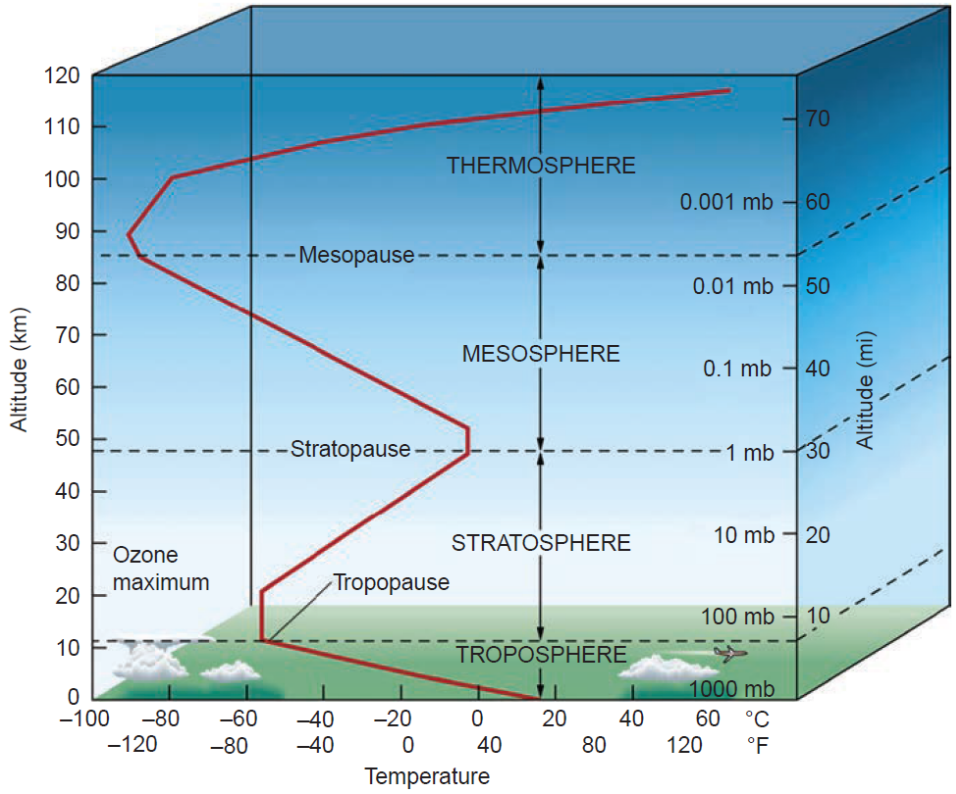


Figure 2.2: Vertical structure of Earth's atmosphere, the exosphere is not shown. Figure has been reproduced from [56].

Simplifying and solving for the pressure leads to:

$$p(z) = p(0) \cdot e^{\frac{-g}{RT(z)}z}. \tag{2.2}$$

GEOPOTENTIAL HEIGHT

Another vertical indicator of relevance is the geopotential height Θ (with units of meters), which is by definition the amount of gravitational potential energy required to lift a unit air mass from the surface up to a geometric altitude z, scaled by Earth's gravitational acceleration at mean sea level (g_0) [49]:

$$\Theta = \int_0^z \frac{g(\phi, z)}{g_0} dz. \tag{2.3}$$

The integrand in Eq. 2.3 is Earth's variable gravity as a function of the latitude ϕ and the geometric altitude z. The geopotential height at constant pressure levels is especially useful in understanding the motion of air masses, as these have a tendency to flow along its contours. Θ is also convenient for identifying high pressure ridges (regions characterized by sinking air) and aiding in anticyclone detection [57, 58].

2.1.2. EARTH'S RADIATION BUDGET

Electromagnetic radiation from the Sun serves as Earth's primary energy source. The Sun emits energy throughout the entire range of the electromagnetic spectrum, with approximately 40% of its energy in the visible light range (400–700 nm) and about 10% in the ultraviolet (UV) range (wavelengths up to 0.4 μm) [50, 59]. In contrast, the Earth emits thermal infrared (IR) radiation at significantly longer wavelengths, up to around 10 μm [49]. Due to this difference in wavelength, solar radiation is commonly referred to as shortwave radiation, whereas terrestrial radiation is classified as longwave radiation. The balance between incoming shortwave solar radiation and outgoing longwave terrestrial radiation primarily determines Earth's surface and atmospheric temperatures.

The total solar energy flux that reaches Earth, known as the solar constant S_0, averages around 1366 W/m^2 at the mean distance of the Earth from the Sun [49, 60]. However, the mean solar flux received by Earth is calculated by scaling this amount by Earth's surface area, approximated using a spherical geometry. This results in an intercepted energy flux of $S_0/4 = 341.5$ W/m^2 [49]. While Earth absorbs a significant portion of this energy, a substantial fraction is re-emitted as IR radiation. Without this re-emission, Earth's surface temperature would reach nearly 800,000 K after 10^9 years [61].

Not all of Earth's thermal emissions return directly to space; some are absorbed and re-emitted by the atmosphere, reflected by clouds and aerosols, or trapped by greenhouse gases (see Fig. 2.1). Additional energy is exchanged as latent heat through processes like H_2O condensation and evaporation. A detailed overview of these processes is shown in Fig. 2.3 [62].

To quantify how these energy flows influence Earth's surface temperature, T_E, a simplified model of the Earth-atmosphere (single-layer atmosphere) is used to derive this value. The following simplifying assumptions and considerations apply to this derivation, which are based on [63]:

1. Planetary albedo α represents the fraction of energy that is reflected and scattered by a body. A value of 30 % is typically assumed for the reflectivity of clouds and the Earth's surface [49]. Specifically, 6 % of the incoming solar energy is back-scattered by the atmosphere, another 20 % is reflected by clouds and the final 4 % is reflected by the planet's surface [59]. In contrast, the absorptivity a indicates the amount of energy absorbed.
2. Earth and atmosphere radiate energy according to the Stefan-Boltzmann law with emissivities of ϵ_E and ϵ_A, respectively. A blackbody is classified as a perfect emitter and absorber of radiation, which then implies $\epsilon = 1$. For a gray body surface ($0 < \epsilon < 1$), the amount of thermal energy Q emitted in W/m^2 as a function of the Stefan-Boltzmann constant ($\sigma = 5.67 \times 10^{-8}$ W/(m^{2}K^4)) and its absolute temperature T is described by Eq. 2.4 [64]:

$$Q = \epsilon \sigma T^4. \tag{2.4}$$

3. The atmosphere is entirely transparent to shortwave solar radiation, but will absorb terrestrial longwave radiation with an absorptivity coefficient of a_A. According to Kirchhoff's thermal radiation law, a good emitter is likewise a good absorber, leading to $\epsilon_A = a_A$ [65].

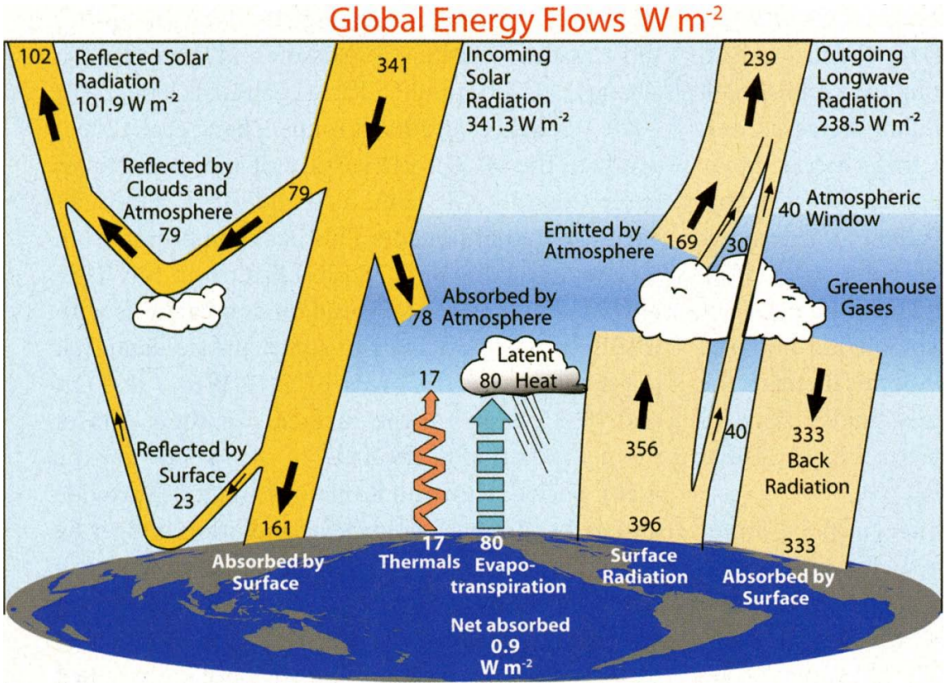


Figure 2.3: Earth's mean annual radiation budget between the years 2000 and 2004. Energy flows are expressed in W/m^2. Figure has been reproduced from [62].

4. The atmosphere is composed of several different gases with varying emissivities, but is assumed to have a uniform emissivity ϵ_A.
5. The Earth-atmosphere system is in radiative equilibrium, i.e., the incoming energy flux is equal to the outgoing energy flux.

Figure 2.4 depicts the flow of energy between a single-layer Earth-atmosphere system and the Sun. By performing an energy balance at both the Earth's surface and at the top of the atmosphere (TOA) and applying the previously outlined assumptions, the following system of equations is obtained (Eq. 2.5):

$$\begin{cases} \frac{S_0}{4}(1-\alpha) = (1-\epsilon_A)\epsilon_E \sigma T_E^4 + \epsilon_A \sigma T_A^4, & \text{TOA} \\ \epsilon_E \sigma T_E^4 = \frac{S_0}{4}(1-\alpha) + \epsilon_A \sigma T_A^4, & \text{Earth's surface.} \end{cases} \tag{2.5}$$

Solving the system shown in Eq. 2.5 for the Earth's surface temperature T_E yields the following expression in terms of the planetary albedo α, the Earth's emissivity ϵ_E, the solar constant S_0 with a value of 1365 W m^{-2} [49] and the emissivity of the atmosphere ϵ_A:

$$T_E = \sqrt[4]{\frac{S_0(1-\alpha)}{2\sigma\epsilon_E(2-\epsilon_A)}}. \tag{2.6}$$

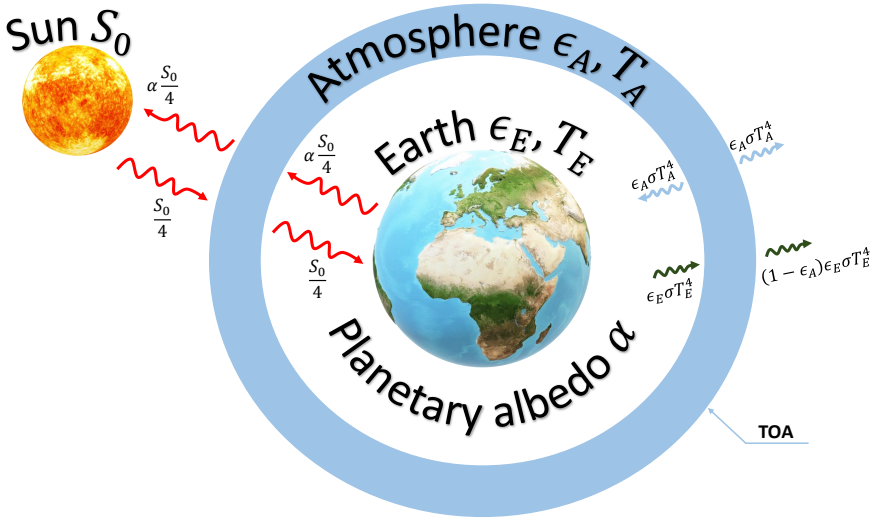


Figure 2.4: A single-layer simplification of the Earth-atmosphere system. The sun provides Earth with an average constant energy flux given by $S_0/4$, where S_0 is the solar constant with a value of of 1366 W m^{-2} [49]. The planetary albedo α represents the amount of solar energy reflected by both the surface of the Earth and by clouds. Seeing as it is assumed that the atmosphere is transparent to solar radiation, $S_0/4$ passes the atmosphere and $\alpha S_0/4$ is reflected back to Space. The red arrows indicate this energy exchange between the Sun and the Earth. Earth itself emits longwave radiation (dark green arrows) at an amount of $\epsilon_E\sigma T_E^4$, of which ϵ_A% is absorbed by the atmosphere and the remaining amount passes through the top of the atmosphere (TOA) and heads into Space. The atmosphere also irradiates an amount shown by the blue arrows in all directions, given by $\epsilon_A\sigma T_A^4$.

Assuming typical values for the parameters of Eq. 2.6 ($\alpha = 0.3$ [49], $\epsilon_A = 0.77$ [66], $\epsilon_E = 0.95$ [67]) leads to a surface temperature of the Earth of approximately 291 K or 18°C, which is a reasonable mean estimate given the adopted simplifications. If the atmosphere had been removed from this calculation altogether, T_E would be approximately 33 K cooler [59].

Equation 2.6 also describes how Earth's surface temperature would respond to specific atmospheric changes. For example, to increase Earth's surface temperature by 1 K, the planetary albedo α would need to decrease by approximately 3%, based on Eq. 2.6. This basic calculation aligns with previous estimates, where a change in albedo ($\Delta\alpha$) of roughly 5% has been calculated for a similar temperature change [68]. In theory, aviation activities can affect Earth's reflectivity and, therefore, α, through mechanisms such as aerosol-cloud interactions, contrail formation, and increased greenhouse gas emissions. However, the expected impact of aviation on global mean surface temperature is comparatively small, with projections indicating a potential increase of about 0.1 K by the year 2050 [28]. Translating this temperature increase into a corresponding change in planetary albedo yields a decrease in α of approximately 0.3%, based on Eq. 2.6[1].

[1] Solving for the scaling factor k in $\sqrt[4]{\frac{S_0(1-k\alpha)}{2\sigma\epsilon_E(2-\epsilon_A)}} - \sqrt[4]{\frac{S_0(1-\alpha)}{2\sigma\epsilon_E(2-\epsilon_A)}} = 0.1 \Rightarrow k \approx 0.9968$.

INTRODUCTION TO RADIATIVE FORCING

The metric commonly used to quantify changes in the Earth's energy flux is known as radiative forcing, measured in W/m^2. The Intergovernmental Panel on Climate Change (IPCC) broadly defines RF as "the net change in the energy balance of the Earth system due to some imposed perturbation" [26]. This energy difference is often evaluated by comparing conditions during a perturbation period with those in preindustrial times (1850-1900). By convention, a positive RF value indicates a net inflow of energy, leading to warming, whereas a negative value represents a net outflow, resulting in cooling. Quantitatively, RF is typically calculated as the difference between incoming shortwave solar radiation and outgoing longwave terrestrial radiation, either at the top of the atmosphere (TOA) or at the climatological tropopause, with the latter generally considered to yield more accurate results [26].

The widespread use of the RF metric is also due to its practical role as a relatively inexpensive proxy for estimating the change in Earth's steady-state global mean surface temperature, T_E, associated with a given RF. This calculation, which would otherwise require resource-intensive climate model simulations, can be approximated through a linear relationship, as shown in Eq. 2.7. In this equation, λ represents the climate sensitivity parameter, with units of $K/(W/m^2)$, which quantifies the temperature response per unit of radiative forcing.

$$\Delta T_E = \lambda \cdot \mathrm{RF} \tag{2.7}$$

A climate sensitivity parameter of 0.73 $K/(W/m^2)$ has been estimated for the climate effects associated with CO_2 emissions ($\lambda_{CO_2} = 0.73$ $K/(W/m^2)$ [69]) and has been shown to be a reliable constant for estimating the impacts of long-lived GHGs. However, when calculating the spatiotemporally heterogeneous effects of various non-CO_2 aviation climate forcers on surface temperature, it becomes necessary to apply distinct climate sensitivity parameters for each forcer i, denoted as λ_i. Therefore, Equation 2.7 is adapted to incorporate the efficacy ratio, $\mathrm{Eff}_i = \frac{\lambda_i}{\lambda_{CO_2}}$, which quantifies the relative impact of each specific climate forcer compared to CO_2:

$$\Delta T_E = \mathrm{Eff}_i \cdot \lambda_{CO_2} \cdot \mathrm{RF}. \tag{2.8}$$

Past studies have calculated efficacy values for several aviation-relevant GHGs, including O_3, CH_4, and H_2O, as well as for contrails. Table 2.1 provides an overview of these values, distinguishing, in particular, the efficacy of O_3 generated at different altitudes: in the lower stratosphere ($O_{3,LS}$) and the upper troposphere ($O_{3,UT}$). In addition, specific efficacy values for aviation-induced O_3 and H_2O are listed [70].

Table 2.1: List of efficacies for aviation-relevant climate forcers. Table has been adapted from [70].

	CO_2	CH_4	$O_{3,LS}$	$O_{3,UT}$	$O_3^{aviation}$	$H_2O^{aviation}$	Contrails
Eff_i	1	1.18	1.80	0.75	1.20-1.56	1.14	0.59

TYPES OF RADIATIVE FORCING

Radiative forcing can be calculated through various approaches, as illustrated in Fig. 2.5 [26]. The simplest type is instantaneous RF (subplot (a)), which measures the net radiative flux at the TOA or at the climatological tropopause, keeping the global temperature profile constant throughout the atmosphere. The second approach is stratosphere-adjusted RF (subplot (b)), where the net radiative flux is measured at the tropopause, allowing the stratospheric temperature profile to adjust to radiation changes until it reaches radiative equilibrium. The next two approaches (subplots (c) and (d)) are calculation variants of what is commonly referred to as the effective radiative forcing (ERF) metric, which measures the net radiative flux at the TOA while permitting rapid adjustments in water vapor, clouds, and atmospheric temperatures. In subplot (c), both land and ocean temperatures (sea surface temperature (SST) and ice cover) are held constant, while in subplot (d), only the ocean temperature is fixed. As ERF focuses on faster feedbacks or adjustments, the ocean temperature in both of these scenarios is fixed to avoid feedbacks that could introduce nonlinear changes over longer timescales. Lastly, subplot (e) illustrates the calculation of the global mean change in Earth's surface temperature once the climate system as a whole reaches radiative equilibrium, at which point RF = 0.

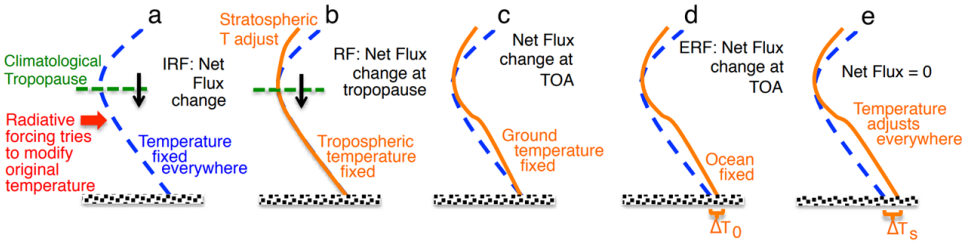


Figure 2.5: A visual summary of the different types of radiative forcing (RF) calculations: (a) the instantaneous RF, (b) the stratospheric-adjusted RF, (c) ERF with fixed land and ocean temperatures, (d) ERF with fixed ocean temperature only and (e) the determination of the global mean change in Earth's surface temperature when the whole climate system is allowed to adjust. ΔT_0 and ΔT_s are the land and complete surface (including land and water) temperature responses, respectively. Figure has been reproduced from [26].

2.1.3. ATMOSPHERIC CIRCULATION

The Sun not only controls Earth's surface and atmospheric temperatures through a complex energy exchange process, as discussed in Section 2.1.2, but also drives atmospheric motion. Although the global net energy flow is balanced in a steady-state system, substantial energy imbalances arise across different latitudes. As illustrated in Figure 2.6, the Tropics (bounded by the latitudes of Cancer at 23.4°N and Capricorn at 23.4°S [71]) receive an excess of incoming shortwave solar energy, while the polar regions experience a net loss of longwave radiation. This imbalance generates a poleward temperature gradient, causing warmer equatorial air masses to rise and flow toward higher latitudes, where they cool and descend. The cooled air subsequently returns toward the tropics near the surface, forming a continuous loop known as atmospheric circulation [59, 72]. The equatorward flow near the surface is driven by a pressure gradient between high pressure regions, where cooler air masses sink, and low pressure areas, where heated air

rises [50]. In essence, this distribution of solar energy generates temperature gradients that produce pressure forces, driving atmospheric motion. This large-scale circulation pattern is fundamental not only to Earth's climate, but also to the long-range transport of pollutants, including those from aviation. As aircraft emissions are released at high altitudes, these atmospheric currents carry them across vast distances, facilitating the global spread of pollutants such as nitrogen oxides, aerosols, and water vapor. Understanding these atmospheric dynamics is essential for evaluating how aviation emissions influence air quality and climate in regions far from their sources.

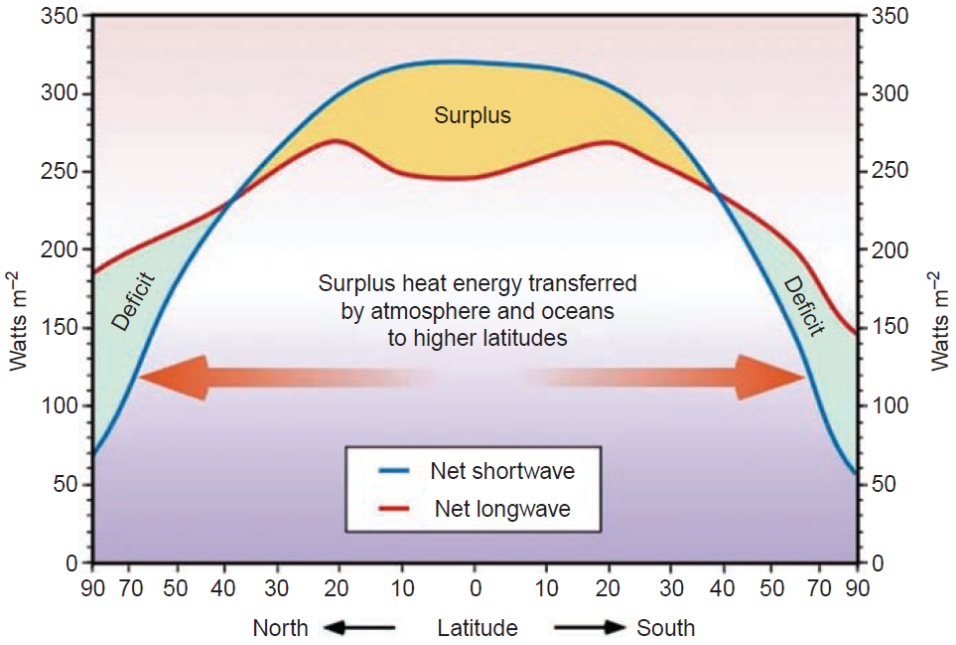


Figure 2.6: Latitudinal distribution of the net energy flow (difference between solar shortwave and terrestrial longwave radiation fluxes). A surplus near the Tropics indicates an excess of shortwave radiation while a deficit near Earth's poles shows a larger amount of outgoing longwave radiation. Figure has been reproduced from [73].

THE ROLE OF PLANETARY ROTATION

Earth's daily rotation at an angular speed of $\omega_E = \frac{2\pi}{86{,}400} \approx 7.3 \times 10^{-5}$ radians/s will also influence the large-scale transport of air masses in the atmosphere. An object moving relative to the rotating Earth will experience an inertial force originating from the Coriolis effect, named after the mathematician Gaspard Gustave de Coriolis. Mathematically, the Coriolis force ($\vec{F}_{\text{Coriolis}}$) will act on a parcel of air with mass m and speed vector $\vec{V}$ according to Eq. 2.9, where the angular velocity vector of the Earth is given by $\vec{\Omega}_E$ [74]:

$$\vec{F}_{\text{Coriolis}} = -2m\vec{\Omega}_E \times \vec{V}. \tag{2.9}$$

The negative sign in Eq. 2.9 indicates that an air parcel moving in the Northern Hemisphere will experience a deflection to the right due to the Coriolis force. For example, northward-moving air in this hemisphere will tend to veer eastward, while eastward-moving air will be deflected southward. In contrast, in the Southern Hemisphere, the Coriolis force nudges air parcels to the left, meaning that a northward-moving air parcel will be deflected westward [74].

THE THREE-CELL CIRCULATION MODEL

To describe Earth's general atmospheric circulation, the three-cell model (illustrated in Fig. 2.7) is commonly used, which accounts for factors such as oceanic presence and the curved paths of air parcels due to the Coriolis effect. This model comprises three primary circulation cells in each hemisphere: the Hadley cell, Ferrel cell, and Polar cell. The Hadley cell, the largest of the three, begins with warm air rising at the equator, moving poleward below the Tropopause, and descending around 30° latitude. In the Northern Hemisphere, this descending air flows back south close to Earth's surface, completing the loop. The air in the tropical region is relatively unstable, so an initial upward displacement will tend to continue in the same direction. However, once at the Tropopause, the stability of the stratosphere limits further ascent, prompting air to flow north or south. The descending air at 30° compresses, warming as it sinks and leading to clear, dry conditions. This results in the formation of major desert regions, such as the Sahara, Gobi and Mojave [59]. This large-scale downward air movement also creates a surface high-pressure region in both hemispheres, known as the subtropical high (indicated in dark yellow in Fig. 2.7). At the surface, air flows back toward the equator, but is deflected by the Coriolis effect—rightward in the Northern Hemisphere and leftward in the Southern Hemisphere—forming the trade winds that blow from east to west. Near the equator, the trade winds from both hemispheres converge in a zone known as the intertropical convergence zone (ITCZ), characterized by low pressure, dense cloud cover, and heavy rainfall. In general, the Hadley cell is a significant driver of global heat distribution, transporting latent heat toward the equator and sensible heat toward the poles [50].

The Ferrel cell is a thermally indirect cell, which means that its circulation is not primarily driven by temperature gradients. Instead, it acts as an intermediary, facilitating mass and heat exchange between the Hadley and Polar cells. Often described as the "gear" that links these cells, the Ferrel cell flows in the opposite direction to the Hadley and Polar cells at their boundaries [76]. Located in the mid-latitudes, it is characterized by westerly winds (blowing from west to east), which are formed as surface air at 30° latitude flows poleward, deflected rightward by the Coriolis effect in the Northern Hemisphere.

At approximately 60° latitude, warm, moist air rises to the Tropopause. From there, some of this air circulates equatorward within the Ferrel cell, while the remaining air moves poleward, entering the Polar cell. Within the Polar cell, air cools and sinks, creating a surface high pressure zone known as the polar high (indicated in dark blue in Fig. 2.7). This cold, dry and dense air flows back toward the equator, where it is again deflected westward by the Coriolis force, forming the polar easterlies that dominate the Polar cell [50].

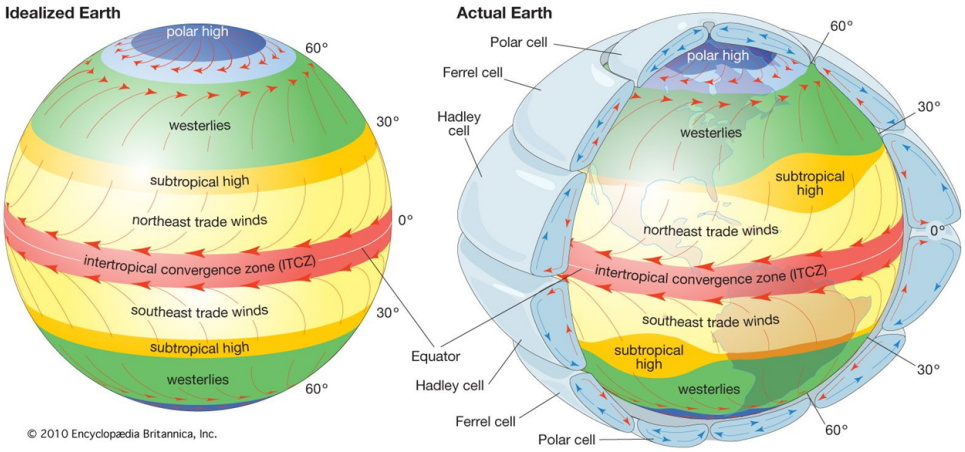


Figure 2.7: The three-cell model of Earth's atmospheric circulation. The Hadley, Ferrel and Polar cells are labelled and the direction of both trade winds (easterlies) and westerlies is shown. The intertropical convergence zone (ITCZ) as well as the subtropical and polar highs are shown in both the idealized and actual representations of the Earth. Figure has been reproduced from [75].

THE BREWER-DOBSON CIRCULATION

Vertical transport between the troposphere and stratosphere is governed by the Brewer-Dobson circulation (BDC). This circulation pattern, shown in Fig. 2.8, begins with air masses rising from the Tropics into the stratosphere, driven by the momentum of vertically propagating atmospheric waves originating in the troposphere [77]. Once in the stratosphere, these air masses flow poleward and descend over the middle and high latitudes. The BDC consists of two main branches: the deep branch and the shallow branch. The deep branch involves mass transport reaching the winter pole at higher altitudes, such as the middle and upper stratosphere, with transport timescales spanning several years. In contrast, the shallow branch operates at lower altitudes in both poles and is faster, with the air completing a full circuit in a few months [77, 78].

The BDC is crucial for the transport of GHGs, particularly ozone and water vapor. This circulation affects the rate of recovery of the stratospheric ozone layer and the amount of water vapor entering the stratosphere [79]. The speed of the BDC also determines the atmospheric lifetime of various chemical species. For example, nitrous oxide (N_2O), a GHG that contributes to O_3 depletion, undergoes photodissociation in the stratosphere; thus, the strength of the BDC directly influences its lifetime, as well as that of chlorofluorocarbons (CFCs). Additionally, ozone recirculates downward from the stratosphere into the troposphere, particularly through the mid-latitudes, constituting a major natural source of tropospheric O_3 [78]. Research indicates that climate change may be accelerating the BDC, leading to an increase in stratospheric O_3 flux into the troposphere, which has implications for tropospheric CH_4 concentrations and overall atmospheric chemistry [80, 81].

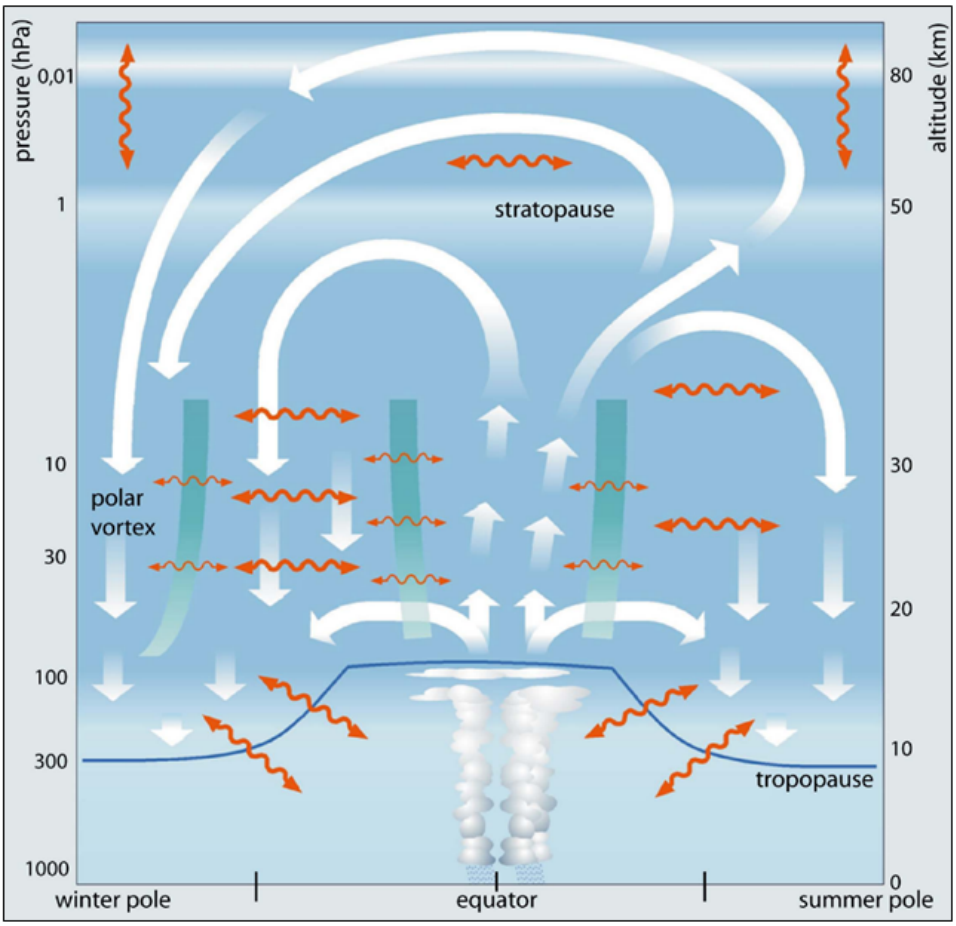


Figure 2.8: An illustration of the Brewer-Dobson circulation. The white arrows represent the mean flow of air that ascends from the troposphere, the orange arrows denote mixing processes and the green lines represent barriers to mixing and transport in the stratosphere. Figure has been reproduced from [82].

2.1.4. ATMOSPHERIC CHEMISTRY

This section outlines the chemical processes most pertinent to understanding the climate impacts of subsonic aviation, with a focus on NO_x-O_3 interactions. Aerosol microphysical processes influencing SO_4 species are discussed later in Section 2.2. Key compounds in tropospheric chemistry include NO_x, O_3, the hydroxyl radical (OH), volatile organic compounds (VOCs), carbon monoxide (CO), methane (CH_4), and non-methane hydrocarbons (NMHCs). These compounds exhibit a wide range of atmospheric lifetimes, impacting their transport distances, as shown in Fig. 2.9. Among them, OH has one of the shortest lifetimes due to its high reactivity with various atmospheric species, limiting its transport range to roughly 1 km. In contrast, CH_4 has a lifetime of approximately 10–12 years, enabling it to be transported across thousands of kilometers, resulting in a globally well-mixed greenhouse gas [83].

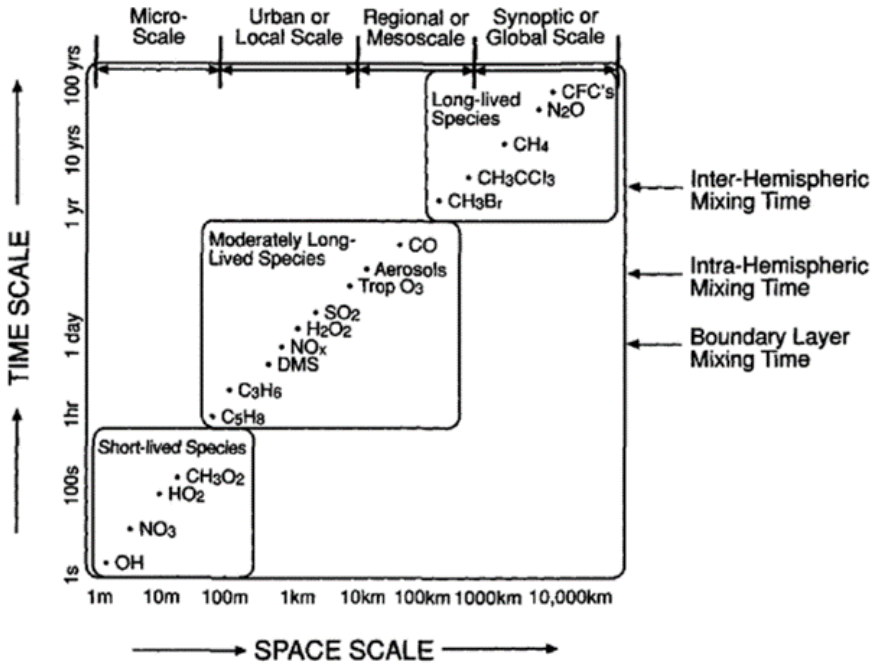


Figure 2.9: A summary of the lifetimes (vertical axis) and the extent to which certain chemical species may be transported in the atmosphere (horizontal axis). Figure has been reproduced from [83].

MIXING RATIOS AND CONCENTRATIONS

To quantify the amount of a chemical species mixed with air in the atmosphere, the following metrics are commonly used: volume mixing ratio (VMR), mass mixing ratio (MMR), and concentration. The volume mixing ratio refers to the dimensionless fraction of the number density of a species, n_i (particles per m^3), relative to that of air (n_{air}). This metric is typically expressed in units of $\frac{\text{mol}_i}{\text{mol}_{\text{air}}}$ or $\frac{\text{m}_i^3}{\text{m}_{\text{air}}^3}$:

$$\text{VMR} = \frac{n_i}{n_{\text{air}}}. \tag{2.10}$$

Similarly, the mass mixing ratio is then the same ratio but with mass densities (kg per m^3) of species i (ρ_i) and of air (ρ_{air}) [49, 83]:

$$\text{MMR} = \frac{\rho_i}{\rho_{\text{air}}}. \tag{2.11}$$

Lastly, the concentration of a species (C_i) is often expressed in units of micrograms per m^3 and can be derived using the definition of VMR with units of $\frac{\text{mol}}{\text{mol}}$:

$$C_i \left[\frac{\mu\text{g}}{\text{m}^3}\right] = \text{VMR}\left[\frac{\text{mol}}{\text{mol}}\right] \times 10^9 \times \frac{\mathscr{M}_i}{\mathscr{M}_{\text{air}}} \times \rho_{\text{air}}, \tag{2.12}$$

where $\mathscr{M}_{\text{air}}$ is the mean molar mass of the air (~29 $\frac{\text{kg}}{\text{kmol}}$).

THE HYDROXYL RADICAL (OH)

The hydroxyl radical is part of the HO_x family ($HO_x \equiv OH + HO_2$) and is often considered an atmospheric detergent given its high reactivity with many trace gases. One of the main processes for the tropospheric production of OH is the reaction between the excited state of atomic oxygen $O(^1D)$ and water vapor (Reaction R1):

$$O(^1D) + H_2O \longrightarrow 2\,OH. \tag{R1}$$

In the troposphere, the atom $O(^1D)$ is produced by the photodissociation of O_3 when it absorbs solar radiation at wavelengths (λ) shorter than approximately 320 nm but greater than 290 nm (Reaction R2) [84, 85]:

$$O_3 + h\nu\,(\lambda < 320\text{ nm}) \longrightarrow O(^1D) + O_2. \tag{R2}$$

The energy absorbed by an O_3 molecule in Reaction R2 is denoted as $h\nu$, where h is Planck's constant ($h = 6.626 \times 10^{-34}$Js) and ν represents the frequency of the radiation, given by the speed of light divided by the wavelength of the absorbed photons [50]. When O_3 absorbs higher-energy radiation with wavelengths below 234 nm, an even more excited form of atomic oxygen, $O(^1S)$, is produced [85]. As summarized in Fig. 2.10, tropospheric OH forms primarily from the interactions between O_3, solar radiation, and water vapor according to Reactions R1 and R2 [86]. This mechanism explains the particularly high OH concentrations in the tropics, a region characterized by intense solar radiation and elevated humidity, which makes aviation emissions released in these areas more prone to enhanced chemical activity.

Although OH does not react with the most abundant atmospheric gases such as N_2 or O_2, it is highly reactive with several trace gases depicted in Figs. 2.1 and 2.10, including some greenhouse gases. Notably, OH initiates the primary catalytic cycle for tropospheric O_3 loss, beginning with Reaction R3, where the hydroxyl radical decomposes ozone into the hydroperoxyl radical (HO_2) and molecular oxygen [50, 85].

$$O_3 + OH \longrightarrow HO_2 + O_2 \tag{R3}$$

The generated HO_2 further depletes O_3, regenerating OH to the atmosphere in the process (Reaction R4):

$$O_3 + HO_2 \longrightarrow OH + 2\,O_2. \tag{R4}$$

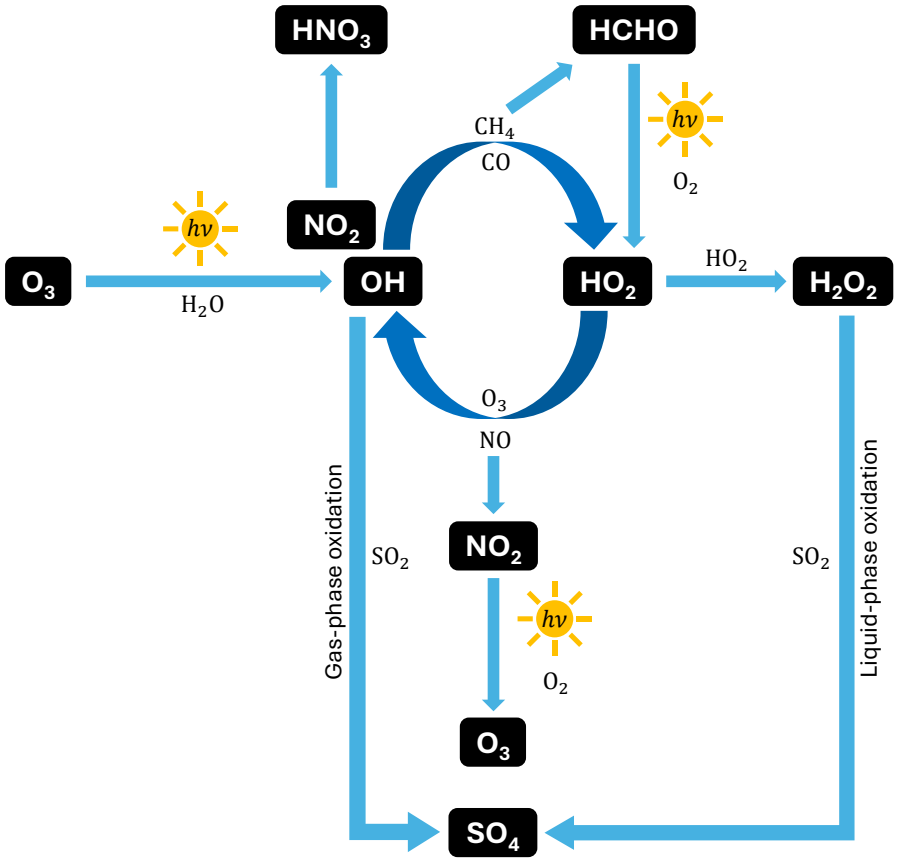


Figure 2.10: HO_x chemistry processes and the link to SO_4 aerosol formation via both gas- and liquid-phase oxidation of SO_2. Figure has been adapted from [86].

Beyond its role in O_3 depletion, the hydroxyl radical acts as a primary oxidant for trace gases such as CH_4 and CO. In methane oxidation, OH initially generates the methyl radical (CH_3) (Reaction R5), which subsequently forms the methylperoxy radical (CH_3O_2) through reactions with O_2; CH_3O_2 can then be converted to formaldehyde (HCHO), as shown in Fig. 2.10. Similarly, OH oxidizes CO, producing CO_2 and HO_2 (Reaction R6) in the process. These reactions with CO and CH_4 serve as primary sinks for OH, with approximately three-quarters of tropospheric OH removed by its reaction with CO. Additional OH loss pathways include reactions with NO_2, forming highly water-soluble nitric

acid (HNO_3), which is eventually removed through wet deposition according to Reaction R7, where M represents an inert molecule [85–87].

$$CH_4 + OH \longrightarrow CH_3 + H_2O \tag{R5}$$

$$CO + OH + O_2 \longrightarrow CO_2 + HO_2 \tag{R6}$$

$$NO_2 + OH + M \longrightarrow HNO_3 + M \tag{R7}$$

The removal of HO_2 occurs primarily through its self-reaction, which leads to the formation of hydrogen peroxide (H_2O_2), as shown in Reaction R8 and in Fig. 2.10.

$$HO_2 + HO_2 + M \longrightarrow H_2O_2 + M \tag{R8}$$

From this point on, the actual removal of HO_2 will depend on the fate of the H_2O_2 molecule: it can either react with OH or be photodissociated. The former leads to the rainout of H_2O_2 following Reaction R9, while the latter results in the restitution of OH through the photolysis of H_2O_2 (Reaction R10) [85].

$$H_2O_2 + OH \longrightarrow HO_2 + H_2O \tag{R9}$$

$$H_2O_2 + h\nu \longrightarrow 2\,OH \tag{R10}$$

Lastly, Fig. 2.10 shows the crucial role that HO_x species play in oxidizing aviation SO_2 emissions into sulfate aerosols. SO_4 can be produced via gas- or liquid-phase oxidation by OH or H_2O_2, respectively. Further details regarding the formation processes of SO_4 are provided in Section 2.2 and in Chapter 6.

NITROGEN OXIDES (NO_x)

Sources of nitrogen oxides ($NO_x \equiv NO + NO_2$) at ground level include volcanic eruptions, the transport sector (such as road traffic and shipping), microbial soil activity, and biomass burning. Within the troposphere, NO_x levels are additionally influenced by aircraft emissions, stratospheric ozone transport, and, notably, lightning activity, which can contribute substantially to atmospheric NO_x concentrations [88]. Lightning-generated NO_x alone can account for over 20% of total NO_x production in tropical regions [89].

An aircraft engine, for instance, may produce nitric oxide (NO) via the Zeldovich mechanism [90], which is based on the dissociation of O_2 molecules into their monatomic counterparts by means of elevated inlet combustion temperatures (~2000 K). Once these oxygen atoms react with N_2 abundantly found in the atmosphere, they form NO and N (Reaction R11). These monatomic nitrogen atoms then react further with available O_2, also from the surrounding air, to once again form NO (Reaction R12) [85].

$$N_2 + O \longrightarrow NO + N \tag{R11}$$

$$N + O_2 \longrightarrow NO + O \tag{R12}$$

In the extended Zeldovich mechanism, a third pathway for NO formation is described, involving the reaction between monatomic nitrogen and the hydroxyl radical, as shown in Reaction R13:

$$N + OH \longrightarrow NO + H\cdot \tag{R13}$$

Nitrogen oxides that originate from the complete Zeldovich mechanism (Reactions R11 to R13) are typically classified as thermal NO_x. A second method by which an aircraft can produce NO is through the amount of nitrogen that is directly attached to the jet fuel, called fuel NO_x. Nitric oxide is then released from the natural combustion of fuel, even at lower temperatures [85, 91, 92]. In general, several design and operational factors can also impact the levels of NO_x produced by an aircraft, some of which include the geometry of the gas turbine, as well as the temperature and pressure values of the combustion chamber. This means that engine thrust settings play a crucial role in the production of NO_x. Figure 2.11, for instance, depicts the emission index of NO_x per flight phase, highlighting that the phase with maximum thrust (Take-off) leads to the largest amount of NO_x production on average [92].

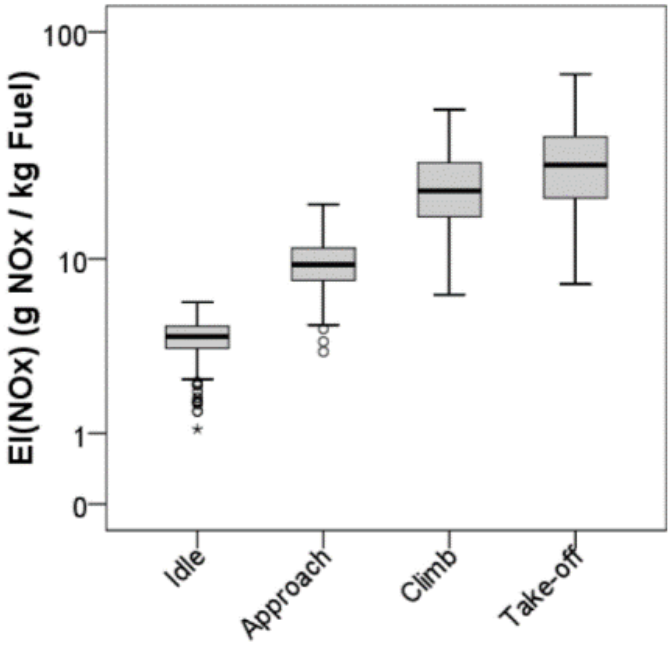


Figure 2.11: Variation of the emission index of NO_x in g(NO_2)/kg of fuel burned with flight phase. Figure has been reproduced from [92], with permission by Elsevier via RightsLink.

The removal of nitrogen oxides from the atmosphere involves their transformation into nitric acid (HNO_3), which contributes to the formation of acid rain—a process to which aviation NO_x emissions may contribute [93]. In daylight conditions, the main tropospheric sink for NO_2 is its reaction with OH, producing HNO_3 (Reaction R7). At night,

however, NO_2 reacts with O_3 to form nitrate (NO_3) and molecular oxygen (Reaction R14). The resulting NO_3 then further reacts with NO_2 to form dinitrogen pentoxide (N_2O_5) through Reaction R15. Finally, N_2O_5 hydrolyzes, generating nitric acid that contributes to acid rain (Reaction R16) [85].

$$NO_2 + O_3 \longrightarrow NO_3 + O_2 \tag{R14}$$

$$NO_2 + NO_3 \longrightarrow N_2O_5 \tag{R15}$$

$$N_2O_5 + H_2O \longrightarrow 2\,HNO_3 \tag{R16}$$

OZONE (O_3)

In the troposphere, O_3 can be produced through interactions involving several chemical compounds, with NO_x, CO, and VOCs being particularly relevant for aviation. For NO_x, although NO can deplete O_3 to form NO_2 according to Reaction R17, O_3 is eventually produced via the photolysis of NO_2 (Reaction R18) followed by the recombination of the monatomic and molecular oxygen atoms (Reaction R19) [92]. When aircraft emit NO, for instance, reactions with HO_2 lead to the production of NO_2 (Reaction R20), after which O_3 production follows via Reactions R18 and R19.

$$NO + O_3 \longrightarrow NO_2 + O_2 \tag{R17}$$

$$NO_2 + h\nu \longrightarrow NO + O \tag{R18}$$

$$O + O_2 \longrightarrow O_3 \tag{R19}$$

$$NO + HO_2 \longrightarrow OH + NO_2 \tag{R20}$$

Emitted carbon monoxide will also eventually lead to the production of O_3 via the same NO_x-related reactions (Reactions R18 and R19) above. The oxidation of CO by OH (Reaction R6) generates HO_2 that then leads to the production of NO_2 via Reaction R20.

Volatile organic compounds encompass a wide range of gaseous organic species, including alkanes (hydrocarbons with the general formula C_nH_{2n+2}) such as methane ($n = 1 \rightarrow CH_4$), alkenes like propene (C_3H_6) of the form C_nH_{2n}, aromatics such as benzene (C_6H_6), and many others [85]. The formation of ozone involving VOCs is based on the creation of organic peroxy radicals (RO_2), which form through the oxidation of VOCs by OH, followed by reactions with O_2. Ozone production is then initiated through Reaction R21, which is analogous to Reaction R20. Subsequent photodissociation of NO_2 ultimately produces ozone, though this pathway primarily occurs in NO_x-rich environments. In regions with limited NO_x, RO_2 is more likely to deplete HO_x radicals and not form ozone [84, 85].

$$RO_2 + NO \longrightarrow RO + NO_2 \tag{R21}$$

Albeit a weaker source, the downward transport of ozone from the stratosphere can contribute approximately 6–15% of the total tropospheric ozone, based on global model simulations. The majority of tropospheric ozone, however, originates from chemical processes occurring within the troposphere itself, exemplified by Reactions R18 to R21. In contrast, solar radiation and interactions with HO_x species serve as the primary mechanisms for ozone removal, accounting for about 78–85% of total tropospheric ozone depletion. For example, radiation with wavelengths below 320 nm can dissociate ozone molecules, as represented in Reaction R2, while interactions with HO_x species contribute to ozone loss through Reactions R3 and R4. The remainder is lost through deposition, which is a comparatively minor sink [94, 95].

The distinction between two primary chemical regimes is critical for understanding O_3 chemistry. The first is the NO_x-limited regime, where O_3 production increases linearly with the amount of NO_x in the atmosphere, rendering the background concentrations of CO and VOCs largely negligible. In this regime, reactions involving VOCs, CO and OH radicals are plentiful (e.g., Reaction R6), and O_3 production ultimately depends on the availability of NO, often initiated by Reaction R20. The second regime, known as the VOC-limited or NO_x-saturated regime, typically occurs in areas with elevated NO_x levels, or during winter, when limited solar radiation reduces the photolysis of NO_2. Here, ozone production increases linearly with the amount of CO and VOCs, due to the competition between VOCs and NO_2 for reactions with OH. While reactions between VOCs and OH promote O_3 formation, the reaction of NO_2 with OH instead yields HNO_3. These regimes are typically illustrated in ozone isopleths such as those in Fig. 2.12, where both regimes are clearly labeled [85, 96].

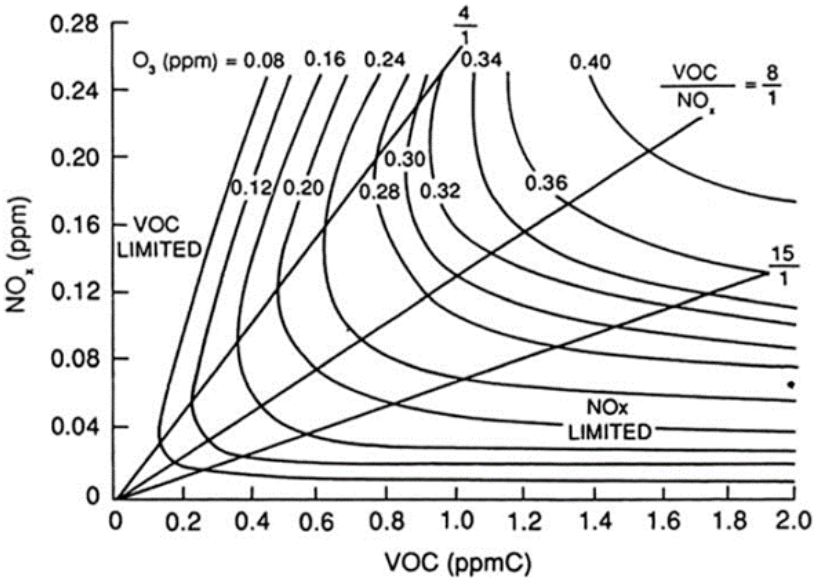


Figure 2.12: The ozone isopleths diagram as a function of VOC and NO_X concentrations. Curved lines are the isopleths that indicate constant O_3 concentrations. The NO_X- and VOC-limited regimes are labeled accordingly. Figure has been reproduced from [96].

2.2. FUNDAMENTALS OF AEROSOLS

AEROSOLS are collections of solid or liquid particles suspended in the atmosphere, including substances such as sea salt, mineral dust, pollen, soot, sulfate and $PM_{2.5}$ (particulate matter with a diameter below 2.5 μm). Cloud droplets and ice crystals are generally excluded from this category, as they are classified separately as hydrometeors [97]. Aerosols play a significant role in Earth's climate and environmental health, as they can directly and indirectly alter the net radiative energy balance reaching the planet and impact human respiratory health [98]. This subchapter discusses the fundamental properties, dynamics, and microphysical processes crucial for understanding the climate effects of aviation-induced aerosols.

2.2.1. AEROSOL PROPERTIES

PARTICLE SIZE

The diameter D of an aerosol particle is a key feature in its classification. Analyzing the statistical distribution of particle diameters is essential to categorize aerosols into four primary size classes: nucleation, Aitken, accumulation, and coarse modes. Nucleation mode particles generally have diameters smaller than 0.02 μm and represent newly formed particles that originate from various microphysical processes, such as binary homogeneous nucleation involving H_2O and H_2SO_4. Aitken mode aerosols have larger diameters, ranging from 0.02 μm to 0.1 μm, and may form from the coagulation of freshly nucleated particles or by the condensation of H_2SO_4 on pre-existing particles, as observed with SO_4. Accumulation mode particles fall within the diameter range of 0.1 to 1.0 μm, while aerosols exceeding this size are classified as coarse mode particles. Examples of coarse mode particles may include volcanic ash, pollen, and debris from wildfires [97, 99]. While these four modes are commonly acknowledged, many climate-chemistry models consider only three of them by excluding the nucleation mode, assuming that particles in this category quickly grow into the Aitken mode [100]. The particle number concentration $n(D)$ across different particle sizes with diameters D can be effectively described using a log-normal distribution, as shown in Eq. 2.13.

$$n(D) = \frac{N_t}{\sqrt{2\pi} D \ln \sigma_g} \exp\left[-\frac{(\ln D - \ln D_g)^2}{2 \ln^2 \sigma_g} \right] \tag{2.13}$$

The total number concentration for a specific aerosol mode is represented by N_t, where D_g is the median diameter and σ_g is the geometric standard deviation [101]. This statistical approach is particularly effective for characterizing polydisperse aerosols, whose diameters span a wide range of sizes, as opposed to monodisperse aerosols, which contain particles of comparable sizes [102]. Figure 2.13 illustrates Eq. 2.13 across the four particle size modes discussed.

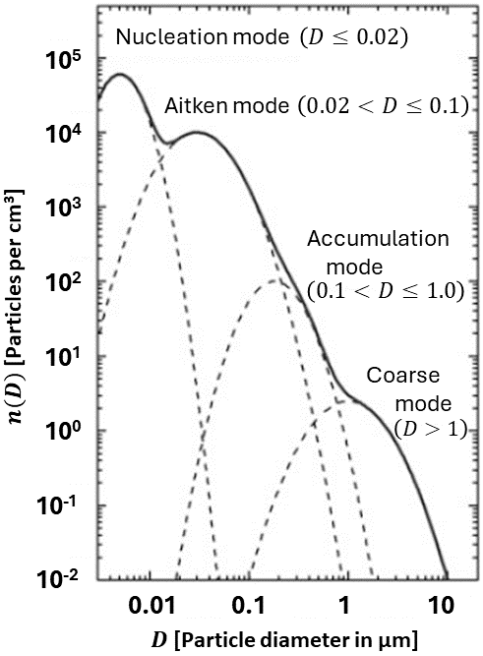


Figure 2.13: The statistical log-normal distributions of all four aerosol size modes: nucleation, Aitken, accumulation and coarse. Figure was adapted from [97].

PARTICLE MIXING STATES

Aerosols can be classified into three mixing states: soluble, externally mixed, and internally mixed. Soluble aerosols consist entirely of soluble species such as SO_4 or NO_3, without any insoluble black carbon or mineral dust components. Externally mixed (insoluble) aerosols contain an insoluble or non-volatile core (e.g., black carbon and/or mineral dust) with a soluble coating mass fraction below a specified threshold, which varies among aerosol models—in this dissertation, the threshold is 10%. Internally mixed (or simply "mixed") aerosols similarly possess an insoluble core, but their soluble coating mass fraction exceeds this threshold (again, defined as 10% within the aerosol model applied here) [85, 100, 101, 103].

HYGROSCOPICITY

An aerosol's capacity for water uptake, known as hygroscopicity, varies with ambient relative humidity. This property is particularly important for cloud formation, as hygroscopic growth helps convert aerosol particles into cloud condensation nuclei and enhances their ability to scatter light and influence cloud properties [97].

2.2.2. AEROSOL MECHANICS

The Reynolds number in the context of aerosol dynamics is defined in terms of the aerosol diameter D_p, the density of the fluid through which the aerosol travels ρ_g, the dynamic viscosity of the fluid μ_g and the velocity V_p of the aerosol relative to the moving

fluid, as is shown in Eq. 2.14 [104]:

$$\mathrm{Re} = \frac{\rho_g V_p D_p}{\mu_g}. \tag{2.14}$$

For flow around spheres, the Reynolds number (Re) classifies flow into three distinct regimes: laminar ($\mathrm{Re} \leq 1$), transitional ($1 < \mathrm{Re} \leq 1000$), and turbulent ($\mathrm{Re} > 1000$). In the laminar regime, viscous forces dominate over inertial forces, resulting in smooth, orderly flow without mixing. The transitional regime marks the onset of turbulence in the wake, where viscous and inertial forces play a comparable role in shaping flow dynamics. In the turbulent regime, inertial forces overpower viscous forces, leading to chaotic flow and extensive mixing [102].

The resistive force exerted on a spherical object moving through a fluid is known as the drag force, F_D, and is typically balanced with an external force, such as gravity, to characterize the object's motion. Isaac Newton first derived a general expression for the drag force in 1687, observing that the drag acting on a large spherical object, such as a cannonball with diameter D_p (and thus an area $A = \frac{\pi D_p^2}{4}$) and velocity V relative to the surrounding fluid, should relate to the motion of the displaced air mass. This principle is known as Newton's resistance law and is expressed mathematically by Eq. 2.15 [102, 105]:

$$\mathrm{F_D} = \frac{1}{2}\rho_g \mathrm{C_D} A V^2 = \mathrm{C_D}\frac{\pi}{8}\rho_g D_p^2 V^2. \tag{2.15}$$

Based on their reduced velocities and microscale particle size distributions, aerosol motion typically occurs in the laminar regime, in which viscous forces dictate the dynamics. In such a regime, Stokes' law is applicable, which was formulated in 1851 by George Gabriel Stokes. It may be derived by applying some of the following assumptions to the Navier-Stokes equations [102, 104]:

- The particle is a rigid sphere and there is only one.
- Low Reynolds number ($\mathrm{Re} \leq 1$) such that viscous forces are dominant over the inertial ones.
- No-slip condition between the particle surface and the surrounding fluid, that is, there is no relative movement between its surface and the fluid. This is the continuum flow assumption.

The expression that ensues from these simplifications is thus known as Stokes' law and is represented by Eq. 2.16:

$$\mathrm{F_D} = 3\pi\mu_g D_p V. \tag{2.16}$$

By equating Newton's resistance law (Eq. 2.15) to Stokes' law (Eq. 2.16), an expression for the drag coefficient in the laminar regime for aerosol particles is found [104]:

$$\mathrm{C_D} = \frac{24}{\mathrm{Re}}. \tag{2.17}$$

A complete summary of the three different regimes along with their applicable equations for the drag coefficients are provided by Fig. 2.14.

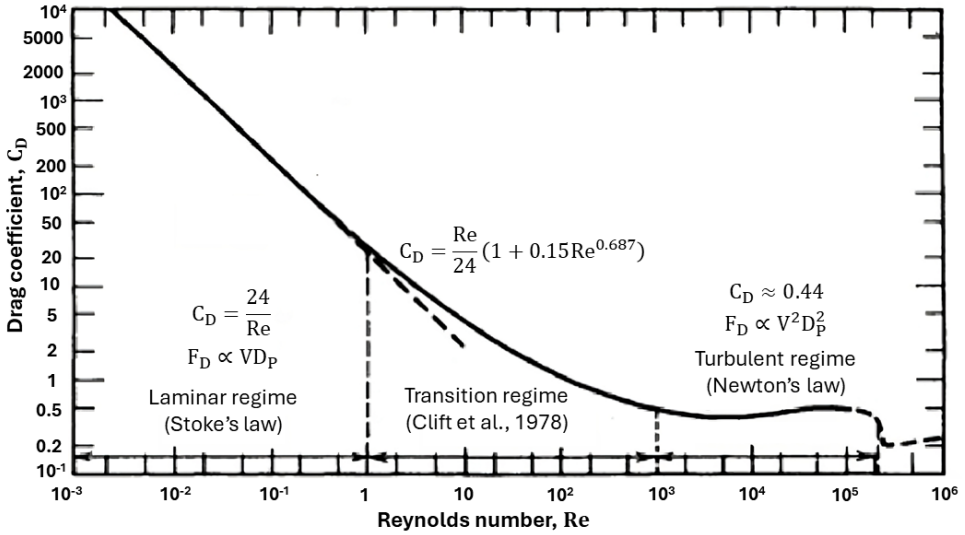


Figure 2.14: The drag coefficient (C_D) as a function of the Reynolds number (Re) for rigid spherical particles. The laminar regime is described by Stokes' law in which the drag force (F_D) is proportional to the product of the relative velocity V of the aerosol particle and the diameter of the aerosol D_P. The transition regime was characterized experimentally by Clift et al. [106] and the turbulent regime is defined by Newton's resistance law in which F_D is proportional the square of the product of V and D_P. Figure has been adapted from [102].

One of the earlier assumptions in the derivation of Stokes' law was the no-slip condition between the fluid and aerosol. To measure whether this situation applies, the dimensionless parameter called the Knudsen number (Kn) is useful. It is the ratio between the mean free path of gas molecules λ, which is the average distance between successive molecular collisions, and the aerosol diameter D_p [107]:

$$\mathrm{Kn} = \frac{\lambda}{D_p}. \tag{2.18}$$

The continuum flow regime is defined for $\mathrm{Kn} \ll 1$, while the transition regime—where non-continuum effects start to become noticeable—is characterized by $\mathrm{Kn} \approx 1$. Finally, the free molecular regime occurs when $\mathrm{Kn} \gg 1$. When an aerosol's diameter is comparable to its mean free path, the no-slip condition is no longer valid, necessitating the application of the Cunningham slip correction factor (C_C) to adjust the drag force as described by Eq. 2.16, resulting in:

$$F_D = \frac{3\pi\mu_g D_p V}{C_C}, \tag{2.19}$$

where the slip correction factor C_C is given by [108]:

$$C_C = 1 + \mathrm{Kn}\left[1.142 + 0.558\exp\left(\frac{-0.999}{\mathrm{Kn}}\right)\right]. \tag{2.20}$$

The vertical equation of motion for small, perfectly spherical aerosols (where particle size is comparable to the mean free path) can be derived by considering three primary forces: the upward buoyant and drag forces and the downward gravitational force, as illustrated in the free-body diagram in Fig. 2.15. The aerosol particle is assumed to have a density ρ_p, a diameter D_p and a velocity V. The density of the surrounding fluid is denoted by ρ_g.

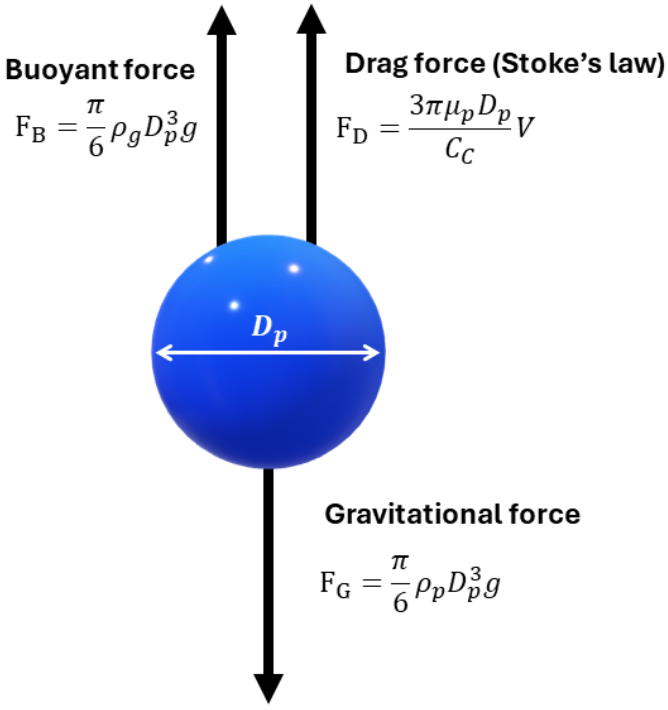


Figure 2.15: Free-body diagram of a small, spherical aerosol with diameter D_p for which the Cunningham slip correction factor C_C is applied to Stoke's law for the calculation of the drag force F_D. The buoyant and gravitational forces, F_B and F_G respectively, act in opposing directions.

By taking the downward direction as positive, the following first-order linear non-homogeneous differential equation is produced from applying Newton's second law of motion:

$$\frac{dV(t)}{dt} = -\frac{18\mu_g}{\rho_p D_p^2 C_c} V(t) + g\left(\frac{\rho_p - \rho_g}{\rho_p}\right). \tag{2.21}$$

Solving Eq. 2.21 with initial condition $V(0) = 0$ leads to the following expression for the velocity $V(t)$ for a single aerosol:

$$V(t) = \frac{g D_p^2 (\rho_p - \rho_g) C_c}{18\mu_g}\left(1 - e^{-\frac{t}{\tau}}\right), \tag{2.22}$$

where $\tau = \frac{\rho_p D_p^2 C_c}{18\mu_g}$ is referred to as the relaxation time and describes the time needed for an aerosol to adjust to a new dynamic state. An important quantity that may be obtained from Eq. 2.22 is the terminal settling or sedimentation velocity V_{TS}, which is relevant in determining both its vertical motion and lifetime. Seeing as this is the maximum velocity that a particle can achieve within a fluid, it may be calculated by finding the limit of Eq. 2.22 as time t approaches infinity [102, 104, 109]:

$$V_{TS} = \lim_{t \to +\infty} V(t) = \frac{g D_p^2 (\rho_p - \rho_g) C_c}{18\mu_g}. \tag{2.23}$$

According to Eq. 2.23, a particle's terminal velocity V_{TS} is proportional to the square of its diameter. This proves that larger and denser aerosols are more likely to be removed by gravitational settling than smaller particles, thereby shortening their atmospheric lifetime.

So far, it has been assumed that aerosols possess a perfectly spherical geometry. However, aerosols can exhibit highly irregular shapes, which alter the drag force they experience. A correction known as the shape factor (S_f) is therefore applied to approximate non-spherical particles as spheres. The shape factor is defined as the ratio of the actual drag force on the non-spherical particle to the drag force on a spherical particle with an equivalent diameter D_e—that is, a sphere with the same volume and velocity as the original particle [102, 104]:

$$S_f = \frac{F_D}{3\pi\mu_g D_e V}. \tag{2.24}$$

The terminal velocity derived in Eq. 2.23 could then be scaled by the shape factor to arrive at an expression for the terminal velocity for non-spherical aerosol particles with an equivalent diameter D_e:

$$V_{TS} = \frac{g D_e^2 (\rho_p - \rho_g) C_c}{18\mu_g S_f}. \tag{2.25}$$

2.2.3. AEROSOL MICROPHYSICAL PROCESSES

The concentration and size distribution of particles are significantly impacted by microphysical processes, some of which include particle nucleation, coagulation and condensation [110].

NUCLEATION

Nucleation, the formation of new particles from gaseous molecules, depends on the clustering of low-vapor-pressure gases. This process can occur through two primary types of nucleation: homogeneous and heterogeneous. Homogeneous nucleation, also known as *self-nucleation*, involves clustering on other gas molecules under supersaturated conditions, while heterogeneous nucleation requires another substance, such as a different liquid or solid particle, to act as a nucleus for new particle formation [50, 110]. Nucleation can further be classified based on the types of molecules involved: homomolecular (one type), binary (two types), or ternary (three types). In the case of SO_4

production, binary homogeneous nucleation between H_2O and H_2SO_4 is the most relevant pathway. Here, the concentration of H_2SO_4 molecules is governed by the balance of addition through molecular collisions and loss through evaporation, with thermodynamically stable clusters then growing by condensation.

Due to the highly non-linear nature of homogeneous nucleation, which depends on factors such as ambient temperature T and relative humidity RH, parameterizations are commonly implemented in climate-chemistry models to account for this complex process at the sub-grid scale. For instance, binary nucleation between H_2O and H_2SO_4 under tropospheric and stratospheric conditions, which is particularly relevant at aircraft cruise altitudes, is often parameterized via the nucleation rate J proposed by Vehkamäki et al. [111] (see Chapter 3 for further details). This specific parameterization can reduce computational time by a factor of up to 500 and is defined by Eq. 2.26, where N_a represents the total gaseous concentration of H_2SO_4, T the absolute temperature, RH the relative humidity, and x^* the H_2SO_4 mole fraction of the critical nucleus[2]. The coefficients $a(T,x^*)$ to $j(T,x^*)$ are cubic polynomials of T and inversely proportional to x^*, with their full expressions provided in [111].

$$\begin{aligned} J = \exp\Bigg\{ & a(T,x^*) + b(T,x^*)\ln\left(\frac{RH}{100}\right) \\ & + c(T,x^*)\left[\ln\left(\frac{RH}{100}\right)\right]^2 + d(T,x^*)\left[\ln\left(\frac{RH}{100}\right)\right]^3 \\ & + e(T,x^*)\ln(N_a) + f(T,x^*)\ln\left(\frac{RH}{100}\right)\ln(N_a) \\ & + g(T,x^*)\left[\ln\left(\frac{RH}{100}\right)\right]^2\ln(N_a) + h(T,x^*)\left[\ln(N_a)\right]^2 \\ & + i(T,x^*)\ln\left(\frac{RH}{100}\right)\left[\ln(N_a)\right]^2 + j(T,x^*)\left[\ln(N_a)\right]^3 \Bigg\} \end{aligned} \tag{2.26}$$

COAGULATION

Coagulation occurs when two aerosol particles collide as a result of Brownian motion and adhere to form a larger particle. Every collision will reduce the number concentration by a particle, so multiple collisions will cause a shift in the particle number distribution from smaller to larger sizes [110]. Coagulation can occur between particles within the same size and mixing mode, known as intramodal coagulation, or between particles of different modes, referred to as intermodal coagulation. The former leads to a decrease in the particle number but has no effect on the mass mixing ratio while the latter decreases the particle number and causes a shift in mass from smaller to larger sizes [113]. The binary coagulation rate between two particle types k and l is proportional to the product of their particle number concentrations N_k and N_l:

$$J_{k,l} = \beta_{k,l} N_k N_l, \tag{2.27}$$

[2] The critical nucleus is the smallest particle size capable of stably growing; particles smaller than this radius are likely to evaporate [112].

where β is the coagulation coefficient that depends on the Knudsen number, the diameters of the colliding particles and a diffusion coefficient [110].

CONDENSATION

Condensation is the process by which gas molecules condense on pre-existing particles, causing them to increase in size. An example would be sulfuric acid vapor condensing on particles and growing hygroscopically to form sulfate. Typically, all three microphysical processes of nucleation, condensation and coagulation act jointly during aerosol gas-to-liquid formations. Initially, a small amount of the new phase spontaneously forms through nucleation. Subsequently, as more material accumulates around the initial nuclei, the new phase grows progressively through condensational growth. Finally, particle growth accelerates as droplets collide and merge through coagulation [114].

2.3. AVIATION: CLIMATE EFFECTS AND TRANSPORT OF EMITTED SPECIES

2.3.1. AVIATION CLIMATE EFFECTS

Aviation climate effects emanate from CO_2 and several non-CO_2 forcers that arise from a myriad of by-products associated with the combustion of hydrocarbon-based (C_xH_y) fuels like kerosene (Fig. 2.16). Equation 2.28a describes the general chemical process of combusting a hydrocarbon fuel, where a-f are stoichiometric coefficients. The by-products depend on the equivalence ratio Φ, which defines whether an air-fuel mixture is fuel-lean (air is in excess: $\Phi < 1$), fuel-rich (fuel is in excess: $\Phi > 1$) or stoichiometric ($\Phi = 1$). For example, in lean combustion, the main by-products will be CO_2, H_2O, O_2 and N_2 as there is enough oxygen to produce CO_2 and H_2O from the carbon and hydrogen atoms in the fuel, so coefficients c and e are both zero (Eq. 2.28b). In rich combustion, the main by-products are again CO_2, H_2O and N_2 but now also CO and H_2 (as well as unburnt hydrocarbons) and there is no O_2 as all of the oxygen is consumed during combustion (Eq. 2.28c). Lastly, in ideal combustion, CO_2, H_2O and N_2 are produced (Eq. 2.28d) [115]. A complete range of climate forcers linked to some of these by-products, their associated warming and cooling effects, along with our current level of understanding are summarized in Fig. 1.2. The present subsection briefly describes each of these forcers.

$$C_xH_y + \underbrace{\left(\frac{x+\frac{y}{4}}{\Phi}\right)}_{a}(O_2 + 3.76\,N_2) \rightarrow b\,CO_2 + c\,CO + d\,H_2O + e\,H_2 + f\,O_2 + 3.76\underbrace{\left(\frac{x+\frac{y}{4}}{\Phi}\right)}_{a}N_2 \tag{2.28a}$$

Fuel-lean ($\Phi < 1$, $c = e = 0$):

$$C_xH_y + \underbrace{\left(\frac{x+\frac{y}{4}}{\Phi}\right)}_{a}(O_2 + 3.76\,N_2) \rightarrow b\,CO_2 + d\,H_2O + f\,O_2 + 3.76\underbrace{\left(\frac{x+\frac{y}{4}}{\Phi}\right)}_{a}N_2. \tag{2.28b}$$

Fuel-rich ($\Phi > 1$, $f = 0$):

$$C_xH_y + \underbrace{\left(\frac{x+\frac{y}{4}}{\Phi}\right)}_{a}(O_2 + 3.76\,N_2) \rightarrow b\,CO_2 + c\,CO + d\,H_2O + e\,H_2 + 3.76\underbrace{\left(\frac{x+\frac{y}{4}}{\Phi}\right)}_{a}N_2. \quad (2.28c)$$

Stoichiometric ($\Phi = 1$, $c = e = f = 0$):

$$C_xH_y + \underbrace{\left(x+\frac{y}{4}\right)}_{a}(O_2 + 3.76\,N_2) \rightarrow x\,CO_2 + \frac{y}{2}H_2O + 3.76\underbrace{\left(x+\frac{y}{4}\right)}_{a}N_2. \quad (2.28d)$$

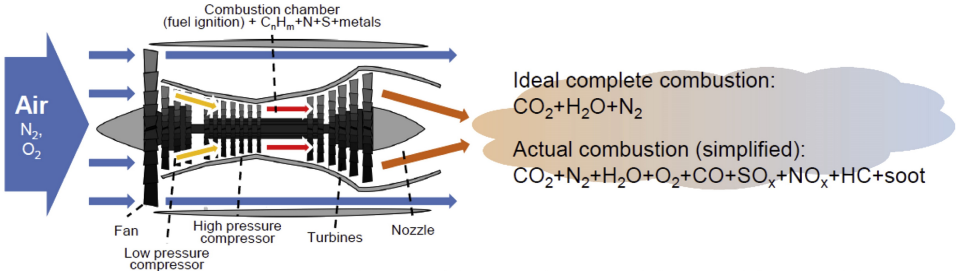


Figure 2.16: Overview of combustion by-products when considering kerosene-powered aircraft. The inlet of the engine receives air, which is primarily composed of N_2 and O_2 and in an incomplete (actual) combustion scenario, a series of by-products like CO_2 and NO_x is generated. Figure was reproduced from [92].

CARBON DIOXIDE (CO_2)

Aviation CO_2 emissions lead to a warming effect. The magnitude of this effect is largely invariable to spatial and temporal factors such as the emission altitude and the season during which the emission occurs because of its long atmospheric lifetimes. This means that transport patterns are not as relevant in influencing CO_2 climate impacts. The range of CO_2 lifetimes depends on exchanges between different reservoirs such as the biosphere, the deep sea, and geological reservoirs such as sediments and rocks, which remove CO_2 across vastly different time scales. Figure 2.17 illustrates the time scales for CO_2 removal across these reservoirs: from decades to centuries in the biosphere (panel (a)), hundreds to thousands of years in the ocean (panel (b)), and tens of thousands of years through reactions with calcium carbonate ($CaCO_3$) in rocks (panel (c)). As a general rule, Fig. 2.17 indicates that 50% of a CO_2 pulse emission is removed by the biosphere after 50 years, with only 40% remaining in the atmosphere after 100 years [116, 117]. This cumulative nature of CO_2 means that emissions from previous decades continue to influence today's atmospheric CO_2 levels and contribute to ongoing climate change.

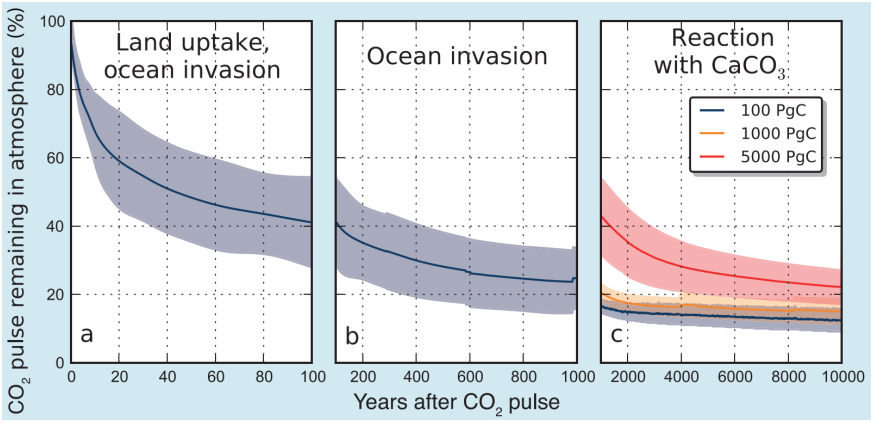


Figure 2.17: Overview of CO_2 lifetimes from three emission scenarios: blue, yellow and red curves arise from pulse emissions of 100, 1000 and 5000 PgC respectively. Panel (a) represents the uptake of CO_2 by the biosphere, (b) its removal by the ocean and (c) its depletion by rocks and sediments. Figure was reproduced from [117].

NITROGEN OXIDES (NO_X)

Nitrogen oxides refer collectively to nitric oxide (NO) and nitrogen dioxide (NO_2), which form at a rate proportional to the combustion flame temperature of an aircraft engine [90]. Although NO_x is not a direct GHG, it still influences Earth's energy balance. In the short term, NO_x emissions increase ozone concentrations, resulting in a warming effect. Over longer timescales, NO_x contributes to methane depletion, which in turn reduces background O_3 concentrations as CH_4 is an O_3 precursor—a chemical feedback process known as primary mode ozone (PMO). This reduction in CH_4 also decreases the production of stratospheric water vapor (SWV) since tropospheric methane transported to the stratosphere by the Brewer-Dobson circulation (see Fig. 2.8) decomposes into CO_2 and H_2O through the net reaction $CH_4 + 2O_2 \longrightarrow CO_2 + 2H_2O$ [41, 118]. Collectively, these long-term effects reduce the overall warming influence of NO_x by lowering the concentrations of these GHGs.

The overall impact of NO_x is generally estimated to be positive, which means that it contributes to warming, although substantial uncertainties persist. Some estimates indicate small positive or even negative effects, heavily influenced by spatio-temporal factors such as the background concentrations of NO_x and CH_4 that the emitted NO_x encounters throughout its atmospheric journey [119, 120]. Recent research predicts increases in O_3 production efficiencies, along with amplified CH_4 cooling effects, driven by projected increases in future background CH_4 and NO_x levels. Additionally, an updated calculation method for the CH_4 RF by Etminan et al. [121] estimates stronger cooling effects. Furthermore, aircraft NO_x emissions can also lead to aerosol formation via the production of the hydroxyl radicals (OH), which enhance the conversion of SO_2 into sulfate and promote the formation of nitrate aerosols, both of which exert secondary cooling effects [120]. Together, these long-term cooling effects raise the possibility of a net negative NO_x effect, driven in part by rising background CH_4 levels and by the role of

NO_x in influencing aerosol species. Overall, NO_x emissions remain highly uncertain due to their nonlinear and heterogeneous chemistry, which varies significantly across space and time.

WATER VAPOR (H_2O)

Aircraft H_2O emissions lead to a comparatively weaker warming impact compared to the other set of forcers in Fig. 1.2. This warming impact is strongly dependent on the cruise altitude of an aircraft as the lifetime of an H_2O perturbation is significantly longer in the lower to middle stratosphere than in the troposphere [45]. This discrepancy is due to the more frequent convective activity and temperature profile that are conducive to the removal of water vapor through precipitation, which is the case for the more unstable troposphere. The main sink for H_2O in the stratosphere involves the condensation of water vapor and its subsequent freezing into ice crystals until they are finally removed via sedimentation. Overall, H_2O perturbation lifetimes tend to increase with altitude until around 40 km (see Fig. 2.18) as a result of increased chemical activity at lower altitudes and more efficient accumulation at higher altitudes. Grewe and Stenke [45], for instance, note that the H_2O perturbation lifetime is around an hour during landing and take-off and close to a month at subsonic cruise altitudes (Fig. 2.18). Therefore, for subsonic aircraft, this means that flying higher may significantly increase the direct warming effect from H_2O [122, 123]. After 40 km of altitude, the lifetime of H_2O begins to decrease due to stronger photolysis and more reactions with $O(^1D)$ [124].

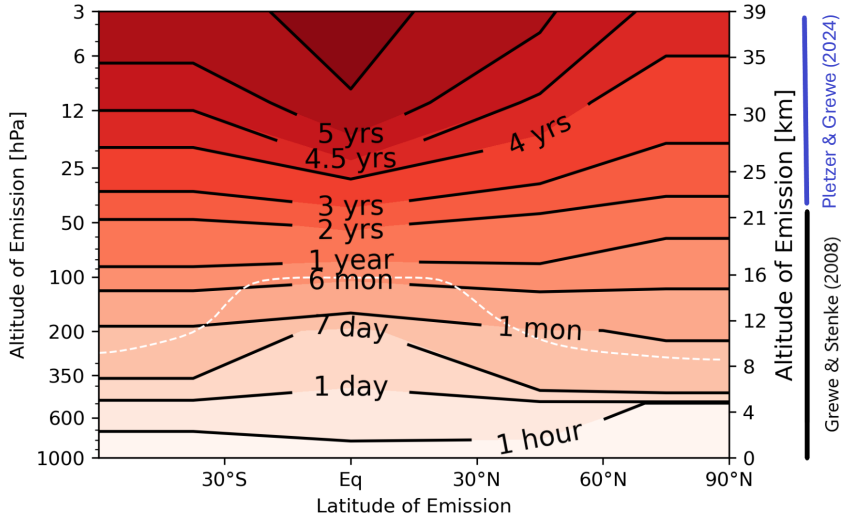


Figure 2.18: Altitudinal variation of the H_2O perturbation lifetime. Grewe and Stenke [45] computed the lifetimes until around 22 km and Pletzer and Grewe [125] extended the analysis to higher altitudes. The figure has been reproduced from [125].

CONTRAILS

Contrails, or condensation trails, are short-lived tubular clouds of ice (lasting from a few minutes to a day [126]) that may form in the wake of aircraft as hot, moist exhaust gases

mix with the colder and drier upper troposphere, typically at altitudes between 8 and 13 km. As the aircraft's fresh plume cools, water droplets condense onto aerosol particles such as soot when the relative humidity (RH) reaches saturation with respect to water. These droplets freeze to form ice crystals once ambient temperatures drop below approximately −40°C at cruise altitudes. If these ice particles remain within an ice-supersaturated region (ISSR), contrails can persist and potentially spread. However, simply flying within warmer ISSRs (that is, above the threshold freezing temperature) does not guarantee contrail formation. Conversely, in regions where RH is sub-saturated with respect to ice, contrails will quickly dissipate as the ice crystals sublimate back into water vapor. These thin ice clouds can expand and evolve into extensive cirrus clouds of anthropogenic origin, whose warming impact is currently considered the largest climate forcer from aviation [27, 126–128]. Due to the strong spatial dependence of contrail formation, the adjustment of flight altitudes to avoid ISSRs has been proposed as a potential mitigation strategy [129].

AEROSOLS: SOOT AND SULFATE (SO_4)

Aviation-induced aerosols like soot or SO_4 can impact Earth's energy budget in two principal ways:

1. Aerosol direct effects: involve the modification of the planetary albedo or reflectivity by directly scattering solar electromagnetic radiation and/or absorbing outgoing thermal radiation. For the case of soot, both radiations are absorbed, resulting in a warming effect. Sulfate, on the other hand, primarily reflects incoming solar radiation, therefore leading to a cooling effect [130].

2. Indirect aerosol effects: involve the alteration of cloud microphysical properties, leading to changes in cloud albedo and lifetime. Aerosols may act as cloud condensation nuclei (CCN) and, as such, may increase a liquid cloud's droplet number concentration (CDNC). If the liquid water content within a cloud is assumed constant, then these droplets will have smaller radii. This integration of more numerous but smaller particles into the composition of a cloud will lead not only to an enhancement of its ability to reflect sunlight, a phenomenon referred to as the Twomey effect [131–133], but also to a lengthening of its lifetime by decreasing its precipitative ability, which is termed the Albrecht effect [134, 135].

As with the other non-CO_2 effects, both direct and indirect aerosol effects are significantly influenced by atmospheric transport processes. Aerosols typically have short lifetimes, in the order of a few days (e.g., around five days for SO_4 [136]), whereas CO_2 has much longer lifetimes. This shorter lifespan means that there is insufficient time for aerosols to become well-mixed throughout the atmosphere to uniformly accumulate before their removal, thereby making spatio-temporal factors like emission altitude and season relevant. Depending on the location and degree of turbulence, the removal velocities (e.g. dry deposition) can vary significantly [137] and the aerosol lifetimes in the lower layers of the troposphere can even be greater by a factor of three depending on the local season [138].

2.3.2. TRANSPORT OF AVIATION-EMITTED POLLUTANTS

The transport of aviation-emitted species is heavily influenced by the prevailing atmospheric circulation patterns. Horizontal transport is shaped by the interactions of the Hadley, Ferrel, and Polar cells (see Fig. 2.7), while vertical transport is largely governed by the Brewer-Dobson circulation (see Fig. 2.8). Previous research has been predominantly conducted with Eulerian models—which compute pollutant concentrations at fixed grid points based on model resolution—and used sensitivity or perturbation approaches to analyze the effects of aviation emissions. These approaches, which assess differences between baseline and perturbed emission scenarios, have consistently demonstrated that subsonic aviation pollutants, such as NO_x, induce the most pronounced atmospheric concentration changes near mid-latitude cruise altitudes. Over time, these pollutants are transported downward to tropical regions, where they are eventually removed through rainout, a process influenced by the Brewer-Dobson circulation [40, 120, 139]. Figure 2.19 illustrates these transport pathways, with particular focus on short-term NO_x-O_3 interactions. The figure shows limited inter-hemispheric transport of emitted species and minimal upward transport into the stratosphere, indicating that subsonic aircraft have a negligible direct impact on stratospheric conditions.

Lagrangian simulations, which track pollutant concentrations along air parcel trajectories, are particularly effective for visualizing atmospheric transport patterns. Studies using this approach, such as those by Schoeberl and Morris [140], generally align with the transport trends shown in Fig. 2.19. Other research, including Grewe et al. [141], has provided valuable insights into the pathways that air parcels must follow to carry emitted species from the troposphere to the stratosphere, offering a level of detail beyond that of Eulerian simulations. According to Fig. 2.20, two types of transport scenarios facilitate this exchange. In the left panel, aviation-induced pollutants descend toward the tropics before recirculating upward into the stratosphere near the equator, a pattern consistent with the Brewer-Dobson circulation. The right panel illustrates a similar scenario but shows the air parcels crossing into the Southern Hemisphere as they ascend near the equator. However, these scenarios represent only about a 5% likelihood of occurrence; by contrast, there is a 90% probability that aviation emissions remain confined to the troposphere. The Lagrangian approach has also proven useful in examining the influence of weather patterns on the transport of emitted species, as demonstrated by Frömming et al. [36] and Grewe et al. [18], who employed a tagging method to track the atmospheric contributions of these species. Figure 2.21 shows how emitted NO_x can be strongly affected by weather conditions: when released west of a high-pressure ridge it follows a trajectory toward the mid-latitudes (blue path), while when emitted within the high-pressure area it is transported to lower altitudes and tropical latitudes (red path). Consequently, the red trajectory enters a region with more active photochemistry, resulting in 50% more O_3 production than along the blue trajectory. A more detailed comparison between Lagrangian and Eulerian methods, as well as between tagging and perturbation approaches, is provided in Chapter 3.

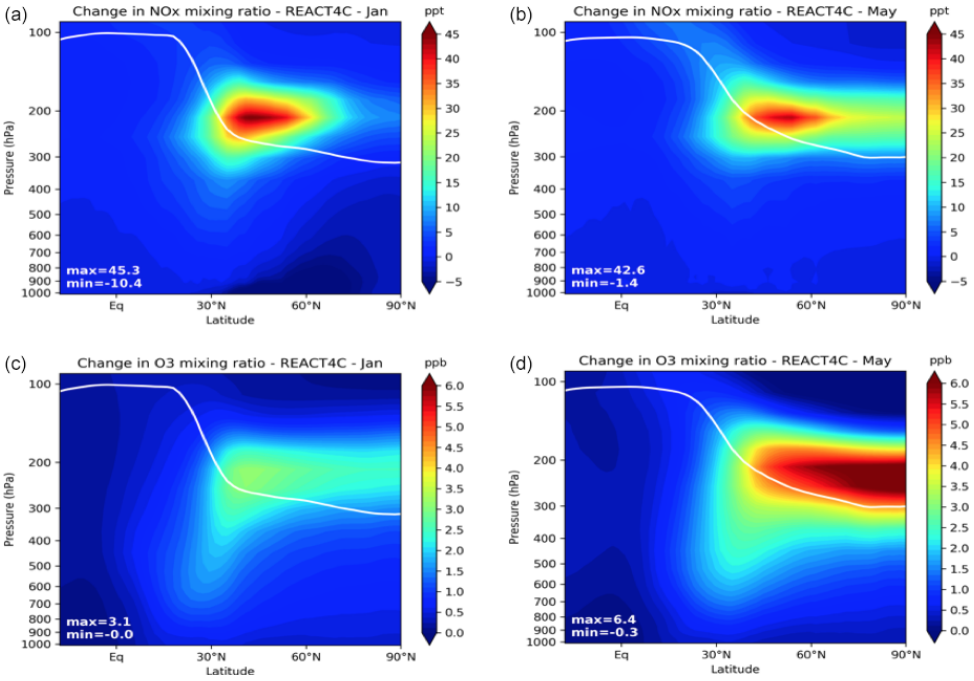


Figure 2.19: (a) - (b) Zonal mean perturbations from aircraft NO_x emissions on atmospheric O_3 (c) - (d). The vertical axis denotes the pressure altitude in hPa and the horizontal axis shows the latitude. The white line represents the climatological tropopause. The colorbar denotes the concentration of the chemical species in ppt (NO_x) or ppb (O_3). Figure was reproduced from [120].

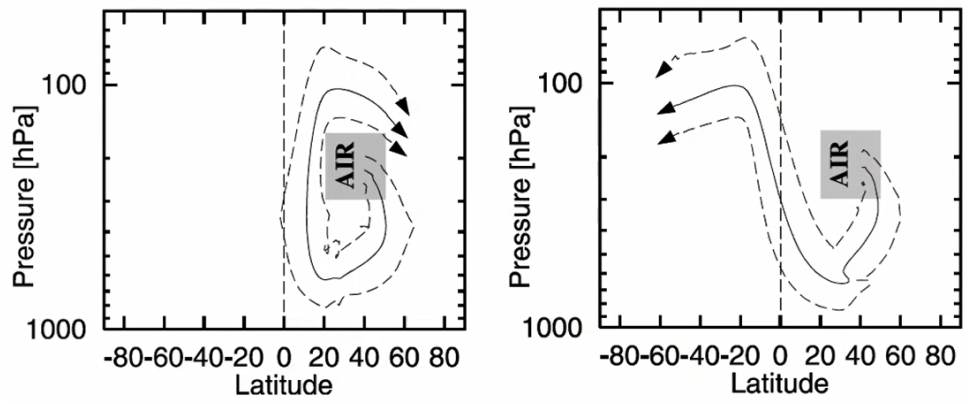


Figure 2.20: Illustration of possible trajectories that could transport aviation emissions from the troposphere to the stratosphere. The left panel depicts the case where this is achieved without inter-hemispheric transport while the panel on the right shows transport from the northern to southern hemispheres. The vertical axis shows the pressure altitude in hPa while the horizontal axis shows the latitude in degrees North. The gray shaded area indicates the starting point of the aviation emission air parcels. Figure was reproduced from [141].

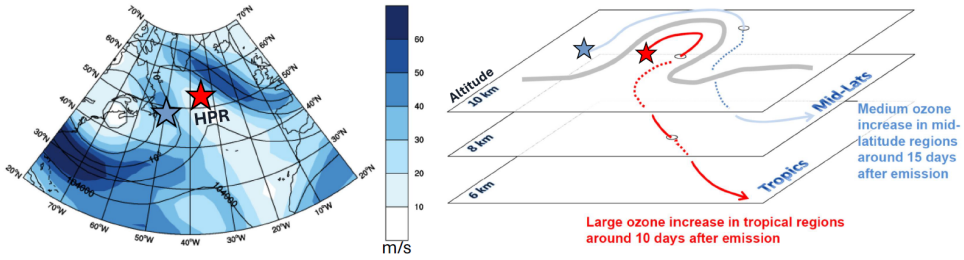


Figure 2.21: Comparison between two different aviation NO_x transport patterns starting at 250 hPa. The left panel is a map plot showing the spatial variation of the wind velocity in m/s, which is indicated by the color bar, and the geopotential in m^2/s^2. A high-pressure ridge (HPR) is also indicated. The red and blue stars indicate air parcels starting within and to the west of the HPR, respectively. The right panel illustrates a red trajectory that is produced when the air parcel starts in the HPR and the blue trajectory characterizes one starting to the west of the HPR. The circular marks indicate the point at which an air parcel descends to another vertical level. Figure was adapted from [18].

In summary, recent research on the transport of pollutants emitted by subsonic aviation has identified several key findings:

- Aircraft pollutants generally follow large-scale atmospheric circulation patterns.
- Aircraft NO_x emitted in high-pressure regions (local subsidence) may lead to increased short-term O_3 production compared to other parts of the atmosphere.
- Pollutants emitted in the troposphere of the Northern Hemisphere are highly unlikely to reach the Southern Hemisphere, as inter-hemispheric transport is rare for subsonic aviation. Similarly, pollutants released into the troposphere rarely penetrate the stratosphere.
- The greatest impact of aviation non-CO_2 pollutants, such as NO_x, occurs primarily in the mid-latitudes of the Northern Hemisphere.

3

MODELING FRAMEWORK

This chapter introduces the fundamentals of atmospheric modeling and presents a comprehensive overview of the EMAC climate-chemistry model, which is applied throughout this dissertation. Key distinctions between the two primary modeling frameworks, Lagrangian and Eulerian, are discussed, along with the differences between source apportionment and sensitivity approaches. In addition, the chapter examines the EMAC submodels most relevant to this research, providing detailed information on their specific roles and functions within the broader modeling framework.

Parts of this chapter belong to Maruhashi et al. [142] that is under preparation and Maruhashi et al. [13, 143].

3.1. AN INTRODUCTION TO ATMOSPHERIC MODELING

EARTH hosts countless physical and chemical phenomena in the atmosphere that affect all living beings. To learn about these processes and understand how anthropogenic activity influences them, it is necessary to construct a simplified scenario, or model, that best approximates reality given the present-day level of computational capacity. Models are especially useful when we seek to visualize a situation that is not easily observable or to predict a system's response to a perturbation in the distant future. With rapidly evolving computational power, these models can include increasingly more complex features for more accurate predictions [144].

The simplest type of model that is relevant for atmospheric research is the box model, which, as its name indicates, assumes that the region to be studied is enclosed by a rectangular space in which chemical species are uniformly mixed. In general, box models are best suited to estimate steady-state concentrations of pollutants, which is appropriate for analyzing species with long lifetimes as they are already well mixed with the atmosphere.

Climate models that mainly capture the circulation of the atmosphere are referred to as General Circulation Models (GCMs), these solve the primitive equations like the Navier-Stokes equations, the continuity equation, the thermodynamic energy equation as well as others. When GCMs are combined with chemical reactions, interactions between land and oceans, carbon and hydrological cycles, clouds, and other processes, they become more complex models called climate-chemistry models (CCMs). Although more encompassing, CCMs may still lack the spatial resolution to adequately represent certain subscale phenomena such as cirrus cloud microphysics, which require simplified representations or parameterizations to study them [145]. There are also Chemistry-Transport Models (CTMs), which focus on processes like advection, deposition and sedimentation that influence the transport of chemical species. The main difference between CCMs and CTMs is that the latter does not solve the primitive equations during the simulation and so relies on meteorological data (e.g. humidity, temperature and wind field) as input [144].

3.1.1. CALCULATION METHODS

AVIATION climate effects may be calculated using one of two methods when using 3D atmospheric models: source apportionment or sensitivity analysis. Each answers fundamentally different research questions. Source apportionment may help in estimating the contribution of a certain emission source or category to the overall concentration of a pollutant, while sensitivity analyses are useful in gauging the marginal impact of a change in the emitted amount of a certain pollutant [146]. The tagging approach is a type of source apportionment that, as its name suggests, involves the labeling or tagging of relevant chemical species to track their evolution throughout their atmospheric journey. The perturbation approach, on the other hand, is an example of a sensitivity analysis that requires finding the numerical difference between two simulations: one with modified emissions and another reference case with unchanged emissions. When applied to a linear phenomenon, both methods will yield mathematically equivalent results [146, 147]. However, when non-linearities abound, as is the case with NO_x-O_3 chemistry, large differences may arise by a factor of more than two [148]. The chosen method must there-

fore be carefully selected according to one's research question.

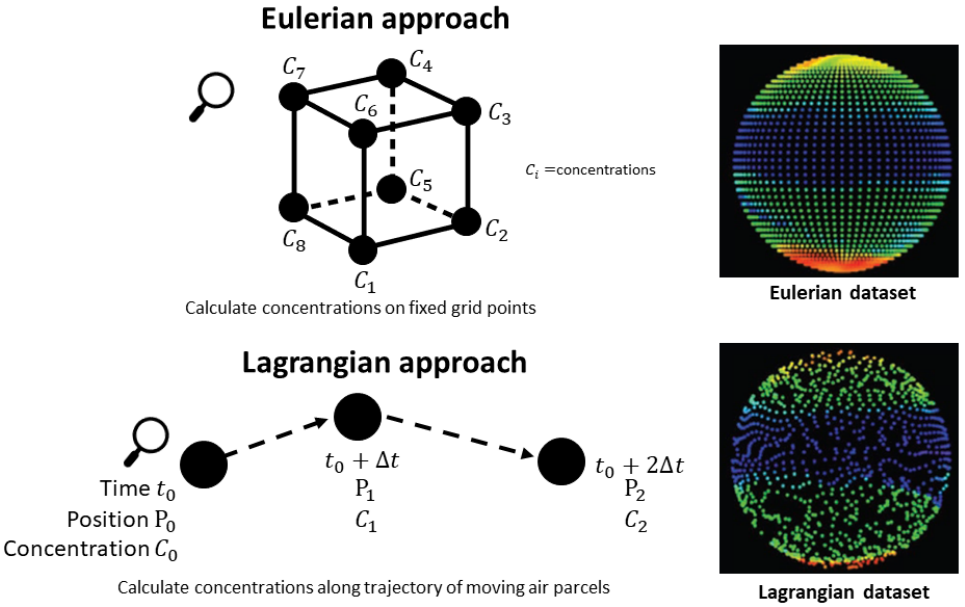


Figure 3.1: Simplified visual summary of the Eulerian and Lagrangian modeling approaches. The two ensembles of colored data points from [144] are examples of outputs of each method, representing concentrations of trace species along fixed grid points (Eulerian) and moving air parcels (Lagrangian).

Along with these two calculation methods, the mathematical representation in which the atmospheric motion of pollutants is defined must also be set. There are two main representations: Eulerian and Lagrangian formulations. The former describes the evolution of a chemical species in terms of a fixed coordinate system, while the latter measures concentration changes in individual air parcel trajectories (i.e., from the perspective of the fluid in motion) [50]. A visual summary of these representations is provided in Fig. 3.1. Each representation presents different advantages and disadvantages. If computational constraints allow, both should be used, as the weaknesses of one are offset by the strengths of the other. The Eulerian approach, for instance, provides concentration fields for the complete domain of an atmospheric model. The Lagrangian alternative, on the other hand, only estimates pollutant concentrations along trajectory coordinates of advected air parcels. Lagrangian models, however, are especially useful for studying aviation's climate effects because of their ability to track the motion of emitted pollutants throughout the atmosphere, which can then be used to connect transport patterns to concentration changes. They are also of great use for source-receptor experiments [144]. Given the strong dependence of aviation climate forcers on transport, the Lagrangian approach is central in this dissertation.

3.2. THE EMAC MODEL

All numerical chemistry simulations in this work were performed with the European Centre for Medium-Range Weather Forecasts – Hamburg (ECHAM)/Modular Earth Submodel System (MESSy) Atmospheric Chemistry (EMAC) model. It is a climate–chemistry model that allows its GCM (here ECHAM5 [149]) to be coupled to a myriad of other submodels via the more recent second version of MESSy [150]. These submodels represent specific atmospheric and chemical processes interacting with the biosphere, land and ocean throughout the troposphere and middle atmosphere [151]. Across all simulations in this thesis, Newtonian relaxation is used to nudge the sea surface temperature, the wind divergence, the vorticity and the logarithm of the sea-level pressure towards ERA-Interim reanalysis data corresponding to the simulation year. All Lagrangian simulations in this thesis were performed using a T42L41 model resolution as a balance between computational costs and resolution. The L41 indicates that 41 discrete vertical hybrid pressure levels ranging from the surface to the uppermost layer centered at 5 hPa are being used, while the T42 value translates to a horizontal discretization of the grid space into 128 longitudes and 64 latitudes, equivalent to a $2.8° \times 2.8°$ quadratic Gaussian grid. This corresponds to a horizontal resolution of about 310 km at the Equator [152].

The MESSy infrastructure is a multi-institutional endeavor that provides a flexible interface based on FORTRAN 95 code standards. It comprises four layers: the base-model layer (BML), the base-model interface layer (BMIL), the submodel interface layer (SMIL) and the submodel core layer (SMCL). The BML includes the GCM, which in this case is ECHAM5. The BMIL functions like a socket system (see Fig. 3.2) through which the GCM is connected to other process-specific submodels as it passes data from submodels to the BML. The SMIL then enables this connection between the BMIL and a submodel by allowing channel objects or data fields specific to a submodel to be passed to other submodels or for GCM-specific variables to be read via the BMIL. Lastly, the SMCL houses the code specific to the functionalities of a submodel [151, 153].

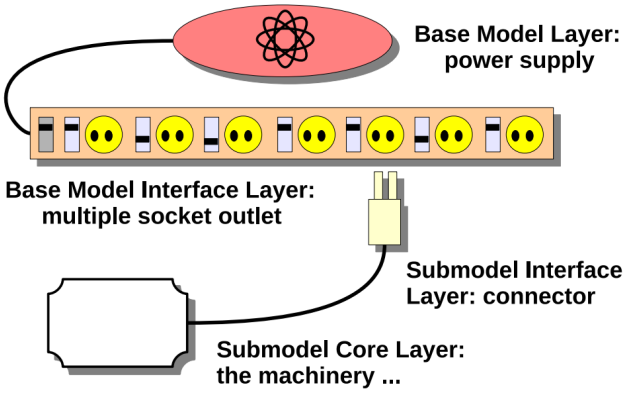


Figure 3.2: Illustration of the Modular Earth Submodel System (MESSy). The base-model layer (BML) is the GCM and acts as the power supply of the configuration. The base-model interface layer (BMIL) is like a socket system, allowing other submodels to be linked to the GCM. The submodel interface layer (SMIL) of each submodel contains the necessary code to connect it to the base. The submodel core layer (SMCL) contains the process-specific code for each submodel. Figure has been reproduced from [153].

3.3. RELEVANT SUBMODELS

The main submodels used in this dissertation are briefly described in this section. The full list of EMAC submodels that were used is provided in Appendix A.

3.3.1. AIRTRAC

AIRTRAC is a Lagrangian tagging box model (each air parcel is treated as a uniformly mixed box) that was originally conceived to analyze the contributions to the atmospheric concentrations of O_3, CH_4, HNO_3 and NO_y species throughout air parcel trajectories that are caused by aviation NO_x and H_2O emissions (Supplement of Grewe et al. [23]). The output of this submodel has been used as the computational basis for the development of CCFs for the North Atlantic flight corridor [23, 36] and more recently for the conception of the paCCFs[154] on a global scale (see Chapter 7).

As a major advantage, AIRTRAC has been constructed as a reduced-order alternative to efficiently computing the effects from multiple emissions scenarios, which are denoted as time-regions. A time-region is simply a geographic location (specified according to the latitude, longitude and altitude) at which a pollutant is released during a user-defined time interval. AIRTRAC is then able to independently calculate the contributions to the various chemical species in the atmosphere from each time-region, as is shown in Fig. 3.3. This has the advantage of avoiding the need to run a simulation for each time-region.

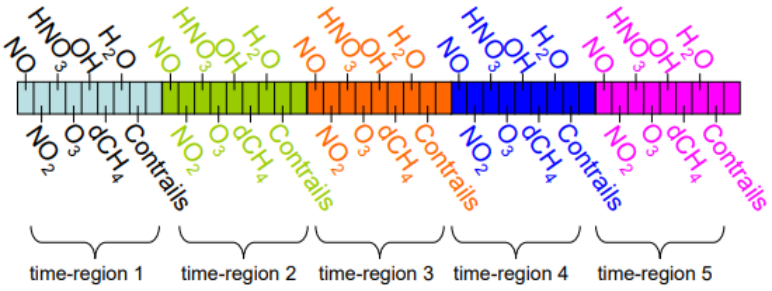


Figure 3.3: Illustration of AIRTRAC's computational efficiency as it is able to independently compute the concentration changes to several chemical species simultaneously for multiple time-regions or emission scenarios within a single simulation. The color-coding represents the output available for each Lagrangian air parcel per time-region. Figure has been reproduced from [23].

On the other hand, AIRTRAC bears limitations stemming from two of its main simplifications: its chemistry mechanism is comparatively simpler than other model schemes (e.g. the TAGGING submodel described in Section 3.3.2) and its chemical reaction rates are linearized using a small perturbation assumption in which the amount emitted by aviation is considered to be small enough so that the specific background reaction rates involved are unaltered [23].

Regarding the former simplification, AIRTRAC uses only one production term and two loss terms to model the evolution of NO_x-O_3 chemistry (see Eq. 3.1):

$$O_{3,\text{net}} = P_{O3N} - L_{O3N} - L_{O3Y}. \tag{3.1}$$

The net ozone production $O_{3,net}$ is driven by the production of O_3 by nitrogen species (P_{O3N}) via NO + HO_2 ⟶ OH + NO_2, and by the losses of O_3 by nitrogen species (L_{O3N}) via NO_2 + O_3 ⟶ NO + 2 O_2 and non-nitrogen species (L_{O3Y}) via OH + O_3 ⟶ HO_2 + O_2. Figure 3.4 depicts the temporal evolution of these terms, where it is clear that the loss of O_3 from non-nitrogen species (i.e. HO_x species) is the dominant loss term.

Regarding the second simplification, AIRTRAC linearizes the complex background reaction rates of the MECCA submodel at each time step [155], which governs the full atmospheric chemistry of EMAC. This approach translates to scaling a non-linear NO_x-O_3 response in proportion to its associated NO emission level. Figure 3.5 (a) demonstrates this linearization by comparing two emission scenarios: one with 5×10^5 kg of emitted NO (purple curve) and another with 10% of that amount (green curve). Due to this linear scaling, AIRTRAC reduces the O_3 response of the purple curve by a factor of 10 to match the reduction in the emitted NO. The constant orange curve, which represents the ratio of O_3 in each scenario over time, confirms this linear relationship, holding steady at a value of 10. This linearization also implies that the O_3 production efficiency (O_3 produced per kg of emitted NO) remains constant within a given time-region, as shown in Fig. 3.5 (b), although it will vary between other time-regions depending on the background chemistry. In summary, this simplification means that there are no chemical feedbacks between the local emission introduced by AIRTRAC and the background.

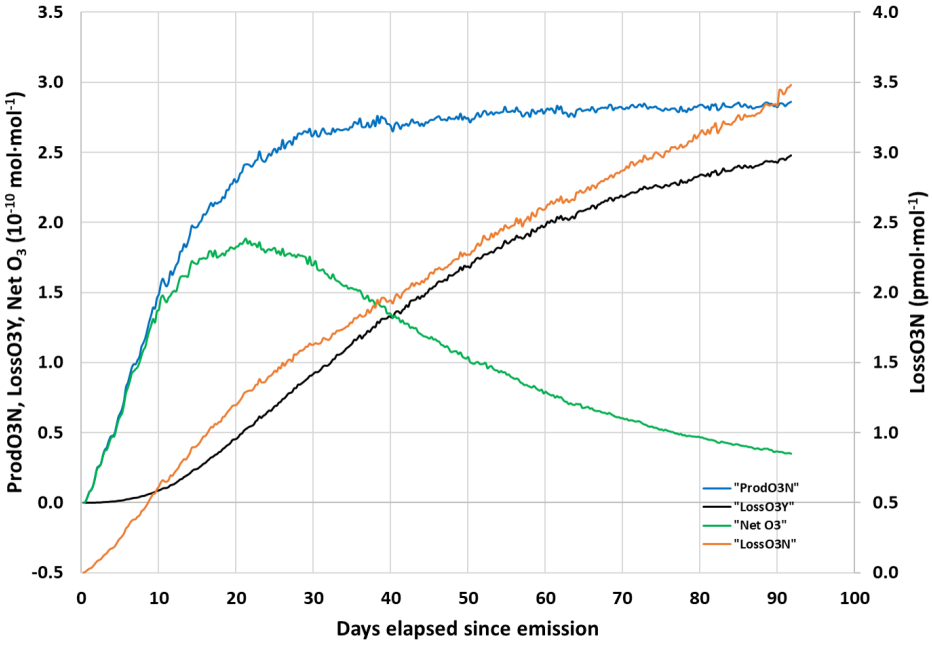


Figure 3.4: Time evolution of O_3 production and loss terms for AIRTRAC. The green curve represents the net O_3 produced ($O_{3,net}$), the blue curve is the nitrogen-based production term (P_{O3N}), the orange curve is the nitrogen-based loss term (L_{O3N}) and the black curve is the O_3 loss from non-nitrogen species (L_{O3Y}).

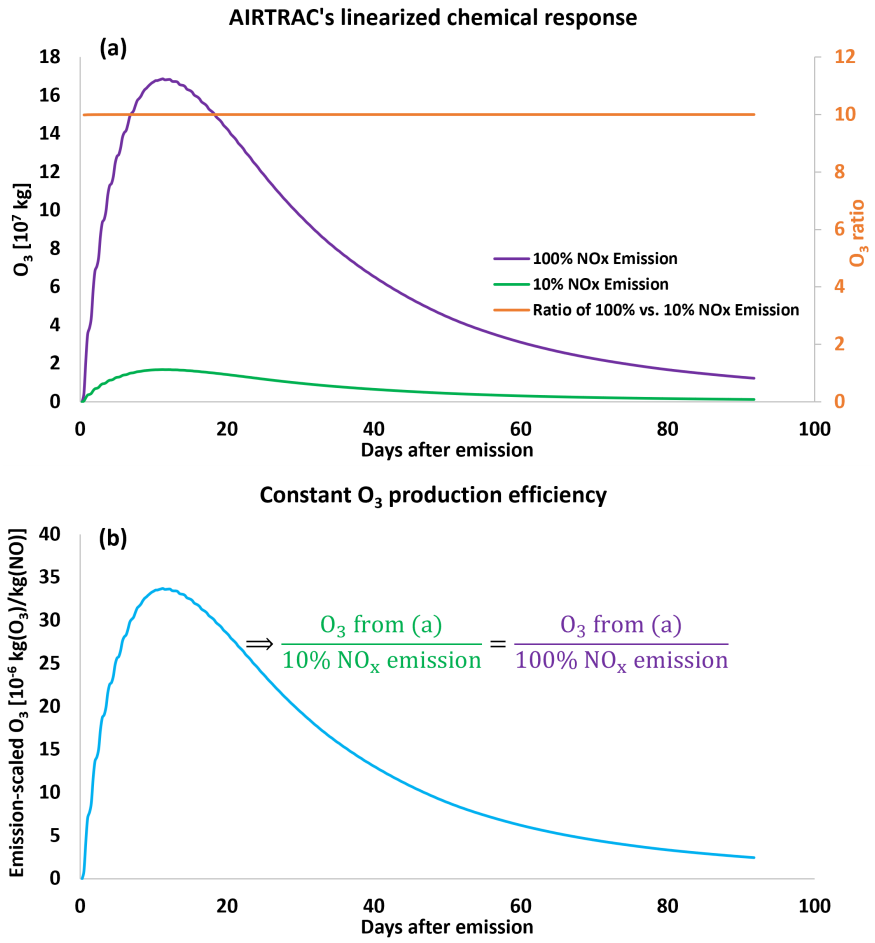


Figure 3.5: Panel (a) illustrates the linearization of AIRTRAC's chemical response. The purple curve shows O_3 produced from 5×10^5 kg(NO) (100% scenario), while the green curve represents O_3 production from an NO amount 10 times smaller. The orange curve shows the constant ratio of O_3 produced between these scenarios. Panel (b) demonstrates the constant O_3 production efficiency obtained by scaling both the purple and green curves from Panel (a) according to their respective NO emissions.

One of the NO_x loss mechanisms included in AIRTRAC is the conversion of NO_2 to HNO_3, followed by the subsequent scavenging of HNO_3, as detailed in Reactions R14–R16 in Chapter 2. This dissertation introduces a key enhancement to the original HNO_3 scavenging algorithm from the initial version of AIRTRAC [23]: the updated algorithm now ensures that the amount of HNO_3 scavenged along an air parcel's trajectory does not exceed the available HNO_3 concentration in the local background. This condition is formalized in Eq. 3.2, where $HNO_3\big|_{traj}$ denotes the HNO_3 scavenged along the trajectory, and $HNO_3\big|_{bg}$ represents the background concentration of HNO_3, thus preventing over-scavenging. This update has been incorporated into AIRTRAC through the commit 6c23c966, titled "AIRTRAC: improved condition for HNO_3 scavenging," which is

accessible upon request from the MESSy gitlab[1].

$$\left| \frac{\mathrm{HNO_3}|_{\mathrm{traj}}}{\mathrm{HNO_3}|_{\mathrm{bg}}} \right| \leq 1 \tag{3.2}$$

AIRTRAC uses the tagging approach described by Grewe [147, 156] to scale the production and loss terms of Eq. 3.1 and estimate the contribution of aviation pollutants from each time-region to the atmosphere. The general tagging formula is given as:

$$\frac{\partial}{\partial t}\mathrm{x}_i^j = P_i^j(t) + F_i(\mathbf{x}) \frac{(\mathbf{x}^j)^{\mathrm{T}} \nabla F_i(\mathbf{x})}{\mathbf{x}^{\mathrm{T}} \cdot \nabla F_i(\mathbf{x})}. \tag{3.3}$$

State variables are represented by x_i^j, where x typically denotes the concentration of a chemical species, i its index and j the index of the sources that contribute to its concentration. The term $P_i^j(t)$ indicates the time-dependent contribution of the source j to the state variable i and F_i is the state-dependent forcing for the state variable i. The tagging approach involves the calculation of a fractional sensitivity term, $\frac{(\mathbf{x}^j)^{\mathrm{T}} \nabla F_i(\mathbf{x})}{\mathbf{x}^{\mathrm{T}} \cdot \nabla F_i(\mathbf{x})}$, that represents the ratio of a source term to a total quantity.

In AIRTRAC's implementation of $\mathrm{NO_x}$-$\mathrm{O_3}$ chemistry, two source types are considered: $j = \mathrm{b}$ for background emissions and $j = \mathrm{e}$ for additional emissions, which in this dissertation specifically refers to aviation. A key advantage of the tagging approach, compared to methods such as the perturbation approach, is the additivity of sources. This ensures that the total rate of change in ozone in the atmosphere, $\frac{\partial}{\partial t}\mathrm{O_3}$, satisfies the following condition:

$$\frac{\partial}{\partial t}\mathrm{O_3} = \frac{\partial}{\partial t}\mathrm{O_3^e} + \frac{\partial}{\partial t}\mathrm{O_3^b}. \tag{3.4}$$

To obtain expressions for the aviation-induced production and loss terms shown in Eq. 3.1, the general tagging formula (Eq. 3.3) should be applied to the corresponding governing chemical reaction, which for generality, is written as $\mathrm{x_1} + \mathrm{x_2} \longrightarrow \mathrm{x_3}$. The differential equation for $\mathrm{x_3}$ then becomes [156]:

$$\frac{\partial \mathrm{x_3}}{\partial t} = F_3(\mathbf{x}) = k\mathrm{x_1}\mathrm{x_2}, \tag{3.5}$$

where k is the reaction rate. The rate of change of $\mathrm{x_3}$ induced by source j is then given as [156]:

$$\frac{\partial \mathrm{x_3^j}}{\partial t} = F_3(\mathbf{x}) \frac{1}{2} \left(\frac{\mathrm{x_1^j}}{\mathrm{x_1}} + \frac{\mathrm{x_2^j}}{\mathrm{x_2}} \right). \tag{3.6}$$

The loss term $\mathrm{L_{O3N}}$ in Eq. 3.1 is associated with the loss of $\mathrm{O_3}$ by its reaction with nitrogen species, i.e. $\mathrm{NO_2} + \mathrm{O_3} \longrightarrow \mathrm{NO} + 2\,\mathrm{O_2}$, which upon applying Eq. 3.6, yields [23]:

$$\mathrm{L_{O_{3N}}^e} = \mathrm{L_{O_{3N}}^b} \cdot \frac{1}{2} \left(\frac{\mathrm{NO_2^e}}{\mathrm{NO_2^b}} + \frac{\mathrm{O_3^e}}{\mathrm{O_3^b}} \right). \tag{3.7}$$

[1] https://gitlab.dkrz.de/MESSy/MESSy

Proceeding with this method for the remaining production and loss terms in Eq. 3.1, as well as assuming that aviation-induced O_3 is produced mainly by NO, AIRTRAC's tagging differential equation for aviation-attributable O_3 (O_3^e) is obtained:

$$\frac{d}{dt}O_3^e = \frac{P^b_{O_{3N}}}{NO_x^b}NO_x^e - \frac{1}{2}L^b_{O_{3N}}\left(\frac{NO_x^e}{NO_x^b} + \frac{O_3^e}{O_3^b}\right) - L^b_{O_{3Y}}\frac{O_3^e}{O_3^b}. \tag{3.8}$$

$L^b_{O_{3N}}$ and $L^b_{O_{3Y}}$ in Eq. 3.8 correspond to the background nitrogen- and non-nitrogen-based O_3 loss rates, respectively. $P^b_{O_{3N}}$ is the background production rate of O_3 and is therefore comparable to P_{O3N} from Eq. 3.1. The integration of Eq. 3.8 with respect to time would then lead to Eq. 3.1, which is expressed in units of volume mixing ratios (see Fig. 3.4).

3.3.2. TAGGING

The TAGGING submodel [157, 158] is capable of estimating the contributions of several sectors (road traffic, shipping, aviation, anthropogenic non-traffic, biogenic, biomass burning and lightning) to chemical species such as O_3, NO_x, CO, NMHC, HO_x and others in the atmosphere. These are also referred to as tagged tracers because they are labeled pollutants that are tracked throughout the simulation. One of the differences between TAGGING and AIRTRAC is that the former calculates contributions using an Eulerian representation. However, the underlying tagging mechanism is also based on the same formulation of Eq. 3.3.

The chemistry mechanism applied by the TAGGING submodel is more detailed than that of AIRTRAC, with a total of seven production and five loss terms, as listed in Table 3.1. Before this dissertation, the TAGGING submodel struggled to accurately represent smaller emission signals, with magnitudes typically around 10^3 kg. As shown in Fig. C.6 of Appendix C, NO signals of this magnitude—such as a 1% signal that corresponds to 5×10^3 kg of NO—were entirely dominated by numerical noise (red curve). The 100% emission amount of 5×10^5 kg of NO is a reference value used in other related EMAC modeling studies [13, 23, 36, 143]. By implementing additional thresholds and preventing the propagation of noise from sectors with negligible contributions, the issue was corrected, as shown by the green curve. A detailed comparison of the NO_x-O_3 responses between the AIRTRAC and TAGGING submodels is presented in Chapter 4.

Table 3.1: Summary of tagged O_3 production and loss terms in the TAGGING submodel.

Term	Meaning
P_{HO_2}	Production via HO_2
P_{RO_2}	Production via RO_2
P_{OH}	Production via OH
P_{NO_y}	Production via NO_y
$P_{HO_2NO_y}$	Production via HO_2 and NO_y
P_{HO_2NMHC}	Production via HO_2 and NMHC
P_{OHNO_y}	Production via OH and NO_y
L_{OH}	Loss via OH
L_{HO_2}	Loss via HO_2
L_{NO}	Loss via NO
L_{RO}	Loss via RO
L_{XO}	Loss via untagged species

3.3.3. MADE3

Aerosol microphysical processes and dynamics are simulated using the third-generation Modal Aerosol Dynamics model for Europe (MADE3) submodel [100, 103], which is the successor to the MADE [159] and MADE-in [101] submodels. The performance of MADE3 has been extensively validated. Its ground-level aerosol mass concentrations have been compared with data from a network of measurement stations and satellite observations, while its vertical profiles for both mass mixing ratios and particle number distributions have been evaluated against aircraft campaign data. Overall, the model demonstrated a satisfactory alignment with observational data, although MADE3 tended to produce larger average sulfate concentrations near the surface, with biases ranging from 13% to 92% when compared to observations from measurement stations. In summary, the model's predictive capabilities have been confirmed, demonstrating consistency with ground-level observations within a factor of two [103, 160].

The MADE3 submodel considers nine types of aerosols: SO_4, black carbon (BC), sea spray (Na), H_2O, chloride (Cl), mineral dust (DU), NH_4, NO_3, and particulate organic matter (POM). Each aerosol type is classified into nine modes, which result from the combination of three size categories and three mixing states. The smallest, the Aitken mode (subscript "k"), includes particles around 10 nm, the accumulation mode (subscript "a") consists of particles roughly 100 nm in diameter, and the largest, the coarse mode (subscript "c"), includes particles approximately 1 µm in size. Each size category is further divided into soluble (subscript "s"), insoluble (subscript "i") and mixed (subscript "m") states [100].

The MADE3 submodel calculates tracer tendencies—concentration rates of change typically expressed in mol mol^{-1} s^{-1} — for both mass and particle number concentrations across these nine modes and species. These tendencies are related to several processes, including gas-particle partitioning (subscript "g/p"), condensation (subscript "cond"), nucleation (subscript "nucl"), coagulation (subscript "coag"), particle growth (subscript "gr"), and aging (subscript "ag"). The general form of the governing differ-

ential equations for the mass mixing ratios $C_{I,M}$ of an aerosol I in mode M is therefore expressed as follows:

$$\frac{\partial C_{I,M}}{\partial t} = R(C_{I,M}) + \frac{\partial C_{I,M}}{\partial t}\Big|_{g/p} + \frac{\partial C_{I,M}}{\partial t}\Big|_{cond} + \frac{\partial C_{I,M}}{\partial t}\Big|_{nucl} + \frac{\partial C_{I,M}}{\partial t}\Big|_{coag} + \frac{\partial C_{I,M}}{\partial t}\Big|_{gr} + \frac{\partial C_{I,M}}{\partial t}\Big|_{ag}. \tag{3.9}$$

The term $R(C_{I,M})$ indicates the variation of aerosol mass concentrations as a result of removal (e.g. dry and wet deposition) and transport phenomena like convection, advection or turbulent mixing processes that are all handled outside of MADE3 by other submodels. Some of these processes include sedimentation (handled by the SEDI submodel), dry deposition (handled by the DDEP submodel), wet deposition (handled by the SCAV submodel) as well as isotropic mixing from atmospheric turbulence (handled by the LGTMIX submodel).

The sulfate aerosol is central to this dissertation, so I= SO_4 and M in Eq. 3.9 will represent one of its nine aerosol modes. For SO_4, the following simplifications apply:

1. $\frac{\partial C_{SO_4,M}}{\partial t}\Big|_{g/p} = 0$. The gas-particle partitioning term in MADE3 can refer to the partitioning between, for instance, gas-phase HNO_3 and NH_3 molecules and the liquid-phase aerosol form of NO_3 and NH_4, respectively. For SO_4, this process is neglected, as it is assumed that H_2SO_4 has an equilibrium vapor pressure that is low enough so that it is fully transferred from the gas phase to the aerosol phase at each time step. This assumption also means that the reverse conversion is not possible, i.e., H_2SO_4 cannot re-evaporate [100].

2. $\frac{\partial C_{SO_4,M\neq ks}}{\partial t}\Big|_{nucl} = 0$. The nucleation term for SO_4 in MADE3 applies exclusively to the mass mixing ratios of the particles in the soluble Aitken mode (M = ks), since the particles freshly formed by the binary homogeneous nucleation of H_2SO_4 and H_2O are assumed to instantaneously produce soluble SO_4 aerosols that are immediately within the Aitken mode size range [100, 101, 103].

3. $\frac{\partial C_{SO_4,M=\{ks,as,cs\}}}{\partial t}\Big|_{ag} = 0$. The aging process changes aerosols from insoluble to mixed modes when their soluble mass fractions exceed a critical threshold of 10%. Experimental studies [161, 162] have shown that aerosols with soluble mass fractions above this threshold will exhibit hygroscopic growth, meaning they readily take up water and expand [101]. Consequently, the aging tendency only influences the insoluble and mixed modes, leaving the soluble modes across the three size classes unaffected.

By applying these three assumptions to Eq. 3.9, the nine differential equations for the mass mixing ratio corresponding to each of the nine SO_4 aerosol modes are derived (Eq. 3.10):

$$\frac{\partial C_{SO_4,M}}{\partial t} = \begin{cases} R(C_{SO_4,M}) + \left.\frac{\partial C_{SO_4,M}}{\partial t}\right|_{cond} + \left.\frac{\partial C_{SO_4,M}}{\partial t}\right|_{nucl} + ... \\ \quad + \left.\frac{\partial C_{SO_4,M}}{\partial t}\right|_{coag} + \left.\frac{\partial C_{SO_4,M}}{\partial t}\right|_{gr}; & M = ks \\ R(C_{SO_4,M}) + \left.\frac{\partial C_{SO_4,M}}{\partial t}\right|_{cond} + \left.\frac{\partial C_{SO_4,M}}{\partial t}\right|_{coag} + ... \\ \quad + \left.\frac{\partial C_{SO_4,M}}{\partial t}\right|_{gr} + \left.\frac{\partial C_{SO_4,M}}{\partial t}\right|_{ag}; & M = ki, km, ai, am, ci, cm \\ R(C_{SO_4,M}) + \left.\frac{\partial C_{SO_4,M}}{\partial t}\right|_{cond} + \left.\frac{\partial C_{SO_4,M}}{\partial t}\right|_{coag} + ... \\ \quad + \left.\frac{\partial C_{SO_4,M}}{\partial t}\right|_{gr}; & M = as, cs. \end{cases} \tag{3.10}$$

THE NUCLEATION TENDENCY

Homogeneous nucleation between H_2SO_4 and H_2O is a critical process behind the formation of SO_4 aerosols in the atmosphere and is modeled in MADE3 by means of a parameterization by Vehkamäki et al. [111] for the nucleation rate J, which is shown in Eq. 2.26 from Chapter 2. The range of applicability of J is for an atmospheric temperature T between 230 and 305 K, which are typical values for the troposphere and stratosphere, a relative humidity (RH) between 0.01% and 100% and sulfuric acid concentrations ($C_{H_2SO_4}$) between 10^4 and 10^{11} molecules per cm^3. In an earlier version of MADE3 (version 2.0b [100]), it was assumed that the newly nucleated sulfate particles were entirely composed of a representative wet diameter of 3.5 nm, although in reality they are likely to be smaller and grow to more comparable sizes after other processes such as coagulation and condensation occur, as is acknowledged by Binkowski and Roselle [163]. In the more recent MADE3 release (version 3.0 [103]), freshly formed particles are considered to have a dry diameter of 10 nm to account for rapid growth to larger sizes within a few hours, a phenomenon that cannot yet be resolved by global models. Compared to tropospheric observations of nucleated particles gathered by other studies [164, 165], such a modification appears to yield more accurate simulation results for the size distribution of aerosol particles and their particle number concentrations [103]. The calculation of the SO_4 nucleation tendency is performed according to Eq. 3.11:

$$\left.\frac{\partial C_{SO_4,ks}}{\partial t}\right|_{nucl} = J(T, RH, C_{H_2SO_4}) \times m_{10nm}(RH) \times \exp\left(\frac{9}{2}\ln^2\sigma_{ks}\right). \tag{3.11}$$

The term m_{10nm} represents the mass of a freshly nucleated, spherical SO_4 particle with a dry diameter of 10 nm and its value is influenced by the ambient relative humidity. The factor $\exp\left(\frac{9}{2}\ln^2\sigma_{ks}\right)$ incorporates the geometric standard deviation of the soluble Aitken mode (σ_{ks}) and originates from the third moment ($\mathscr{M}^{(3)}$) of a lognormal aerosol size distribution, as expressed in Eq. 2.13. Conceptually, the third moment is

proportional to the total volume of aerosol particles in a certain mode, which in this case is ks. Similarly, the zeroth moment represents the total particle number while the second moment ($\mathscr{M}^{(2)}$) is proportional to the total aerosol surface area [163]. More generally, the k$^{\text{th}}$ moment for a distribution of aerosols in mode M is defined by Eq. 3.12 [101]:

$$\mathscr{M}_{\mathrm{M}}^{(\mathrm{k})} = \int_{-\infty}^{\infty} D_{\mathrm{M}}^{\mathrm{k}}\, n(\ln D)\, d(\ln D) = N_t D_{\mathrm{M}}^{\mathrm{k}} \exp\left[\frac{\mathrm{k}^2}{2} \ln^2 \sigma_{\mathrm{M}}\right]. \tag{3.12}$$

It should be noted that nucleation involves only the amount of H_2SO_4 that has not yet been consumed by condensation. In reality, both processes simultaneously compete for H_2SO_4, but within the MADE3 code the condensation process has been set to occur before nucleation. Consequently, this amplifies the influence of SO_4 nucleation at locations in which the condensation-related sinks for H_2SO_4 are low [100].

THE CONDENSATION TENDENCY

The condensation of H_2SO_4 onto pre-existing particles leads to an overall gain in the mass concentration of SO_4. As was mentioned, it is assumed that all of the sulfuric acid is converted entirely from the gas to the aerosol phase and that no re-evaporation occurs in the opposite direction [100]. This SO_4 gain ($\frac{\partial \mathrm{C}_{\mathrm{SO_4,M}}}{\partial t}\Big|_{\mathrm{cond}}$) is quantified by Eq. 3.13 and may be expressed in terms of the dimensionless coefficients $\Omega_{\mathrm{SO_4,M}}$ and the amount of condensed sulfuric acid, represented by $\Delta \mathrm{H_2SO_4}\big|_{\mathrm{cond}}$, for each aerosol mode M [101, 166]:

$$\frac{\partial \mathrm{C}_{\mathrm{SO_4,M}}}{\partial t}\Big|_{\mathrm{cond}} = \Omega_{\mathrm{SO_4,M}} \times \frac{\Delta \mathrm{H_2SO_4}\big|_{\mathrm{cond}}}{\Delta t}. \tag{3.13}$$

The coefficients $\Omega_{\mathrm{SO_4,M}}$ measure the modal contribution of the SO_4 growth term for mode M ($\mathrm{G}^{(3)}_{\mathrm{SO_4,M}}$) relative to the sum of growth terms of all nine aerosol modes. These growth terms are proportional to the time rate of change of the third moment (see Eq. 3.12) of mode M, which means that $\frac{\partial \mathscr{M}^{(3)}_{\mathrm{M}}}{\partial t} \propto \mathrm{G}^{(3)}_{\mathrm{M}}$, and are defined by Eq. 3.14. The variable $\Delta \mathrm{H_2SO_4}\big|_{\mathrm{cond}}$ is calculated by solving a first-order linear differential equation (Eq. 3.15) that describes the difference between the gas-phase production rate of sulfuric acid (P) and its condensation loss rate L as follows [100, 101]:

$$\Omega_{\mathrm{SO_4,M}} = \frac{\mathrm{G}^{(3)}_{\mathrm{SO_4,M}}}{\sum_{j=1}^{9} \mathrm{G}^{(3)}_{\mathrm{SO_4,j}}}, \tag{3.14}$$

$$\frac{d\mathrm{C}_{\mathrm{H_2SO_4}}(t)}{dt} = \mathrm{P} - \mathrm{L} \cdot \mathrm{C}_{\mathrm{H_2SO_4}}(t). \tag{3.15}$$

The growth rates G featured in Eq. 3.14 may be computed by finding the harmonic mean of the growth rates for the SO_4 aerosol in mode M for two regimes: the free-molecular regime in which collisions between gas molecules are not as frequent and the near-continuum regime in which collisions are frequent enough for the gas to be considered a continuous fluid. Other variables like the saturation vapor pressure and diffusion coefficients of sulfuric acid are also necessary to calculate $\Omega_{\mathrm{SO_4,M}}$. Further details on the

calculation of the terms in Eq. 3.13 are provided by Aquila et al. [101] and Kaiser et al. [100].

THE COAGULATION TENDENCY

Two types of coagulation processes are distinguished: intramodal and intermodal. The former occurs between particles of the same mode and produces aerosols that belong to the same class as the original ones. The latter occurs between particles from different size and mixing states and results in particles with diameters comparable to the larger of the colliding aerosols. The resulting mode for each type of collision in MADE3 is governed by a categorical variable τ_{lm} where l and m are the two colliding modes. The possible values of τ_{lm} are shown in Table 3.2. As an example, an aerosol in a mixed Aitken mode (km) colliding with another particle in a soluble accumulation mode (as) will produce a particle in the mixed accumulation mode (am).

Table 3.2: Values of τ_{lm} based on origin modes l (rows) and m (columns), which are numbered as follows: ks=1, km=2, ki=3, as=4, am=5, ai=6, cs=7, cm=8 and ci=9. The * denotes a case in which the coagulated particle is placed in one of two modes depending on its soluble mass fraction x relative to water. If $x = 1$, then the resulting particle is placed in the soluble mode, if $x \in [0.1, 1)$, it is placed in the mixed mode and if $x \in [0, 0.1)$, it is allocated to the insoluble mode [100, 101]. This table has been adapted from Kaiser et al. [100].

Modes	**ks**	**km**	**ki**	**as**	**am**	**ai**	**cs**	**cm**	**ci**
ks	1	2	2/3*	4	5	5/6*	7	8	9
km	2	2	2/3*	5	5	5/6*	8	8	9
ki	2/3*	2/3*	3	3/5*	3/5*	6	8	8	9
as	4	5	3/5*	4	5	5/6*	7	8	8/9*
am	5	5	3/5*	5	5	5/6*	8	8	8/9*
ai	5/6*	5/6*	6	5/6*	5/6*	6	6/8*	6/8*	9
cs	7	8	8	7	8	6/8*	7	8	8/9*
cm	8	8	8	8	8	6/8*	8	8	8/9*
ci	9	9	9	8/9*	8/9*	9	8/9*	8/9*	9

When quantifying aerosol mass mixing ratios, only intermodal coagulation is therefore relevant for the spatio-temporal evolution of aerosol mass mixing ratios. The contribution to mode M of SO_4 resulting from the coagulation of an aerosol in mode p and another in mode q is given by Eq. 3.16:

$$\begin{aligned}\frac{\partial C_{\mathrm{SO_4,M}}}{\partial t}\Big|_{\mathrm{coag}} = \frac{\pi}{6}\sum_{p=1}^{9}\sum_{q=1}^{9}\Bigg[&(\delta_{\mathrm{M},\tau_{pq}} - \delta_{\mathrm{M},p})\frac{C_{\mathrm{SO_4},p}}{\sum_{s=1}^{A} C_{s,p}}\rho_p \int_0^\infty\int_0^\infty (D_1)^3\beta(D_1,D_2)n_p(D_1)n_q(D_2)\,dD_1\,dD_2 \\ &+(\delta_{\mathrm{M},\tau_{pq}} - \delta_{\mathrm{M},q})\frac{C_{\mathrm{SO_4},q}}{\sum_{s=1}^{A} C_{s,q}}\rho_q \int_0^\infty\int_0^\infty (D_2)^3\beta(D_1,D_2)n_p(D_1)n_q(D_2)\,dD_1\,dD_2\Bigg].\end{aligned} \tag{3.16}$$

The symbol $\delta_{x,y}$ denotes the Kronecker delta, which, by definition, assumes a unit value only when both subscripts x and y refer to the same aerosol mode. The resulting aerosol mode, as mentioned above, is determined by τ_{pq}. The mass mixing ratios of SO_4 corresponding to modes p and q are indicated as $C_{\mathrm{SO_4},p}$ and $C_{\mathrm{SO_4},q}$ and their densities as ρ_p and ρ_q, respectively. The upper bound A of the summation notation indicates the

total number of tracer species s in MADE3, i.e., SO_4, NH_4, NO_3, Na, Cl, POM, BC, DU and H_2O. The particle number distribution for modes p and q with particle diameters D_1 and D_2 are written as $n_p(D_1)$ and $n_q(D_2)$. Lastly, the Brownian coagulation kernels for particles with diameters D_1 and D_2 are expressed as $\beta(D_1, D_2)$, which vary according to the flow regime, i.e., free-molecular or near-continuum, and with parameters like the particle diameters, the atmospheric temperature and pressure, particle densities and dynamic viscosity. From a more intuitive perspective, they describe the probability of collision between particles of diameters D_1 and D_2 based on Brownian motion [166].

THE GROWTH AND AGING TENDENCY

Although in theory the growth and aging processes are distinct, as was depicted by Eq. 3.10, they are coupled and therefore not given each their own tendency in MADE3. The collective tendency in MADE3 that describes growth and aging is called "rename" and is impacted by both the condensation and the coagulation processes. The growth process, for instance, refers to the possibility of aerosols growing as they either coagulate or condense onto other pre-existing particles. This may lead to a redistribution in the aerosol modes from smaller to larger, i.e., a reclassification from the Aitken to the accumulation mode. The aging process, in turn, is related to the transformation of insoluble particles via the acquisition of a soluble coating that alters their state from hydrophobic to hydrophilic. As was referred earlier in this section, when the soluble mass fraction of an insoluble mode reaches a critical threshold of 10%, the mode is turned into a mixed mode. Therefore, aging only affects the insoluble and mixed modes of SO_4. Further technical details on the implementation of these processes are provided in Aquila et al. [101] and Kaiser et al. [100].

The transport term, $R(C_{I,M})$, encompasses removal processes like dry deposition, sedimentation and wet scavenging, which are discussed in the next subsections about the DDEP, SEDI and SCAV submodels respectively.

3.3.4. DDEP AND SEDI

Dry deposition refers to the removal of atmospheric aerosols through various interactions with surfaces, such as land or sea, and includes mechanisms such as gravitational settling (sedimentation), impaction (where aerosols adhere to surfaces like vegetation), interception (where aerosols are intercepted by objects within their airstream, such as leaves), and diffusion [137]. While sedimentation is a form of dry deposition, there are two key distinctions between them that are reflected in the way each process is coded. Firstly, sedimentation, managed by the SEDI submodel, is applied across the entire vertical domain of the simulation, whereas dry deposition, handled by the DDEP submodel, only affects the lowest atmospheric layer near the surface. Secondly, sedimentation primarily concerns the removal of aerosols rather than gaseous species, due to mass considerations [167].

The dry deposition flux for aerosols is proportional to the dry deposition velocity v_d, which can vary according to three types of surfaces: vegetation (subscript "veg"), soil and snow (subscript "slsn") and water (subscript "wat"). The dry deposition tendency for the SO_4 aerosol is expressed in the submodel according to Eq. 3.17, where parameters β_1, β_2 and β_3 depend on the surface type:

$$\left.\frac{\partial C_{SO_4,M}}{\partial t}\right|_{DDEP} \propto \underbrace{\beta_1 \times v_{d,veg}(SO_{4,M}) + \beta_2 \times v_{d,slsn}(SO_{4,M}) + \beta_3 \times v_{d,wat}(SO_{4,M})}_{v_d}. \quad (3.17)$$

The sedimentation tendency (Eq. 3.18) is in turn proportional to the terminal sedimentation velocity v_t, which depends on the Stokes velocity v_{Stokes}, the Cunningham slip flow correction factor (similar to Eq. 2.20, but now denoted as f_{csf}) and lastly the Slinn factor f_s. The product of f_{csf} and v_{Stokes} has been derived in Chapter 2 in Eq. 2.23.

$$\left.\frac{\partial C_{SO_4,M}}{\partial t}\right|_{SEDI} \propto \underbrace{v_{Stokes}(SO_{4,M}) \times f_{csf}(SO_{4,M}) \times f_s(SO_{4,M})}_{v_t} \quad (3.18)$$

The Cunningham correction factor in SEDI (Eq. 3.19) is defined using slightly different coefficients as the previous expression of Eq. 2.20. The Knudsen number in the equation below will vary according to the aerosol mode M given its dependence on the particle diameter (see Eq. 2.18).

$$f_{csf} = 1 + Kn\left[2.514 + 0.8\exp\left(\frac{-0.55}{Kn}\right)\right] \quad (3.19)$$

The Slinn factor is used to correct for the fact that the average sedimentation velocity of the lognormal population of aerosols is larger than the sedimentation velocity of a particle with an average particle diameter [167].

3.3.5. SCAV

Wet deposition refers to the scavenging of aerosols as a result of precipitation of either ice or liquid water. Aerosol lifetimes are strongly influenced by the interaction between wet and dry deposition processes. Global-scale studies have shown that wet deposition is, however, more significant in removing aerosols, but that dry deposition is naturally dominant in cloud-free regions in which precipitation is unlikely [137]. Within EMAC, wet deposition may be calculated with the SCAV submodel [168], which considers two mechanisms: nucleation scavenging (or rainout) and impaction scavenging (or washout). The former involves the removal of chemical species from the atmosphere by means of nucleation and subsequent growth of cloud droplets that dissolve them and are then rained out. The latter process refers to the removal of aerosols and gases via their direct collision with raindrops. In a cloud-free region, nucleation scavenging is ignored and only impaction scavenging is considered. Both mechanisms in general are accounted for via parameterizations that depend on, e.g., the Brownian motion of aerosols. These are described in further detail by Tost et al. [168]. The distinction between large-scale (subscript "ls") and convective (subscript "cv") precipitation events is provided in SCAV so that the scavenging effects of each type of rain can be isolated and quantified. The total scavenging tendency provided by this submodel is therefore the sum of both of these precipitation tendencies, as is expressed by Eq. 3.20:

$$\left.\frac{\partial C_{SO_4,M}}{\partial t}\right|_{SCAV} = \left.\frac{\partial C_{SO_4,M}}{\partial t}\right|_{SCAV,cv} + \left.\frac{\partial C_{SO_4,M}}{\partial t}\right|_{SCAV,ls}. \quad (3.20)$$

3.3.6. ATTILA AND LGTMIX

ATTILA or Atmospheric Tracer Transport In a LAgrangian model is a Lagrangian transport scheme within EMAC. Unlike Eulerian approaches, which may suffer from issues such as numerical diffusion or negative concentrations in the presence of large gradients, Lagrangian approaches overcome these and are also mass-conserving [169, 170]. They function by introducing a large number of air parcels (in the order of 10^5) into the atmosphere (or more depending on the available computational power) and advecting their centroids. Within these air parcels, each chemical species has a mass mixing ratio defined at every centroid. Regardless of the number of total species, the computational effort depends mainly on the number of air parcels, which is advantageous when modeling involves an extensive set of pollutants. However, one of the possible disadvantages is that the spatial resolution covered by the air parcels is only controlled indirectly based on where they are initialized in the simulation and on their quantity, unlike an Eulerian approach, where the resolution is defined by the model grid [170].

Advection refers to the transport of pollutants by air movement. The trajectories of these advected air parcels were calculated using the 3D wind field from ECHAM5. For horizontal transport (across latitude and longitude), the wind velocity at the parcel's position is derived through linear interpolation, while the vertical component is interpolated using cubic polynomials. Within the planetary boundary layer, turbulence is represented as a stochastic mixing process, with air parcels undergoing random vertical displacements within each grid cell to simulate turbulent motion.

Convection, in contrast, refers to the movement of air parcels driven by temperature gradients. The temperature-driven mass fluxes within each grid cell, which transport air parcels vertically, are derived from the CONVECT submodel [168], EMAC's convection scheme. Air parcels can follow an updraft, downdraft, or subsidence pathway—the latter acting as a compensatory mechanism to maintain local mass balance. Figure 3.6 illustrates these three scenarios: red circles represent air parcels in updrafts, dark blue circles in downdrafts, green circles in subsidence, and light blue circles are air parcels unaffected by these processes. To satisfy mass conservation, the total number of air parcels in each grid cell remains constant after each time step. For example, in the top grid cell containing four parcels (n = 4), an updraft adds an air parcel from below. Since there are no downdrafts to balance this addition, subsidence compensates by removing an air parcel, ensuring that the count remains unchanged. Consequently, the net flow in each grid cell is zero, maintaining local mass equilibrium [169].

Turbulence will cause Lagrangian air parcels to mix in a process known as interparcel mixing, which alters the mixing ratios of the pollutants that they carry. This phenomenon is parameterized according to Eq. 3.21 [169, 170]:

$$C_i^{new} = C_i + (\overline{C} - C_i)\, d. \tag{3.21}$$

The mixing ratio of a chemical species within the air parcel after mixing, C_i^{new}, is determined by the initial mixing ratio C_i, the mean background mixing ratio $\overline{C}$ and the dimensionless mixing parameter d in the range [0,1]. Mixing becomes stronger as this parameter increases. For all Lagrangian simulations in this thesis, the standard values established by Reithmeier and Sausen [170] are applied: $d = 10^{-3}$ for the troposphere and $d = 5 \times 10^{-4}$ for the stratosphere. It is therefore assumed that turbulent mixing is

twice as strong in the troposphere. The mean value of $\overline{C}$ is determined by finding the average mixing ratio of all air parcels within a given grid box according to Eq. 3.22, where again, n is the number of air parcels:

$$\overline{C} = \frac{1}{n} \sum_{i=1}^{n} C_i. \tag{3.22}$$

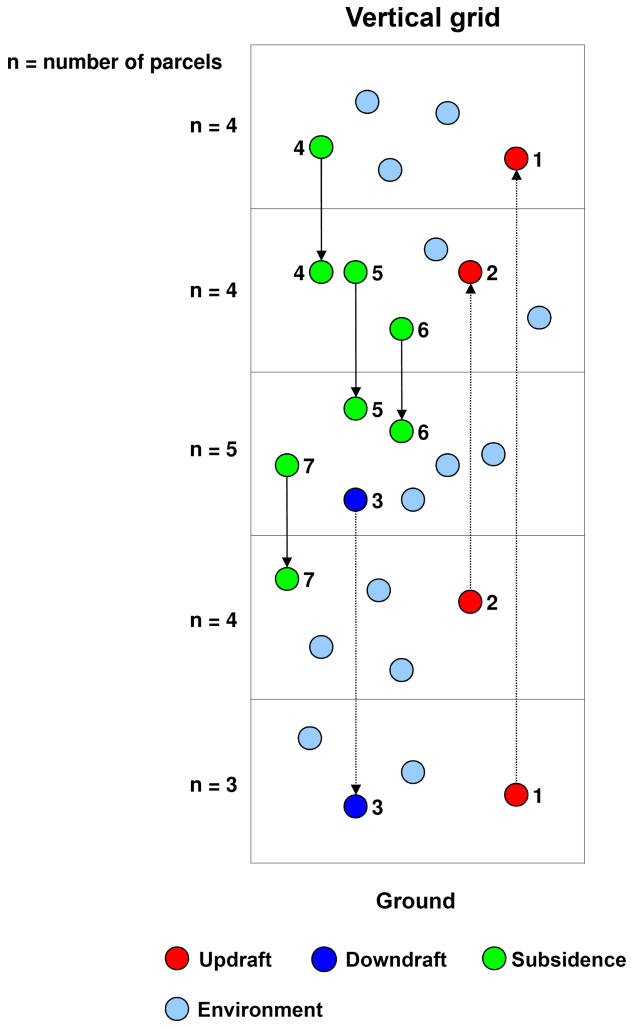


Figure 3.6: Illustration of the Lagrangian convection scheme in ATTILA. Circles represent air parcels. The original number of air parcels in each grid box is labelled by n. Due to mass conservation, this value of n should be constant after each convection event. Figure is reproduced from [169].

4

A MULTI-METHOD COMPARISON OF THE ALTITUDINAL SENSITIVITY OF AVIATION NO_X-O_3 CLIMATE EFFECTS

Flight altitude is relevant to the climate effects resulting from aircraft emissions. Other research has shown that flying higher within the troposphere leads to a larger warming from O_3 production. Aircraft NO_x emissions are of particular interest, as they lead to warming through short-term production of O_3, but also to reduced warming via processes like CH_4 depletion. The focus is on short-term O_3 production, as it constitutes one of aviation's largest warming components. Understanding how O_3 formation varies altitudinally throughout the upper troposphere/lower stratosphere is essential for designing climate-compatible aircraft and routing. This variation is quantified by performing simulations with the EMAC model for three representative cruise altitudes, five regions and two seasons using three methods: Eulerian tagging, perturbation and Lagrangian tagging. This multi-method, regional approach overcomes limitations of previous studies that utilize only one of these methods and apply global emission inventories biased towards present-day flight distributions, thus limiting their applicability to future aviation scenarios. Results highlight that underrepresenting emissions in areas with growing flight activity (e.g. Asia Pacific) may lead to significant, regional underestimations of the altitudinal sensitivity of short-term NO_x-related O_3 warming effects in certain cases. Emitting in southern regions, like Australasia, leads to a larger warming by a factor of two compared to global averages. These findings also suggest that flying lower translates to lower warming from short-term O_3 production and that this effect is strongest during the local summer. Differences ranging from a factor of 1.2–2.6 are estimated between tagging and perturbation

Parts of this chapter are based on Maruhashi et al. [143], which has been published in the Environmental Research Letters journal [143].

results that are attributable to non-linearities of NO_x-O_3 chemistry. Regional correction factors are also derived for the AIRTRAC submodel. Overall, a combination of all three methods is necessary for a robust assessment of aviation climate effects as they address fundamentally different questions.

4.1. INTRODUCTION

THIS chapter focuses on aviation nitrogen oxide emissions given their potential to instigate one of aviation's largest warming effects via short-term, indirect ozone formation, a process that bears large uncertainties across NO_x-related processes [27]. Furthermore, NO_x emissions can degrade air quality [7, 12] and are projected to outpace the growth in fuel consumption, making them a pressing concern, especially as they cannot be effectively mitigated even with the use of sustainable aviation fuels [171]. More efficient engine technologies also fall short in this regard as they often equate to larger pressure ratios and turbine inlet temperatures that reduce CO_2, but at the cost of increasing NO_x [172, 173].

Varying the flight altitude, however, is an operationally feasible mitigation option for the near-term. Research has shown that flying lower within the UTLS (here referring to altitudes between 9–12 km) leads, overall, to smaller non-CO_2 climate effects [30, 31, 174, 175]. Several of these studies, however, are limited, since their emission inventories were based on flight patterns from the early 2000s, when routes in the North American and European airspace represented roughly 80% of all air traffic [31, 38–40]. These analyses thus underrepresent spatial sensitivities of NO_x-O_3 climate effects in regions that are projected to grow in terms of air traffic, like Asia Pacific, thereby limiting their applicability to future aviation scenarios given aviation's spatially heterogeneous growth [47, 176].

To quantify such regional sensitivities to aviation-induced short-term NO_x-O_3 impacts, two main calculation methods are available when using 3D models: source apportionment (tagging) and sensitivity analysis (perturbation). The former estimates the contribution of different sources to a total pollutant concentration by labeling pertinent chemical species and tracking them across relevant reaction pathways, thereby guaranteeing a closed budget. The latter, on the other hand, is not additive and calculates the impact from an emission change using two simulations: one with a particular emission change and another without [41, 147, 156, 177, 178]. In this chapter, source apportionment is performed via a tagging approach [157, 158, 179] and a sensitivity analysis [180] is conducted via a perturbation method. If the relationship between emission and concentration is linear, then both methods yield identical results [146, 147]. Given the strong non-linearity of NO_x-O_3 chemistry [181, 182], large differences ranging from a factor of 2–5 have been previously reported [41, 148, 177, 178, 182–184]. These differences highlight each method's suitability to address distinct research questions. Tagging addresses 'what is a sector's contribution towards O_3?' while perturbation addresses 'what is the marginal impact of a sector on O_3 if its NO_x emissions are changed?'. Both questions should be addressed concurrently when assessing mitigation options for aviation's climate impact as it is insufficient to quantify a sector's contribution to total O_3 (tagging) without also gauging the impact of an emissions reduction (perturbation).

The EMAC model is used to compute the short-term O_3 produced from aviation NO_x

for both methods. Eulerian and Lagrangian simulations are run, where the former calculates physical processes on an Earth-fixed frame and the latter along trajectories of advected air parcels [144]. The computational cost of conducting the high-fidelity Eulerian tagging simulations increases significantly when having to analyze multiple emission scenarios. A more computationally efficient approach to tagging is provided by the reduced-order Lagrangian submodel AIRTRAC (see Sub-section 3.3.1), which has been used to create the CCFs [23, 36] that estimate the climate impact of a local emission. AIRTRAC-derived CCFs could play a crucial role in supporting climate-optimal operations, such as guiding shifts to an aircraft's cruise altitude. AIRTRAC is, however, limited by its simplified and linearized chemistry scheme, which is why correction factors are calculated to improve its accuracy.

This chapter has three main objectives: firstly, to understand how short-term NO_x-induced O_3 production from aviation and consequent RF vary geographically, altitudinally and seasonally, especially when compared to studies that assume present-day flight traffic distributions. Secondly, to quantify the differences between tagging and perturbation, which address distinct questions. Thirdly, to compare the linearized Lagrangian tagging submodel AIRTRAC with the non-linear TAGGING submodel (see Subsection 3.3.2) to derive regional correction factors that can leverage AIRTRAC's computational efficiency for decision-making applications.

4.2. METHODOLOGY

All simulations are performed with the EMAC model (MESSy version 2.55.2) using three approaches: Eulerian tagging, perturbation and Lagrangian tagging. Overall, 74 simulations were run, totaling approximately 218 000 CPU hours. Altogether, these simulations currently form one of the most extensive datasets to assess short-term climate warming effects from aviation NO_x-induced O_3. The full dataset is openly available [185].

4.2.1. EMAC MODEL CONFIGURATION

The basic overview of the EMAC model may be found in Sub-chapter 3.2. All Lagrangian simulations were performed using a T42L41 resolution. Eulerian simulations were performed with a T42L90MA resolution, indicating the same resolution in the horizontal grid, but with a different vertical resolution of 90 layers ranging from the surface to the uppermost layer at 0.01 hPa. Common to all approaches is the use of the MECCA submodel [186] for background chemistry calculations and the RAD submodel [187], which estimates the instantaneous RF relative to the tropopause. However, all three methods have a common limitation: plume-scale chemical processes are disregarded, leading to a possible overestimation of the short-term O_3 impact by about 20-30% [188–191].

4.2.2. NO_X EMISSIONS

A pulse emission of 5×10^5 kg of NO [1] is introduced at 0600 UTC within a 15-min. interval at each of the 28 points per region across five regions (North America, Eurasia, South America, Africa and Australasia) and three pressure altitudes (200, 250 and 300 hPa) on 1 January and July 2014. This NO emission per point represents on average about 40%

[1] Amount chosen for comparability with Grewe et al. [23].

of total annual NO emissions by commercial aircraft flying over North America [13, 192]. Each simulation tracks the production of O_3 from NO emitted on one of these two days for three months. The coordinates of all emission points (28 points × 5 regions × 3 altitudes = 420) are displayed in Fig. 4.1 (see Table B.1 from Appendix B for exact coordinates). An enlarged depiction of these points for the 250 hPa level is shown in Fig. 5.1. An overview of the methodology is provided in Fig. 4.2.

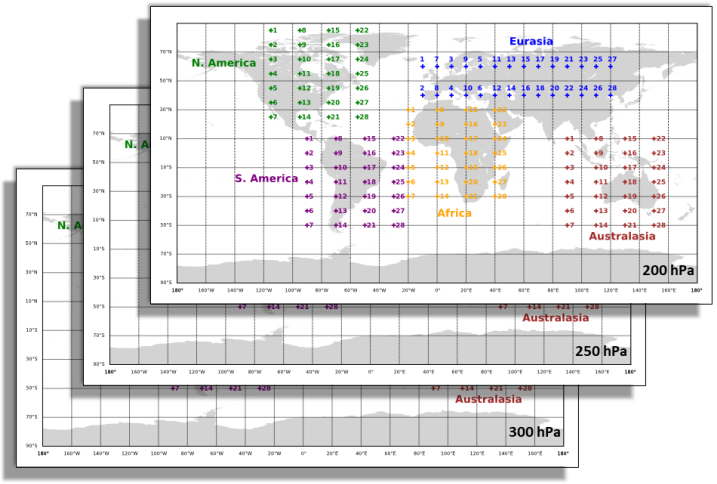


Figure 4.1: Illustration of geographic coordinates of all emission points at which 5×10^5 kg of NO are emitted.

4.2.3. EULERIAN SIMULATIONS

The Eulerian tagging method applies the TAGGING submodel, which has been improved for this study by reducing the signal-to-noise ratio for small emissions (see Sub-section 3.3.2). A set of 30 simulations based on the coordinates in Fig. 4.1 was performed, with an additional 12 simulations to assess the altitudinal variability of the O_3 production efficiency in North America for different NO emission amounts in July (Fig. 4.4). This simulation setup resembles that of Jöckel et al. [193].

TAGGING is unable to independently consider multiple emission scenarios in parallel within one simulation since the chemical interaction between neighboring emissions is non-zero. Instead, due to computational constraints, each Eulerian simulation simultaneously emits NO at the 28 emission points per region. In doing so, however, interaction effects between emissions are introduced. The O_3 production efficiency from each Eulerian simulation, $O^{\mathrm{Eul}}_{3,\mathrm{Net}}$, is normalized by the emission amount of $28 \times 5 \times 10^5$ kg of NO.

This scaled mean Eulerian net O_3 production, $O^{\mathrm{Eul}}_{3,\mathrm{Net}}$ (Eq. 4.1, which uses the terms from Table 3.1), includes seven production, five loss and one interaction term, which represents the non-linearity arising from interactions between emissions and saturation effects, $O_{3,\mathrm{Int}}$ (not explicitly part of the model output). The source-specific factor γ rep-

resents one of the main differences between tagging and perturbation as the former will scale the non-linear effects according to the mass contribution of each emission category [31, 146].

$$O_{3,\mathrm{Net}}^{\mathrm{Eul}} = \frac{1}{\underbrace{28\times5\times10^{5}}_{\text{NO per simulation}}}\Big(P_{HO_2}+P_{RO_2}+P_{OH}+P_{NO_y}+P_{HO_2NO_y} \\ +P_{HO_2NMHC}+P_{OHNO_y}-L_{OH}-L_{HO_2}-L_{NO}-L_{RO}-L_{XO}+\gamma O_{3,\mathrm{Int}}\Big) \tag{4.1}$$

The perturbation method is applied also using an Eulerian reference frame. The net O_3 produced using this approach is the difference between two simulations:

1. NO is simultaneously emitted at the 28 points in Fig. 4.1, causing an NO disturbance of $28\times\delta$NO, per region. Combining this with the background concentration, O_3^{REF}, the total O_3 field function becomes: $O_3(28\times\delta\mathrm{NO}+O_3^{\mathrm{REF}})$.

2. Additional reference simulation without any additional NO emissions. The O_3 field is simply the background O_3: O_3^{REF}. In total, two reference simulations are needed, one for each emission day (1 January and 1 July).

The net O_3 production, $O_{3,\mathrm{Net}}^{\mathrm{Pert}}$, is given by Eq. 4.2, where a disturbance of δNO per emission point is introduced in the perturbed simulation that reflects the full chemical processes of EMAC. The result is normalized by the NO disturbance $28\times5\times10^5$ kg of NO:

$$O_{3,\mathrm{Net}}^{\mathrm{Pert}} = \frac{\overbrace{O_3\left(28\times\delta\mathrm{NO}+O_3^{\mathrm{REF}}\right)}^{\text{Perturbed simulation}}-\overbrace{O_3^{\mathrm{REF}}}^{\substack{\text{Reference}\\ \text{simulation}}}+O_{3,\mathrm{Int}}}{\underbrace{28\times5\times10^{5}}_{\text{NO in perturbed simulation}}}. \tag{4.2}$$

It is worth acknowledging once again the existence of the interaction term $O_{3,\mathrm{Int}}$. However, unlike with tagging, it attributes all non-linearities to the source from which the emission change is assumed to emanate, ergo $\gamma = 1$.

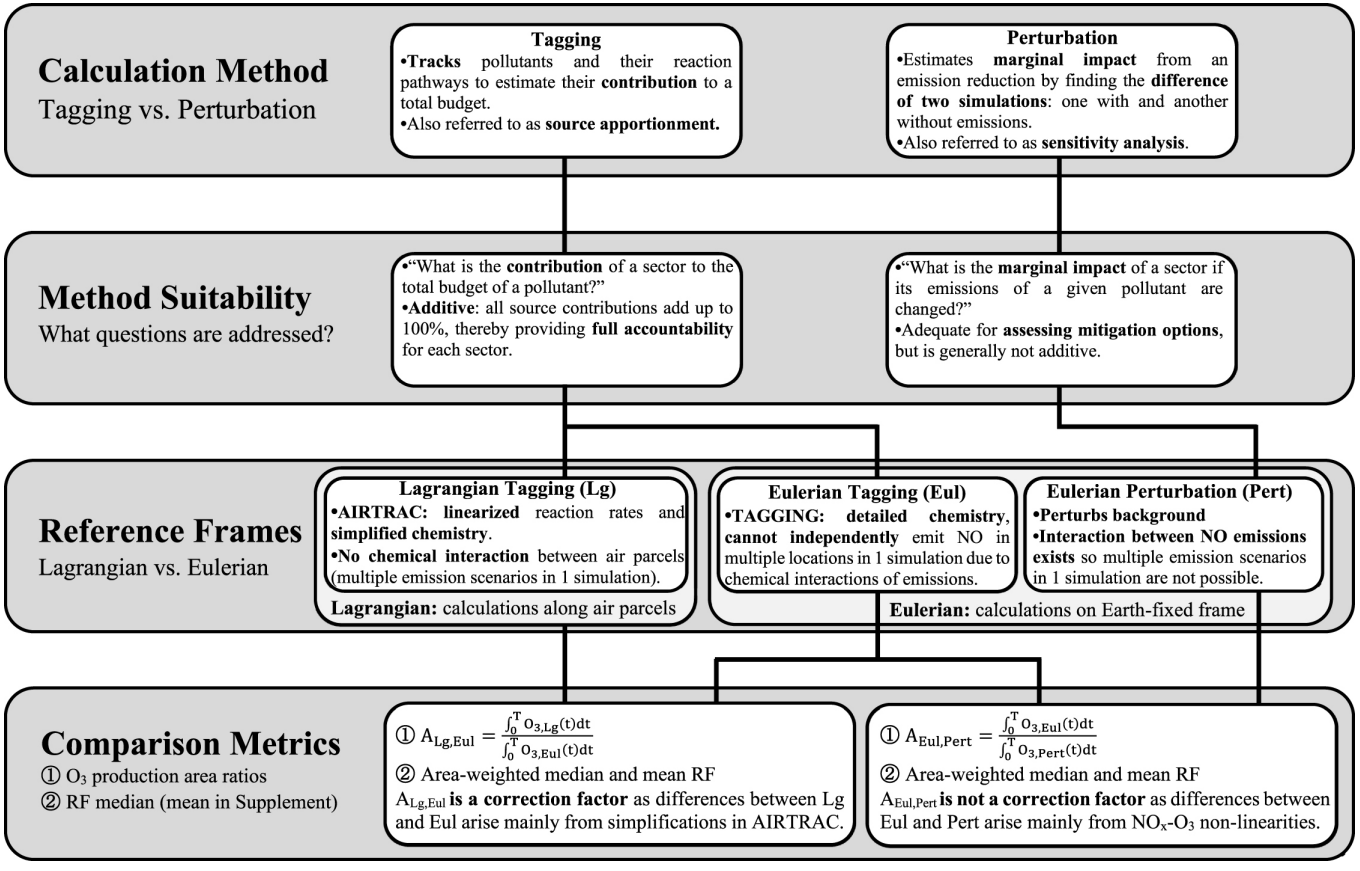


Figure 4.2: Summary of features across calculation methods (tagging and perturbation), questions addressed by each method, reference frames (Eulerian and Lagrangian) and comparison metrics (① area ratios of O_3 production efficiency curves and ② RF median (RF mean in Appendix C.4)).

4.2.4. LAGRANGIAN SIMULATIONS

Lagrangian simulations are performed via a setup nearly identical to the one in Maruhashi et al. [13], presented in Chapter 5. AIRTRAC computes O_3 contributions from aviation NO_x emissions along air parcel trajectories via a tagging approach. An advantage of this submodel is the possibility to simultaneously consider 28 emission scenarios in parallel within a single simulation, since there is no chemical interaction with neighboring NO_x emissions. This therefore makes it the most computationally efficient approach. It also allows for greater ease in the quantification of NO_x-O_3 uncertainties as more independent scenarios may be studied. At each of the 28 emission points are 50 emission-carrying air parcels that are initialized at the start of the simulation [23]. This has been deemed the optimal number of trajectories per emission point according to a sensitivity study performed by Grewe et al. [23] in which the standard deviations of NO_x and O_3 mixing ratios were found to already decrease to under 10 % if more than 20 air parcels are used.

A shortcoming of AIRTRAC, is its linearized reaction rates (constant O_3 production efficiency) and its simplified chemistry mechanism (fewer chemical processes tracked) that are likely to provide less accurate estimates for the highly non-linear NO_x-O_3 chemistry. As has been detailed in Sub-section 3.3.1, AIRTRAC only has one production term from nitrogen compounds and two loss terms. Averaging Eq. 3.1 across the 28 emission points for a given region and subsequently normalizing it by the amount of NO emitted per emission point (5×10^5 kg) yields the equation for the Lagrangian net O_3 production from NO ($O^{Lg}_{3,Net}$):

$$O^{Lg}_{3,Net} = \frac{1}{\underbrace{5 \times 10^5}_{\text{NO per simulation}}} \left(\overbrace{\frac{\sum_{i=1}^{28} \left(P_{O3N,i} - L_{O3N,i} - L_{O3Y,i} \right)}{28}}^{\text{Mean of 28 emission points}} \right). \tag{4.3}$$

4.2.5. METHOD COMPARISON METRICS

To compare O_3 production efficiencies (i.e. emission-scaled O_3 production) across methods, the area ratios of their respective O_3 production efficiency curves as a function of time (i.e. O_3 curves) are evaluated. A_{M_1,M_2} (Eq. 4.4) is defined in terms of two integrals: one for method 1 (M_1) and another for method 2 (M_2) being compared. M_1 and M_2 can correspond to Lagrangian tagging (Lg), Eulerian tagging (Eul), or the perturbation approach (Pert). The integration bounds encompass the full simulation period T of about 90 days. Correction factors compare the Lagrangian and Eulerian tagging methods so are, by definition, denoted as $A_{Lg,Eul}$.

$$A_{M_1,M_2} = \frac{\int_0^T O^{M_1}_{3,Net}(t)\, dt}{\int_0^T O^{M_2}_{3,Net}(t)\, dt} \tag{4.4}$$

The RF definition of Maruhashi et al. [13] shown in Chapter 5 is followed, where it is expressed as the change in the net instantaneous long- and shortwave radiative fluxes

from a pulse emission. Additionally, RF estimates in this chapter have been converted into annual means by division by a factor of 4 to make the estimate from a three-month pulse emission comparable to annual values from literature.

In all simulations, RF is computed online by the RAD submodel and subsequently mapped to the climatological tropopause by the VISO submodel [150] (see Appendix A). To obtain a point estimate per scenario, area-weighted medians are computed, as they are unaffected by extreme values, thereby making them a more robust indicator. However, area- and time-averaged means are also computed in Appendix C.4.

The net instantaneous radiative forcing, denoted as $\mathrm{iRF_{Net}}$ in the equations below, is represented as a 3D array derived from the radiative fluxes produced by the RAD submodel. These fluxes are computed at the climatological tropopause and are expressed as functions of time (t), latitude (ϕ), and longitude (ψ): $\mathrm{iRF}(t,\phi,\psi)$. The net flux is determined according to Eq. 4.5 by calculating the difference between the longwave (LW) and shortwave (SW) fluxes for two scenarios: (S_1) where both background and aviation-induced O_3 are included, and (S_2) where only the background O_3 is considered (see README file in Maruhashi et al. [185]).

$$\mathrm{iRF_{Net}}(t,\phi,\psi) = \underbrace{\left(\mathrm{iRF_{SW}}(t,\phi,\psi) + \mathrm{iRF_{LW}}(t,\phi,\psi)\right)\Big|_{S_1}}_{\text{Net flux for scenario } S_1} - \underbrace{\left(\mathrm{iRF_{SW}}(t,\phi,\psi) + \mathrm{iRF_{LW}}(t,\phi,\psi)\right)\Big|_{S_2}}_{\text{Net flux for scenario } S_2} \tag{4.5}$$

The area-weighted time series for iRF ($\mathrm{iRF'_{Net}}(t)$) was calculated by determining grid cell areas $A(\phi,\psi)$ following the method described by Kelly and Šavrič [194] for a T42 resolution (64 latitudes and 128 longitudes) and subsequently summing all scaled terms, as shown in Eq. 4.6:

$$\mathrm{iRF'_{Net}}(t) = \frac{1}{A_T}\sum_{i=1}^{64}\sum_{j=1}^{128}\mathrm{iRF_{Net}}(t,\phi_i,\psi_j)\times A(\phi_i,\psi_j). \tag{4.6}$$

The surface area of a grid cell with dimensions $\Delta\phi$ and $\Delta\psi$ is calculated as $A(\phi,\psi) = \Delta\phi\times\Delta\psi\times\cos\phi$. The sum of all of these grid cell areas yields A_T. To then approximate the time-averaged iRF point estimate, denoted as $\overline{\mathrm{iRF}}$, the trapezoidal rule is applied to Eq. 4.6 using N evenly-spaced trapezoids:

$$\overline{\mathrm{iRF}} = \frac{1}{T}\int_0^T \mathrm{iRF'_{Net}}(t)\,dt \approx \frac{\Delta t}{2T}\sum_{k=1}^{N}\left(\mathrm{iRF'_{Net}}(t_{k-1}) + \mathrm{iRF'_{Net}}(t_k)\right), \tag{4.7}$$

where T is the total simulation length (about 90 days) and Δt is the uniform time interval, which is constant within each setup (Lagrangian simulations = 0.25 days, Eulerian simulations=0.42 days). It is worth noting that both Eq. 4.6 and Eq. 4.7 apply to all three calculation methods (Lg, Eul and Pert), with the caveat that all 28 individual iRF fields belonging to each emission point were first added together in the Lagrangian tagging case: $\mathrm{iRF_{Lg}} = \sum_{i=1}^{28}\mathrm{iRF}_i$. The median values shown in Fig. 4.5 were found by first calculating the area-weighted iRF time series according to Eq. 4.6, time-averaging with Eq. 4.7 and then by finding its median. To visualize the spread of the iRF time series, kernel density estimators (KDEs) were computed for all cases (see Fig. C.3).

4.3. RESULTS AND DISCUSSION

Initially, the O_3 production efficiencies of the three calculation methods (Eulerian tagging, Lagrangian tagging and perturbation) are compared. Correction factors to improve AIRTRAC's accuracy are derived by comparing the Eulerian and Lagrangian tagging methods. Next, the regional sensitivities of these O_3 production efficiencies with emission altitude are quantified for each method. Lastly, the altitudinal variation of the short-term radiative forcing from NO_x-induced O_3 is plotted for all regions and seasons.

4.3.1. COMPARISON OF O_3 PRODUCTION BETWEEN METHODS

The O_3 production efficiency across the Eulerian tagging and perturbation methods is first compared. Figure 4.3 (a) displays the case when NO is emitted at 300 hPa in North America during January. The former method (blue curve) leads to larger O_3 production when compared to the latter (orange curve). According to Table 4.1, the Eulerian tagging estimates for this case are larger than the perturbation by a factor of 1.48. Across all simulations (see Fig. C.1 for O_3 production efficiencies corresponding to emissions in January and Fig. C.2 for emissions in July), Eulerian tagging is larger by a factor of $A_{\text{Eul,Pert}}$ ranging from 1.16 to 2.55, with a mean of 1.83. This is consistent with past studies, where differences ranging from a factor of 2 to 5 were reported for road traffic and shipping [177, 182] and around 1.6 for short-term aviation O_3 effects [11, 41].

The tagging method, however, will not always overestimate relative to the perturbation approach, as this depends on the type of linearity underlying the studied phenomenon [147]. Thunis et al. [178] and Dedoussi et al. [184], for instance, found larger values by a factor of up to 3 for the perturbation approach when considering ground-level particulate matter. Such differences are due to a combination of non-linear compensation effects arising from other emission sources, where total O_3 non-linearities are either shared across individual sources (tagging) or are fully allocated to a single source (perturbation), oftentimes by means of distinct reaction rates [31, 148, 182].

Differences between Lagrangian and Eulerian tagging submodels, are however, mainly attributable to AIRTRAC's simplifications. The green shaded area indicates the range of O_3 estimates from 28 independent emission scenarios considered by the Lagrangian approach, contrasting with only one scenario of the Eulerian alternative. Likely, the difference by a factor of 4.6 between the areas of the green and blue O_3 curves in Fig. 4.3 (a) arises from the lack of chemical interaction between Lagrangian air parcels ($O_{3,\text{Int}} = 0$), simplified chemistry and AIRTRAC's linearized reaction rates that translate to constant O_3 production efficiencies. Unlike the Eulerian tagging and perturbation methods, where O_3 production efficiencies vary with the amount of emitted NO, AIRTRAC's O_3 production efficiency is invariant to emission strength (i.e. amount emitted). This equates to discarding shifts in the local NO_x regime from varying the amount of NO emitted as there is no feedback between emission and background. However, to leverage the computational efficiency of AIRTRAC despite these simplifications, correction factors $A_{\text{Lg,Eul}}$ are derived in Table 4.1. Figure 4.3 (b) illustrates the application of a correction factor ($A_{\text{Lg,Eul}} = 4.6$) for the scenario of Fig. 4.3 (a), where the corrected Lagrangian curve (purple) now more closely resembles the Eulerian tagging curve (blue). More simulations would be required, however, to capture O_3 behavior in other aviation emission scenarios considered in Grewe et al. [23], as is indicated by the gray line in Fig. 4.3 (a).

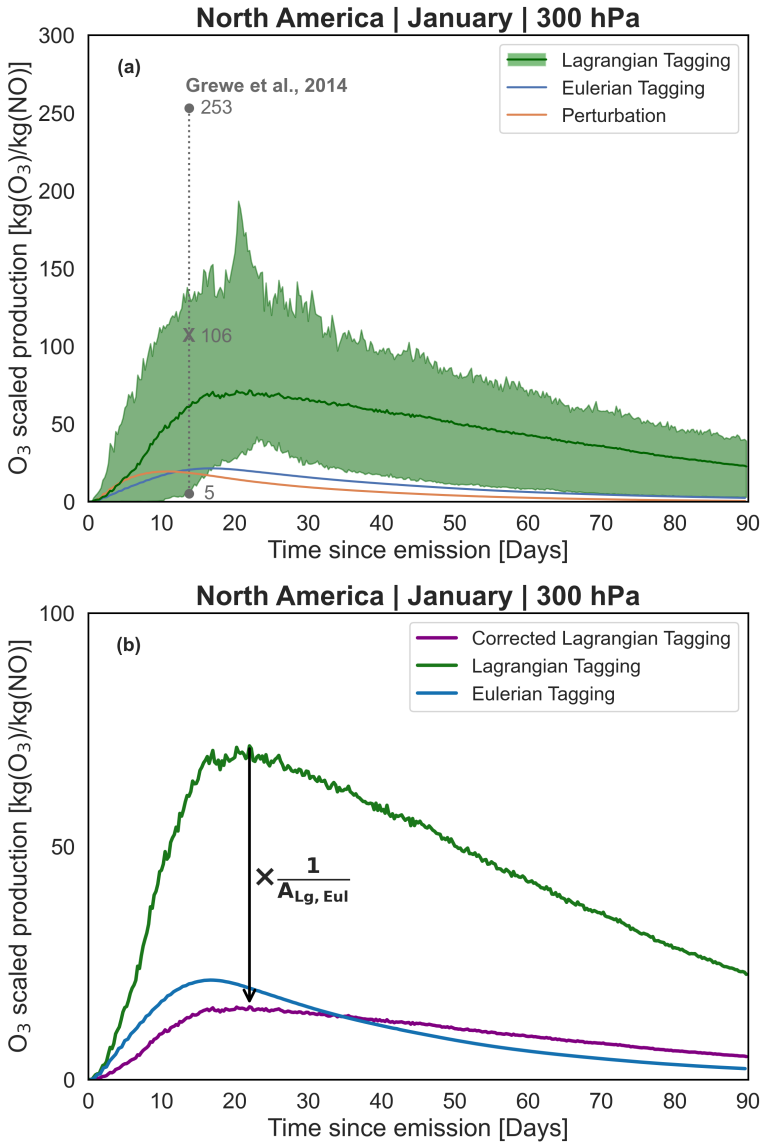


Figure 4.3: Normalized NO_x-induced O_3 production in North America. (a) Comparison between emission-scaled O_3 mass curves [$kg(O_3/kg(NO))$] as estimated by the Lagrangian tagging (green), Eulerian tagging (blue) and perturbation (orange) methods for NO emitted at 300 hPa in January. The AIRTRAC and TAGGING sub-models were applied for the Lagrangian and Eulerian tagging methods, respectively. No specific submodel is required for the perturbation method. The shaded green area represents the range of Lagrangian O_3 estimates for 28 independent emission scenarios based on the coordinates shown in Fig. 4.1. The green curve is the average of these 28 scenarios. The dotted gray line denotes the range of O_3 estimates (13.75 days after emission) obtained by Grewe et al. [23] using AIRTRAC to also study 5×10^5 kg of NO released at 200, 250, 300 and 400 hPa during 06h00, 12h00 and 18h00 UTC in January. The gray 'X' marks the mean value. (b) Application of the correction factor $A_{\mathrm{Lg,Eul}} = 4.6$ from Table 4.1 to the same emission scenario shown in (a). The green curve is the original O_3 estimated by the Lagrangian tagging curve, the purple curve is the corrected green curve and the blue curve is from the Eulerian tagging method.

Table 4.1: Calculation of the ratio of O_3 curve areas for the tagging and perturbation methods for all emission altitudes (200, 250 and 300 hPa), regions (NA=North America, SA=South America, EU=Eurasia, AF=Africa and AU=Australasia) and emission days (1 January and 1 July 2014). Area ratios $A_{Lg,Eul}$ and $A_{Lg,Eul}$ refer to the application of Eq. 4.4 to the different methods (Lg=Lagrangian Tagging, Eul=Eulerian Tagging and Pert=Perturbation).

	Emission on 1 January 2014						Emission on 1 July 2014					
	$A_{Lg,Eul}$[a]			$A_{Eul,Pert}$			$A_{Lg,Eul}$[a]			$A_{Eul,Pert}$		
[hPa]	200	250	300	200	250	300	200	250	300	200	250	300
NA	2.38	3.62	4.59	2.10	1.74	1.48	1.71	2.17	2.23	2.55	2.37	2.27
SA	1.92	1.91	1.98	1.86	1.78	1.76	2.23	2.57	2.98	1.81	1.60	1.51
EU	2.62	4.38	5.91	2.07	1.44	1.16	1.68	1.99	2.68	2.38	2.34	2.04
AF	1.97	2.08	2.40	1.93	1.92	1.90	2.26	2.70	3.44	1.90	1.78	1.66
AU	1.96	1.98	2.03	1.60	1.62	1.64	2.50	3.20	3.81	1.70	1.53	1.38

[a] Correction factors refer specifically to $A_{Lg,Eul}$ as they consider differences between the tagging methods arising from the limitations of AIRTRAC. These factors will then enable AIRTRAC to more accurately calculate 28 independent emission scenarios in a single simulation.

4.3.2. ALTITUDINAL VARIATION OF O_3 PRODUCTION EFFICIENCIES

To understand the differences between linear and non-linear response models in the context of NO_x-O_3 chemistry, the altitudinal variation of O_3 production efficiency is investigated using the Eulerian tagging and perturbation methods. This is achieved through 12 additional simulations conducted at three altitudes with NO emission strengths varying from 1%, 50%, 150%, and 200% in North America during July, a period of heightened photochemical activity. Due to AIRTRAC's reaction rate linearization, the O_3 production efficiency is constant for each region, altitude and emission day and is therefore not included in Fig. 4.4.

Emitting in the lower stratosphere at 200 hPa shows a 15% reduction between the areas under the 1% and 200% cases when applying the tagging method (Fig. 4.4 (a)) and 24% with the perturbation method (Fig. 4.4 (d)). For the lowest emission altitude of 300 hPa in the troposphere, the disparity between the extreme cases of 1% and 200% grows by approximately a factor of 2 relative to the 200 hPa scenario for tagging (Fig. 4.4 (a) vs. Fig. 4.4 (c)). This suggests that NO_x-O_3 chemistry is more linear towards higher altitudes, near the stratosphere, and non-linearities accentuate towards the troposphere, where there are more removal processes and therefore less efficient accumulation of of chemical species. In other words, both methods suggest that varying the emission strength in the stratosphere leads to the smallest changes in the O_3 production efficiency (Fig. 4.4 (a) and Fig. 4.4 (d)). Also, the perturbation approach is less suited for when the added emission is very small, i.e., in the order of 10^3 kg of NO, due to numerical noise, as indicated by the noisy 1% curves in Figures 4.4 (d) - (f). Overall, O_3 production efficiency varies inversely with NO emission strength, with larger sensitivities towards lower altitudes.

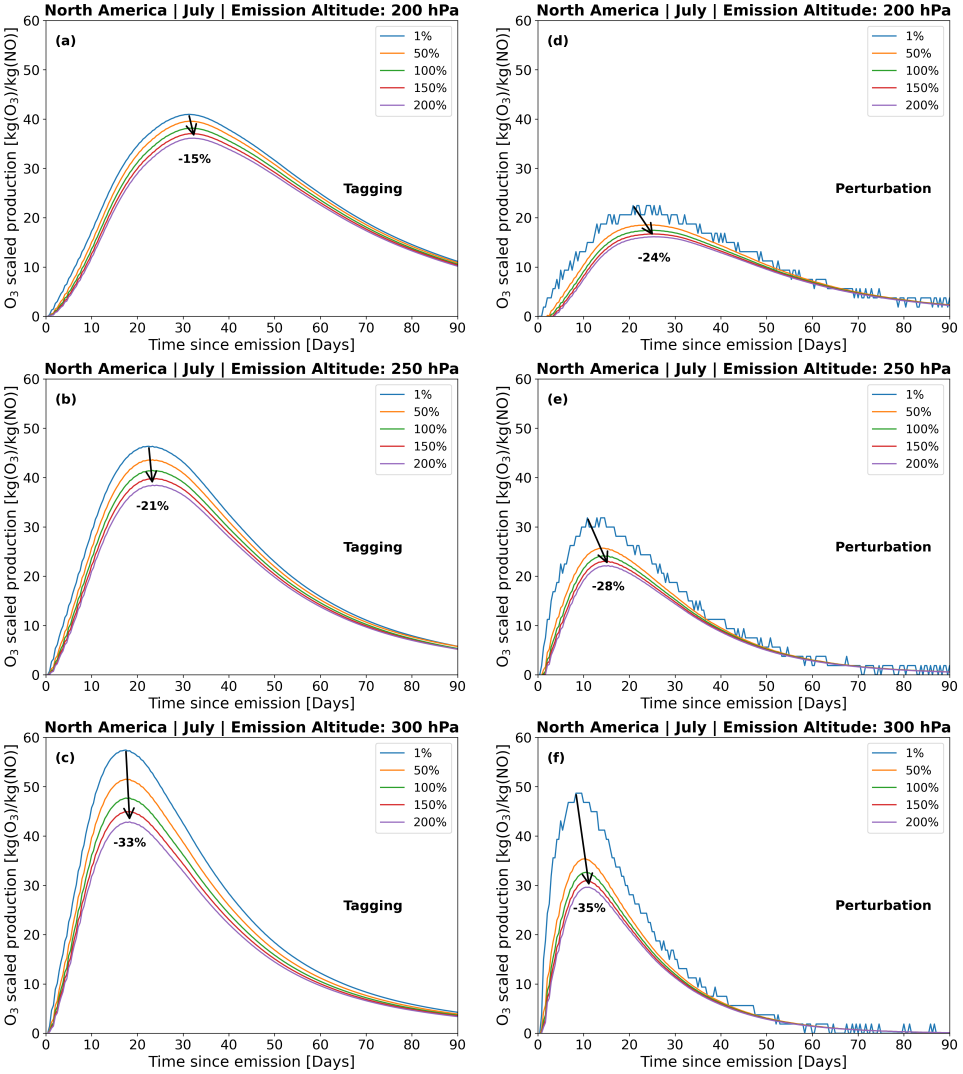


Figure 4.4: Sensitivity of O_3 production efficiency [kg(O_3)/kg(NO)] with NO emission strength assuming values of 1%, 50%, 100% and 200% for the Eulerian tagging approach using the TAGGING submodel (a)-(c). The scenarios considered are for emissions in North America during July at altitudes of 200, 250 and 300 hPa. The 100% scenario refers to an emission amount of 5×10^5 kg of NO. (d)-(f) the same is depicted, but for the perturbation method. The percentage shown in each subplot represents the reduction in the area under the O_3 curve from the 1% to the 200% scenario. The Lagrangian method is not shown as it does not exhibit any sensitivity to emission strength changes given AIRTRAC's linearization of reaction rates. Such a simplification could lead to differences of at least 30% between the 1% and 200% scenarios in the troposphere (300 hPa).

4.3.3. ALTITUDINAL VARIATION OF SHORT-TERM RF FROM AVIATION NO_X-O_3 INTERACTIONS

The variation between short-term O_3 median RF from aviation NO_x with emission altitude for all three methods is presented in Fig. 4.5. For the Eulerian tagging and perturbation methods, emitting at higher altitudes always leads to a larger median RF per Tg(N). The Lagrangian tagging method also largely predicts a similar relation, but displays some cases of inversions, e.g. in North America the RF is largest at 250 hPa. Frömming et al. [36] also report a non-monotonic relation with altitude for aviation's net NO_x warming effect using AIRTRAC while Matthes et al. [31], via a multi-model aproach involving EMAC, also found a non-monotonic relation for lower altitudes (~ 300 hPa). One of the inversions in Fig. 4.5 (a), for instance, may be explained by larger O_3 production efficiency maxima occurring at 250 hPa during January for North America (see Fig. C.1 (b) in Appendix C). The predominant trend, however, is to witness warming effects from aircraft NO_x emissions increase with altitude within the troposphere, as there is a more efficient accumulation of NO at higher altitudes from fewer removal processes [30, 31, 174, 195].

There are significant regional and seasonal variations in the estimated RF. During January, Fig. 4.5 (a) presents larger values in the southern hemisphere (SA, AF and AU) while in July (Fig. 4.5 (b)), warming in NA and EU increases, but decreases for the remaining three southern regions. Such a seasonal shift occurs from the strong photochemical dependence of O_3 production [13, 35, 36, 38]. Seasonality also significantly impacts the altitudinal sensitivity of O_3 RF. Flying higher in Eurasia during January from 250 to 200 hPa leads to an increase in short-term O_3 warming by ~ 20% according to the Eulerian tagging approach (Fig. 4.5 (a)). In July, the same altitudinal shift would lead to an increase of 50% (Fig. 4.5 (b)). This suggests that altitudinal measures for the short-term mitigation of NO_x-O_3 impacts are most effective during the local summer. Across all methods, Australasia generates the largest RF for a January emission (as is also seen by the wider spread of the RF KDEs in Fig. C.3 in Appendix C), which is explained by the lower background NO concentrations in its vicinity [13, 34, 196].

Comparing RF perturbation estimates in Fig. 4.5 with Lee et al. [27] reveals regional differences, particularly for low-altitude emissions in North America and Eurasia. For a January emission at 300 hPa in North America (Fig. 4.5 (a)), for example, our RF value is smaller by a factor of 3 relative to their lower bound estimate of 16 $(mWm^{-2})/Tg(N)$. When juxtaposed with Eulerian tagging estimates by Matthes et al. [31], our Eulerian tagging results from July emissions (Fig. 4.5 (b)) compare well, albeit with larger discrepancies observed at the highest emission altitude. Even larger differences of a factor of 2 emerge when comparing our Eulerian tagging estimates with Matthes et al. [31] for January in Southern regions (SA and AU). Our study therefore underscores that estimates based on global emission inventories, if used to evaluate the effects of increasing emissions in underrepresented regions, could over- or underestimate aviation NO_x-O_3 warming impacts depending on the region and method. A robust, global assessment of aviation's evolving non-CO_2 effects should take into account the dynamic shift in air traffic distribution given the heterogeneity in regional NO_x-O_3 responses.

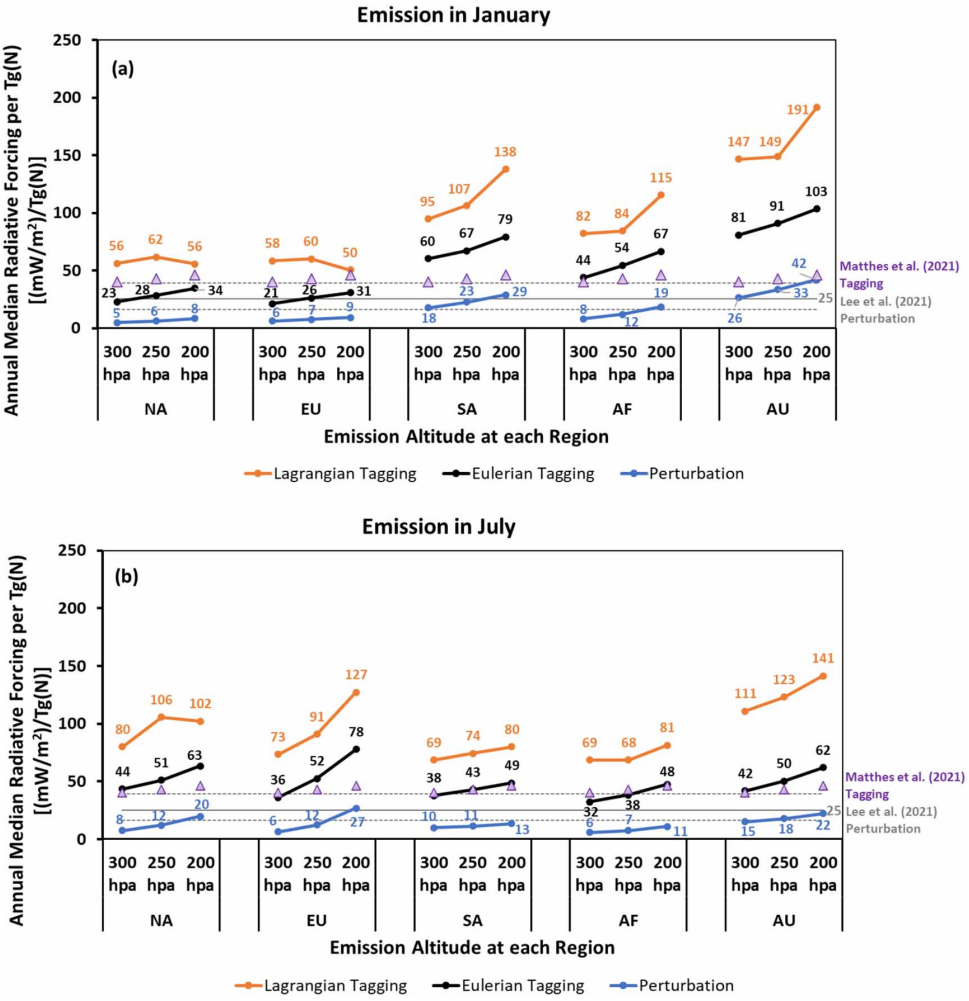


Figure 4.5: Annualized, area-weighted median radiative forcing point estimates (see Eqs. 4.6 and 4.7) from short-term NO_x-induced O_3 for emission altitudes of 300 hPa (~ 9.2 km), 250 hPa (~ 10.4 km) and 200 hPa (~ 11.8 km) across all five regions (North America (NA), South America (SA), Eurasia (EU), Africa (AF) and Australasia (AU)) during (a) 1 January and (b) 1 July of 2014. The solid gray line represents the corresponding mean RF estimate for short-term O_3 effects from Lee et al. [27] using a perturbation approach. The dotted gray lines demarcate the 90% confidence interval of the same study, where the 5% lower limit is 16 and 95% upper limit is 39 mWm^{-2}. The purple triangles depict the tagging estimates in mWm^{-2} of Matthes et al. [31], who calculated 43 for a base flight altitude (compared to this chapter's 250 hPa scenario), 46 for a *flying higher* and 40 for a *flying lower* scenario, which were compared to the 200 and 300 hPa estimates, respectively. For clarity, these values are not labeled above. All RF estimates presented in (a) and (b) have been scaled to represent the equivalent value for a 1 Tg of nitrogen (N) emission.

These disparities also bring to light the large uncertainties surrounding aviation NO_x-O_3 effects that arise from distinct methods and may increase further from adopting additional model types like CTMs or climate-response models (CRMs) [197]. Comparison with our mean RF values leads to similar conclusions as those mentioned in the previous paragraph (Fig. C.4 in Appendix C). Relative to tagging estimates, TAGGING consistently exhibits larger RF in Pacific regions when compared to AIRTRAC, which may explain some magnitude differences in Fig. 4.5. During a northern emission in January for instance, TAGGING estimates larger warming in the southern Pacific relative to AIRTRAC (Figs. C.5 (d) - (f) and (j) - (l)), leading to smaller differences between their RF estimates for NA and EU in Fig. 4.5 (a).

Figure 4.5 should also be interpreted in terms of the distinct research questions that the tagging and perturbation approaches address. Eulerian tagging is represented by the black line and indicates aviation's sectoral contribution to the overall O_3 budget and how this varies with altitude, region and season. In Fig. 4.5 (b), for instance, flying higher from 250 to 200 hPa in Eurasia could lead to a strong increase in aviation's contribution to total O_3 via an increase in its short-term O_3 production, assuming the amount emitted by other sectors is unchanged. In contrast, perturbation (shown in blue) investigates the impact on RF that would result at each corresponding scenario if aviation emissions were regionally increased by 28×0.5 Gg. A more detailed discussion of how to combine these two methods is found in Mertens et al. [177].

4.4. SUMMARY AND CONCLUSIONS

The variation between aircraft NO_x emission altitude and short-term climate warming from O_3 production has been assessed using three methods (Eulerian tagging, perturbation and Lagrangian tagging), all within the framework of the EMAC model. A total of 74 simulations were performed across five regions and three altitudes during the summer and winter seasons to account for seasonal and regional differences. This study does not include NO_x terms that lead to a reduced warming, which, when combined with the short-term O_3 warming component, may lead to a negative net-NO_x forcing [119, 120].

In the process, differences between estimates from these approaches were discussed, in the context of the questions that they can be used to answer, and a set of correction factors $A_{\mathrm{Lg,Eul}}$ (Table 4.1) was calculated for the widely-used Lagrangian AIRTRAC submodel (used in e.g. CCFs ([23, 36])).

The findings regarding the altitudinal relationship of aircraft climate effects from short-term NO_x-O_3 interactions only partly align with previous studies, which based their analyses on emission inventories influenced by the larger density of flights in the Northern trans-Atlantic. Such approaches may underestimate the altitudinal sensitivity of RF for Southern regions, like Australasia, particularly for emissions in January. The proportional relationship between O_3 RF and altitude has been verified regionally for all five regions during both seasons using the Eulerian tagging and perturbation methods. A few exceptions were observed for the Lagrangian method, but certain non-monotonic trends have also been reported in earlier studies [31, 36]. Additionally, the change in short-term O_3 RF with altitude is found to be more pronounced when flying higher or lower during seasons with greater solar radiation.

Differences between the Eulerian tagging and perturbation approaches range from a

factor of 1.16 to 2.55 with a mean of 1.83 for the O_3 mass curves. These estimates agree well with the range of 2-5 provided by literature [31, 41, 148, 177, 178, 182–184]. The Lagrangian tagging submodel exhibits larger differences likely due to a combination of reasons: the lack of inter-parcel chemical interaction effects, the relatively simplified chemistry scheme and the linearization of the NO_x-O_3 response. To correct for these shortcomings, correction factors are provided.

Although O_3 mass estimates from tagging and perturbation methods can differ by almost a factor of 3, both should still be considered in tandem for a comprehensive assessment of aviation climate effects, given that they address distinct questions. Each of the three methods presented here can play a unique role in the mitigation decision-making process. Tagging identifies mitigation opportunities by determining the share of each sector to the total O_3 budget. The perturbation method may be applied to evaluate an emissions reduction measure of a certain sector. Lastly, the corrected Lagrangian tagging method can help us efficiently gauge the uncertainty levels in these estimates by providing more data for more scenarios and better understand transport-related phenomena [13]. When addressing technological, operational or regulatory decisions, these methods would provide valuable, complementary insights.

4.5. ACKNOWLEDGMENTS

We would like to express our gratitude to Anke Roiger from DLR (German Aerospace Center) for providing valuable feedback. This research used the Dutch national e-infrastructure with the support of the SURF Cooperative (Grant Nos. EINF-441 and EINF-2734) as well as resources from the Deutsches Klimarechenzentrum (DKRZ) granted by its Scientific Steering Committee (WLA) under project ID bd1063.

4.6. DATA AVAILABILITY STATEMENT

The simulation data produced and analyzed for this assessment are openly available in the following repository:
https://doi.org/10.4121/56327667-69f1-4340-be45-9f9a6bd80584.

4.7. FUNDING

This research is embedded within the ACACIA (Advancing the Science for Aviation and Climate; www.acacia-project.eu) project, which is funded by the European Commission, Horizon 2020 Framework Programme (ACACIA under the Grant No. 875036).

5

ANALYSIS OF GLOBAL TRANSPORT PATTERNS OF AVIATION NO_X AND THEIR LINK TO ATMOSPHERIC O_3

The previous chapter compared the altitudinal variation of aviation-induced NO_x-O_3 climate effects in the short-term across three different calculation methods. This chapter focuses on detailing the transport patterns of emitted NO_x and how their climate effects vary with respect to regions (North America, South America, Africa, Eurasia and Australasia) and seasons (January–March and July–September in 2014) by leveraging AIRTRAC's capacity to consider multiple emission scenarios in a single simulation. We quantify the short-term O_3 climate effects from NO_x emissions, but now released at only one of the three pressure altitudes considered in Chapter 4: 250 hPa (~ 10.4 km). The emitted NO_x is transported via Lagrangian air parcels within the EMAC model. To identify the main global transport patterns and associated climate impacts of ~14 000 simulated air parcel trajectories, an unsupervised clustering algorithm is adapted and applied. Results reveal a strong seasonal dependence of the contribution of NO_x emissions to O_3. For most regions, an inverse relationship is found between an air parcel's downward transport and its mean contribution to O_3, indicating faster chemical removal towards lower altitudes. NO_x emitted in the northern regions experience the longest residence times in the larger midlatitudes, while those beginning in the south remain mostly in the Tropics. Due to elevated O_3 sensitivities, emissions in Australasia induce the highest overall radiative forcing. The emission location does not necessarily correspond to the region that will be most affected – for instance, NO_x over North America in July will induce the largest radiative forcing in Europe. Overall, this chapter highlights the spatially and temporally heterogeneous nature of NO_x–O_3 chemistry from a global perspective, which needs to be accounted for to minimize aviation's climate impact, given the sector's resilient growth.

Parts of this chapter are based on Maruhashi et al. [13]. which has been published in the Atmospheric Chemistry and Physics journal [13].

5.1. INTRODUCTION

SIMILAR to Chapter 4, Chapter 5 focuses on the NO_x-induced short-term impact on O_3. NO_x affects the climate by increasing the amount of O_3 and decreasing the levels of CH_4, stratospheric water vapor and the amount of background O_3 or PMO in the longer term [41], in addition to other pathways subjected to even larger uncertainties (e.g. nitrates and sulfates) [120, 198]. As has been concluded from Chapter 4, the impact of NO_x-O_3 effects depends strongly on the aircraft's emission altitude. For tropospheric NO_x emissions, the production mechanism of O_3 is initiated via HO_2 and NO, followed by the photodissociation of NO_2 along with the combination of monatomic and molecular oxygen atoms. Within the UTLS, NO_x emissions still lead to a quasilinear production of O_3 [31]. Slightly above it, between 13 - 14 km in altitude, one finds the O_3-neutral region in which emitted NO_x would lead to a net null disturbance in the O_3 column seeing as the tropospheric O_3 production is counteracted by its stratospheric destruction. Above this region, O_3 is consumed by NO to produce NO_2 and O_2 [199]. The ability of NO_x to oxidize CH_4, producing H_2O in the process, results in a reduction in CH_4 concentration; this eventually leads to a decrease in the production of SWV as less CH_4 enters the stratosphere [200]. Combining these latter effects yields a cooling effect, as both are greenhouse gases. In the long run, a decrease in O_3 concentration is also induced, since CH_4 is a precursor to O_3 [201].

The climate impact associated with aviation NO_x emissions has been studied in terms of varying the cruise flight altitude [30, 31], emission locations [32, 33], seasons [34, 35], background O_3 concentrations [11] and weather patterns [36, 37]. In regard to research focusing on the spatial relationship between emission location and NO_x environmental effects, the work by Stevenson and Derwent [32] may be referred. Therein, an O_3 anomaly is introduced and followed via the STOCHEM Lagrangian CTM across nine distinct regions, where it was concluded that emissions in less polluted areas (lower NO_x levels) led to larger instantaneous radiative forcings compared to those in which the emission occurred at locations of larger background NO_x concentrations. In other words, flying over cleaner areas is more likely to generate more substantial short-term O_3 climate impacts. Skowron et al. [196] found a significant geographic dependence, through a subdivision of the globe in 10 regions, between emissions and the subsequent RF according to simulations from the MOZART-3 model. They found that the largest O_3 burden and consequent disturbance in RF occurred in Australia and the lowest in Europe, due to varying levels of O_3 production efficiencies. Overall, the North Atlantic and tropical regions in Brazil showed the strongest net NO_x RF effects. Köhler et al. [33] examined aircraft NO_x in four regions (USA, Europe, India and China) with the p-TOMCAT CTM and found that lower-latitude emission perturbations have RF magnitudes that are 6 times larger than those due to emissions at higher latitudes, agreeing well with findings from Grewe and Stenke [45]. Gilmore et al. [34] also found larger O_3 sensitivities in the tropics, particularly near the Australasian region. Recent studies by Frömming et al. [36] and Rosanka et al. [37] have adopted a Lagrangian approach to investigate the impact of emitting NO_x and H_2O in different weather conditions across summer and winter in the North Atlantic using the EMAC model. The former investigated trajectories starting at emission regions within and to the west of a high-pressure ridge, analyzing how they contribute differently to O_3. In summary, none of these examples have comprehensively

studied the complete and intercontinental journey of aviation NO_x from its point of release, intermediate transport pathways, until most of the resulting O_3 is removed from the atmosphere three months later (typical O_3 lifetime). The present chapter therefore seeks to bridge this gap by characterizing this multi-stage, spatiotemporal evolution of emitted NO_x on a large scale across several regions globally during different seasons.

As has been discussed in Sub-chapters 3.1.1 and 3.3.6, a Lagrangian approach rests on the idea of following an individual air parcel in space as a function of time. The evolution of specific quantities, such as mixing ratios of chemical species, may be tracked along an air parcel's pathway. The method thus allows for a complete and detailed accompaniment of the different trajectories that gas-phase emissions may take on an individual basis. Such an approach, however, naturally yields large amounts of data from the necessity to include close to 170 000 air parcels per simulation to both ensure realistic transport and inter-parcel mixing. All of these trajectories can, however, be efficiently grouped together with the integration of unsupervised machine learning techniques such as clustering. In other words, clustering offers a systematic way of categorizing thousands of air parcels based on common features, which ultimately allows for a faster identification of patterns in very large datasets. Outside of aviation and atmospheric sciences, trajectory clustering has been applied in various contexts to improve pattern recognition of e.g., deer movements, cyclist trails, pedestrian paths and naval vessel traffic [202, 203]. Within aviation, aircraft routes have been grouped according to methods like the Density-Based Spatial Clustering of Applications with Noise (DBSCAN) or the Hierarchical DBSCAN (HDBSCAN) as applied by Corrado et al. [204], Basora et al. [205], Olive and Basora [206] and Olive and Morio [207]. Within atmospheric sciences, other techniques like K-means clustering have been used to systematically categorize different types of aerosol regimes at distinct altitudes and regions [208]. Another example is Kassomenos et al. [209], who applied several clustering approaches like K-means and self-organizing maps (SOMs) to isolate the pathways with highest PM_{10} concentrations. Clustering has also been applied to output from the EMAC model and O_3 observations by Tarasova et al. [210], in which an agglomerative hierarchical clustering algorithm with a squared Euclidean distance metric was used to discern patterns in the distribution of surface O_3 mixing ratios in the extra-tropics. In this chapter, trajectory clustering is performed with an algorithm from neuroscience called QuickBundles with a newly proposed clustering function. To the author's best knowledge, this is the first time that a global characterization of Lagrangian air parcel trajectories from the EMAC model is performed with this approach.

We perform Lagrangian simulations with the EMAC model in which aviation NO_x emissions are released in five regions (North (N.) America, South (S.) America, Africa, Eurasia and Australasia) at a representative aircraft cruise level altitude of 250 hPa in January and July of 2014 and tracked in terms of their chemical impact (via their O_3 atmospheric disturbance for 3 months following their release). Overall, this chapter addresses the following research questions: (1) what are the main aviation NO_x transport pathways depending on the emission location and season, and which ones exhibit the largest O_3 production? (2) Under which conditions are the RFs largest, and where are these effects expected to occur?

5.2. METHODOLOGY

This section describes the relevant simulations that were performed for the analysis of NO_x-O_3 transport patterns. The overall EMAC setup is the same as the one applied in Chapter 4. For every region, 28 emission points were defined from which the emitted NO_x (in the form of NO) is divided into 50 air parcels. A total of 28 median trajectories are then derived for each point to summarize the transport behavior of the aforementioned 50 air parcels for each of the five regions (N. America, S. America, Eurasia, Africa and Australasia). Based on these emission regions, a source–receptor analysis is performed, for which the receptor boundaries are defined in Fig. 5.2. The altitude and latitude along with the RF for these median trajectories then serve as input for the QuickBundles clustering algorithm; the choice for this particular clustering method from among other viable alternatives is justified. Lastly, the definition of the rate of descent is introduced, which is used to characterize the transport patterns.

5.2.1. THE MODELING SETUP

The details regarding the EMAC model are provided mainly in Chapters 3 and 4. A total of 10 simulations (five regions × two seasons) were performed, consuming approximately 35 000 CPU hours of computation time on the Dutch supercomputer Cartesius (now Snellius). The first season encompasses a 3-month period spanning 1 January–31 March, while the second season ranges from 1 July–30 September, both in 2014. As stated in Chapter 3, meteorological variables including the logarithm of the pressure field at the surface, the wind field and lastly the temperature within these simulations were nudged by Newtonian relaxation towards 2014 ERA-Interim reanalysis data.

Version 5.3.02 of the ECHAM5 base model and MESSy version 2.55.0 were used, contrasting with the newer MESSy version 2.55.2 that was applied in Chapter 4. The same three submodels that were useful in Chapter 4 are again of relevance in this analysis: TREXP, ATTILA and AIRTRAC (see Chapter 3 for more details). A total of 28 emission points per region at an altitude of 250 hPa at 06:00 UTC were chosen to be representative of an aircraft flying at a typical cruise level in a given region. This emission time choice brings forth the added benefit of making the results more comparable to previous research [23, 36, 37]. In each emission point, an amount of 5×10^5 kg (NO) is injected into the atmosphere within a 15-min time step (the output frequency for the air parcel spatial coordinates is 6h), and 50 air parcel trajectories are then pseudo-randomly initialized according to a uniform distribution between 0 and 1 within the grid cell of each emission point. To contextualize this amount of emitted NO, it is compared to total yearly NO emissions at cruise (~250 hPa) from commercial aircraft for all five regions (defined in Fig. 5.1) using the most recently updated aviation emissions inventory [192]. According to this inventory, the emitted NO amount of 0.5 Gg constitutes roughly 40% of mean total yearly emissions by commercial aircraft for N. America, 32% for Eurasia, 186% for S. America, 323% for Africa and 118% for Australasia. AIRTRAC linearizes the background chemistry rates from MECCA (see Appendix A and Chapter 3) along air parcel trajectories at every time-step and grid point. Therefore, the amount of NO emitted is not of particular relevance since the resulting volume mixing ratios will be scaled linearly according to changes in this emission quantity (see Sub-chapter 3.3.1 for more details). In terms of the background NO_x levels, typical volume mixing ratios near N. America in July

2014 at 250 hPa range between 5×10^{-10} and 9×10^{-10} mol mol^{-1}. As was stressed in Subsection 4.2.4, this Lagrangian approach can calculate the contribution of a NO_x emission to atmospheric O_3 for all 28 emission points in parallel for a given region based on the 50 emission-carrying air parcels (the choice for 50 air parcels is explained in Sub-section 4.2.4) that are released at each of these emission points [23]. This therefore equates to having a total of $28 \times 50 \times 5 = 7000$ air parcels that are initially responsible for the transport of NO_x to other parts of the world. This number is tripled when considering three pressure altitudes, as has been done in Chapter 4. There are approximately 170 000 other air parcels that are initialized throughout the different layers of the atmosphere and outside of the grid cells with emissions. These are used to simulate diffusive effects and mixing between air parcels via the TREXP submodel. AIRTRAC then calculates the chemical contributions of the NO_x emissions at each air parcel using the background concentrations from the MECCA submodel.

The RF from NO_x-induced O_3 is calculated using the RAD submodel [187] in which the iRF for all available vertical levels, given the selected resolution, is first computed after transforming the Lagrangian O_3 disturbance field into grid-point or Eulerian space. By RF, the definition that pertains to the difference in RF contributions since pre-industrial times up to a given year is not referred; rather, it is defined as the mean radiative impact arising from a pulse emission. The RF relative to the climatological tropopause is again the chosen measure in this chapter (as was the case in Chapter 4), since the stratospheric-adjusted RF and the ERF are not applicable to the pulse emissions used. Warming occurs whenever iRF >0 and cooling when iRF <0. The net change in iRF for O_3 is calculated as the difference of the forcings between two O_3 fields: (1) the sum of the background O_3 and the additional O_3 disturbance from the NO_x emission and (2) the background O_3 volume mixing ratio (undisturbed scenario). Given the current simulation setup, the RAD submodel can only calculate the long- and shortwave fluxes for the O_3 disturbance field arising collectively from the emitted NO_x that is transported by 50 air parcels at each emission point in Fig. 5.1. It is therefore not possible to track the individual O_3 disturbance fields generated by each of these 50 air parcel trajectories. A one-to-one association between RF and geometry is then established via the median trajectory, which more realistically represents the dynamical characteristics of a set of trajectories compared to the mean. In this setup, the RAD submodel computes short- and longwave fluxes every 2h, and the values that are computed instantaneously at every 6h output frequency are used. A more complete discussion of the underlying submodels and their functionalities is provided in Chapter 3.

5.2.2. NO_x EMISSION LOCATIONS

Each '+' in Fig. 5.1 represents the point at which a NO_x emission was released as well as the location in which 50 Lagrangian trajectories were pseudo-randomly initialized within the grid cell that comprises this emission. A total of 28 emission points per region was used as a compromise between the level of detail in the analysis for all five regions and the available computational resources. Although these emission points are not representative of the present-day spatial distribution of aviation emissions (e.g. elevated flight traffic in the North Atlantic flight corridor), one of the aims of this chapter is to understand the underlying processes at a global scale, and as such the emission points are

distributed across a wider spatial scale globally. In addition, the predictions for the shift in global flight distribution indicate a likelihood of reduced traffic in the North Atlantic given likely decreases in RPK from 26% to 17% and from 23% to 17% for North America and Eurasia respectively [47]. As a result, knowledge on less commonly flown areas at the present time will also be needed to accompany studies that already provide an in-depth examination of aviation climate effects for current flight patterns [23, 36, 37, 211].

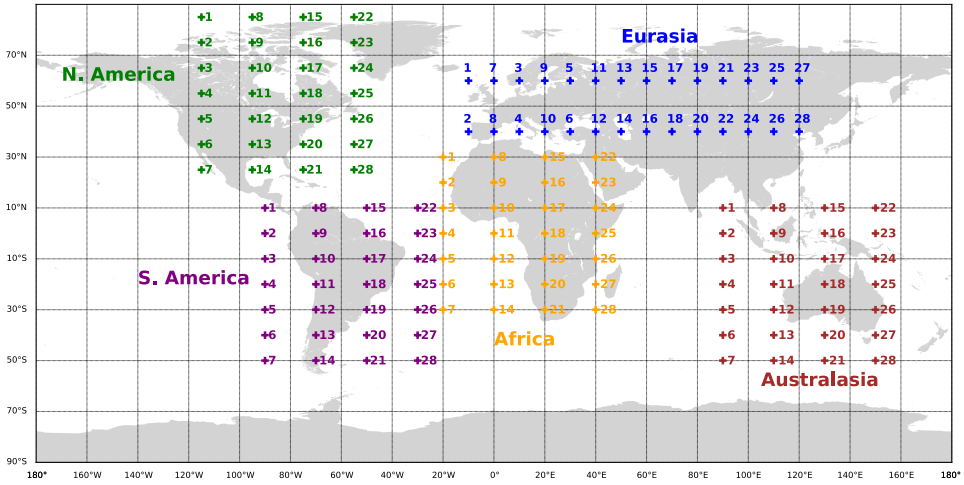


Figure 5.1: Numbered NO_x point source emissions by region. Emission point coordinates are included in Appendix B.

5.2.3. SOURCE-RECEPTOR ANALYSIS

To better understand the relation between the location of emission and the location of largest RF, and to therefore answer the second research question, a source–receptor analysis is conducted. Past studies, within the context of aviation air quality effects, have adopted a similar approach to comprehend if, in terms of aviation-induced O_3 and $PM_{2.5}$, the source of the emission directly corresponded to the most affected region [12]. The regional division in Fig. 5.2 is inspired by Stevenson and Derwent [32], who similarly analyzed which areas would exhibit the largest instantaneous RF based on an aviation NO_x emission in N. America. This chapter investigates aviation climate effects by considering the iRF that is calculated with the RAD submodel with respect to the climatological tropopause (see Eq. 4.5) and subsequently averaging it over the receptor regions in Fig. 5.2.

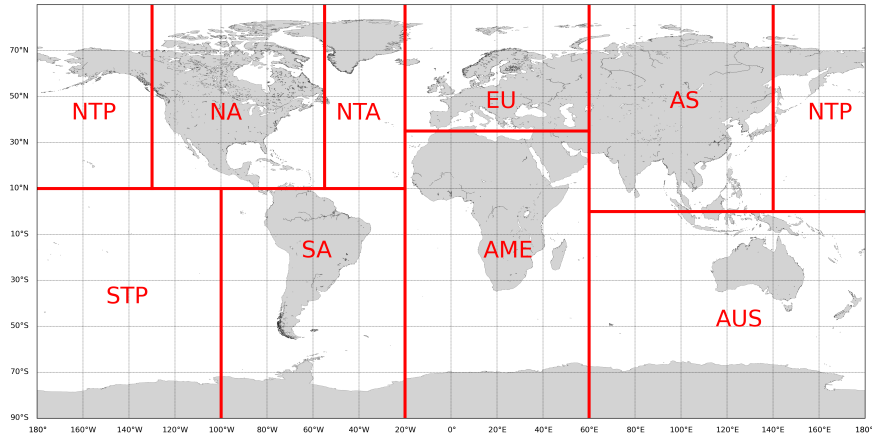


Figure 5.2: Regional divisions for source-receptor analysis based on RF (NTA: Northern Trans-Atlantic, NA: North America, NTP: Northern Trans-Pacific, EU: Europe, AS: Asia, STP: Southern Trans-Pacific, SA: South America, AME: Africa and Middle East and AUS: Australasia).

5.2.4. TRAJECTORY CLUSTERING

To systematically group the output trajectories of the Lagrangian approach within EMAC in terms of their geometric similarities in altitude and latitude, as well as their RF effects, a clustering algorithm is incorporated into the methodology. This firstly enables the identification of different types of transport geometries across all regions and then the association of an average RF estimate to each in an orderly fashion. Firstly, for each emission point in each region, a representative (median) trajectory is computed. For each region, these median trajectories are clustered using the QuickBundles approach. The air parcel trajectories that are clustered in this study are therefore all median trajectories, each being constructed from the median values of longitude, latitude and altitude. A total of 28 median trajectories is generated per region; each is defined from the 50 trajectories that are initialized within the grid box comprising the NO_x emission.

QUICKBUNDLES APPLICATION TO MEDIAN AIR PARCEL TRAJECTORIES

QuickBundles [212] was originally developed to help neuroscientists group large datasets arising from magnetic resonance imaging, called tractographies (consisting of streamlines in the order of 10^6 that represent cerebral nerve tracts), and therefore simplify the subsequent analyses. Here, this method is applied to air parcel trajectories. This method has been selected for three reasons:

1. QuickBundles was designed to cluster nerves in the form of streamlines, which greatly resemble air parcel trajectories.

2. It facilitates the integration of a customizable distance metric or clustering function (used for the attribution of the trajectories into clusters).

3. It has a low computational cost compared to alternative methods because it is, on average, linear in complexity, i.e., O(n) [212].

The QuickBundles tractography clustering software has been implemented in Python 3 and is openly available at https://dipy.org (last access: 16 December 2021). Figure 5.3 provides an overview of the QuickBundles algorithm as a sequence of five steps, when it is applied to median air parcel trajectories. The median trajectory is chosen as it is composed entirely of original coordinate points, unlike the more artificial mean trajectory. This allows for the median trajectory to more accurately represent the dynamical behavior of a set of trajectories.

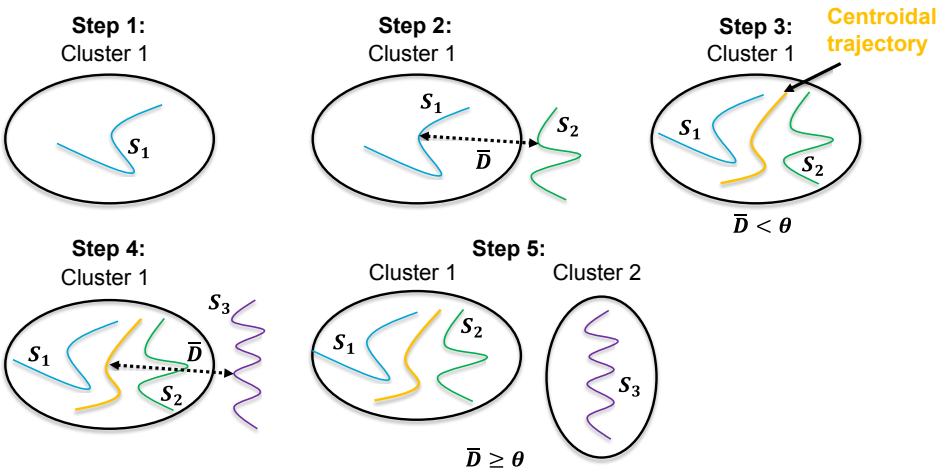


Figure 5.3: Illustration of the five steps of the QuickBundles clustering algorithm. Air parcel trajectories are denoted by S_1 through S_3, θ is the user-defined clustering threshold and $\overline{D}$ is the mean element-wise distance between trajectories according to Eq. 5.1.)

In the first step, air parcel trajectory S_1 is directly placed within the first cluster as there are no pre-existing groups. At this stage, the centroidal trajectory, which is the average path of all trajectories within a given cluster, coincides with the coordinates of S_1. In step 2, the mean element-wise distance $\overline{D}$ between the centroidal trajectory of cluster 1 and the next trajectory S_2 is calculated. The method for computing this value varies according to the distance function that is defined by the user. One of the simplest and most widely used metrics is the Euclidean distance in which a 3-dimensional length is calculated based on the latitude, longitude and altitude [204, 206]. However, this metric has been adapted in this chapter to account for the impact of NO_x emissions on the Earth's energy balance during the clustering process by replacing the longitude of the air parcels with their RF, where the former variable exhibits less variation between the trajectories in each region than the latter. The dimensionless, averaged function $\overline{D}(S_i, S_j)$ is defined by Eq. 5.1, with ϕ being the latitude in degrees, H the altitude in kilometers and $\overline{\mathrm{RF}}$ the mean RF per emission point in watts per square meter or $\mathrm{W\,m^{-2}}$:

$$\overline{D}(S_i, S_j) = \frac{1}{T}\sum_{t=1}^{T}\sqrt{\left(\frac{\phi_t^i - \phi_t^j}{\max\phi}\right)^2 + \left(\frac{H_t^i - H_t^j}{\max H}\right)^2 + \left(\frac{\overline{\mathrm{RF}}_t^i - \overline{\mathrm{RF}}_t^j}{\max\overline{\mathrm{RF}}}\right)^2}. \tag{5.1}$$

Given that the latitudes vary from -90° to 90° and that the altitude is between the surface and the point of release at 250 hPa, the maximum differences are maxϕ = 180° and max$H \approx 10$ km. This newly adapted and normalized Euclidean average distance function proposed here describes similarities in both the geometry and RF of air parcels and is performed between a pair of 3D trajectories S_i and S_j with the following structures: $S_i = \left[\left(\phi_1^i, H_1^i, \overline{\mathrm{RF}}_1^i\right), \left(\phi_2^i, H_2^i, \overline{\mathrm{RF}}_2^i\right), \ldots, \left(\phi_T^i, H_T^i, \overline{\mathrm{RF}}_T^i\right)\right]$ and $S_j = \left[\left(\phi_1^j, H_1^j, \overline{\mathrm{RF}}_1^j\right), \left(\phi_2^j, H_2^j, \overline{\mathrm{RF}}_2^j\right), \ldots, \left(\phi_T^j, H_T^j, \overline{\mathrm{RF}}_T^j\right)\right]$ for which T represents the total number of discrete time steps along a trajectory. The mean RF estimate per emission point from RAD is calculated for each of these 28 points per region, and this value then becomes the third component in each triple $\left(\phi_1, H_1, \overline{\mathrm{RF}}_1\right)$ for S_i and S_j. All air parcel trajectories are discretized with the same time step length of Δt = 15 min and are followed for three months after the emission date. The value of T, however, is 360 given that the model output frequency for the air parcel spatial coordinates is 6 h ($3 \times 30 \times 24/6$). The normalizations of Eq. 5.1 are necessary, given the largely differing magnitudes of ϕ, H and $\overline{\mathrm{RF}}$. Once the average distance $\overline{D}$ is found, the result is compared to a user-defined clustering threshold θ. If $\overline{D} < \theta$, as in step 3 of Fig. 5.3, the candidate trajectory (green) is added to the first cluster, and the coordinates of the centroidal trajectory (yellow) are updated. This on-the-fly updating of the centroidal trajectory avoids the need for a full recalculation within the cluster itself, thereby speeding up the overall algorithm [212]. If, on the other hand, $\overline{D} \geq \theta$ after comparing S_3 with the centroidal trajectory (step 4), then a new cluster is created for this third candidate trajectory S_3 (step 5). The process is continued for the remaining trajectories. This approach to process Lagrangian air parcel trajectories from the ATTILA submodel using the distance metric (i.e., clustering function) of Eq. 5.1 is novel. QuickBundles has, however, previously been applied in atmospheric sciences to cluster cloud movements from radar imagery [213].

In summary, the QuickBundles algorithm systematically groups median trajectories based on geometric similarities (altitude and latitude) and their climate effects (mean RF associated with an emission point). The first trajectory simply becomes the first cluster, and all subsequent trajectories are allocated based on the calculation of a metric (Eq. 5.1) that is proposed here that accounts for both transport features and climate effects. At every step in the clustering process, the distance between the centroidal trajectory of a cluster and the candidate trajectory is calculated using Eq. 5.1 and depending on the user-defined parameter θ, it will either be placed within a pre-existing cluster or in an entirely new one. The optimal selection of θ is discussed in the next section.

SELECTION OF AN OPTIMAL THRESHOLD θ

One of the challenges of applying clustering techniques is determining the optimal number of clusters, which, in the case of QuickBundles, is determined indirectly via the user-defined threshold θ. It is typical to combine the evolution of a sum of squared errors (SSE) function with silhouette coefficients to arrive at the most efficient number of clusters, as has been done in a recent aerosol clustering study with a K-means method [208]. This is a grouping technique that seeks to distribute data points across an optimally chosen number of clusters based on the minimization of a within-cluster sum of squares [214]. The approach chosen here is based on the L-method, developed by Salvador and

Chan [215] and applied by Kassomenos et al. [209]. It consists of finding the intersection between two linear regressions that model each half of a curve generated from plotting the evolution of a trajectory-based metric, specifically here the average distance within clusters, as a function of the cluster number ($E(\theta)$), as is exemplified in Fig. 5.4 (a). Possible other metrics as described by Kassomenos et al. [209] could be the SSE, a similarity function, or another distance metric. The red dot in Fig. 5.4 (a) may be viewed as a partitioning point as it divides the curve in two quasilinear sections: left and right. The final linear regression (dotted red line) for the points on the left may be obtained iteratively by beginning with the most basic case of regressing the first two leftmost data points. The fit of such a linear function may then be improved gradually by adding more and more points in each iteration. According to Salvador and Chan [215], the optimal distribution of points to be regressed by each side could be achieved by iteratively selecting the partitioning point that minimizes the total root mean squared error of both linear regressions. Kassomenos et al. [209], whose approach is followed here, however, have also tested this method by applying different curve modeling techniques that include higher-order polynomials and splines and obtained consistent results relative to the linear approach.

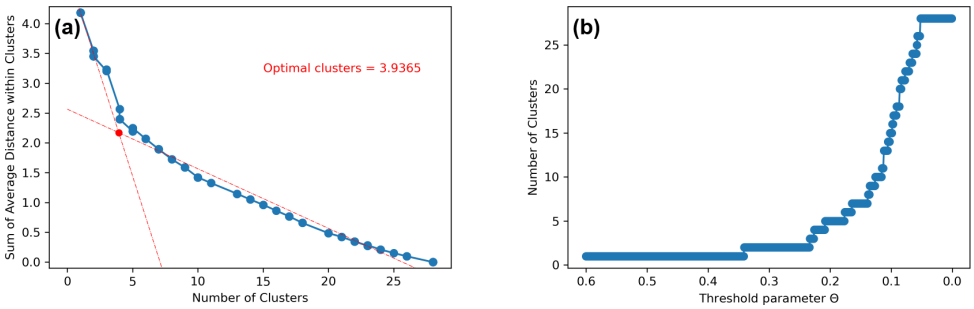


Figure 5.4: Determination of optimal clustering threshold θ for N. America during July-September 2014. (a) Sum of averaged distance $E(\theta)$ as a function of the number of clusters (blue). Two linear regressions (red) are added. The intersection (red dot) gives the optimal number of clusters. (b) Variaion of the number of clusters with θ.

The evaluation metric $E(\theta)$, given by Eq. 5.2, is the sum of mean "distances" (based on the adapted Euclidean function of Eq. 5.1) to the centroidal trajectory within a cluster c_k with $k = 1, 2, ..., N(\theta)$, where N is the total number of clusters that depends on θ, across all clusters. The number of median trajectories within a cluster c_k is given by $L(c_k)$ (and therefore also depends on θ), and $\overline{\mu_k}$ is the centroidal trajectory for the k th cluster. Radiative forcing is included in the clustering process via Eq. 5.1 and therefore also in the evaluation metric in Eq. 5.2. This evaluation metric, as well as the L-method, is applied entirely to median trajectories, which are shown in red in Fig. 5.5.

$$E(\theta) = \sum_{k=1}^{N(\theta)} \sum_{l=1}^{L(c_k)} \overline{D}(S_l, \overline{\mu}_k) \tag{5.2}$$

Since QuickBundles uses θ as the user input, a range of values of θ is tested with Eq. 5.2 until an optimal cluster is found according to Kassomenos et al. [209] via the inter-

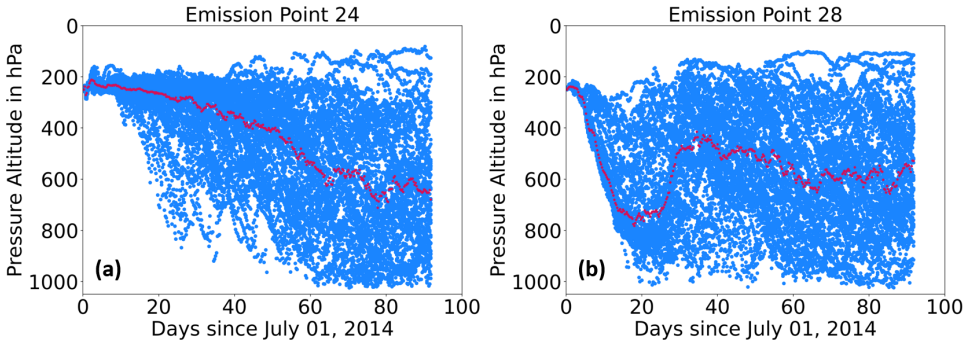


Figure 5.5: Temporal evolution of the air parcel trajectory pressure altitude of median trajectories (red) based on 50 Lagrangian paths (blue) in (a) emission point 24 and in (b) emission point 28 for N. America for July-September 2014. Figures D.1 and D.2 show all 28 emission points for N. America during January-March and July-September 2014, respectively. The trajectories for all regions and seasons are included in the Supplement of Maruhashi et al. [13].

section of two regression lines (dotted red lines in Fig. 5.4 (a)). Once the optimal cluster number is found, the corresponding value of θ is chosen (Fig. 5.4 (b)). The calculations of the optimal cluster numbers for N. America are represented by Fig. D.5 and Fig. D.6 for January and July respectively.

5.2.5. THE RATE OF DESCENT $\dot{H}$

To quantitatively distinguish between vertical transport patterns, the rate of descent $\dot{H}$ in hectopascals per day (hPa d^{-1}) is used, defined here according to Eq. 5.3. It is the rate of change in altitude of an air parcel from its point of release until it first reaches its global minimum altitude at a time t^*. As the release altitude is constant in all scenarios, $H(0) = 250$ hPa. The quantity $\dot{H}$ is calculated for all regions and is intended as a metric to understand if the initial downward transport has an impact on the atmospheric concentrations of O_3.

$$\dot{H} = \frac{|H(0) - H_{\min}(t^*)|}{t^*} \tag{5.3}$$

5.3. RESULTS

First, the variability of NO_x transport patterns is examined as a function of emission location and season by relating the rate of air parcel descent ($\dot{H}$) to the resulting O_3 production and estimating the latitudinal residence times of the 1400 Lagrangian trajectories within each region. The median trajectories are then grouped into clusters and assessed in terms of their characteristic transport pathways. Finally, the spatial characteristics of the resulting RF from NO_x over different regions are presented.

5.3.1. SEASONALITY AND METEOROLOGICAL CONDITIONS AS DRIVERS OF NO_X TRANSPORT AND CHEMISTRY

The air parcel rate of descent (Eq. 5.3) is used to describe the differences in O_3 disturbances induced by different NO_x-carrying air parcels. Since the O_3 lifetime varies with altitude, a lower rate of descent $\dot{H}$ (and thus longer residence time at higher altitudes) is expected to result in a higher O_3 disturbance than an air parcel with a faster downward transport (larger $\dot{H}$). Figure 5.6 depicts the variation of the mean O_3 disturbance with $\dot{H}$ of the median trajectories for all regions during both seasons. Apart from Africa during July, between 50–100% of the top 20% largest O_3 disturbances show $\dot{H} < 10$ hPa d^{-1}, indicating that longer residence near the emission region leads to a larger impact on the atmospheric composition of O_3. This inverse relationship between $\dot{H}$ and mean O_3 is likely owed to faster O_3 removal rates at lower altitudes compared to more efficient accumulation of chemical species at higher altitudes, therefore leading to lower O_3 lifetimes in the lower troposphere (Fig. 4 in Grewe et al. [174] and [30, 38]). The rate of descent for a 40-day window, as opposed to the 90-day window presented here, performs slightly better in capturing the immediate downward behavior of certain transport patterns, as is the case for emission point 19 in Eurasia in July (see Fig. S25 in the supplementary figures of Maruhashi et al. [13]), but the overall negative trend relative to the mean O_3 disturbance is maintained. The same negative correlation is found, if the mean O_3 disturbance is replaced with the RF that it induces. To ascertain whether a statistically significant correlation exists between the average descent rates $\dot{H}$ and the mean O_3 contribution, as well as to quantify the strength of this correlation, three metrics are calculated: the Pearson, Kendall and Spearman rank correlation coefficients. These have also been applied by Rosanka et al. [37] to better understand the interactions between relevant chemical species, i.e., NO_x and O_3 volume mixing ratios. Table 5.1 summarizes the values for these coefficients for all regions for emitted NO_x during January and July. During January, the correlation coefficients are mostly negative and, with the exception of Eurasia, are also statistically significant based on a level of significance of $\alpha = 5\%$, since their p values are below this threshold for at least one of the three chosen correlation coefficients. The strongest negative correlations exist for S. America and Africa, where all three metrics are statistically significant with a magnitude of about 0.5. During both periods, for air parcels released in Eurasia, no significant correlation is found between $\dot{H}$ and the mean O_3 contribution. The only statistically significant positive correlation is found for Africa during July, according to the Spearman and Kendall coefficients. Australasia and Eurasia during July appear to not exhibit any correlation at all.

Table 5.1: Statistical correlations between $\dot{H}$ and mean O_3 contribution using the Pearson, Kendall and Spearman correlation coefficients. P values are shown for each corresponding metric. The null hypothesis assumes that no correlation exists between $\dot{H}$ and the mean O_3 contribution.

	January						July					
	Pearson	p value	Spearman	p value	Kendall	p value	Pearson	p value	Spearman	p value	Kendall	p value
N. America	−0.3556	0.0633	−0.4143	0.0284	−0.2698	0.0453	−0.3813	0.0453	0.0066	0.9735	−0.0053	0.9844
S. America	−0.4368	0.0201	−0.5216	0.0044	−0.3598	0.0068	−0.3810	0.0455	−0.3492	0.0685	−0.3175	0.0177
Eurasia	−0.1693	0.3891	0.0421	0.8314	0.0053	0.9844	0.2640	0.1747	0.3645	0.0565	0.2328	0.0857
Africa	−0.5061	0.0060	−0.4959	0.0073	−0.3280	0.0141	0.2405	0.2177	0.3815	0.0452	0.2751	0.0411
Australasia	−0.4028	0.0336	−0.2151	0.2716	−0.1587	0.2463	−0.2817	0.1464	−0.1598	0.4166	−0.1270	0.3564

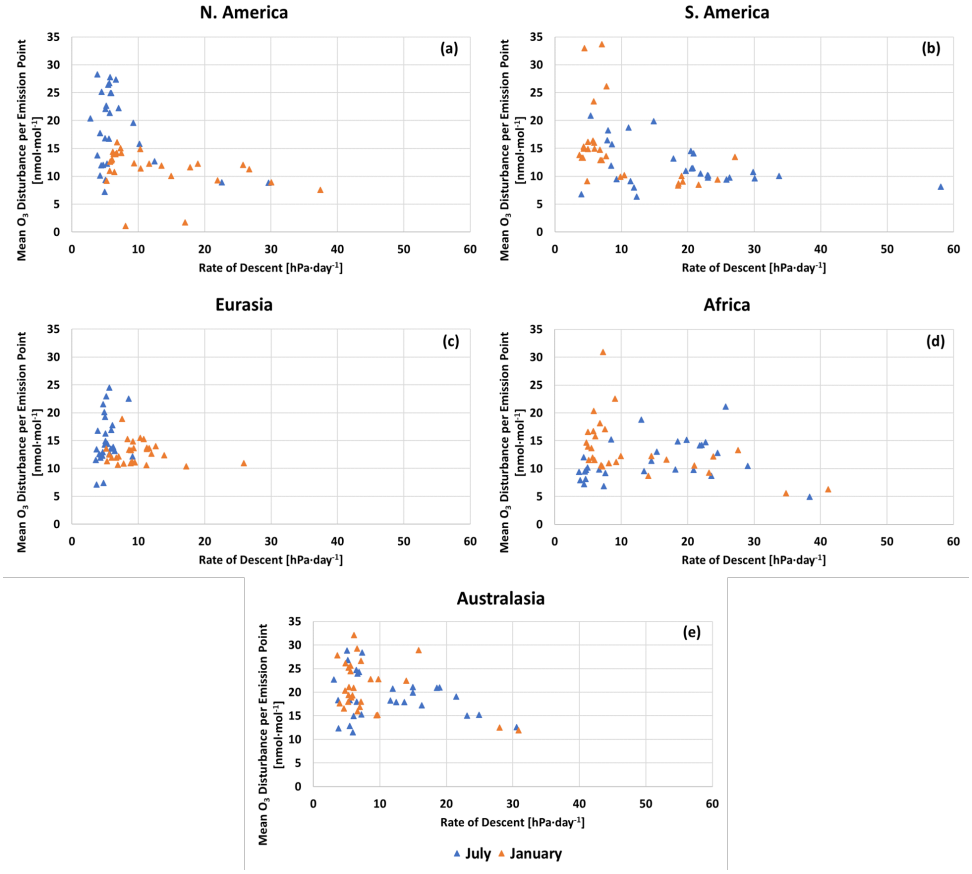


Figure 5.6: Variation of the 90-day rate of descent $\dot{H}$ with the mean O_3 disturbance for each of the 28 median NO_x-carrying Lagrangian air parcel trajectories for January (orange) and July (blue) for each region.

The link between smaller mean O_3 production and an air parcel's faster downward transport is also evident after applying the clustering method; i.e., the two clusters identified by the QuickBundles algorithm for N. America during January–March that are presented in Fig. 5.7 illustrate the association between descent rates $\dot{H}$ and O_3 disturbances. During this season, the vertical pattern of Cluster 2 (C2 in Fig. 5.7 (b)) occurs more often (61%) and is characterized by a slow downward transport until 40–60 days, staying between 600 and 800 hPa afterwards. Compared to Cluster 1 (C1 in Fig. 5.7 (a)), however, C2 exhibits a much lower mean descent rate of 7.7 hPa d^{-1} compared to 20.5 hPa d^{-1} for C1. The C2 trajectories will therefore remain closer to their original emission altitude for a longer period of time, thereby reducing the NO_x and O_3 loss rates and inducing a stronger $\overline{O_3}$ disturbance of 13 nmol mol^{-1}. If the air parcel is immediately transported downwards, as in Fig. 5.7 (a), the induced O_3 disturbance is generally smaller, at 9 nmol mol^{-1}, as the emitted NO_x is converted to HNO_3 and likely washed out faster. After 40 days, C2 still displays an O_3 disturbance between 20–30 nmol mol^{-1} while C1 mostly in-

duces a weaker disturbance of less than 10 nmol mol^{-1}. Both the mean O_3 perturbation and the RF are slightly larger throughout the 90 days for the scenario of slower descent (C2 in Fig. 5.7 (b)). However, the trajectory with the faster descent rate experiences a larger maximum O_3 of 38 nmol mol^{-1} compared to the maximum of 34 nmol mol^{-1} attained by the type of transport of C2. Such a result agrees with findings by Rosanka et al. [37], who explain that air parcels transporting emitted NO_x will generally attain a larger initial O_3 gain if they undergo a fast downward transport, since at lower altitudes the background NO_x and HO_2 concentrations are smaller and larger, respectively. This increases O_3 production via the reaction initiated between NO and HO_2 followed by the photodissociation of NO_2 into NO and O. On average however, the smaller lifetimes for O_3 at lower altitudes will dominate and lead to a smaller mean O_3 production for C1 compared to C2. Air parcels that remain at higher altitudes, near the tropopause for instance, are subjected to areas in which NO reacts less frequently with HO_2, which then leads to lower O_3 formation but also smaller NO_x removal rates. One of the determining drivers for the vertical pattern is the vertical wind component, which may be consulted in Fig. D.7 (b) and (d) from Appendix D. Regions of intensified downdrafts (e.g., within a subsidence or near gravity waves) will lead to vertical pathways similar to Cluster 1. Figure 5.7 (c) and (d) show the horizontal distributions for C1 and C2. It is evident how the trajectories from C1 that have a faster downward transport also travel to lower latitudes compared to C2. Although C1 induces a smaller O_3 disturbance, because it travels closer to the tropics, the RF generated is comparable to that of C2. The O_3 produced by the 50 air parcel trajectories for each emission point for all regions and seasons as well as their consequent RF may be found in the supplementary figures in Maruhashi et al. [13].

Figure 5.8 presents the individual trajectory residence times of the 1400 trajectories initialized across the 28 emission points in each region (e.g., the blue trajectories in Fig. 5.5, 7000 trajectories across the five regions) per time period in the following latitudinal bands: Arctic, Northern Midlatitudes and Subtropics, Tropics, Southern Subtropics and Midlatitudes, and the Antarctic. Emissions initialized in the N. Hemisphere (N. America and Eurasia) will mainly reside in the Northern Midlatitudes, spending on average ~39 days between latitudes 35 and 65° N. The Tropics are then the second most likely region, with a mean residence time of 25 days. Analogously, for emissions released in the south (S. America, Africa and Australasia), the Tropics display the greatest residence time of 46 days, followed by 17 days for the Southern Midlatitudes. The distribution across these latitude bands is similar in both seasons for most cases, with a larger 11% increase in residence time in the Tropics for air parcels initiated in Africa in July relative to January, which is likely explained by the stronger northern westerly displacing the air parcels mainly to the north during January (Fig. D.7)

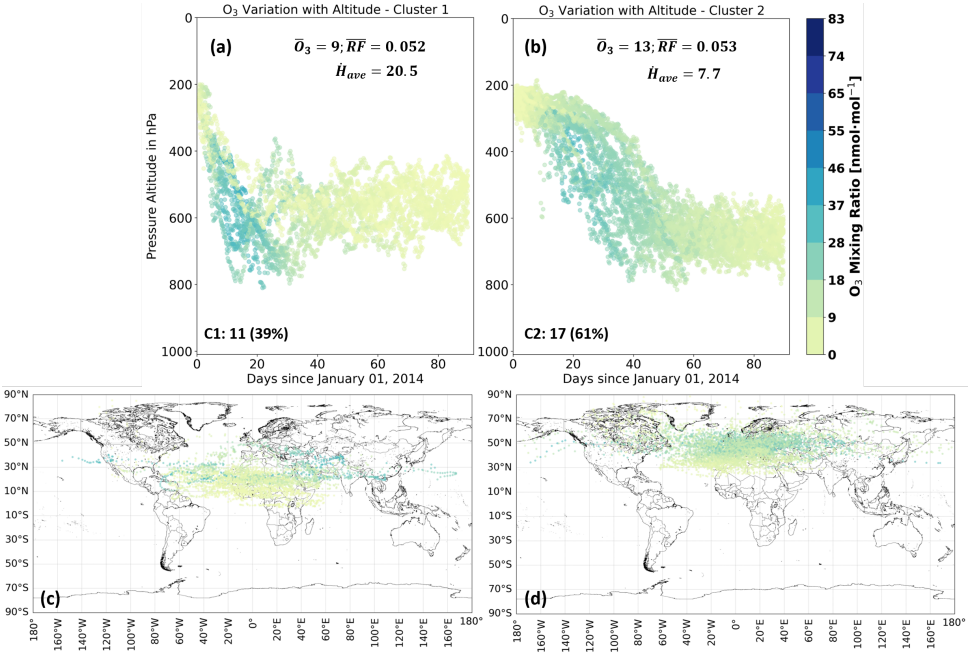


Figure 5.7: (a) Vertical profile of Cluster 1 (C1) of NO_x transport pathways over 90 days following an emission on 1 January 2014 for N. America. The color bar represents the mean O_3 disturbance in nanomoles per mole (nmol mol^{-1}) caused by the median trajectory. Each cluster label is followed by the number of median trajectories that it comprises both in absolute and relative terms (bottom left of (a) and (b)). The mean rate of descent for a 90-day period in hectopascals per day (hPa d^{-1}) for all median trajectories in a cluster is defined as $\dot{H}_{ave}$. The cluster radiative forcing contribution in milliwatts per square meter (mW m^{-2}) is labeled as $\overline{RF}$, and the mean O_3 disturbance in nmol mol^{-1} is $\overline{O}_3$. Panel (b) represents the same quantities but for Cluster 2 (C2), panel (c) is the horizontal distribution of C1 and panel (d) is the horizontal distribution of C2.

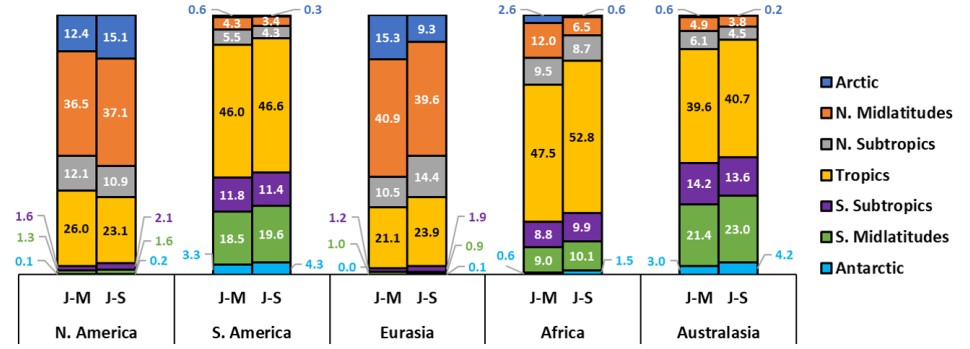


Figure 5.8: Distribution of residence times in days of 1400 Lagrangian trajectories per emission region and per time period throughout the course of a 90-day path. 'J-M' is the period January-March 2014 and 'J-S' the period July-September 2014. The latitudinal bands are based on Najibi and Devineni [216] and are defined as Arctic=[65, 90° N], N. Midlatitudes=[35, 65° N), N. Subtropics=[23.5, 35° N), Tropics=[23.5° S, 23.5° N), S. Subtropics=[35, 23.5° S), S. Midlatitudes=[65, 35° S) and Antarctic=[90, 65° S).

The distribution of latitudinal residence times in Fig. 5.8 also solidifies the reduced tendency for transhemispheric transport and mixing between air parcels released in the north and in the south. Air masses released within the northern region mainly remain within their hemisphere as more than 70% of their residence time is distributed among the Arctic, Northern Subtropics and Northern Midlatitudes. This does not hold for the southern regions, where on average slightly more than 50% of trajectories reside in the Tropics for both S. America and Africa and 45% for Australasia. However, we note that the emission points in S. America, Africa and Australasia are on average closer to the Equator than the ones of N. America and Eurasia, which could be driving this difference. Despite the increased likelihood for transhemispheric transport of trajectories initialized in the south, Fig. 5.8 generally supports the argument for the limited potential of air parcels to travel to the opposite hemisphere, as is dictated by the Brewer–Dobson circulation and verified by earlier multi-model studies like the one by Danilin et al. [139] as well as more recent ones [40]. Other Lagrangian studies [140, 217] found the same result for current aviation emissions of NO_y species.

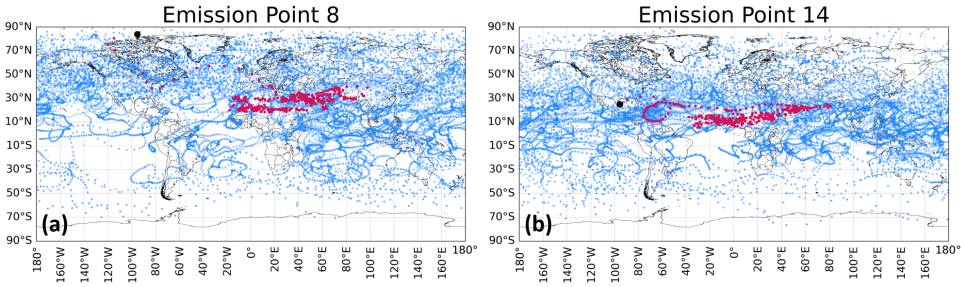


Figure 5.9: Horizontal trajectories for air parcels released in N. America. The black dots denote the emission starting points. Both are located on the Northern Hemisphere in winter (January–March). The red dots represent the median trajectory, while the blue dots represent the 50 Lagrangian trajectories from (a) emission point 8 within the meridional tilt and (b) emission point 14 within the westerly and outside of the meridional tilt. The age of the air parcel trajectories is accounted for with variable blue transparency so that ending points appear darker.

It has been observed that the transport behavior and ensuing chemical repercussions vary depending on the meteorological conditions in terms of the existing vertical wind component. The magnitude and direction of the horizontal wind, however, are also drivers. This is evident for emission points 8 and 14 in Fig. 5.9 from N. America during January 2014. Figure 5.9 illustrates two distinct horizontal transport patterns that are generated as a result of varying the point of emission relative to the predominant zonal jets. According to the meteorological situation (see Fig. D.7 (a)), the northern region is affected by a strong westerly with a pronounced meridionally tilted jet near the west coast of N. America during January. Thus, most air parcels starting in N. America, Eurasia and part of Africa will be advected by this jet, as will air parcels emanating from S. America and Australasia by the southern westerly. If an emission is released well within the westerly and away from the meridional tilt, as is the case in Fig. 5.9 (b), the ensuing trajectory is mainly contained within the latitudinal bands in which the jet acts during its entire lifetime. However, if the air mass is introduced near the tilt, as is the case in

Fig. 5.9 (a), then it is likely to be transported farther to the south in the direction of the tilt. The vertical and latitudinal evolution of Fig. 5.9, shown in Fig. D.8, also shows distinct patterns. For emission point 8, Fig. D.8 (a) first shows a southern shift, followed by a pronounced downward motion caused by the air parcel's proximity to an area of stronger downdrafts near 85° W and 35° N (Fig. D.7 (b)). Emission point 14 is vertically characterized by an almost immediate drop (Fig. D.8 (b)) as it is initialized outside of the tilt, directly within a westerly that constrains its latitudinal range and within the same region of stronger downdrafts. From Fig. 5.9, it is also clear why the longitude was not used as a representative variable in the clustering function (Eq. 5.1). As the trajectories spread and wrap around the globe, they mostly arrive within a similar longitudinal range. For this particular case, the median trajectories mainly end near the prime meridian. The other emission points for N. America for a January NO_x emission may be consulted in Fig. D.3. The same plots for the remaining regions may also be viewed in the supplementary figures in Maruhashi et al. [13].

The O_3 disturbance and consequent RF associated with these transport patterns occur along the horizontal trajectories of Fig. 5.9, as is shown in Fig. 5.10. A trajectory beginning directly in the northern westerly (emission point 14) will lead to an increase in O_3 production mostly within the latitude band of the jet stream. As such, the RF contribution is also maximal in the same area (Fig. 5.10 (d)). Per contra, an emission in the vicinity of a meridionally tilted jet (emission point 8) will produce the greatest amount of O_3 in a region south of the emission point. Figure 5.10 (a) and (c) identify the tropics as the most affected region; i.e., an emission in Canada will likely induce the largest climate impact in Asia.

The seasonal dependence of transport, O_3 production and RF may be understood by again considering the same emission points as in Fig. 5.10 and comparing them to the scenario in July 2014, as shown in Fig. 5.11. When considering the Northern Hemisphere winter, there is generally a larger O_3 production towards the tropics and the Equator (up to 40° N at most during December-February), as there is amplified solar input. The increased sunlight then leads to more frequent photolysis of NO_2, followed by the combination of monatomic and molecular oxygen to produce O_3. This is consistent with findings by Gauss et al. [38] and is evidenced in Fig. 5.10 (a) and (b). Other past studies [33, 36] have also verified this tendency for emissions at lower latitudes to generate higher disturbances during the Northern Hemisphere winter months like January and February. Frömming et al. [36], for instance, use a similar Lagrangian approach with the EMAC model to conclude that during this northern winter period, an air parcel emitted within a high-pressure ridge reaches lower altitudes and latitudes along its path and therefore exhibits a larger O_3 production, between 30–40 nmol mol^{-1}. For a similar time period (Fig. 5.10 (b)), this chapter estimates a similar mixing ratio 30 - 45 nmol mol^{-1} for the trajectory traveling mainly in the lower latitudes. When comparing RF values during March 2014 for the North Atlantic flight corridor, the time-averaged RF per emission point that considers all of the overlapping points between Fig. 5.1 and their emission time region yields the range $[5.3 \times 10^{-3}, 6.9 \times 10^{-2}]$ mW m^{-2}. Frömming et al. [36] estimated the range $[1.2 \times 10^{-2}, 4.7 \times 10^{-2}]$ mW m^{-2} for their stratospheric-adjusted RF.

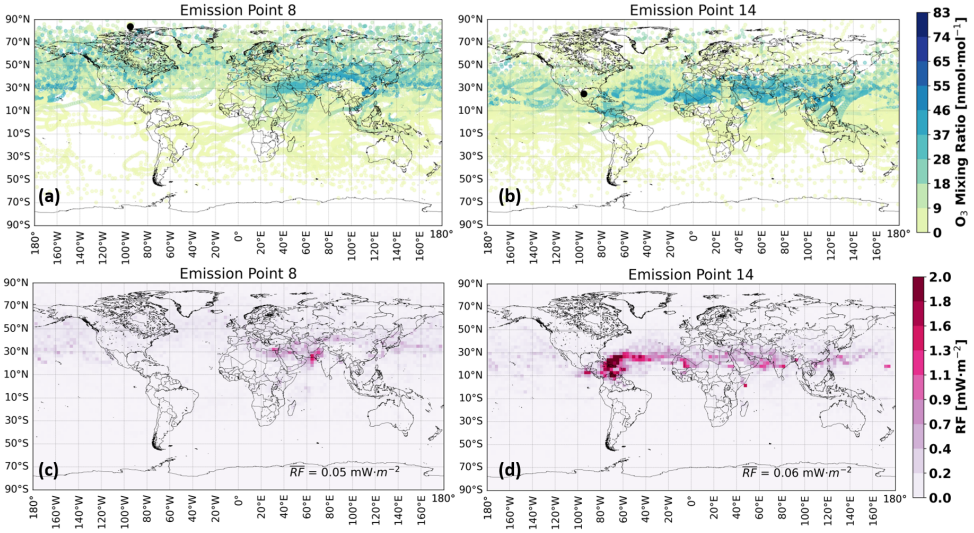


Figure 5.10: Horizontal profiles of mean O_3 disturbances in N. America in nmol mol^{-1} during January 2014 for (a) emission point 8 and (b) emission point 14. The mean radiative forcing $\overline{RF}$ in mWm^{-2} for (c) emission point 8 and (d) emission point 14. The black dots in (a) and (b) represent the emission starting points.

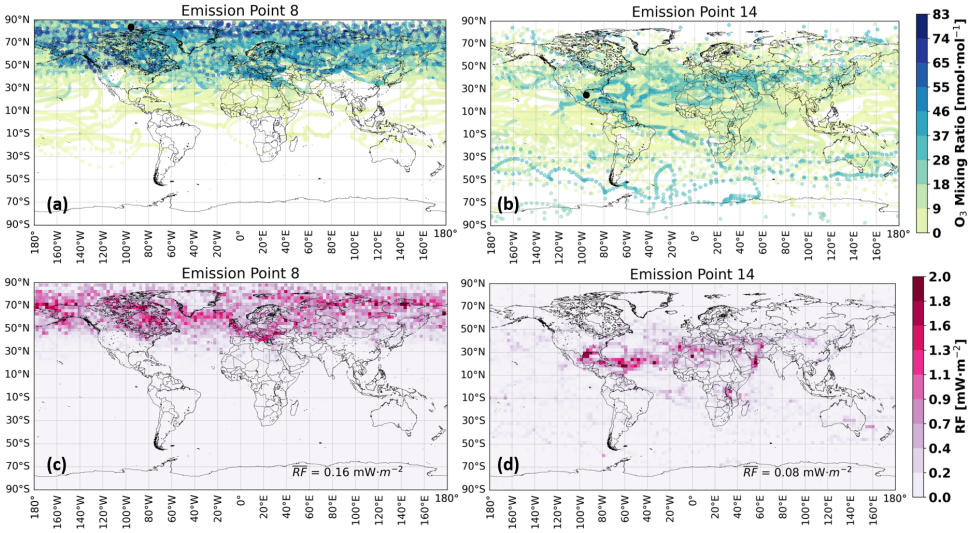


Figure 5.11: Horizontal profiles of mean O_3 disturbances in N. America in nmol mol^{-1} during July 2014 for (a) emission point 8 and (b) emission point 14. The mean radiative forcing $\overline{RF}$ in mWm^{-2} for (c) emission point 8 and (d) emission point 14. The black dots in (a) and (b) represent the emission starting points.

During the Northern Hemisphere summer, there is a significant decrease in the intensity of the northern westerly, along with an attenuation of its meridional tilt in N. America according to Fig. D.7 (c). The main region of O_3 production and RF for an air parcel starting at emission point 14 (Fig. 5.11 (b) and (d) respectively) remains the same as before: near the tropics. However, the magnitude of the mean RF contribution ($\overline{RF}$) is now larger (Fig. 5.11 (d)). Consistency with the results of Gauss et al. [38] for N. America during the Northern Hemisphere summer is again seen, as the air parcels transported in the north now experience stronger solar input, and in some regions like the Arctic, the exposure to sunlight continues during the whole day. This shift in the exposure to sunlight then translates to a larger O_3 production and RF contribution in the Northern Mid-latitudes and high latitudes as is evidenced in Fig. 5.11, particularly in Fig. 5.11 (a) and (c). As a result of a weaker meridional tilt, the trajectory from emission point 8 spends most of its 90-day lifetime in the higher latitudes (Fig. D.4) and is therefore exposed to increased solar radiation, which then generates more O_3 (~ 70 nmol mol^{-1} compared to ~ 40 nmol mol^{-1} for emission point 14) and, according to Fig. 5.11 (c) and (d), a stronger RF by a factor of 2 compared to a trajectory released closer to the Equator.

5.4. PROFILES OF CLUSTERED TRAJECTORIES

The main transport pathways that result from the NO_x emissions across the five regions in Fig. 5.1 are presented based on the adopted clustering approach with QuickBundles. Their horizontal distributions and vertical profiles for all regions and both time periods are included for emissions in January and July respectively. The O_3 disturbance and consequent RF associated with each of these transport patterns are also shown.

5.4.1. PROFILES FOR JANUARY 2014

The clustering output in Fig. 5.12 (a) summarizes the vertical profiles of the main transport patterns that were identified for emissions in January. The corresponding horizontal distributions are then depicted in Fig. 5.12 (b). Each panel in this figure depicts the same information that is shown in Fig. 5.7: the spatial evolution of a cluster along with its mean $\overline{O_3}$ and $\overline{RF}$.

As shown in Fig. 5.12 (a) and (b), there are two clusters and therefore two distinct transport pathways for trajectories that are released in N. America at 250 hPa. The vertical profiles (Fig. 5.12 (a)) depict two different kinds of behavior: C1 shows a faster initial descent compared to C2. Their rates of descent, $\overline{O_3}$ and $\overline{RF}$ in relation to their vertical behavior have been analyzed earlier in detail in Fig. 5.7. When considering their corresponding horizontal distributions in Fig. 5.12 (b), C1 mostly resides closer to the tropics compared to C2. Consequently, there is more solar input in the region of the ozone disturbance produced by the C1 trajectories. This allows C1 to generate a comparable $\overline{RF}$ value relative to C2 but for a smaller average $\overline{O_3}$ disturbance of 9 nmol mol^{-1} compared to 13 nmol mol^{-1}.

The clustering for S. America led to a total of four clusters, with close to 90% of trajectories being categorized in either C1 or C2. The most probable pathway for NO_x released in this region is therefore to follow one of these clusters, especially C1. The vertical profiles for both are similar, where C2 displays a longer average residence time as its rate of

descent is lower than in C1. Between these higher-density clusters, the trajectory with the lower rate of descent of 7.4 hPa d^{-1} (C2) leads to stronger O_3 perturbations of 14 nmol mol^{-1} compared to 11 nmol mol^{-1} of C1. In terms of their horizontal profiles, C1 travels mainly at higher latitudes than C2. As was discussed earlier, the emissions at lower latitudes during this time period are exposed to more solar radiation and therefore result in a larger RF. However, the largest RF and O_3 disturbances occur for air parcels in C3 and C4, which have the lowest rates of descent over 90 days.

The transport patterns of Eurasia are similar to those of N. America, where C1 and C2 from Eurasia essentially correspond to those of C2 and C1 from N. America, respectively. The same conclusion is again possible, where the trajectory with the longest residence time (lowest $\dot{H}_{ave}$) exhibits the highest $\overline{O}_3$. Nonetheless, it appears that the path that descends earlier (e.g., C2 from Eurasia) will lead to a larger maximum of O_3 disturbance within the first 20 days upon the NO_x emission, as has been found by Rosanka et al. (2020). Based on the dynamics of all 1400 NO_x-carrying trajectories in Eurasia, the trajectory in C1 is the dominant path with a probability of 75% and is characterized by a slightly lower rate of descent and elevated residence time in the upper northern latitudes (Fig. 5.12 (a) and (b)).

For Africa, the most probable path is given by C1, involving almost half of all air masses released (46%). This cluster exhibits the fastest descent and shortest residence time in terms of its O_3 disturbance out of all four clusters. The negative correlation between $\dot{H}_{ave}$ and $\overline{O}_3$ is again evident (see Table 5.1) as C1 has both the smallest O_3 disturbance and fastest descent. In terms of the horizontal distributions, C1 resides predominantly near the tropics, but given its high rate of descent, the NO_x is washed out faster, and $\overline{O}_3$ drops under 10 nmol mol^{-1} earlier than C2. The clusters that induce the largest O_3 perturbation are C2 and C4, which also travel mainly through the equatorial region and additionally benefit from lower $\dot{H}_{ave}$ compared to C1. C3 is the only transport pathway along which the air masses have an initial tendency to be lifted higher than their emission altitude.

Across all regions, Australasia displays the highest O_3 disturbances throughout its five clusters and produces the largest RF. The transport pattern from cluster C3 has the greatest probability of occurrence (64%) and travels mainly in the southern subtropics, according to Fig. 5.12 (b), with an approximate rate of descent of 8 hPa d^{-1}. The air parcel with the largest O_3 mixing ratio along its path is represented by a single trajectory, C2, which implies that the likelihood of occurrence is low (~4%). Its O_3 maximum occurs when the trajectory is again near its lowest point. The mean RF contributions per region and per cluster for NO_x emissions in January may be found in Table D.1.

Overall, the horizontal distributions across the regions are strongly influenced by the atmospheric circulation (zonal jet streams) present in both the Northern and Southern Hemisphere. According to Fig. D.7 (a), the northern zonal jet is constrained within latitudes 60 to 10° N and the southern between 30 and 70° S. The former jet splits into two meridionally tilted streams near 150° W: one is directed towards the northeast and the other towards the southeast. The two clustered horizontal distributions for N. America and Eurasia are each determined by these meridional tilts. The largest northernmost clusters, C2 for N. America (61% of trajectories) and C1 for Eurasia (75% of trajectories), show how the air parcels released in these regions are driven by the north-

eastward meridional tilt. The behavior of the smaller clusters, C1 for N. America and C2 for Eurasia, is influenced by the south-eastward meridional tilts. These clusters therefore lie slightly to the south relative to their larger counterparts. A similar rationale is applicable to the southern zonal jet as it strongly influences the horizontal distribution of the majority of air parcels released from Australasia, as can be seen by the presence of its highest-density cluster C3 (64% of trajectories) along the latitudinal bounds of this jet.

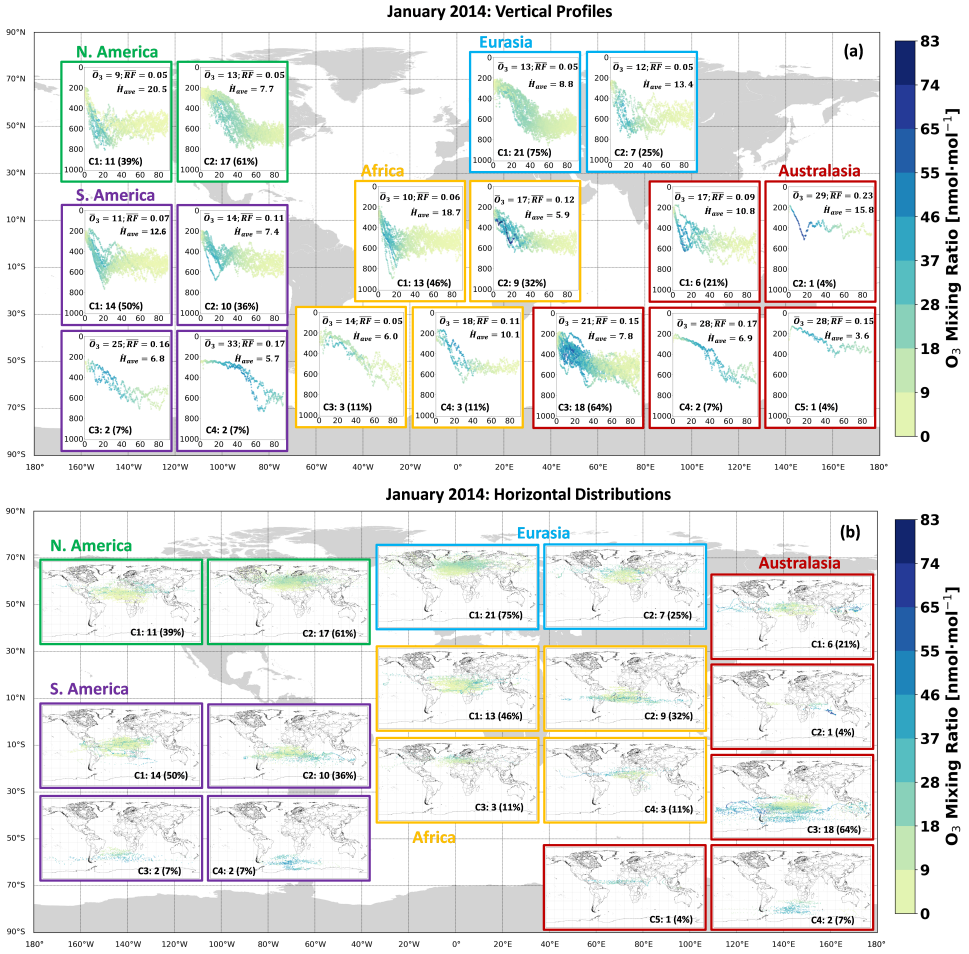


Figure 5.12: (a) Vertical profile of clusters of NO_x transport pathways during January 2014. The color bar represents the mean O_3 disturbance in nmol mol^{-1} caused by the emission transported along a median trajectory. Each 'C' represents a distinct and independent cluster; i.e., C1 from N. America is not related to C1 from S. America. Each cluster label is followed by the number of median trajectories that it comprises, both in absolute and relative terms. The 90-day mean rate of descent in hPa d^{-1} for all median trajectories in a cluster is defined as $\dot{H}_{ave}$. The cluster radiative forcing contribution in mW m^{-2} is labeled as $\overline{\text{RF}}$, and $\overline{\text{O}}_3$ is the mean disturbance of the median trajectories in nmol mol^{-1}. Panel (b) uses the same notation but for the horizontal distributions. The axes for (a) are defined in Fig. 5.7 (a) and (b), while the axes for panel (b) are specified in Fig. 5.7 (c) and (d). Meteorological conditions considered are specific to the period 1 January - 31 March 2014.

5.4.2. PROFILES FOR JULY 2014

Figure 5.13 provides the vertical and horizontal distributions of the resulting clusters for all regions and emissions in July. The mean O_3 disturbances are now larger in the Northern Hemisphere, i.e., in N. America and Eurasia and on average lower in the Southern Hemisphere. Despite this shift, Australasia continues to globally display some of the largest values in terms of O_3 mixing ratios and therefore RF given the lower background NO_x mixing ratios. In other words, the larger O_3 production efficiency, promoted by the cleaner background, increases the amount of O_3 produced per unit kilogram of NO_x emitted, as has also been found by Skowron et al. [196] and Gilmore et al. [34].

During July, the most probable path for NO_x emissions in N. America would be C1, with a likelihood of 43% followed by C2 with 36%. C1 also exhibits the highest O_3 perturbation and is characterized by a gradual decrease in altitude, according to Fig. 5.13 (a) at a rate of descent of 6.3 hPa d^{-1}, and remains mainly within the higher northern latitudes (Fig. 5.13 (b)). For S. America, C2 is the most commonly occurring trajectory type (50%) and also displays the fastest descent at 23.6 hPa d^{-1}, followed by an increase in altitude. Trajectory clusters C1–C3 for S. America continue to support the tendency highlighted by Frömming et al. [36] and Rosanka et al. [37], namely that a faster initial descent will yield larger O_3 maxima until washout after reaching the minimum in altitude. For Eurasia, all trajectories exhibit similar vertical profiles with relatively low rates of descent compared to C2 in Eurasia during January–March 2014. The mean O_3 perturbations are, as expected, larger than during January, likely due to differences in exposure to solar radiation, and are greatest for C2, which also boasts the largest $\overline{RF}$ in Eurasia among both seasons. For Africa, C2 is the main trajectory (40%), which translates to having most of the emissions quickly descend to lower altitudes and exhibiting the largest O_3 maxima along the way, until some of the altitude is recovered. Lastly, for Australasia, the most probable path for an air mass is no longer characterized by a gradual vertical decrease like in cluster C3 during January but now shows a shorter residence time (cluster C2 occurring 46% of the time). The overall decrease in solar radiation towards the lower latitudes is reflected by the lower $\overline{O}_3$ of the air parcel trajectories that are closer to the Equator (Fig. 5.13 (b)). The mean RF contributions per region and per cluster for NO_x emissions in July may be found in Table D.2.

Similar to what was stated earlier for the clustering results in Sub-section 5.4.1 for January, it is still clear that the atmospheric circulation strongly influences the geometry of the horizontal distributions shown in Fig. 5.13 (b) for July. The intensity of the wind field in Fig. D.7 (c), however, is much smaller for the northern zonal jet compared to January, and the southern zonal jet is stronger relative to January. Due to this weaker jet stream in the north, not all air parcel trajectories become constrained along the latitudinal band in which they act. Different transport patterns that now reach the lower tropics and mid-tropics arise for N. America, as can be seen by clusters C2 and C3, together representing almost 50% of trajectories. The southern zonal jet again strongly influences the transport for S. America (cluster C3) and Australasia (clusters C2 and C3).

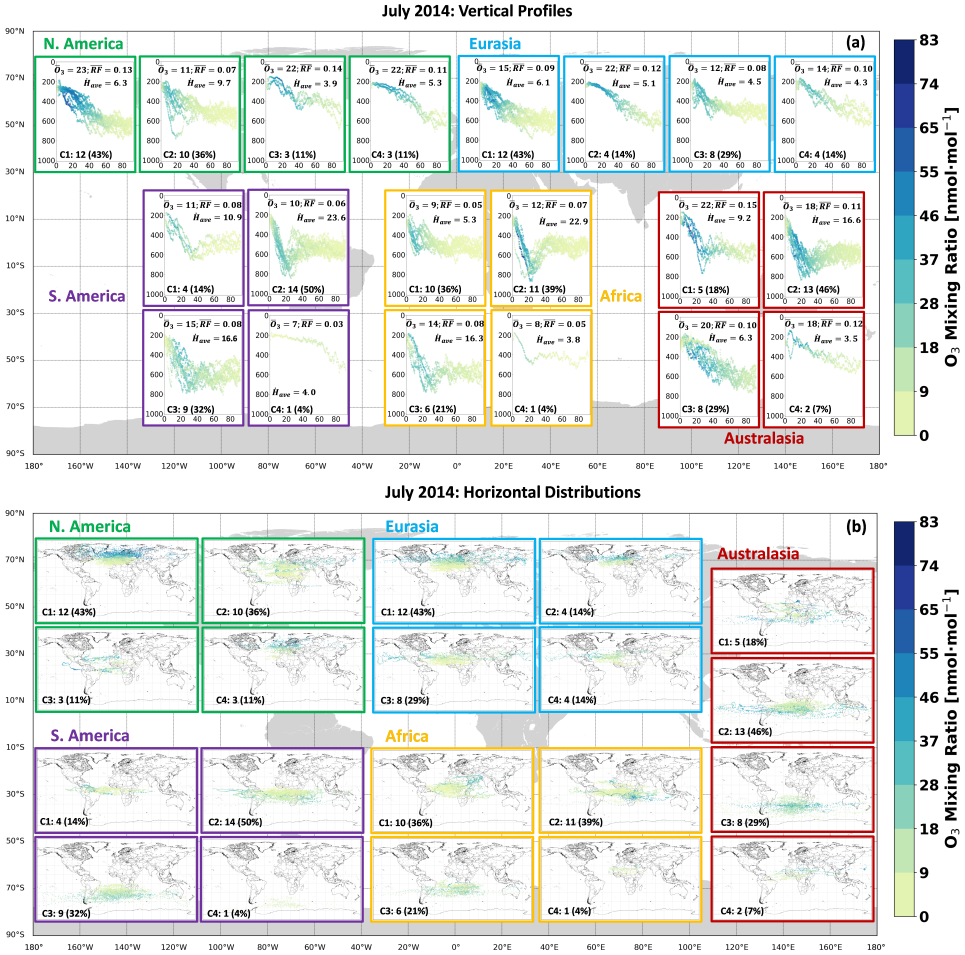


Figure 5.13: (a) Vertical profile of clusters of NO_x transport pathways during July 2014. The color bar represents the mean O_3 disturbance in nmol mol^{-1} caused by the emission transported along a median trajectory. Each 'C' represents a distinct and independent cluster; i.e., C1 from N. America is not related to C1 from S. America. Each cluster label is followed by the number of median trajectories that it comprises, both in absolute and relative terms. The 90-day mean rate of descent in hPa d^{-1} for all median trajectories in a cluster is defined as $\dot{H}_{ave}$. The cluster radiative forcing contribution in mW m^{-2} is labeled as $\overline{\text{RF}}$, and $\overline{O}_3$ is the mean disturbance of the median trajectories in nmol mol^{-1}. Panel (b) uses the same notation but for the horizontal distributions. The axes for (a) are defined in Fig. 5.7 (a) and (b), while the axes for panel (b) are specified in Fig. 5.7 (c) and (d). Meteorological conditions considered are specific to the period 1 July - 30 September 2014.

5.4.3. SPATIAL VARIATION OF RADIATIVE FORCING

This sub-section presents the global RF associated with emissions in each region and the source–receptor relationships between them. The RF shown here represents the difference between the scenario in which an additional NO_x perturbation (5×10^5 kg (NO) per emission point) is introduced and the base scenario in which no aircraft NO_x emissions were added at 250 hPa. As a comparison, this NO_x perturbation in each emission point represents about 40% of the mean total yearly NO_x emitted by commercial aviation in N. America (as defined by the boundaries in Fig. 5.1) between the years 2017–2020 at a pressure altitude of 250 hPa [192].

GLOBAL RADIATIVE FORCING - MOST SIGNIFICANT EMITTER

The RF from the emitting regions of Fig. 5.1 is shown in Fig. 5.14. An aircraft emitting NO_x near Australasia is most likely to induce a larger (by a factor of 2.7) climate warming during January–March as well as during July–September (by a factor of 1.2) compared to an emission in Eurasia during the same months. Flying near Eurasia and N. America during January would, on the other hand, lead to the smallest climate impact globally. The seasonal switch of $\overline{RF}$ between January and July is apparent in all regions. This suggests that, when considering only the short-term O_3 increase from NO_x, flying over the North Atlantic in January (local winter) will lead to a RF that is almost half compared to the one induced in July (local summer). In other words, the RF is larger when flying in their respective summer seasons (or dry season for the tropics) for all regions.

These results agree with those of Skowron et al. [196], who also performed a global study (regional breakdown includes Europe, N. America, Southeast Asia, N. Pacific, N. Atlantic, Brazil, South Africa and Australia) with the MOZART-3 CTM to understand the RF from aircraft NO_x emissions. Cooling effects from CH_4, SWV reductions, long-term O_3 considerations (PMO) and lastly warming from the short-term increase in O_3 were studied. Although Australia did not have the highest net NO_x effect, it did exhibit the largest warming from short-term O_3 effects, as is also seen in Fig. 5.14. The reason for this, compared to other regions, is the larger solar input and reduced background NO_x concentrations in the Australasian region, which then leads to an enhanced O_3 production efficiency. Research by Gilmore et al. [34], using the GEOS-Chem adjoint CTM, also helps to justify this result by noting that flights originating from Australia presented the most elevated O_3 burdens due to the larger O_3 production sensitivities to additional NO_x emissions.

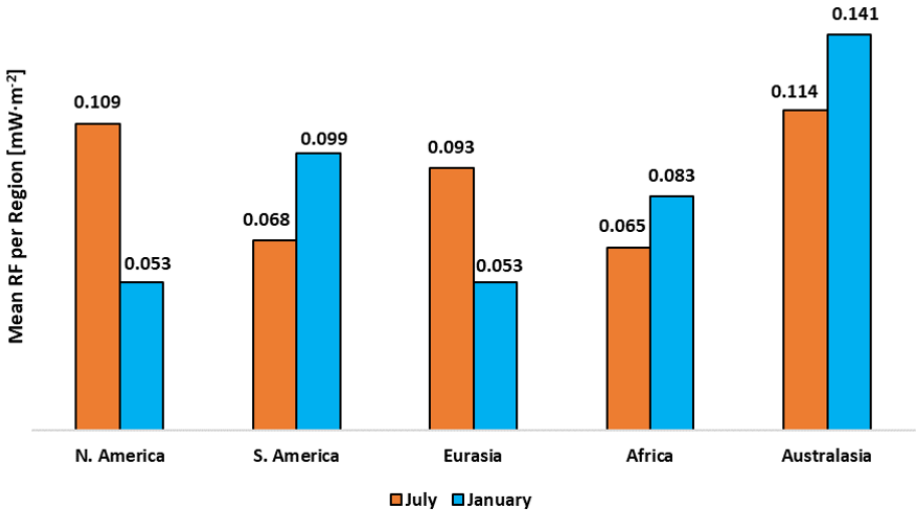


Figure 5.14: Mean RF in mW m^{-2} by region of emission during January and July of 2014 for a 5×10^5 kg (NO) emission.

GLOBAL RADIATIVE FORCING - REGIONS IMPACTED (RECEPTORS)

The degree of the impact by emissions released from each of the five source regions (Fig. 5.1) on the nine receptor regions defined by Fig. 5.2 is studied in terms of $\overline{RF}$. The RF distribution is summarized in Table 5.2.

Table 5.2 highlights the notion that the area that will be most affected by an emission will not necessarily coincide with its area of emission. As an example, NO_x emitted in N. America in July will induce the largest climate impact in Europe, with a value of 0.295 mW m^{-2}, the second largest in the Northern Trans-Atlantic (NTA) with 0.220 mW m^{-2}, and followed finally by its original emission region, with an $\overline{RF}$ of 0.205 mW m^{-2}. This is likely owed to the fact that NO_x-carrying air parcels spend more time during their peak O_3 production per unit area within Europe (5.52×10^{-4} h km^{-2}) than in any of the other receptor regions (see Table 5.3). For N. America during an emission on 1 July 2014, Fig. 5.15 (e) estimates that the maximum O_3 production occurs between 14.25 and 20 days after emission. Compared to the Northern Trans-Atlantic region, which bears the second largest $\overline{RF}$ impact, air parcels during this time interval spend 15% more time per square kilometer in Europe, as is shown by Table 5.3. This implies that NO_x removal rates, which set the time for the peak location of the O_3 production curve, along with the strong westerlies in the Northern Hemisphere, may cause a regional emission to induce a larger $\overline{RF}$ effect farther away from its source. A similar example would be an emission in Australasia in January producing a stronger $\overline{RF}$ signature in S. America (0.225 mW m^{-2}) compared to its own region of emission (0.200 mW m^{-2}). This impact on S. America by Australasia is even stronger than the effect of an emission from S. America itself, with $\overline{RF}$ values of 0.132 and 0.148 mW m^{-2} during July-September and January-March, respec-

tively. This may, in part, be explained by the increased amounts of O_3 produced near the Australasian region due to its production efficiency, that are then transported by dominant westerlies to neighboring areas (Fig. D.7). A study by Quadros et al. [12], using the GEOS-Chem CTM, also concluded the existence of pronounced cross-regional impacts for ground-level $PM_{2.5}$ and O_3, wherein for instance, an emission in Europe would induce larger impacts in Asia than an emission within Asia itself. It is also worth highlighting again that transhemispheric effects are limited; i.e., emissions occurring in the Northern Hemisphere will mainly impact regions in the same hemisphere, and the same applies to the Southern Hemisphere.

Table 5.2: Source-receptor matrix. Receptor regions defined according to Fig. 5.2. NA: North America, NTA: Northern Trans-Atlantic, SA: South America, EU: Europe, AME: Africa and Middle East, AS: Asia, AUS: Australasia, NTP: Northern Trans-Pacific, STP: Southern Trans-Pacific. Results are for a 5×10^5 kg (NO) emission. The figures in bold represent the maximum RF values attained at a receptor for a given source.

			Receptor									
	Mean RF [mW m^{-2}]		NA	NTA	SA	EU	AME	AS	AUS	NTP	STP	Global
Source	N. America	Jan–Mar	0.112	**0.113**	0.014	0.109	0.033	0.086	0.005	0.105	0.007	0.053
		Jul–Sep	0.205	0.220	0.039	**0.295**	0.056	0.178	0.020	0.186	0.025	0.109
	S. America	Jan–Mar	0.026	0.033	0.148	0.008	0.151	0.055	**0.157**	0.030	0.132	0.099
		Jul–Sep	0.012	0.020	**0.132**	0.003	0.096	0.012	0.109	0.008	0.110	0.068
	Eurasia	Jan–Mar	0.101	0.123	0.008	**0.132**	0.026	0.087	0.004	0.113	0.007	0.053
		Jul–Sep	0.192	0.190	0.020	**0.218**	0.042	0.128	0.014	0.217	0.019	0.093
	Africa	Jan–Mar	0.063	0.071	0.095	0.036	**0.124**	0.081	0.086	0.070	0.077	0.083
		Jul–Sep	0.016	0.036	0.083	0.009	**0.143**	0.028	0.096	0.016	0.064	0.065
	Australasia	Jan–Mar	0.050	0.054	0.225	0.016	0.147	0.058	0.200	0.084	**0.259**	0.141
		Jul–Sep	0.016	0.032	0.178	0.008	0.160	0.025	0.192	0.024	**0.206**	0.114

Table 5.3: Total time spent by all air parcels within a receptor region (Fig. 5.2) during their maximum O_3 peak production period (between 14.25 and 20 days upon emission), as estimated by the O_3 production curve for N. America during a NO_x emission in July 2014 (Fig. 5.15 (e)). This total is then scaled by the respective area to allow for a direct comparison across all receptors. In these estimates we account for the 1400 NO_x-carrying air parcels released from the 28 emission points for N. America in July (Fig. 5.1). The percentage values in parentheses represent in relative terms the total time spent by air parcels during peak O_3 production for each receptor.

Receptor	Area (10^7 km^2)	Total time spent by air parcels during peak O_3 production in hours (h)	Total time spent by air parcels in peak O_3 production per km^2 (10^{-4} h km^{-2})
NA	7.28	34 062 (16.9 %)	4.68
NTA	3.40	16 344 (8.1 %)	4.80
SA	9.70	7662 (3.8 %)	0.79
EU	4.32	23 826 (11.8 %)	5.52
AME	9.81	21 528 (10.7 %)	2.2
AS	8.89	47 676 (23.6 %)	5.36
AUS	13.3	744 (0.4 %)	0.56
NTP	9.28	47 238 (23.4 %)	5.09
STP	9.70	2520 (1.3 %)	0.26

5.5. DISCUSSION

The first research question that this chapter addresses pertains to the identification of the main transport pathways of gas-phase emitted species (NO_x) in the form of clusters across five representative regions (N. America, S. America, Eurasia, Africa and Australasia) and how they are affected by factors like the location of release, seasonality and meteorological conditions. Distinct patterns in emission trajectories were systematically found with the QuickBundles clustering algorithm based on their positional variables (altitude and latitude) and mean RF. As a second objective, the heterogeneity in the repercussions of different transport patterns on the atmospheric composition of O_3 and the consequent RF was studied. The short-term $\overline{RF}$ of the five emission regions and the main areas of impact are examined from a global, non-clustered perspective. Considering these results, the viability of the QuickBundles algorithm in atmospheric modeling, the main drivers behind the spatiotemporal heterogeneity of short-term NO_x effects and, finally, some limitations of the simulation outcomes will be discussed.

QuickBundles adds value to this chapter by facilitating the identification of transport patterns while also accounting for their climate impact in a systematic manner. One of the main methodological novelties presented here is the integration of this clustering algorithm that enables the consideration of positional and radiative changes per trajectory via a new distance function shown in Eq. 5.1. Although QuickBundles, in general, has consistently categorized trajectories based on their positional and radiative changes, there are cases in which one or two trajectories appear to be misplaced. One such example is cluster C3 from Eurasia during July in Fig. 5.13 (a), in which two of the trajectories display a faster rate of descent compared to the rest of the group. This cluster C3 may also appear misleading at first, since it mostly contains trajectories that descend downward earlier, than say cluster C2 with an $\dot{H}_{ave}$ of 5.1 hPa d^{-1}, and yet quantitatively it has a slower average rate of descent ($\dot{H}_{ave}$ of 4.5 hPa d^{-1}). This highlights how the definition given by Eq. 5.3 may, in cases in which most trajectories reach a value close to their minimum altitude early on and then proceed to gradually and continually descend to slightly lower altitudes until the remaining 90 days, prove to be misleading when comparing vertical transport patterns of median trajectories. As was briefly mentioned in Sub-section 5.3.1, one possible improvement would be to define an initial rate of descent in which only the first 40 or so days are considered. Another limitation is the small-density clusters comprising a single median trajectory in certain cases like C4 in Africa during July, which would appear to have been better placed in C1 based on the similarities in $\overline{RF}$, $\dot{H}_{ave}$ (Fig. 5.13 (a)) and their latitudinal range (Fig. 5.13 (b)). Such shortfalls may be addressed in a future study potentially by introducing weights to each of the three terms of Eq. 5.1, as was done similarly by Corrado et al. [204] in their clustering of aircraft trajectories with a weighted distance function. It is worth noting, however, that some single-trajectory clusters like C4 in S. America during July 2014 (Fig. 5.13 (a)) are justified, given their unique nature relative to the rest of the clusters. The robustness of the clustering also needs to be further investigated in terms of the determination of the optimal cluster number. Kassomenos et al. [209], in their calculation of the optimal cluster number for the K-means method, stress the volatility of this value based on one's choice of evaluation metric as well as on the method, like trial and error with manual verification. The optimal value found in this chapter, which is calculated based on

the L-method, is likely to vary if another method is employed, like the combined use of the sum of squared errors (SSE) with the silhouette coefficients, as was done by Li et al. [208]. Another important note on the robustness of the clustered results pertains to the strong dependence of the horizontal transport distributions on the atmospheric circulation, i.e., on the wind field and more specifically on the dominant westerlies in both the Northern and Southern Hemispheres. This implies that during an event with more extreme weather conditions, the clusters produced are likely to differ significantly from the ones obtained under more regular meteorological conditions. It is unlikely, however, that current results were significantly biased by any particular event with more drastic wind conditions. In 2014, for instance, the El Niño–Southern Oscillation (ENSO) was unlikely to have conditioned the clustering since its occurrence is considered to have been thwarted that year by a pronounced easterly [218].

The results presented here largely agree with those of other studies that have investigated the short-term effects of the NO_x–O_3 dynamic. A strong spatial dependence of NO_x emissions was found, arising from the differing meteorological conditions at the location as well as the level of background NO_x concentrations. Frömming et al. [36], who also use a similar simulation setup in the EMAC model, found a strong dependence between the ensuing transport pattern and a trajectory's proximity to areas of elevated subsidence and pressure. The current study also found a similar correlation with emission points 8 and 14 during January (Fig. 5.9). The former air parcel is initiated within a pronounced meridional tilt of a northern westerly, while the latter is directly placed within said westerly but outside of the tilt. From Fig. D.8 (a), it is evident that the trajectory consists of an initial southern shift resulting from the tilt until it reaches a region of stronger downdrafts near 85° W and 35° N, as can be seen in Fig. D.7 (b). The trajectory from emission point 14, however, experiences an almost direct downward motion, as it is released in the same region of larger subsidence and remains constrained within the latitude band of the northern westerly. The significance of zonal jet streams in the transport of pollutants has also been noted by Barrett et al. [219], with a transport pattern close to their Fig. 2 arising in Fig. D.8 (a). The finding of augmented O_3 production and $\overline{RF}$ in areas of reduced background NO_x concentrations like Australasia (Fig. 5.14) has also been found in past studies [32, 34, 196] that have confirmed larger instantaneous RF from O_3 and CH_4 in areas of lower background NO_x. It was also found that due to the existence of zonal jet streams, the regions impacted by an emission can vary largely from its origin, as has also been stated by Quadros et al. [12] in the context of air quality. Table 5.3, along with Fig. 5.15 (e), also imply that the time taken to reach the peak O_3 production (which is influenced by NO_x removal rates) along with the total duration spent by NO_x-carrying air parcels during this interval may also contribute towards producing an $\overline{RF}$ impact larger than near the emission source itself. Latitudinal variations for the different seasons are consistent with a recent assessment by Derwent et al. [220].

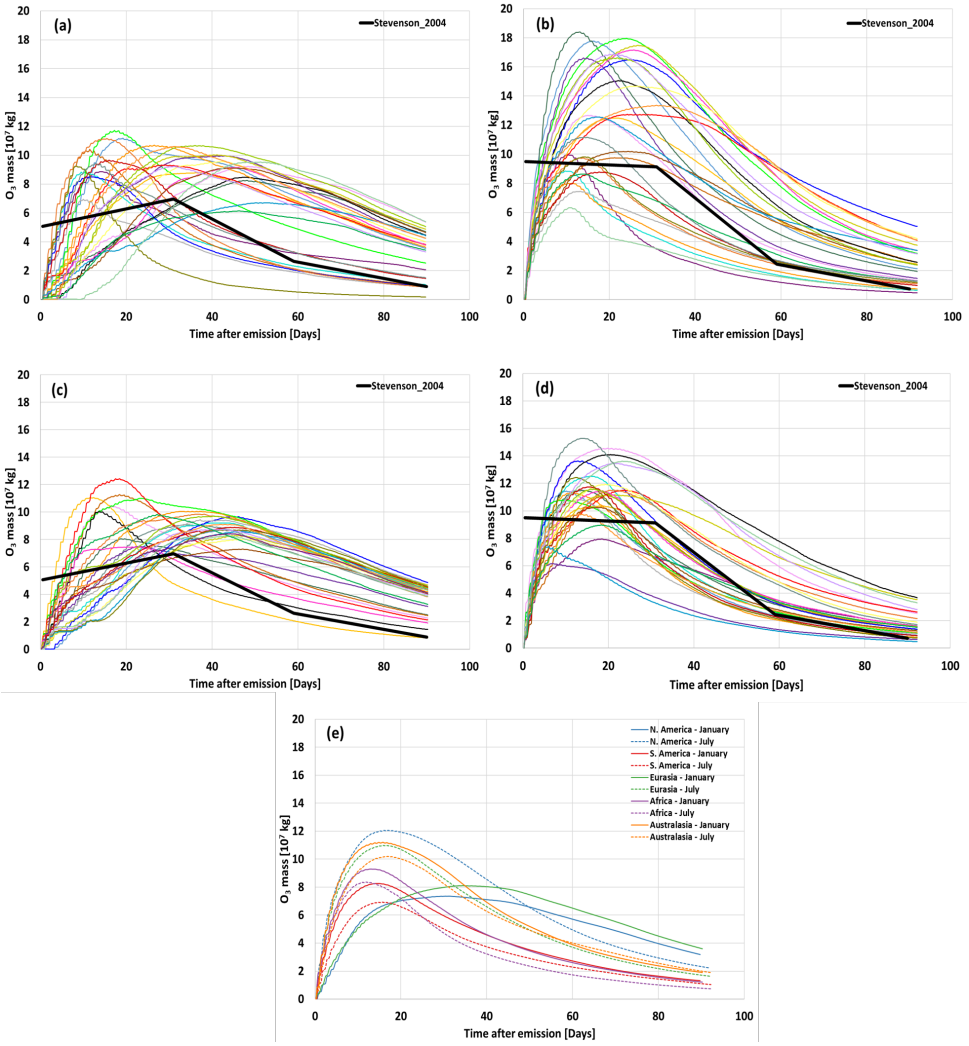


Figure 5.15: The colored lines represent the mean temporal evolution of the NO_X-induced short-term O_3 mass, in kilograms, across 50 air parcel trajectories that are initialized in each of the 28 emission points for N. America during January (a) and July (b) as well as for Eurasia during January (c) and July (d). The thicker dark line represents scaled results from Stevenson et al. [35] to adjust to the same initial NO_X that is released in this study. The scaling factor for a January NO_X emission is 6.97×10^{-3} and for a July NO_X emission is 1.22×10^{-2}. The O_3 averaged across all 28 emissions for each region and season is represented in (e).

Seasonality is another driving factor behind the type of transport and consequent O_3 disturbances and RF. This study finds that, during the Northern Hemisphere winter for instance, there is increased solar radiation in the lower latitudes near the tropics, which then translates to larger $\overline{RF}$, as is seen for the southern regions (S. America, Africa and Australasia) of Fig. 5.12. During the Northern Hemisphere summer, this effect is inverted as the largest $\overline{RF}$ occurs for the northern regions (N. America and Eurasia), as they benefit from increased solar radiation now in the upper northern latitudes. This agrees with past studies [33, 36, 38].

The tagging contribution calculations performed by AIRTRAC are based on the linearization of the inherently nonlinear background chemistry computed by MECCA (see Appendix A). This means that AIRTRAC considers nonlinear chemical production and loss terms from the background, but linearly scales them in proportion to the amount of aviation-emitted NO to calculate the contribution of relevant tagged species at each time step and grid point [23]. Additionally, these computations are carried out independently from other emission points, and as a result there are no second-order feedback effects considered relative to the background chemistry. This linearization of nonlinear chemical processes, such as the NO_x–O_3 interaction, makes a direct inter-comparison with other models challenging. The background chemistry from MECCA itself, however, has already been evaluated by Jöckel et al. [221] against observations from 1983–2001 of Emmons et al. [222]. Mixing ratios of NO for the simulation year of 2000 were compared to these observations to reveal good skill in the simulated output, having concluded that there is a tendency for the largest NO_x mixing ratios to be underestimated likely due to a lack of NO_x sources and/or an excessively rapid conversion to HNO_3. Further validation of the background reaction rates, some of which are used by AIRTRAC, have also been performed by Pozzer et al. [223]. The distribution of background O_3 volume mixing ratios simulated by EMAC in the UTLS was recently evaluated against aircraft in-situ measurements from the In-service Aircraft for a Global Observing System (IAGOS) campaign by Pletzer et al. [124]. This comparison showed strong agreement between model and aircraft O_3 data (correlation coefficient ~0.95), with a slight mean underestimation of the O_3 column by the model (~10%). Additionally, in the upper stratosphere, the multi-annual mean O_3 profile from EMAC was compared to satellite observations, revealing only a minor average model overestimation of approximately 5% [125]. Similarly to Grewe et al. [23], the resulting O_3 disturbance fields from AIRTRAC are compared with past research from Stevenson et al. [35]. Figure 5.15 shows how their results are well constrained within the variation of AIRTRAC's O_3 mass curves for N. America during January (Fig. 5.15 (a)) and July (Fig. 5.15 (b)) and for Eurasia during January (Fig. 5.15 (c)) and July (Fig. 5.15 (d)). It is also worth noting that large differences may result depending on the method (either tagging or perturbation) chosen to assess aviation's climate effects. A tagging or source apportionment method consists of finding the amount contributed by a certain emission source to the concentration of a chemical species while a perturbation analysis involves estimating the impact of an emission source on the concentration of a chemical species using two simulations. The differences between these methods has been discussed in detail in Chapter 4. Figure 5.15 (e) shows the O_3 mass temporal evolution averaged across all 28 emission points for each region and time period. Seasonal differences in the O_3 production are evident, and it is also clear that during January in

the Northern Hemisphere, the O_3 production peak is lower and occurs later relative to all other scenarios.

In terms of other limitations of this study, the robustness of the results and of the clustering has not been tested for emission altitudes other than 250 hPa, to verify how the O_3 production and $\overline{RF}$ vary with altitude. Emissions at other times during the day, other than at 06:00 UTC, would also be interesting in order to assess diurnal effects as well as emissions during other representative days to determine how these results would change for other meteorological situations. A full seasonal analysis with emissions during spring and autumn would therefore be worthwhile. Findings from this chapter are specific to meteorological conditions from two time periods in 2014: January–March and July–September in 2014. Studying emission points in regions near the Indian Ocean, India and China as well as the North Atlantic may reveal additional transport patterns. There are also two emission points (21 and 28) from N. America during January in which the 50 air parcels did not equally transport the emitted NO_x, likely due to the randomized initialization of the trajectories within the grid cell. Figure 5.6 (a) depicts these points as outliers. For a more complete assessment needed for mitigation considerations, other non-CO_2 drivers should be considered, like the decrease in PMO and CH_4, aerosol indirect effects and contrail climate impacts, as well as H_2O. Lastly, the current resolution of T42L41 was chosen as a compromise between resolution and computational cost, and a more detailed inspection of the vertical transport for air parcels via a setup with a higher vertical resolution like T42L90MA may provide further insight into the advective and convective impacts on the trajectories across the different regions.

5.6. SUMMARY AND CONCLUSIONS

This chapter has assessed the influence of location and seasonality on the transport pathways and climate effects of aircraft NO_x emissions on a global level, using Lagrangian simulations with the EMAC model. The focus has been on the RF arising from the short-term increase in O_3. A clustering algorithm, called QuickBundles, was integrated into the workflow to more efficiently identify the different types of air parcel trajectory groups based on their position (altitude and latitude) as well as on their climate impact ($\overline{O_3}$ and $\overline{RF}$). To the author's best knowledge, this approach has never been used with GCM results. The outcome of the clustering itself provides a global overview of the possible transport paths that gas-phase emission species may take and their likelihood given the specific meteorological conditions of January–March and July–September 2014.

Results have shown a strong dependence between the location of emission and the ensuing transport type, which is influenced by the wind field. Two dominant zonal jets or westerlies were identified in both the Northern and Southern Hemispheres and have proven to dictate air parcel motion along the horizontal direction. An emission occurring in proximity with the meridional tilt of a westerly will tend to travel to the south along the tilt and then stay constrained within the latitudinal band of the jet, while one initialized outside of the tilt will immediately remain constrained to this latitudinal range. Residence times throughout 90-day simulations are also inferred, and it is seen that northern emissions (N. America and Eurasia) spend about 40 days in the northern midlatitudes and then around 20 days in the Tropics. For emissions in the southern regions (S. America, Africa and Australasia), ~50% of the lifetime of the trajectories is spent within

the Tropics. It was also statistically confirmed that trajectories with a faster downward transport will on average produce less O_3 given that NO_x removal rates are larger at lower altitudes. Seasonality plays an important role in understanding when certain types of trajectories would have larger O_3 perturbations and RF. During Northern Hemisphere summer (July), air parcels near the higher latitudes will produce more O_3 than those to the south, given the more active photochemistry due to more incoming solar radiation. The opposite is true for winter (January). Globally speaking, NO_x emissions from Australasia are likely to yield the largest climate impact, given their enhanced potential to form O_3 in lower-NO_x backgrounds. A source–receptor analysis has determined that an emission at a given location may induce a larger climate effect onto a neighboring region. Overall, all distinct transport pathways have been summarized per cluster for each region based on their O_3 disturbance and $\overline{RF}$ signatures.

The results obtained here have the potential to contribute to climate-optimized aircraft operations by expanding the CCFs. Frömming et al. [36] have recently produced CCFs for contrail cirrus, aviation-induced O_3 by NO_x emissions, total NO_x effects (O_3, CH_4 and PMO effects) and H_2O for the North Atlantic during the winter and summer seasons. Since CCF calculation is intensive in terms of computational cost, it is not viable to directly integrate them into flight planning tools. To address this shortcoming, the aCCFs were developed [46]. This chapter therefore provides additional data points that may be applied towards expanding current aCCFs, which focus mainly on the North Atlantic flight corridor, to other regions like Eurasia, Africa, Australasia and S. America. Chapter 7 discusses how AIRTRAC has contributed to the development of a new generation of CCFs called paCCFs.

5.7. ACKNOWLEDGMENTS

We would like to express our gratitude to Sabine Brinkop from DLR (German Aerospace Center), who was kind enough to share her expertise regarding the EMAC submodels, particularly with ATTILA, and to Alina Fiehn, also from DLR, for providing an internal review.

This work made use of the Dutch national e-infrastructure with the support of the SURF Cooperative (grant nos. EINF-441 and EINF-2734).

5.8. DATA AVAILABILITY STATEMENT

The Modular Earth Submodel System (MESSy) is continuously being further developed and applied by a consortium of institutions. The usage of MESSy and access to the source code is licenced to all affiliates of institutions which are members of the MESSy Consortium. Institutions can become a member of the MESSy Consortium by signing the MESSy Memorandum of Understanding. More information can be found on the MESSy Consortium website (http://www.messy-interface.org, last access: 1 November 2021). The code presented here has been based on MESSy version 2.55 and will be available in the next official release (version 2.56).

The QuickBundles clustering code is openly available at https://dipy.org [224].

EMAC simulation output data that were produced and analyzed in this paper are openly available at https://doi.org/10.4121/16886977.

Supplementary figures S1-S60 are included in the following data repository: https://doi.org/10.4121/20338212.

6

DEVELOPMENT AND APPLICATION OF A NEW LAGRANGIAN SO_4 TAGGING METHOD

AIRTRAC 2.0 represents the latest advancement in the Lagrangian tagging submodel AIRTRAC, developed within the EMAC modeling framework. This release introduces expanded capabilities for quantifying the impacts of aviation-induced SO_2 and H_2SO_4 emissions on SO_4 aerosol formation and transport. Through detailed analysis of SO_4 pathways, AIRTRAC 2.0 facilitates the identification of atmospheric regions where enhanced SO_4 mixing ratios increase the likelihood of aerosol-cloud interactions at lower altitudes. This functionality is exemplified by combining cloud satellite data from the European Space Agency (ESA). Overall, these newly added capabilities can offer valuable insights into the transport of aviation sulfate and its probability of impacting low-level cloud microphysical properties.

Parts of this chapter will be submitted to the Geoscientific Model Development journal [142].

6.1. INTRODUCTION

RECENT estimates suggest that in 2018, aviation was responsible for approximately 2% of global anthropogenic radiative forcing from CO_2 emissions alone [28]. When considering additional non-CO_2 effects, aviation's contribution rises to around 3.5% of total anthropogenic warming—equivalent to roughly 150 mW m^{-2}, with a 90% confidence interval of [70–229] mW m^{-2} [27]. This more encompassing estimate, however, carries significant uncertainties due to the intricate interactions and tradeoff effects between various climate forcers, including NO_x, H_2O, and contrails. It accounts for the direct warming effect of soot aerosols and the cooling effect of SO_x emissions, but excludes indirect cooling effects via cloud interactions. Furthermore, Lee et al. [27] do not include the potential influence of aviation NO_x on SO_4 and NO_3 aerosol formation, both of which may contribute with substantial cooling [120].

Notably, the indirect cooling effect of SO_4 aerosols alone could reduce aviation's net radiative forcing considerably. Some estimates indicate that this cooling could match or even exceed the largest warming impact from contrails, estimated at around 100 mW m^{-2} [27, 225]. One study further proposes that the total cooling effect from both direct and indirect SO_4 forcing may surpass the warming associated with aircraft-induced cirrus [226]. These combined effects introduce the possibility of a near-zero or even negative RF from kerosene-powered aviation. However, this outcome is speculative and highly uncertain due to complexities in quantifying SO_4 indirect effects. More robust estimates, generated by independent models and informed by a deeper understanding of critical factors like pollutant transport patterns, are crucial. Without clearer insights into these climate forcers, effective development and evaluation of mitigation strategies will remain challenging.

Aerosols are collections of solid or liquid particles suspended in the atmosphere, with sizes ranging from 0.001 μm to 100 μm [97, 110]. Among the primary aerosols resulting from aviation are soot and sulfate. Soot is produced by the incomplete combustion of aromatic compounds in jet fuel [27, 227], while SO_4 forms indirectly from the emissions of SO_2 and H_2SO_4. Experimental studies indicate that aircraft convert approximately 97% of the sulfur content in fuel into SO_2, with SO_2 emissions nearly directly proportional to fuel sulfur levels. The remaining 2–3% is emitted as H_2SO_4 [228–230]. The gas-phase conversion of SO_2 to H_2SO_4 involves a series of reactions (R22 - R24), where the oxidation of SO_2 by OH radicals ultimately results in the production of H_2SO_4 [231]:

$$SO_2 + OH \longrightarrow HSO_3 \tag{R22}$$

$$HSO_3 + O_2 \longrightarrow SO_3 + HO_2 \tag{R23}$$

$$SO_3 + 2H_2O \longrightarrow H_2SO_4 + H_2O\cdot \tag{R24}$$

The formation of SO_4 aerosols can proceed through multiple mechanisms. One pathway involves the condensation of H_2SO_4 vapor onto pre-existing particles, followed by particle growth through coagulation and further condensation [101, 232, 233]. SO_4 aerosols may also form via binary homogeneous nucleation between H_2SO_4 and H_2O, a process influenced by factors such as atmospheric relative humidity and temperature [100, 111].

Additionally, SO_4 production can occur through the reaction of H_2SO_4 with gaseous ammonia (NH_3), resulting in the formation of ammonium sulfate ($(NH_4)_2SO_4$) or ammonium bisulfate (NH_4HSO_4), which subsequently dissociate to yield SO_4, ammonium (NH_4), and hydrogen [234]. An alternative pathway involves the liquid-phase oxidation of sulfurous acid (H_2SO_3) by hydrogen peroxide (H_2O_2) [235, 236]. Figure 6.1 illustrates the primary reaction mechanisms leading to SO_4 formation via SO_2 and H_2SO_4.

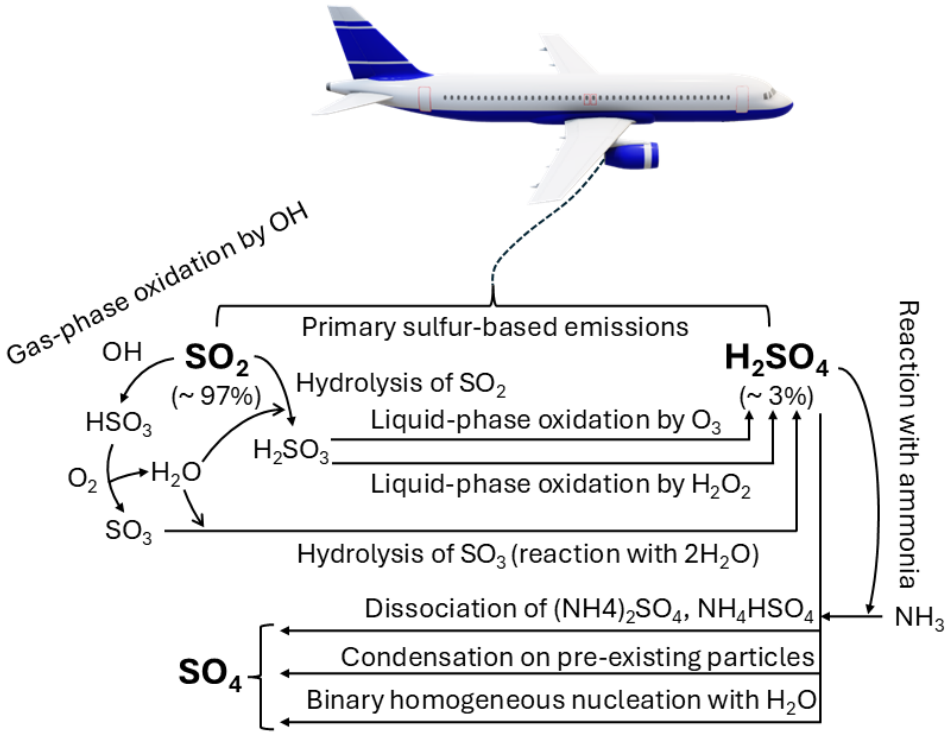


Figure 6.1: Production mechanisms of sulfate (SO_4) from aviation emissions of sulfur dioxide (SO_2) and sulfuric acid (H_2SO_4).

Aerosols directly impact Earth's energy balance by scattering and absorbing solar and infrared radiation, depending on their optical properties. Sulfate aerosols primarily scatter incoming shortwave solar radiation, resulting in a cooling effect, whereas soot particles predominantly absorb this radiation, leading to a warming effect [27, 130, 237]. In addition to these direct effects, aerosols also have indirect effects through their influence on cloud microphysical properties, such as albedo and lifetime. These effects are known as the Twomey and Albrecht effects, respectively, and are discussed in Chapter 2. In Chapter 6, the focus is specifically on SO_4 aerosols, which are known to be highly efficient cloud condensation nuclei (CCN) for liquid clouds. In contrast, soot is less hygroscopic and generally only acts as a CCN when internally mixed with more hygroscopic aerosols, such as SO_4 [27, 42].

The significantly greater uncertainties in estimating SO_4 indirect effects, as opposed to direct effects, arise from several factors. One primary challenge is accurately modeling complex cloud microphysical processes, which occur on sub-grid scales and often require parameterization [132, 135]. Additionally, limited understanding of aerosol transport pathways—including vertical transport and large-scale horizontal advection—and the variations in microphysical and removal processes along these paths contribute to this uncertainty [43, 44]. These transport dynamics are particularly relevant in the context of aviation emissions, which occur at higher altitudes than ground-level sources such as shipping. Model intercomparison studies, such as the Comparison of Large Scale Sulfate Aerosol Models (COSAM), have demonstrated that the conversion of SO_2 to SO_4 is challenging to predict, resulting in model variability of 10–50% and discrepancies of up to a factor of two compared with observational data from aircraft campaigns. These variations lead to uncertainties not only in the vertical distribution profiles of SO_4, but also in the resulting number of cloud condensation nuclei (CCN) produced, both of which directly influence estimates of SO_4 indirect forcing [43, 238]. Consequently, these knowledge gaps have prevented Lee et al. [27] from providing a best estimate of aerosol indirect effects in their comprehensive assessment (see Fig. 1.2).

The studies summarized in Table 4 of Haywood and Boucher [239] provide a range of estimates for anthropogenic SO_4 direct and indirect effects, with the latter spanning from -30 mW m^{-2} to -178 mW m^{-2}. However, few studies have specifically quantified these effects from an aviation perspective. Righi et al. [225] assessed both direct and indirect SO_4 effects across the transport sector (land, shipping, and aviation) and estimated aviation's contribution to range from -69.5 mW m^{-2} to 2.4 mW m^{-2}. They found that larger SO_4 particle sizes resulted in weaker cooling effects. Similarly, Gettelman and Chen [226] investigated the influence of particle size on RF indirect effects, noting that the smallest particles (8 nm diameter) led to the strongest cooling at -160 mW m^{-2}.

Kapadia et al. [240] examined how variations in aircraft fuel sulfur content (FSC) affect the Twomey effect and found that higher sulfur content produced more pronounced cooling effects. Specifically, they reported that an FSC of 6000 ppm yielded an RF of -82.1 mW m^{-2}, while sulfur-free fuel reduced this value to -16.6 mW m^{-2}. Although outside the scope of this chapter, Kapadia et al. [240] highlighted an important policy consideration: while low-sulfur fuels reduce premature mortality linked to lower particulate matter ($PM_{2.5}$) emissions in the short-term, they also diminish cooling from indirect effects, which may exacerbate global warming in the long-term.

Matthes et al. [31] provide estimates of aviation-induced aerosol effects, considering both direct and indirect impacts as a function of cruise altitude. They applied the same simulation setup as Righi et al. [225], but replaced the CMIP5 emissions inventory with the REACT4C inventory [40]. For a reference cruise altitude, the study calculated an RF of -15.1 mW m^{-2}, finding that this cooling effect intensifies at lower altitudes and diminishes at higher cruise levels.

In a more recent study, Righi et al. [160] utilized the CMIP6 emissions inventory [241] for 2015 (updating results from Righi et al. [225] for 2000 that used the CMIP5 inventory from Lamarque et al. [242]) and estimated aviation's combined SO_4 direct and indirect effects at -64 mW m^{-2}. They also analyzed shared socioeconomic pathways (SSPs) for 2050 under an SSP2-4.5 scenario [243], where a forcing of 4.5 W m^{-2} is projected by 2100

relative to pre-industrial levels. Under this scenario, aviation's RF reached -126 mW m^{-2}. Table 6.1 provides an overview of the most recent studies on aviation-related SO_4 indirect effects.

Table 6.1: An overview of studies that have estimated RF from aviation-induced SO_4 direct and indirect effects. The * indicates the amount of emitted SO_2 as referred in the comprehensive study of Lee et al. [27]. **Emitted SO_2 in Tg estimated assuming an emission index of 0.8 g/kg of fuel [244]. FSC denotes fuel sulfur content.

Study	Emission details	Calculation method	RF estimate [mW·m^{-2}]
Righi et al. (2013) [225]	CMIP5 emissions (Lamarque et al. [242] for the year 2000. Emission varies from 0.0008 to 0.1216 Tg(SO_2)*.	Perturbation approach	Includes direct and indirect effects: RF = [-69.5, 2.4]
Gettelman and Chen (2013) [226]	Emission of 0.2257 Tg(SO_2)* for the year 2006.	Perturbation approach	Sensitivity of indirect effect to SO_4 particle sizes: RF (8 nm) = -160 RF (14 nm) = -44 RF (21 nm) = -22
Kapadia et al. (2016) [240]	Range of emission cases for the year 2000 (FSC levels): Large = 2.358 Tg(SO_2) Normal = 0.236 Tg(SO_2) Low = 0.006 Tg(SO_2) No sulfur = 0 Tg(SO_2).	Perturbation approach	Only Twomey effect: $RF_{Large\ FSC}$ = -82.1, $RF_{Normal\ FSC}$ = -23.6, $RF_{Low\ FSC}$ = -16.8, $RF_{No\ FSC}$ = -16.6
Matthes et al. (2021) [31]	Simulation setup identical to Righi et al. (2013) [225], but with the REACT4C emissions inventory for 2006 [40]. Emission ≈ 0.143 Tg(SO_2)**.	Perturbation approach	Includes direct and indirect effects: -15.1 (reference case of aircraft flying at their optimal altitude)
Righi et al. (2023) [160]	CMIP6 emissions (Feng et al. [241]) for 2015. Emission in 2015 ≈ 0.284 Tg(SO_2) [160].	Perturbation approach	Includes direct and indirect effects: RF_{2015} = -64 $RF_{SSP2\ 2050}$ = -126

Aviation's climate impacts are generally estimated using one of two main approaches: source apportionment or sensitivity analysis. The distinctions between these methods have been thoroughly examined in Chapters 3 and 4, primarily in the context of aviation NO_x-O_3 climate effects. According to Table 6.1 and to the best of the author's knowledge, aviation-specific SO_4 indirect effects have thus far only been approximated using the perturbation method. Righi et al. [160] highlight the difficulty in applying a tagging method for aerosols due to the challenges of tracking their complex liquid- and gas-phase transformations and cloud interactions.

Only a handful of Eulerian and Lagrangian sulfate tagging schemes exist. Eulerian model studies include Yang et al. [236], who used the Community Atmosphere Model (CAM) within the Community Earth System Model (CESM) framework to quantify global SO_4 contributions from 16 sources and assess both direct and indirect radiative forcing effects between 2010–2014. Other Eulerian approaches target regional impacts in China. For example, Wu et al. [245] utilized an online tagging method within the Nested Air Quality Prediction Model System (NAQPMS) to reveal that SO_4 levels in Shanghai were significantly influenced by non-local sources. Similarly, Itahashi et al. [246], employing the Particulate Source Apportionment Technology (PSAT) algorithm [247] with the sixth version of the Comprehensive Air quality Model (CAMx), assessed SO_4 contribu-

tions from 31 Chinese provinces and found that emissions from the central and northern regions notably affected sulfate levels in Taiwan, Korea and Japan. Lagrangian approaches include the study by Riccio et al. [248], which used the Hybrid Single-Particle Lagrangian Integrated Trajectory (HYSPLIT) model to show that $PM_{2.5}$ levels in Naples were substantially impacted by emissions from other parts of Europe and dust transport from the Sahara. Despite methodological differences, these studies highlight the influence of cross-territorial emissions on regional SO_4 levels as a result of long-range transport. None of these studies, however, have specifically characterized the global transport patterns of aviation SO_4 emitted from subsonic cruise altitudes.

This chapter addresses a critical knowledge gap by introducing the first Lagrangian aerosol tagging method for SO_4 within the EMAC modeling framework, enabling a detailed analysis of aviation SO_4 transport patterns. AIRTRAC 2.0 represents a significant advancement, extending the original Lagrangian AIRTRAC submodel (see the Supplement of Grewe et al. [23]) to incorporate aerosol processes along air parcel trajectories—capabilities unique to this updated version. Specifically, aerosol mixing ratios are computed using the extensively validated MADE3 submodel, while aviation-specific contributions are quantified by AIRTRAC. Previously, AIRTRAC was limited to the study of gas-phase emissions such as NO_x and H_2O [36], primarily aimed at quantifying their contributions to atmospheric concentrations of reactive nitrogen species (NO_y), including nitric acid (HNO_3), ozone (O_3), the hydroperoxyl radical (HO_2), hydroxide (OH) and methane (CH_4). This Lagrangian approach offers a substantial computational advantage over resource-intensive Eulerian simulations by enabling the simultaneous analysis of multiple emission scenarios (see Chapter 4). A comprehensive overview of the original version of AIRTRAC is provided in Chapters 3 and 4.

With AIRTRAC 2.0, a detailed dataset spanning two seasons (summer and winter) has been generated to examine the transport patterns of aviation-derived SO_2, H_2SO_4, and two modes of SO_4 (soluble Aitken and accumulation modes) [249]. The inclusion of additional modes is planned for future research. This chapter thus aims to (1) introduce the new Lagrangian aerosol tagging submodel from a technical standpoint, and (2) analyze the transport patterns of SO_4 produced by aviation emissions of SO_2 and H_2SO_4 at 28 points along current flight routes at a representative cruise altitude (240 hPa, approximately 10.6 km), while highlighting how transport patterns may vary across emission location and time. Additionally, satellite cloud data from ESA is used to exemplify AIRTRAC's potential in predicting the likelihood that aviation SO_4 will reach regions that are most likely to have lower-level liquid clouds. Finally, we attempted to validate this model by comparing its transport patterns with those generated by perturbation simulations conducted with EMAC.

6.2. MODELING FRAMEWORK

The main characteristics of the EMAC modeling setup applied in this chapter are summarized in this section. The emission conditions for the performed simulations are also described.

6.2.1. THE EMAC MODEL SETUP

The EMAC model is described in detail in Chapter 3. For the analyses presented in this chapter, the most relevant coupled submodels include MADE3, ATTILA, LGTMIX, MECCA, SCAV, DDEP, SEDI, and AIRTRAC. While some of these submodels are discussed in Chapter 3, the rest are briefly defined in the comprehensive list of EMAC submodels used in this thesis, provided in Appendix A. The development of AIRTRAC 2.0 builds on process-specific aerosol tendencies from the MADE3 submodel. These tendencies are converted to a Lagrangian framework and applied using the tagging formulation (Eq. 3.3) introduced in Section 3.3.1. The Lagrangian setup implemented here adheres to the methodology described in Chapters 4 and 5.

6.2.2. SO_2 AND H_2SO_4 EMISSION POINTS

Two three-month simulations were conducted to model the chemical transport of aviation-emitted SO_2 and H_2SO_4 and their conversion to SO_4 across 28 emission points, all positioned throughout a pressure altitude of 240 hPa, as shown in Fig. 6.2. To ensure stable background conditions, each simulation was preceded by a four-month spin-up period. The simulations start in January and July, representing northern winter and summer, respectively. This emission altitude was chosen based on the pressure altitude corresponding to the maximum zonally averaged aviation SO_2 mass flux, expressed in units of kg m^{-3} s^{-1}, as indicated by the CMIP6 aviation emissions inventory (see Fig. E.1). A Python-based tool [249] was developed to systematically identify the top 28 emission points according to their relative contributions to the total SO_2 mass flux (see Eq. E.1). The combined emissions of SO_2 and H_2SO_4 across these points were scaled to represent the approximate global aviation SO_x emissions in one day (~0.5 Gg of sulfur, assuming an FSC of 600 ppm [192]). The emitted amounts of SO_2 at each point were determined by multiplying each grid cell's relative SO_2 mass flux contribution from CMIP6 at the cruise altitude of 240 hPa by 98% of the daily total. The remaining 2% of the daily total sulfur emitted by aviation is assumed to come from H_2SO_4 and was found according to Eq. E.3.

6.3. THE NEW AIRTRAC 2.0 SUBMODEL

The newly developed AIRTRAC 2.0 submodel calculates the contributions of aviation emissions of H_2SO_4 and SO_2 to two sulfate aerosol modes: the soluble Aitken (ks) mode and the accumulation (as) mode. These modes have been prioritized given their increased potential to act as CCN and alter liquid cloud properties [250, 251]. Using a tagging approach similar to the gas-phase scheme described in Grewe [156] (as shown in Eq. 3.3), AIRTRAC 2.0 determines these source contributions in terms of volume mixing ratios. The SO_4 aerosol modes are represented by the state variables x_i, where x denotes the chemical species (e.g. SO_4) and i denotes the aerosol mode. The index j counts the number of sources that contribute to x_i. In this chapter, two sources are considered: aviation (indexed as avi) and other remaining sources (indexed as rem), which include agricultural activity, other transportation sectors such as shipping and road transport, biogenic emissions, and more. The tagging approach incorporates a fractional term, $\frac{(\mathbf{x}^j)^T \nabla F_i(\mathbf{x})}{\mathbf{x}^T \cdot \nabla F_i(\mathbf{x})}$, representing the contribution of a specific source j to a total amount (for details, see Chapter 3). This fraction is applied to aerosol microphysical tendencies from

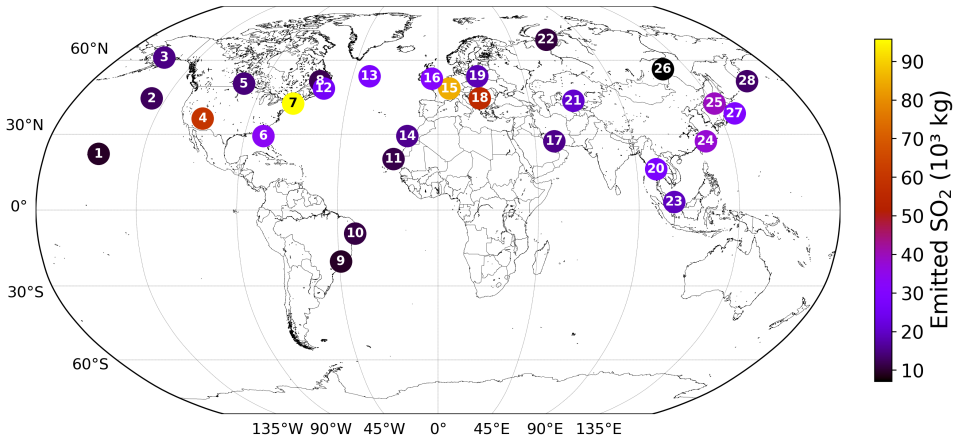


Figure 6.2: The 28 emission points at which SO_2 and H_2SO_4 are emitted are represented as numbered circles. This horizontal distribution of points is shown for a pressure altitude of 240 hPa (~10.6 km). The amounts emitted at each point vary according to the CMIP6 aviation emissions inventory and are distinguished by the color bar. The exact coordinates and emitted amounts for SO_2 and H_2SO_4 are specified in Table B.2 of Appendix B.

MADE3, allowing the model to calculate aviation-attributable contributions to SO_4 enhancement. As in Eq. 3.4, the tagging approach ensures source additivity, thus maintaining a closed sulfate budget. This approach guarantees that the total atmospheric SO_4 is the sum of contributions from aviation and all other sources (avi and rem, respectively):

$$\frac{\partial C_{SO_4,M}}{\partial t} = \frac{\partial C_{SO_4,M}}{\partial t}\bigg|_{avi} + \frac{\partial C_{SO_4,M}}{\partial t}\bigg|_{rem}. \tag{6.1}$$

6.3.1. SUBMODEL INFRASTRUCTURE

AIRTRAC 2.0 builds upon the technical infrastructure of its predecessor, introducing new Lagrangian tracers dedicated to SO_4, SO_2, and H_2SO_4 chemistry. These include tracers specific to individual aerosol microphysical processes, such as coagulation, enabling the estimation of each process's influence on an aerosol mode (see Figs. E.21 and E.28). Additionally, four grid-point (Eulerian) tracers have been added to represent the background concentrations of SO_2, H_2SO_4 and the two SO_4 aerosol modes. A new subroutine, "airtrac_aerosol_integrate," has been introduced to manage aerosol chemistry calculations along Lagrangian air parcel trajectories. The AIRTRAC namelist has also been updated to allow users to specify "Aerosol_mode," which should be set to "1" for SO_4 aerosol studies and "2" for gas-phase analyses. The code for AIRTRAC 2.0 is available in the DKRZ Gitlab upon reasonable request (see Section 6.10).

6.3.2. TRACKING AVIATION SO_2 AND H_2SO_4 EMISSIONS

Since SO_2 and H_2SO_4 are both precursors to SO_4 and are directly emitted by aircraft, tracking their evolution throughout a simulation is essential for accurately assessing aviation's impact on sulfate levels. To account for this, the chemistry mechanism used in

this chapter's simulations includes the gas-phase reaction in the troposphere that converts SO_2 to H_2SO_4, as represented by reaction R25.

$$SO_2 + OH \longrightarrow H_2SO_4 + HO_2 \tag{R25}$$

In the current assessment, the evolution of aviation SO_2 is simplified and modeled as a pure loss process in which SO_2 is oxidized to form H_2SO_4 according to reaction R25. While real-world processes such as scavenging do contribute to SO_2 removal, these are excluded from the analysis due to computational constraints arising from the difficulty of storing all of the liquid-phase tracers associated with the production of SO_4 from SO_2 [168]. These removal processes primarily affect liquid-phase species anyway and thus have minimal impact on the modeled gas-phase SO_2. Consequently, the concentration of aviation-attributable SO_2, $C_{SO_2}\big|_{avi}$ (see Eq. 6.2), is based on the initial amount released into the atmosphere, $C_{SO_2}(t=0)$, set by the TREXP submodel (emission values are provided in Table B.2), and the rate of H_2SO_4 production from SO_2 ($P_{H_2SO_4}$) as calculated by the MECCA submodel. Unlike in Eqs. 3.9 and 3.10, the term $R(C_{SO_2})$ in Eq. 6.2 does not include loss processes such as scavenging, only isotropic mixing from atmospheric turbulence according to Eq. 3.21.

$$C_{SO_2}\big|_{avi} = \underbrace{C_{SO_2}(t=0)}_{\text{Emission}} - \underbrace{\frac{C_{SO_2}\big|_{avi}}{C_{SO_2}\big|_{avi} + C_{SO_2}\big|_{rem}}}_{\text{Tagging ratio}} \times \underbrace{\frac{M_{SO_2}}{M_{H_2SO_4}}}_{\text{Molar masses}} \times \underbrace{P_{H_2SO_4}}_{\text{Production rate}} \times \Delta t + \underbrace{R(C_{SO_2})}_{\text{Turbulence}} \tag{6.2}$$

In theory, the tagging ratio that scales the aviation-attributable SO_2 in Eq. 6.2 should account for OH that is indirectly produced from aviation activities. However, this OH contribution is omitted from Eq. 6.2 as this chapter focuses specifically on the impacts of aviation-emitted SO_2 and H_2SO_4 on SO_4 levels. While OH has already been implemented as a diagnostic tracer in AIRTRAC, it currently operates within the model's gas-phase mode and is not yet linked to the new aerosol scheme. Connecting these functionalities is beyond the scope of this chapter, but is discussed as a worthwhile advancement in section 6.8. The production rate, $P_{H_2SO_4}$, represents the quantity of H_2SO_4 formed from SO_2 oxidation. To calculate the equivalent SO_2 loss, this rate is adjusted by the molar mass ratio $\frac{M_{SO_2}}{M_{H_2SO_4}}$, as shown in Eq. 6.2.

To track the evolution of gas-phase, aviation-attributable H_2SO_4, the production from SO_2 oxidation, as described in Eq. 6.2, must be considered alongside two primary sinks: the binary nucleation of H_2SO_4 with H_2O and the condensation of H_2SO_4 onto pre-existing particles, as represented in Eq. 6.3.

$$
\begin{aligned}
C_{H_2SO_4}\big|_{avi} = \underbrace{C_{H_2SO_4}(t=0)}_{\text{Emission}} &+ \underbrace{\frac{C_{SO_2}\big|_{avi}}{C_{SO_2}\big|_{avi} + C_{SO_2}\big|_{rem}} \times P_{H_2SO_4} \times \Delta t}_{\text{Oxidation of } SO_2} \\
&\underbrace{- \frac{C_{H_2SO_4}\big|_{avi}}{C_{H_2SO_4}\big|_{avi} + C_{H_2SO_4}\big|_{rem}} \times \frac{\partial C_{H_2SO_4}}{\partial t}\Big|_{nucl} \times \Delta t}_{\text{Nucleation of } H_2SO_4 \text{and } H_2O} \\
&\underbrace{- \frac{C_{H_2SO_4}\big|_{avi}}{C_{H_2SO_4}\big|_{avi} + C_{H_2SO_4}\big|_{rem}} \times \frac{\partial C_{H_2SO_4}}{\partial t}\Big|_{cond} \times \Delta t}_{\text{Condensation of } H_2SO_4} \\
&+ \underbrace{R(C_{H_2SO_4})}_{\text{Turbulence}}
\end{aligned}
\tag{6.3}
$$

Similar to the limitation described in Eq. 6.2, Eq. 6.3 considers only the gas-phase formation of H_2SO_4, which occurs via the hydrolysis of SO_3, as shown in Fig. 6.1. Liquid-phase production of H_2SO_4, involving the oxidation of H_2SO_3 by O_3 and H_2O_2 [252, 253], is excluded. While this pathway is a significant source of sulfuric acid, incorporating it is challenging due to the cloud evaporation assumption described in Tost et al. [168], which states that clouds and aqueous-phase species are fully evaporated at the end of each time step. This assumption is used to avoid the high computational costs that would otherwise be required to transport not only gas-phase species, but also those in the liquid phase. The term $R(C_{H_2SO_4})$ again represents turbulent isotropic mixing.

6.3.3. AVIATION'S CONTRIBUTION TO SO_4 VIA NUCLEATION AND CONDENSATION OF H_2SO_4

In the governing equations for the SO_4 mixing ratios (Eq. 3.10), it was shown that the binary nucleation of H_2SO_4-H_2O affects only the soluble Aitken mode. Consequently, aviation's contribution via nucleation is also limited to the ks mode and is quantified based on the amount of H_2SO_4 emitted by aircraft, as represented in Eq. 6.4:

$$
\frac{\partial C_{SO_4,ks}}{\partial t}\Big|_{nucl}^{avi} = \frac{C_{H_2SO_4}\big|_{avi}}{C_{H_2SO_4}\big|_{avi} + C_{H_2SO_4}\big|_{rem}} \times \frac{\partial C_{SO_4,ks}}{\partial t}\Big|_{nucl}. \tag{6.4}
$$

The relative contribution of aviation to SO_4 via H_2SO_4 condensation is estimated similarly to Eq. 6.4, as the tagging ratio remains the same due to the central role of H_2SO_4 in SO_4 condensation. The key difference, however, is that condensation can contribute to the growth of any aerosol mode M of SO_4:

$$
\frac{\partial C_{SO_4,M}}{\partial t}\Big|_{cond}^{avi} = \frac{C_{H_2SO_4}\big|_{avi}}{C_{H_2SO_4}\big|_{avi} + C_{H_2SO_4}\big|_{rem}} \times \frac{\partial C_{SO_4,M}}{\partial t}\Big|_{cond}. \tag{6.5}
$$

6.3.4. AVIATION'S CONTRIBUTION TO SO_4 VIA PARTICLE COAGULATION, GROWTH AND AGING

COAGULATION

To derive an expression for aviation's contribution to the soluble Aitken mode (M = ks) resulting from particle coagulation, the tagging formulation from Eq. 3.3 is applied. For clarity and conciseness in representing the full coagulation equation (Eq. 3.16), vector notation is introduced for the state variables, **x**. The formulation is extended to encompass all nine aerosol modes detailed in Chapter 3. As an example, the mass mixing ratio for the ks mode is denoted as $x_1 \equiv C_{SO_4,ks}$. The mass mixing ratios of all background aerosol modes are calculated using the MADE3 submodel, while aviation source contributions to these mass mixing ratios are determined by AIRTRAC. Each state variable, x_i, represents the aggregate contribution of all sources. Two distinct source categories are defined: aviation (avi) and non-aviation (rem). These are denoted as $j = \{\text{avi}, \text{rem}\}$, where j specifies the source category.

$$\mathbf{x} = \begin{bmatrix} x_1 \\ x_2 \\ x_3 \\ x_4 \\ x_5 \\ x_6 \\ x_7 \\ x_8 \\ x_9 \end{bmatrix} = \begin{bmatrix} x_1^{avi} + x_1^{rem} \\ x_2^{avi} + x_2^{rem} \\ x_3^{avi} + x_3^{rem} \\ x_4^{avi} + x_4^{rem} \\ x_5^{avi} + x_5^{rem} \\ x_6^{avi} + x_6^{rem} \\ x_7^{avi} + x_7^{rem} \\ x_8^{avi} + x_8^{rem} \\ x_9^{avi} + x_9^{rem} \end{bmatrix} = \begin{bmatrix} C_{SO_4,ks} \\ C_{SO_4,km} \\ C_{SO_4,ki} \\ C_{SO_4,as} \\ C_{SO_4,am} \\ C_{SO_4,ai} \\ C_{SO_4,cs} \\ C_{SO_4,cm} \\ C_{SO_4,ci} \end{bmatrix} \tag{6.6}$$

The coagulation kernels are also more compactly rewritten (see Eqs. 6.7 and 6.8), where p and q are the modes of the colliding particles. Additionally, the summation in the denominator of Eq. 3.16 for an aerosol in mode p with diameter D_1 will be reformulated more succinctly as $\sum_{s=1}^{A=9} C_{s,p} = x_1 + C_p$, where $C_p = C_{NH_4,p} + C_{NO_3,p} + C_{Na,p} + C_{Cl,p} + C_{POM,p} + C_{BC,p} + C_{DU,p} + C_{H_2O,p}$. The upper bound A of the summation indicates the type of tracer species s from the nine possibilities in MADE3, i.e., SO_4, NH_4, NO_3, Na, Cl, POM, BC, DU and H_2O.

$$f_{p,q} = \int_0^\infty \int_0^\infty (D_1)^3 \beta(D_1, D_2) n_p(D_1) n_q(D_2) \, dD_1 \, dD_2 \tag{6.7}$$

$$f'_{p,q} = \int_0^\infty \int_0^\infty (D_2)^3 \beta(D_1, D_2) n_p(D_1) n_q(D_2) \, dD_1 \, dD_2 \tag{6.8}$$

It should also be noted from Eqs. 6.7 and 6.8 that $f_{p,q} = f'_{q,p}$.

DERIVATION OF THE COAGULATION TENDENCY FOR SO_4KS FOR AVIATION

When evaluating the double summations of Eq. 3.16 for the case M = ks, it is important to note that for intermodal coagulation, i.e., $p \neq q$, the resulting mode is never ks (i.e., $\tau_{pq} \neq$ ks) according to Table 3.2. In other words, when two particles from different classes collide, the resulting destination mode will never be the soluble Aitken mode, translating into a loss process for mode ks. Consequently, since $\tau_{pq} \neq$ ks, the Kronecker

deltas dependent on τ_{pq} are zero: $\delta_{\mathrm{ks},\tau_{pq}} = 0$. By contrast, the Kronecker deltas $\delta_{\mathrm{ks},p}$ and $\delta_{\mathrm{ks},q}$ evaluate to 1 whenever either mode p or q corresponds to ks. When $p = q$, the coagulation tendency is zero because intramodal collisions do not affect mass concentrations. Evaluating all Kronecker deltas for ks yields eight unique, non-zero combinations: $(p,q) = \{(1,2),(1,3),(1,4),(1,5),(1,6),(1,7),(1,8),(1,9)\}$. It is also essential to recall that the destination mode of coagulating particles depends on the soluble mass fraction θ (denoted as x in Section 3.3.3) of the final particle and water. This dependency implies that the coagulation tendency for each of the nine modes will be a piecewise function of θ. By combining Eqs. 3.16, 6.7, and 6.8, the following compact formulation for the coagulation tendency of the ks mode is obtained (Eq. 6.9):

$$\left.\frac{\partial \mathrm{x}_1}{\partial t}\right|_{\mathrm{coag}} = \mathrm{F}_1(\mathbf{x}) = \begin{cases} -\mathrm{A}\frac{\mathrm{x}_1}{\mathrm{x}_1+\mathrm{C}_1} & ;\ \theta = 1 \\ -\mathrm{A}'\frac{\mathrm{x}_1}{\mathrm{x}_1+\mathrm{C}_1} & ;\ \theta \in [0.1, 1[\\ -\mathrm{A}''\frac{\mathrm{x}_1}{\mathrm{x}_1+\mathrm{C}_1} & ;\ \theta \in [0, 0.1[. \end{cases} \tag{6.9}$$

The coefficients A, A' and A" are given as follows:

$$\mathrm{A} = \rho_1 \frac{\pi}{6}\left[f_{1,4} + f_{1,7}\right]$$

$$\mathrm{A'} = \rho_1 \frac{\pi}{6}\left[f_{1,3} + f_{1,5} + f_{1,6} + f_{1,8} + f'_{2,1}\right]$$

$$\mathrm{A''} = \rho_1 \frac{\pi}{6}\left[f_{1,3} + f_{1,6} + f_{1,9}\right].$$

The negative sign present across all cases of θ in Eq. 6.9 reflects that any intermodal coagulation event involving a particle in the ks mode will always result in the formation of particles in other aerosol modes, aligning with the outcomes shown in Table 3.2. For instance, when the resulting particle is fully soluble (i.e., $\theta = 1$), coefficient A accounts for two specific collision scenarios involving a ks mode particle: either it collides with a particle in the as mode, with the coagulated product transferring to the as mode, or it collides with a particle in the cs mode, resulting in the product being transferred to the cs mode.

For all values of θ, Eq. 6.9 resembles the following form, where K is assumed to be independent of the state variables:

$$\left.\frac{\partial \mathrm{x}_1}{\partial t}\right|_{\mathrm{coag}} = -\mathrm{K}\frac{\mathrm{x}_1}{\mathrm{x}_1+\mathrm{C}_1}. \tag{6.10}$$

Applying the tagging method (Eq. 3.3) to Eq. 6.10 results in the following, where $\mathrm{F}_1(\mathbf{x}) = -\mathrm{K}\frac{\mathrm{x}_1}{\mathrm{x}_1+\mathrm{C}_1}$:

$$\left.\frac{\partial \mathrm{x}_1^{\mathrm{avi}}}{\partial t}\right|_{\mathrm{coag}} = \mathrm{F}_1(\mathbf{x})\frac{\mathrm{x}^{j^T}\nabla \mathrm{F}_1(\mathbf{x})}{\mathrm{x}^T\nabla \mathrm{F}_1(\mathbf{x})}. \tag{6.11}$$

Evaluating the sensitivity fraction leads to the final expression for $\left.\frac{\partial \mathrm{x}_1^{\mathrm{avi}}}{\partial t}\right|_{\mathrm{coag}}$:

$$\left.\frac{\partial x_1^{avi}}{\partial t}\right|_{coag} = F_1(\mathbf{x}) \frac{\left(x_1^{avi}, x_2^{avi}, x_3^{avi}, \ldots, x_9^{avi}\right)\left(\frac{-KC_1}{(x_1+C_1)^2}, 0, 0, \ldots, 0\right)^T}{(x_1, x_2, x_3, \ldots, x_9)\left(\frac{-KC_1}{(x_1+C_1)^2}, 0, 0, \ldots, 0\right)^T} = F_1(\mathbf{x}) \frac{x_1^{avi}}{x_1}. \tag{6.12}$$

Based on the result from Eq. 6.12, the tagging ratio $\frac{x_1^{avi}}{x_1}$ for the coagulation tendency of SO_4 in mode ks is the ratio of the soluble Aitken mode sulfate to the total amount of this aerosol across all sources, i.e., $\frac{x_1^{avi}}{x_1} = \frac{C_{SO_4,ks}|_{avi}}{C_{SO_4,ks}|_{avi} + C_{SO_4,ks}|_{rem}}$. Typically, this ratio varies with the soluble mass fraction θ relative to water, but for mode ks, the same expression is obtained for all real values of θ. The final equation for aviation's contribution to the ks mode of SO_4 via the coagulation process is therefore given by Eq. 6.13. The derivations for the remaining eight aerosol modes are included in Appendix E.2. Given the complexity of the tagging ratios for the remaining modes, difficulty in isolating the appropriate coagulation kernels and significant computational cost required with implementing θ-dependent piecewise functions, Eq. 6.13 is also assumed for the as mode. This approximation is reasonable as the tagging ratio in Eq. 6.13 appears in at least one of the cases in each of the nine aerosol modes (see derivations in Appendix E.2).

$$\left.\frac{\partial C_{SO_4,M}}{\partial t}\right|_{coag}^{avi} \approx \frac{C_{SO_4,M}|_{avi}}{C_{SO_4,M}|_{avi} + C_{SO_4,M}|_{rem}} \times \left.\frac{\partial C_{SO_4,M}}{\partial t}\right|_{coag} \tag{6.13}$$

The derivation above and those in Appendix E.2 apply the following assumptions:

1. Coagulation kernels and terms C_p are independent of the state variables x_i.
2. Coagulation between modes p and q leads to the same outcome as the coagulation between modes q and p.

GROWTH AND AGING

The growth and aging processes are contemplated by the rename tendency within the MADE3 submodel, as has been described in greater detail in Section 3.3.3. Given that both of these processes are affected by coagulation and condensation, their tagging formulation is analogous to Eq. 6.13. The rename tendency, $\left.\frac{\partial C_{SO_4,M}}{\partial t}\right|_{rename}$, contemplates effects from the tendencies $\left.\frac{\partial C_{SO_4,M}}{\partial t}\right|_{gr}$ and $\left.\frac{\partial C_{SO_4,M}}{\partial t}\right|_{ag}$ specified in Eq. 3.10. Its tagging formulation is given by Eq. 6.14:

$$\left.\frac{\partial C_{SO_4,M}}{\partial t}\right|_{rename}^{avi} = \frac{C_{SO_4,M}|_{avi}}{C_{SO_4,M}|_{avi} + C_{SO_4,M}|_{rem}} \times \left.\frac{\partial C_{SO_4,M}}{\partial t}\right|_{rename}. \tag{6.14}$$

6.3.5. AVIATION-ATTRIBUTABLE SO_4 REMOVAL PROCESSES

The amount of aviation-produced SO_4 that is removed according to the three removal processes introduced in Chapter 3 (dry deposition, sedimentation and wet scavenging) is adjusted following the same methodology as the coagulation (Eq. 6.13) and renaming

(Eq. 6.14) tendencies. The tagging ratio is therefore once again $\frac{C_{SO_4,M}|_{avi}}{C_{SO_4,M}|_{avi}+C_{SO_4,M}|_{rem}}$. The reasoning behind this is that the removal rates should be proportional to the amount of the aerosol present in the atmosphere and approximately zero once the aviation-induced aerosols are nearly depleted. The dry deposition, sedimentation and scavenging tendencies for aviation aerosols are therefore given as follows:

$$\left.\frac{\partial C_{SO_4,M}}{\partial t}\right|^{avi}_{DDEP} = \frac{C_{SO_4,M}|_{avi}}{C_{SO_4,M}|_{avi}+C_{SO_4,M}|_{rem}} \times \left.\frac{\partial C_{SO_4,M}}{\partial t}\right|_{DDEP}, \tag{6.15}$$

$$\left.\frac{\partial C_{SO_4,M}}{\partial t}\right|^{avi}_{SEDI} = \frac{C_{SO_4,M}|_{avi}}{C_{SO_4,M}|_{avi}+C_{SO_4,M}|_{rem}} \times \left.\frac{\partial C_{SO_4,M}}{\partial t}\right|_{SEDI}, \tag{6.16}$$

$$\left.\frac{\partial C_{SO_4,M}}{\partial t}\right|^{avi}_{SCAV} = \frac{C^{avi}_{SO_4,M}}{C^{avi}_{SO_4,M}+C^{rem}_{SO_4,M}} \times \left[\left.\frac{\partial C_{SO_4,M}}{\partial t}\right|_{SCAV,cv} + \left.\frac{\partial C_{SO_4,M}}{\partial t}\right|_{SCAV,ls}\right]. \tag{6.17}$$

6.3.6. AN OVERVIEW OF THE TAGGING EQUATIONS FOR AVIATION SO_4

By combining the tagging formulations for all aerosol microphysical and removal processes, a consolidated overview of the governing differential equations implemented in AIRTRAC 2.0 is provided. These allow for the tracking of atmospheric changes to SO_4 as a result of aviation-induced SO_2 and H_2SO_4 emissions. The isotropic turbulent mixing parameterization from LGTMIX is represented by $R(C_{SO_4,ks})$. The complete non-linear equation for the SO_4 ks mode is given by Eq. 6.18:

$$\begin{aligned}\left.\frac{\partial C_{SO_4,ks}}{\partial t}\right|^{avi} = {} & \frac{C^{avi}_{H_2SO_4}}{C^{avi}_{H_2SO_4}+C^{rem}_{H_2SO_4}} \times \left(\underbrace{\left.\frac{\partial C_{SO_4,ks}}{\partial t}\right|_{nucl}}_{\text{nucleation}} + \underbrace{\left.\frac{\partial C_{SO_4,ks}}{\partial t}\right|_{cond}}_{\text{condensation}}\right) \\ & + \frac{C^{avi}_{SO_4,ks}}{C^{avi}_{SO_4,ks}+C^{rem}_{SO_4,ks}} \times \left(\underbrace{\left.\frac{\partial C_{SO_4,ks}}{\partial t}\right|_{coag}}_{\text{coagulation}} + \underbrace{\left.\frac{\partial C_{SO_4,ks}}{\partial t}\right|_{rename}}_{\text{growth \& aging}}\right) \\ & - \frac{C^{avi}_{SO_4,ks}}{C^{avi}_{SO_4,ks}+C^{rem}_{SO_4,ks}} \times \left(\underbrace{\left.\frac{\partial C_{SO_4,ks}}{\partial t}\right|_{DDEP}}_{\text{dry deposition}} + \underbrace{\left.\frac{\partial C_{SO_4,ks}}{\partial t}\right|_{SEDI}}_{\text{sedimentation}}\right. \\ & \left. + \underbrace{\left.\frac{\partial C_{SO_4,ks}}{\partial t}\right|_{SCAV,cv} + \left.\frac{\partial C_{SO_4,ks}}{\partial t}\right|_{SCAV,ls}}_{\text{scavenging}}\right) + R(C_{SO_4,ks}).\end{aligned} \tag{6.18}$$

For the remaining eight modes (M={km,ki,as,am,ai,cs,cm,ci}):

$$\begin{aligned}\left.\frac{\partial C_{SO_4,M}}{\partial t}\right|^{avi} = &\frac{C^{avi}_{H_2SO_4}}{C^{avi}_{H_2SO_4}+C^{rem}_{H_2SO_4}} \times \left(\underbrace{\left.\frac{\partial C_{SO_4,M}}{\partial t}\right|_{cond}}_{\text{condensation}} \right) \\ &+ \frac{C^{avi}_{SO_4,M}}{C^{avi}_{SO_4,M}+C^{rem}_{SO_4,M}} \times \left(\underbrace{\left.\frac{\partial C_{SO_4,M}}{\partial t}\right|_{coag}}_{\text{coagulation}} + \underbrace{\left.\frac{\partial C_{SO_4,M}}{\partial t}\right|_{rename}}_{\text{growth \& aging}} \right) \\ &- \frac{C^{avi}_{SO_4,M}}{C^{avi}_{SO_4,M}+C^{rem}_{SO_4,M}} \times \left(\underbrace{\left.\frac{\partial C_{SO_4,M}}{\partial t}\right|_{DDEP}}_{\text{dry deposition}} + \underbrace{\left.\frac{\partial C_{SO_4,M}}{\partial t}\right|_{SEDI}}_{\text{sedimentation}} \right. \\ &\left. + \underbrace{\left.\frac{\partial C_{SO_4,M}}{\partial t}\right|_{SCAV,cv} + \left.\frac{\partial C_{SO_4,M}}{\partial t}\right|_{SCAV,ls}}_{\text{scavenging}} \right) + R\left(C_{SO_4,M}\right). \end{aligned} \tag{6.19}$$

Both Eqs. 6.18 and 6.19 display non-linear responses according to the tagging ratios involving H_2SO_4 and SO_4 from aviation, since increasing either $C^{avi}_{H_2SO_4}$ or $C^{avi}_{SO_4}$ does not lead to a linearly proportional change in $\left.\frac{\partial C_{SO_4,M}}{\partial t}\right|^{avi}$. In fact, their ratios will tend to one as aviation emissions grow. Within AIRTRAC, the relationship between the emitted quantity of a pollutant and its chemical response was originally linearized to allow multiple emission scenarios to be run in parallel within a single simulation. This linearization translates to constant production and loss efficiencies [143] for each pollutant. Although this approach simplifies the chemical mechanisms—such as neglecting feedbacks between emissions and the background—it offers the advantage of reducing computational costs by one to two orders of magnitude. This reduction is achieved not only by eliminating the need to run a separate simulation for each emission scenario, as previously mentioned, but also by avoiding the calibration of the mixing parameter in the LGTMIX submodel (see Section 3.3.6) based on the emitted amount. If, for instance, the same mixing parameter that was used to study the effects of an SO_2 emission in the order of 10^4 kg were also applied to SO_2 emission magnitudes in the order of $\sim 10^{10}$ kg, the mixing between the Lagrangian air parcels would artificially dominate over the aerosol microphysical processes. To avoid this, the tagging ratios of Eqs. 6.18 and 6.19 are linearized using Maclaurin series. Both tagging ratios, $\frac{C^{avi}_{H_2SO_4}}{C^{avi}_{H_2SO_4}+C^{rem}_{H_2SO_4}}$ and $\frac{C^{avi}_{SO_4,M}}{C^{avi}_{SO_4,M}+C^{rem}_{SO_4,M}}$, may be compared mathematically to the function $f(x)=\frac{x}{x+k}$, where k is a constant real number. $C^{rem}_{H_2SO_4}$ and $C^{rem}_{SO_4}$ are treated as constants as the amounts emitted by aviation do not influence background concentrations. The linearization of $f(x)$ using a first-order Maclaurin polynomial may then be achieved as follows:

$$f(x) = \frac{x}{x+k} = \sum_{n=0}^{\infty} \frac{f^{(n)}(0)}{n!} \cdot x^n \approx f(0) + f'(0) \cdot x = \frac{x}{k}. \tag{6.20}$$

Applying Eq. 6.20 to Eqs. 6.18 and 6.19 yields their complete, linearized versions. This linearization, however, does not excuse further investigation regarding the appropriateness of using the gas-phase mixing parameter d within the context of aerosol microphysics, which is discussed later in Section 6.8 and shown in Appendix E.8.

$$\begin{aligned}\frac{\partial C_{SO_4,ks}}{\partial t}\Big|^{avi} = {} & \frac{C^{avi}_{H_2SO_4}}{C^{rem}_{H_2SO_4}} \times \left(\frac{\partial C_{SO_4,ks}}{\partial t}\Big|_{nucl} + \frac{\partial C_{SO_4,ks}}{\partial t}\Big|_{cond} \right) \\ & + \frac{C^{avi}_{SO_4,ks}}{C^{rem}_{SO_4,ks}} \times \left(\frac{\partial C_{SO_4,ks}}{\partial t}\Big|_{coag} + \frac{\partial C_{SO_4,ks}}{\partial t}\Big|_{rename} \right. \\ & - \frac{\partial C_{SO_4,ks}}{\partial t}\Big|_{DDEP} - \frac{\partial C_{SO_4,ks}}{\partial t}\Big|_{SEDI} - \frac{\partial C_{SO_4,ks}}{\partial t}\Big|_{SCAV,cv} \\ & \left. - \frac{\partial C_{SO_4,ks}}{\partial t}\Big|_{SCAV,ls} \right) + R\left(C_{SO_4,ks}\right)\end{aligned} \tag{6.21}$$

$$\begin{aligned}\frac{\partial C_{SO_4,M}}{\partial t}\Big|^{avi} = {} & \frac{C^{avi}_{H_2SO_4}}{C^{rem}_{H_2SO_4}} \times \frac{\partial C_{SO_4,M}}{\partial t}\Big|_{cond} + \frac{C^{avi}_{SO_4,M}}{C^{rem}_{SO_4,M}} \times \left(\frac{\partial C_{SO_4,M}}{\partial t}\Big|_{coag} + \frac{\partial C_{SO_4,M}}{\partial t}\Big|_{rename} \right. \\ & \left. - \frac{\partial C_{SO_4,M}}{\partial t}\Big|_{DDEP} - \frac{\partial C_{SO_4,M}}{\partial t}\Big|_{SEDI} - \frac{\partial C_{SO_4,M}}{\partial t}\Big|_{SCAV,cv} - \frac{\partial C_{SO_4,M}}{\partial t}\Big|_{SCAV,ls} \right) \\ & + R\left(C_{SO_4,M}\right).\end{aligned} \tag{6.22}$$

6.4. ESA CLOUD SATELLITE DATA

To demonstrate AIRTRAC's capability in predicting interactions between SO_4 aerosols and low-level liquid clouds, satellite data from the Cloud_cci project[1], part of the ESA Climate Change Initiative (CCI), is utilized to identify the approximate locations of these clouds. Specifically, version 3 of the Advanced Very High Resolution Radiometer ante meridiem (AVHRR-AMv3) dataset [254, 255] at Level-3C (monthly means) is applied, covering the period from 1982 to 2016. Cloud properties up until June 2007 were captured using National Oceanic and Atmospheric Administration (NOAA) morning satellites equipped with the AVHRR sensor, which measures solar and thermal radiation at the TOA. From July 2007 onward, data collection was conducted using the European MetOp-A satellite. This comprehensive dataset comprises 174 variables stored in netCDF format with a latitude-longitude grid resolution of 0.5° × 0.5° [256, 257]. To pinpoint the location of liquid clouds during the AIRTRAC simulation periods (January–March, 2015 and July–September, 2015), the liquid cloud fraction (LCF) and cloud top pressure (CTP) variables were analyzed.

[1] https://climate.esa.int/en/projects/cloud/

LIQUID CLOUD FRACTION (LCF)

The liquid cloud fraction quantifies the proportion of a grid cell area that is covered by liquid clouds. This dimensionless variable is called "cph" within the dataset and provides an approximate location of liquid clouds in terms of latitude and longitude.

CLOUD TOP PRESSURE (CTP)

The cloud top pressure indicates the pressure altitude in hPa of the uppermost region of a cloud. It is denominated "ctp_corrected" within the dataset and may provide an approximate location of the altitude of liquid clouds when paired with LCF. The equivalent variable in km is provided by the cloud top height or "cth_corrected".

6.5. APPLICATION AND EVALUATION OF AIRTRAC 2.0

This section explores the applications of AIRTRAC 2.0 in examining the transport patterns of aviation-induced SO_2 and H_2SO_4 emissions and their role in SO_4 formation, with a particular focus on the soluble Aitken and accumulation modes. The analysis is structured around emission scenarios for SO_2 and H_2SO_4 in January 2015 (representative of northern winter) and July 2015 (representative of northern summer). The seasonal mean concentrations of SO_4 in the ks and as modes are then compared to results from a perturbation simulation using EMAC based on the CMIP6 aviation emissions inventory.

6.5.1. EMITTED SPECIES: SO_2 AND H_2SO_4

Figure 6.3 illustrates the differing transport pathways and impacts of SO_2 emissions originating from emission points 8 and 9, situated in the North and South Atlantic regions, respectively (see Fig. 6.2). For comparison, Fig. 6.4 presents analogous information for H_2SO_4 emissions for the same points. Both figures pertain to a 90-day period during the northern winter (January to March 2015).

SO_2

In AIRTRAC 2.0, SO_2 is treated as a pure loss process within Lagrangian air parcels, as outlined in Eq. 6.2. Figures 6.3 (a) and (b) depict the temporal evolution of SO_2 e-folding times for two emission scenarios, calculated by solving for τ under the exponential decay law $C(t) = C_0 \cdot e^{-\frac{t}{\tau}}$, where C_0 is the initial concentration and t is the time since emission. The mean e-folding time for emissions at point 8, approximately 33 days, is 60% larger than the 21-day estimate at point 9. This disparity is likely due to the rapid downward transport at point 9, illustrated in Fig. 6.3 (d), which accelerates SO_2 depletion. In contrast, SO_2 emitted at point 8 remains at higher altitudes, where stability in the upper atmosphere leads to slower depletion rates (Fig. 6.3 (c)). A similar mechanism was observed for NO_x-O_3 chemistry in Chapter 5: pollutants transported to lower atmospheric levels are removed more rapidly due to greater atmospheric instability and enhanced chemical reactivity driven by larger HO_x concentrations in the lower troposphere (i.e. both O_3 and SO_2 are oxidized by OH). Conversely, pollutants residing at higher altitudes experience slower removal rates because of the increased atmospheric stability and significantly lower HO_x concentrations characteristic of the upper troposphere [37, 86].

The horizontal distribution associated with emission point 8 (Fig. 6.3 (e)) shows that air parcels predominantly remain within the Northern Hemisphere, in line with previous

findings that inter-hemispheric transport is limited [13, 141]. Meanwhile, SO_2 emitted from point 9 in the Southern Hemisphere eventually reaches the northern tropical region, following the horizontal wind patterns (Fig. 6.3 (f)). This tropical transport to lower altitudes likely drives the rapid SO_2 depletion, attributed to higher OH concentrations at lower altitudes, especially near the tropics [86]. Equivalent analyses for other emission points, detailing the temporal evolution and spatial distribution of SO_2, are available in Appendix E.3. SO_2 emission scenarios during July, for instance, are considered in Figs. E.4, E.6 and E.8. In addition to emission point 9, point 24 in the northern Pacific (Fig. E.7) exemplifies another rare instance of inter-hemispheric transport, where air masses move toward South America.

H_2SO_4

AIRTRAC 2.0 calculates H_2SO_4 concentrations along air parcel trajectories using Eq. 6.3, whereby the conversion of SO_2 directly contributes to H_2SO_4 formation. Consequently, the longer e-folding time for SO_2 observed at emission point 8 (Fig. 6.3 (a)) also appears to prolong the lifetime of H_2SO_4. Figure 6.4 (a) indicates that H_2SO_4 persists beyond the 80-day mark for emissions from point 8, whereas emissions from point 9 are fully depleted around 50 days after emission (Fig. 6.4 (b)). This dependency on the amount of aviation-derived SO_2 suggests that H_2SO_4 production can peak not only several days after the initial emission but also at locations significantly distant from the original emission source. Figures 6.4 (c) and (d) illustrate that peak H_2SO_4 production at each emission point shifts towards lower altitudes over time. Similarly, Figures 6.4 (e) and (f) reveal enhanced production efficiency in regions displaced from the initial emission sites. Comprehensive plots illustrating the spatial and temporal variations of H_2SO_4 across all emission points are available in Appendix E.4. The transport patterns for emissions occurring in July are shown in Figs. E.10, E.12 and E.14.

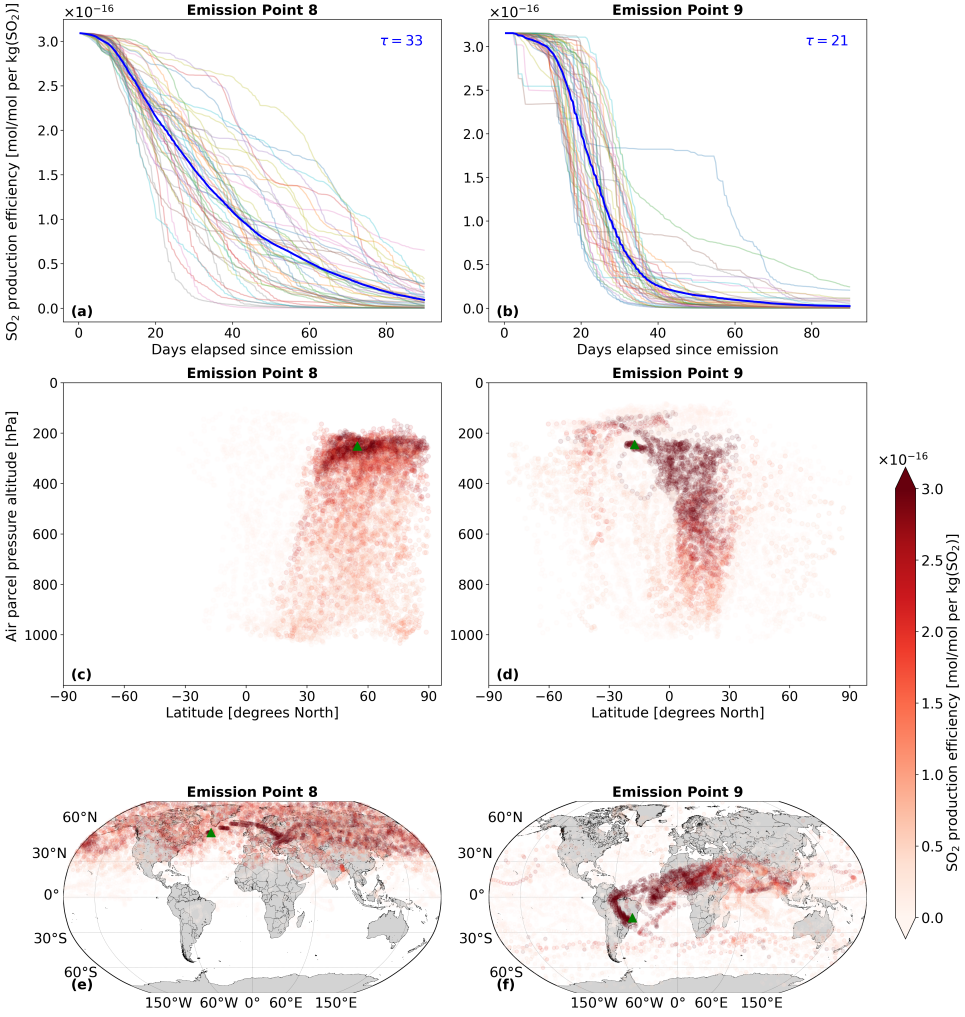


Figure 6.3: The spatio-temporal variation of aviation-induced sulfur dioxide (SO_2) for emission points 8 and 9 (see Fig. 6.2). Sub-plots (a) - (b) display the temporal evolution of the SO_2 production efficiency throughout the 90-day simulation period (January - March of 2015). The multi-colored lines denote the production efficiencies across 50 air parcel trajectories initialized at the selected emission points. The thicker dark blue curve is the mean of these 50 trajectories. The values of τ represent the e-folding times in days for this mean curve. Sub-plots (c) - (d) represent the spatial variation of the production efficiency as a function of the pressure altitude and latitude. Sub-plots (e) - (f) illustrate the spatial variation of the production efficiency as a function of latitude and longitude. The green triangles indicate the approximate location of emission points 8 and 9.

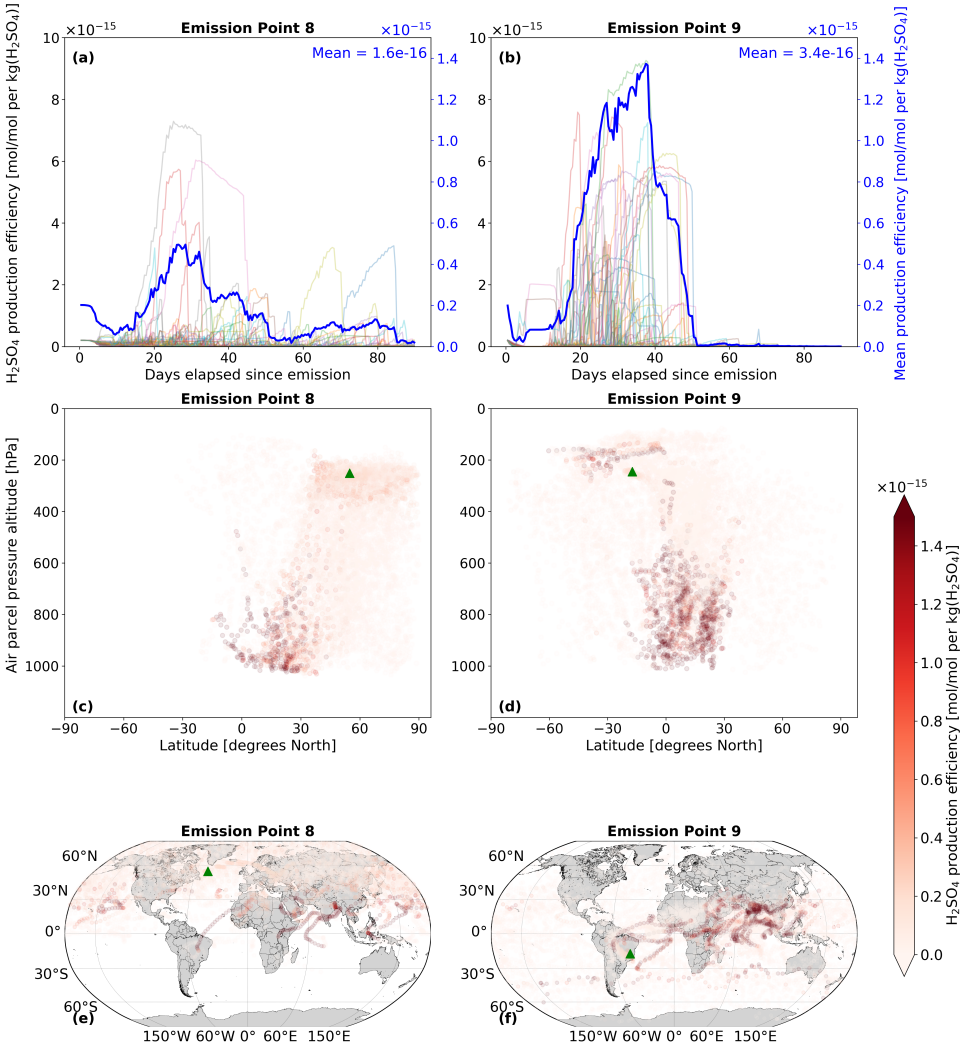


Figure 6.4: The spatio-temporal variation of aviation-induced sulfuric acid (H_2SO_4) for emission points 8 and 9 (see Fig. 6.2). Sub-plots (a) - (b) display the temporal evolution of the H_2SO_4 production efficiency throughout the 90-day simulation period (January - March of 2015). The multi-colored lines denote the production efficiencies across 50 air parcel trajectories initialized at the selected emission points. The thicker dark blue curve is the mean of these 50 trajectories and is represented on the secondary blue axis. The mean value of this blue curve is shown at the top right corner. Sub-plots (c) - (d) represent the spatial variation of the production efficiency as a function of the pressure altitude and latitude. Sub-plots (e) - (f) illustrate the spatial variation of the production efficiency as a function of latitude and longitude. The green triangles indicate the approximate location of emission points 8 and 9.

6.5.2. IMPACT ON SULFATE: SO_4 KS AND AS MODES

The production of SO_4 in both the soluble Aitken and accumulation modes, stemming from aviation emissions of SO_2 and H_2SO_4 analyzed in the previous section, is calculated by AIRTRAC for the same emission points 8 and 9 using Eqs. 6.21 and 6.22, respectively.

IMPACT ON SOLUBLE AITKEN MODE: SO_4KS

Despite differences in transport patterns between emission points 8 and 9, the average production efficiency of SO_4ks remains similar across the two, with emission point 9 showing a slightly higher efficiency. This modest increase for point 9 likely arises from early downward transport into more chemically active regions, as was referred earlier. According to Figs. 6.5 (a) and (b), the mean values (in blue) reveal this similarity. According to Fig. E.21, the gradual decline in SO_4ks aerosol concentrations at both emission points is primarily due to the growth/aging process, which shifts these aerosols into the larger accumulation (as) mode. Horizontal transport patterns in Fig. 6.5 (e) confirm that SO_2 and H_2SO_4 emitted from point 8 produce SO_4ks aerosols exclusively in the Northern Hemisphere, while emissions from point 9 lead to ks-mode sulfate production across both the northern Tropics and southern mid-latitudes (Fig. 6.5 (f)). Appendix E.5 provides the complete set of SO_4ks transport plots across all emission points.

IMPACT ON SOLUBLE ACCUMULATION MODE: SO_4AS

The temporal evolution of SO_4as shown in Figs. 6.6 (a) and (b) reveals a consistent upward trend over time. This behavior is primarily driven by the growth and aging of SO_4ks particles into the as mode, as illustrated in Fig. E.28. As discussed in Chapter 3, aerosols in the Aitken mode can grow through coagulation and condensation, transitioning into the accumulation mode. The mean production efficiency of SO_4as and its rate of increase (slope) are notably higher for emission point 9, approximately 70% greater than point 8. A possible explanation for this difference is the increased availability of SO_4ks during the second half of the simulation, particularly towards the end (between days 80 and 90), which promotes the enhanced growth of ks aerosols into the accumulation mode. The vertical and horizontal transport patterns for SO_4as exhibit larger magnitudes compared to SO_4ks precisely due to this growth process acting as a sink for ks-mode particles. However, both modes display similar spatial distributions, as seen when comparing Figs. 6.5 (c)-(f) with Figs. 6.6 (c)–(f). The full set of spatio-temporal variations for SO_4as across all emission points is included in Appendix E.6. The upward trend in these time series indicates that peak production efficiencies can occur far from the emission origin, underscoring the potential for long-range aerosol transport to contribute significantly to surface-level concentrations from distant sources, a phenomenon also observed by Yang et al. [236].

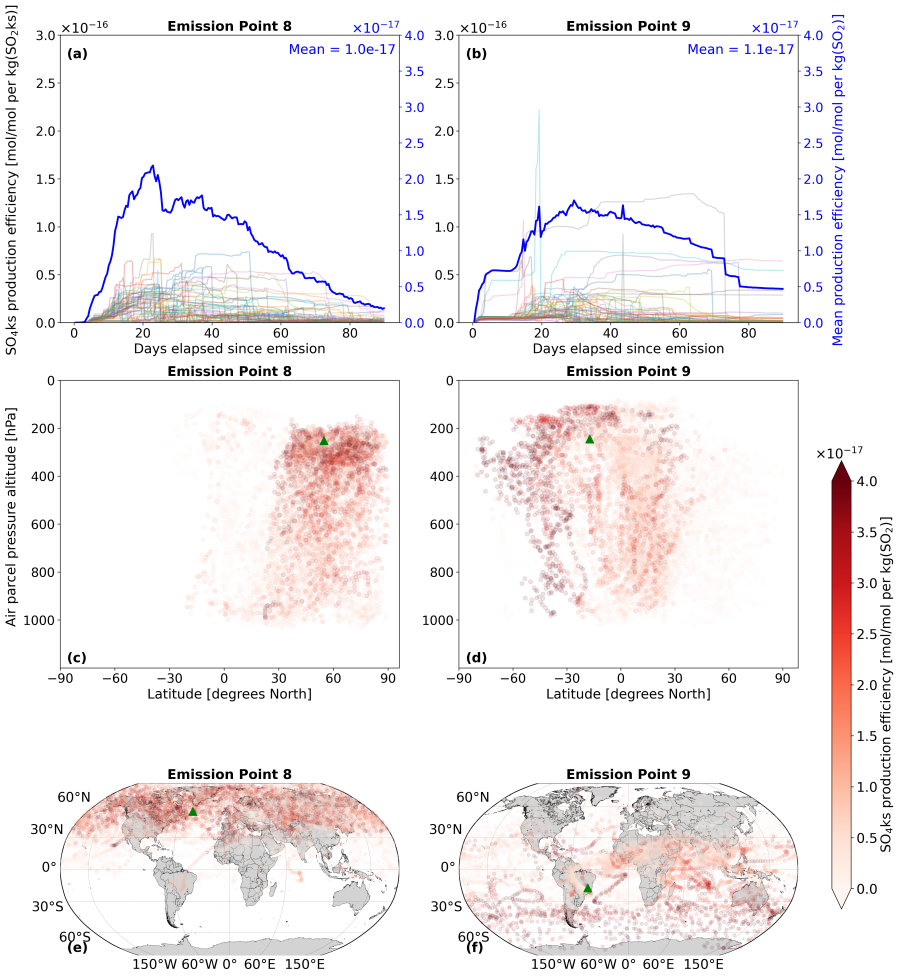


Figure 6.5: The spatio-temporal variation of aviation-induced sulfate in the soluble Aitken mode (SO_4ks) for emission points 8 and 9 (see Fig. 6.2). Sub-plots (a) - (b) display the temporal evolution of the SO_4ks production efficiency throughout the 90-day simulation period (January - March of 2015). The multi-colored lines denote the production efficiencies across 50 air parcel trajectories initialized at the selected emission points. The thicker dark blue curve is the mean of these 50 trajectories and is represented on the secondary blue axis. The mean value of this blue curve is shown at the top right corner. Sub-plots (c) - (d) represent the spatial variation of the production efficiency as a function of the pressure altitude and latitude. Sub-plots (e) - (f) illustrate the spatial variation of the production efficiency as a function of latitude and longitude. The green triangles indicate the approximate location of emission points 8 and 9.

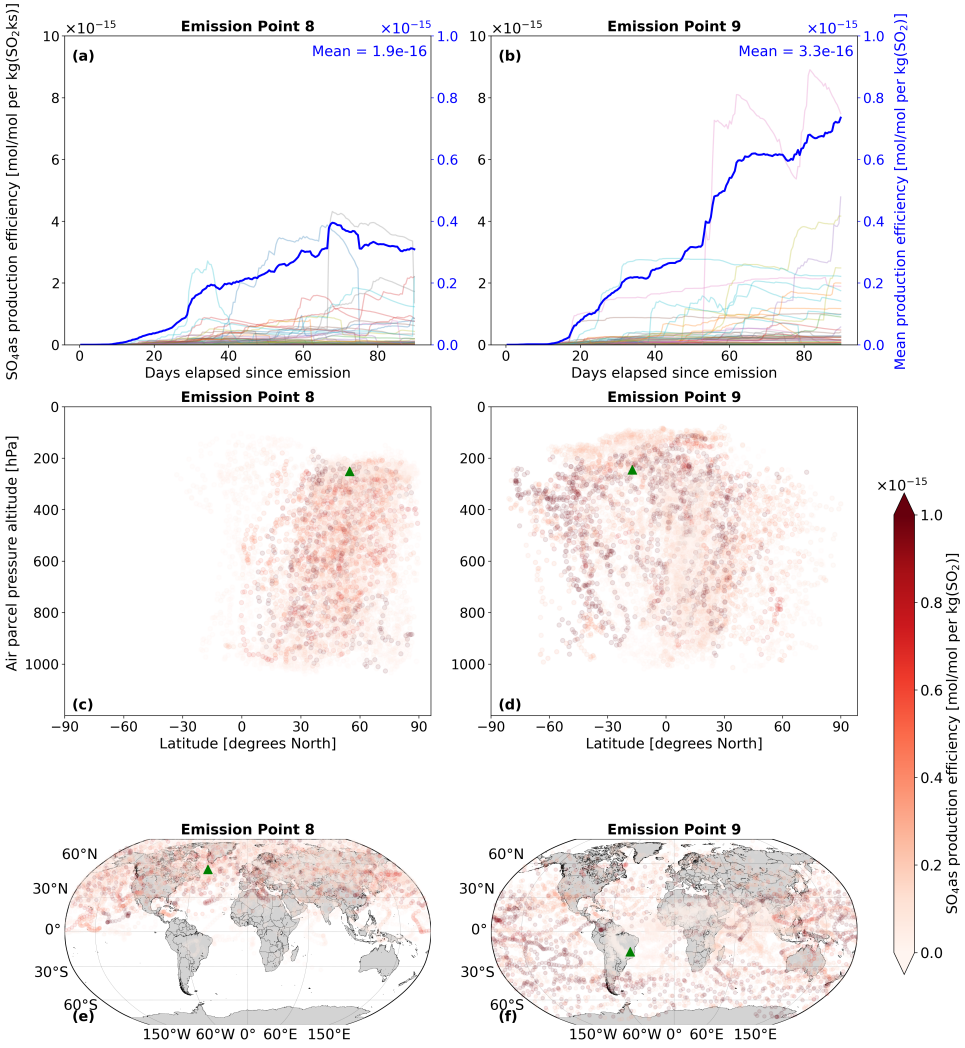
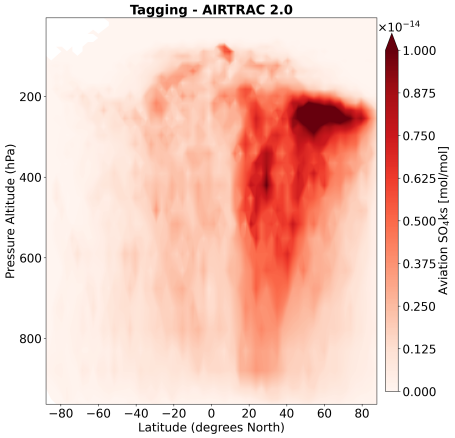


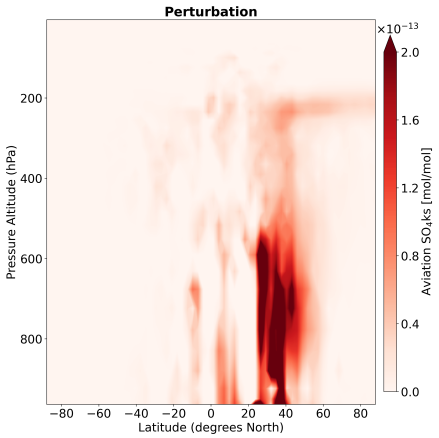
Figure 6.6: The spatio-temporal variation of aviation-induced sulfate in the soluble accumulation mode (SO_4as) for emission points 8 and 9 (see Fig. 6.2). Sub-plots (a) - (b) display the temporal evolution of the SO_4as production efficiency throughout the 90-day simulation period (January - March of 2015). The multi-colored lines denote the production efficiencies across 50 air parcel trajectories initialized at the selected emission points. The thicker dark blue curve is the mean of these 50 trajectories and is represented on the secondary blue axis. The mean value of this blue curve is shown at the top right corner. Sub-plots (c) - (d) represent the spatial variation of the production efficiency as a function of the pressure altitude and latitude. Sub-plots (e) - (f) illustrate the spatial variation of the production efficiency as a function of latitude and longitude. The green triangles indicate the approximate location of emission points 8 and 9.

6.5.3. EVALUATION OF AIRTRAC 2.0

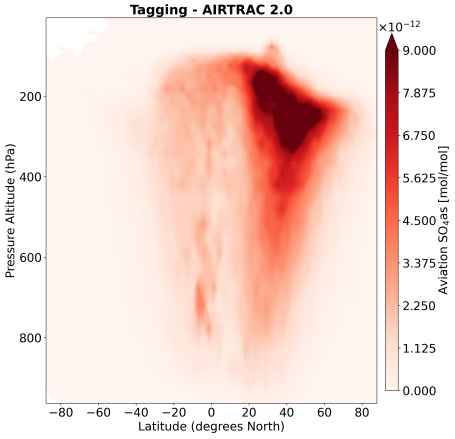
AIRTRAC 2.0 relies on aerosol tendencies from MADE3, which have been extensively validated against observational data (see Section 3.3.3). To evaluate AIRTRAC 2.0, comparisons with other sulfate tagging approaches, such as the method by Yang et al. [236], are necessary. However, since no sulfate tagging scheme is currently available within EMAC, the perturbation approach described by Righi et al. [160] is used instead, who estimated sulfate impacts from various transport sectors. Their simulation setup provides a suitable basis for comparison due to the use of the same EMAC model framework and emissions inventories, ensuring consistent background conditions. Therefore, additional simulations were performed following the setup of Righi et al. [160].



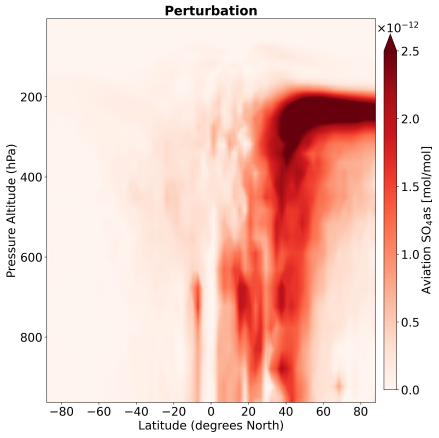
(a) Tagging: July SO_4ks



(b) Perturbation: July SO_4ks



(c) Tagging: July SO_4as



(d) Perturbation: July SO_4as

Figure 6.7: Comparison of AIRTRAC's tagging estimates with the perturbation method using a modeling setup similar to Righi et al. [160] for SO_4ks and SO_4as during the period July - September 2015.

Figure 6.7 presents a comparison of the volume mixing ratios (VMRs) for SO_4ks and SO_4as predicted by AIRTRAC 2.0 (subplots (a) and (c)) for July emissions against estimates obtained using a perturbation approach (subplots (b) and (d)), following a setup similar to that of Righi et al. [160]. In AIRTRAC, each of the 28 emission points is treated as an independent scenario, with no interaction between emissions (see Chapter 4 for details). Consequently, the VMRs in subplots (a) and (c) represent the total SO_4 VMRs across all emission points, making them more comparable to the perturbation method, which considers emissions collectively. However, a direct comparison of magnitudes is still challenging, not only due to the differing research objectives of each method (perturbation vs. tagging approaches as discussed in Chapter 4), but also due to the nature of the emissions considered (i.e., pulse vs. sustained). Therefore, this discussion primarily focuses on the similarities between the transport patterns of both methods rather than their absolute magnitudes.

Both methods reveal fairly similar transport patterns, with AIRTRAC indicating the highest VMRs in the local emission region for both the ks and as modes, while the perturbation method identifies a concentration peak in this vicinity only for the as mode (Fig. 6.7 (d)). Both approaches largely agree that the latitudinal band between 20–40° is most affected near the surface under the specified flight pattern (Fig. 6.2), which aligns with findings from Righi et al. [160] for total aviation SO_4 profiles in 2015. The predicted transport patterns for the July-September period show congruence between AIRTRAC and the perturbation method. However, for the January-March period, discrepancies arise, particularly with the perturbation method indicating peak concentrations of the ks mode near the surface, while AIRTRAC predicts these peaks closer to the emission source (see Fig. E.29 (a) and (b) in Appendix E.7). Regarding magnitude, although a direct comparison between the two setups is difficult, Fig. 6.7 consistently shows that sulfate aerosols in the accumulation mode are produced at levels at least an order of magnitude higher than those in the Aitken mode for both methods.

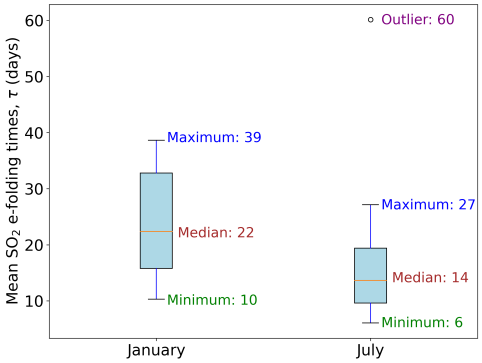
These differences are expected due to AIRTRAC's use of a 15-minute pulse emission compared to the perturbation method's sustained emission over three months. AIRTRAC's simulations also focus exclusively on emissions at a 240 hPa pressure altitude, whereas the perturbation method includes all flight phases, potentially explaining its stronger surface signal for the ks mode. Limiting the perturbation approach to the 240 hPa altitude would improve comparability, but risks obscuring the aviation emission signal in numerical noise, as 240 hPa emissions represent only about 20% of the total aviation emissions (as discussed with the TAGGING submodel in the NO_x-O_3 context, see Fig. C.6 and the blue curves representing the perturbation approach in Figs. 4.4 (d), (e), and (f)).

Lastly, AIRTRAC's results in Fig. 6.7 are based on injecting 1-day equivalent aviation SO_2 emissions without altering the baseline CMIP6 aviation emissions. In contrast, the perturbation approach assesses transport solely by adjusting these background aviation fluxes. These differences currently present significant challenges in directly comparing the two approaches.

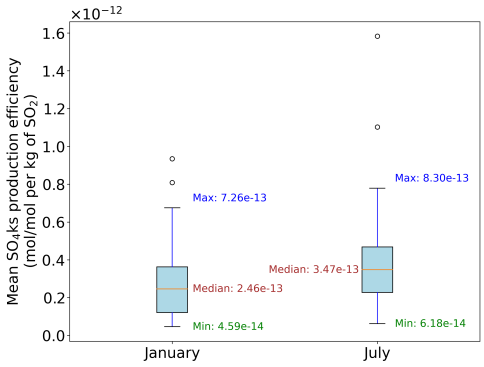
6.6. SEASONAL DEPENDENCE OF AVIATION SULFUR SPECIES

The production of sulfate aerosols from aviation exhibits a strong seasonal dependence as a result of variations in atmospheric chemistry and photochemistry. Seasonal changes in sunlight intensity and background water vapor concentrations significantly influence the chemical processes that convert sulfur species into sulfate aerosols. These variations, in turn, affect the efficiency of oxidation pathways and the overall lifetime of sulfur compounds in the atmosphere.

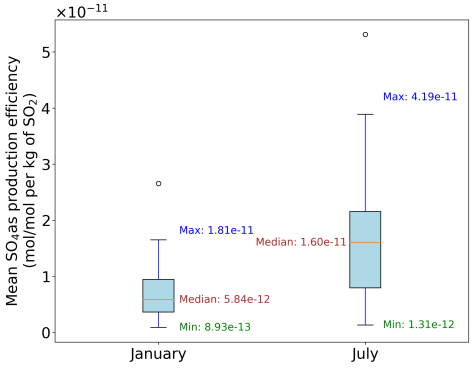
As with most chemical species in the troposphere, the lifetime of SO_2 is highly dependent on the presence of the OH radical, which drives the gas-phase oxidation of SO_2 into SO_4. OH is produced primarily through the photodissociation of O_3 and subsequent reaction with H_2O, meaning that both seasonality and altitude play pivotal roles in aviation SO_x chemistry. These factors modulate sunlight availability and background humidity levels, thereby impacting the concentration of OH and, consequently, the rate of SO_2 oxidation.



(a) SO_2 mean e-folding times (τ).



(b) SO_4ks mean production efficiency.



(c) SO_4as mean production efficiency.

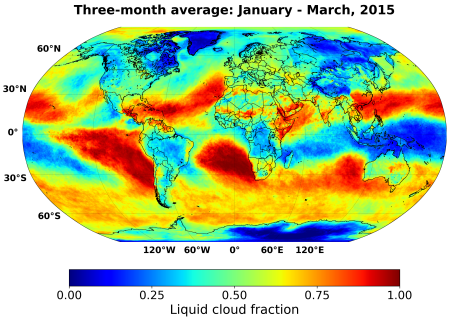
Figure 6.8: Seasonal comparison of SO_2 e-folding times (see τ values in Figs. E.3 and E.4) and SO_4ks and as mean production efficiencies (based on Figs. E.15 and E.16). The horizontal axes describe the month of emission: January denotes the period January-March 2015 and July denotes the period July-September 2015.

Figure 6.8 (a) illustrates the range of SO_2 e-folding times for emissions in January (January - March 2015) and July (July - September 2015). The median e-folding time of 22 days in winter (January) is nearly 60% longer than the summer (July) median of 14 days, which is expected, given the stronger solar radiation in the northern hemisphere during the latter. This increased solar exposure enhances OH production, leading to faster SO_2 depletion. Consequently, the increased depletion rate of SO_2 results in higher SO_4 production, as reflected by the greater SO_4ks and as mean production efficiencies shown in Figs. 6.8 (b) and (c). From January to July, for instance, the median production efficiencies for SO_4ks and SO_4as increase by 41% and 174%, respectively.

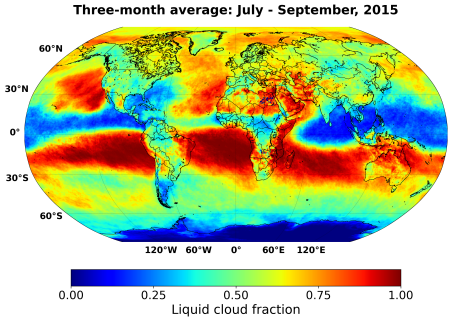
6.7. EXTENSION TO AEROSOL-CLOUD INTERACTIONS

To identify which SO_4 transport patterns are more likely to cause changes in cloud properties, it is essential to first approximate the location of liquid clouds. For this purpose, the AVHRR-AMv3 dataset was used to examine the spatial distribution of LCF and CTP during the two simulation periods. As shown in Figs. 6.9 (a) and (b), liquid clouds are primarily concentrated in the Northern Atlantic and Southern tropics, with a notably higher mean LCF observed during the summer months (July - September, 2015). During this period, liquid clouds are predominantly found between 0°-30°S across all longitudes. These horizontal cloud distributions align with those reported by Stengel et al. [257] for June 2014. Similarly, Lauer et al. [258], using annual mean satellite data from the International Satellite Cloud Climatology Project (ISCCP) for the period 1983-2004, confirm a significant presence of low-level liquid clouds in the North Atlantic, North Pacific, and South Atlantic regions. According to the mean CTP values shown in Figs. 6.9 (c) and (d), liquid clouds in areas with the highest LCF predominantly occur at pressure altitudes below 800 hPa.

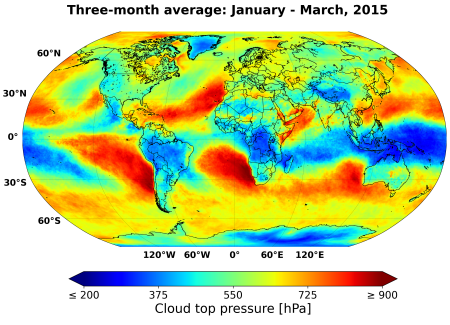
The regions most likely for low-level liquid clouds are highlighted with a blue rectangle for emission points 8 and 9 during July 2015 emissions in Fig. 6.10. When emissions occur near the Northern midlatitudes (Fig. 6.10 (a)), SO_4 tends to have an extended residence time near the cruise altitude, resulting in slower transport to lower altitudes. The green median trajectory shows that air parcels following this path remain close to the emission pressure altitude of approximately 240 hPa for around 8 days before descending toward the surface, eventually reaching latitudes between 30°-60°N. Although it is unlikely that SO_4 will reach the primary region with liquid clouds indicated in blue, it could still interact with some clouds present in the North Atlantic (see Fig. 6.9). In contrast, emissions in the Southern tropics (Fig. 6.10 (b)) present a higher likelihood for interactions between aviation SO_4 and the abundant liquid clouds in the Southern tropical region.



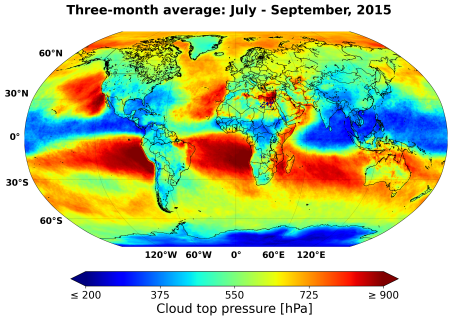
(a) LCF: January - March, 2015



(b) LCF: July - September, 2015



(c) CTP: January - March, 2015



(d) CTP: July - September, 2015

Figure 6.9: Three-month means for the liquid cloud fractions (LCF) between (a) January - March of 2015 and (b) July - September of 2015. Panels (c) and (d) represent the same time periods as (a) and (b) respectively, but for the three-month means of the cloud top pressure (CTP) in hPa.

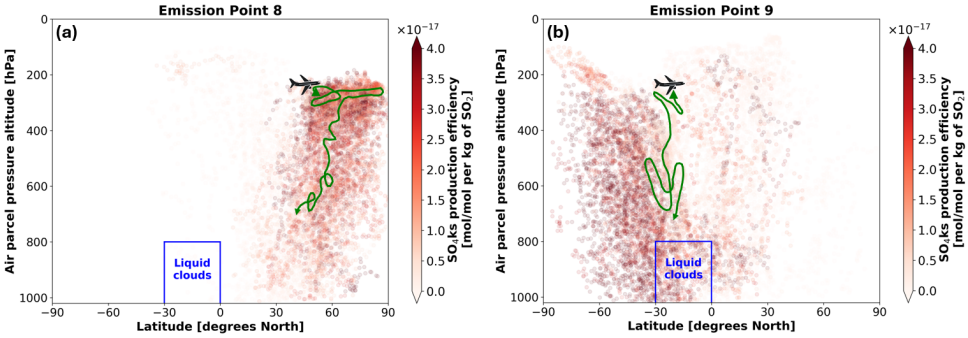


Figure 6.10: Transport patterns for aviation-induced sulfate aerosols when SO_2 and H_2SO_4 are jointly emitted during July 2015 at (a) emission point 8 and at (b) emission point 9. The green curves represent the median trajectories in each case. The green triangles next to the aircraft icon indicate the emission points. The blue region denotes the most probable location of lower-level liquid clouds between July - September of 2015 according to the AVHRR-AMv3 dataset.

6.8. DISCUSSION

This section highlights the uniqueness of AIRTRAC 2.0 within the EMAC modeling framework, underlining its ability to provide new insights into transport patterns that are most likely to influence aerosol-cloud interactions. It also critically examines key limitations of the submodel and concludes by proposing directions for future research and potential enhancements.

6.8.1. ACHIEVEMENTS

AIRTRAC 2.0 is the first Lagrangian sulfate tagging scheme within EMAC, uniquely enabling the characterization of the complete atmospheric journey of aviation-emitted sulfur compounds in the gas and aerosol phases. In the context of aviation, AIRTRAC 2.0 advances our understanding of one of the most uncertain aviation-related climate effects: aerosol-cloud interactions. This is achieved by tracking the long-range transport of sulfur species, beginning with the emission of SO_2 and H_2SO_4 at subsonic cruise altitudes, through their chemical conversion into sulfate, and finally to their descent into the lower troposphere where they might interact with liquid clouds.

As demonstrated in Section 6.5, the submodel effectively captures differences in aerosol production efficiencies for two soluble sulfate modes based on the location of emission. Furthermore, AIRTRAC 2.0 identifies the contributions of various aerosol microphysical processes—such as coagulation and nucleation—to sulfate mixing ratios throughout an air parcel's trajectory. This capability provides a nuanced understanding of the dominant processes at different atmospheric altitudes and regions, with a detailed summary presented in Appendix E (see Figs. E.21 and E.28). By delivering such detailed insights, AIRTRAC 2.0 not only improves our understanding of aviation-induced aerosol impacts, but also offers a comprehensive picture of the global transport patterns of sulfate aerosols, paving the way for more informed assessments of their climatic implications.

6.8.2. LIMITATIONS

The linearization of production and loss rates, along with the simplified chemistry in AIRTRAC 2.0 (e.g., neglecting the liquid-phase production of H_2SO_4), introduces comparable limitations to those discussed in Chapters 4 and 5 in the context of NO_x-O_3 chemistry. A new consideration specific to AIRTRAC 2.0 involves assessing whether the LGTMIX mixing parameters $d = 1 \times 10^{-3}$ in the troposphere and 5×10^{-4} in the stratosphere (see Eq. 3.21), which were initially applied mainly for gas-phase chemistry, realistically capture mixing dynamics for aerosol species. It is reasonable to assume these values of d still apply to SO_2 and H_2SO_4, as they are considered to be in gaseous form throughout the simulations. However, uncertainty remains around whether turbulent mixing intensities relative to aerosol microphysical processes are realistic or if adjustments to the mixing parameters might be required. Additional sensitivity simulations have been conducted to begin addressing this question (see Appendix E.8). Figures E.30 and E.31 indicate that as turbulent mixing intensifies (increasing d), SO_4ks and as VMRs tend to decrease due to stronger interactions with neighboring air parcels with smaller or even null SO_4 mixing ratios. Choosing optimal mixing parameters will require further validation, ideally including comparisons with aircraft observations, as detailed in van Donkelaar et al. [259]. The recent launch of NASA's Plankton, Aerosol, Cloud, and ocean Ecosystem (PACE)[2] satellite could also provide new opportunities to better validate AIRTRAC through global measurements of sulfate aerosol optical thickness.

A current limitation of AIRTRAC 2.0 is its inability to track SO_4 particles that have been scavenged and later re-evaporated back into the atmosphere, which may lead to underestimations in aerosol mixing ratios. This limitation also applies to gas-phase species. Another factor potentially contributing to underestimated mixing ratios is the exclusion of the aqueous-phase SO_4 production pathway via SO_2 oxidation by H_2O_2 (see Fig. 6.1). Conversely, the exclusion of plume-scale processes could lead to overestimations. For NO_x-O_3 chemistry, plume-scale processes are estimated to contribute approximately 20-30% of overestimation, but this effect is less certain for aerosol processes.

Another limitation of AIRTRAC 2.0 is the exclusion of interactions between aviation NO_x and SO_4 aerosols, despite their mutual dependence on the OH radical. As extensively discussed in Chapters 2, 4, and 5, NO_x emissions contribute to indirect O_3 formation and produces OH in the process. This OH radical is essential for oxidizing SO_2 and initiating gas-phase SO_4 formation. Consequently, to fully understand aviation NO_x climate impacts, incorporating SO_4 tracking becomes essential. AIRTRAC 2.0 will therefore be useful in allowing assessments of both the complete NO_x impacts and SO_4 indirect effects for conventional kerosene-powered aircraft and emerging hydrogen-powered aircraft, many of which will continue to emit NO_x [260]. By expanding to include SO_4, AIRTRAC 2.0 can independently track both NO_x-O_3 chemistry and SO_4 microphysics along Lagrangian air parcel trajectories. However, these processes are currently implemented separately and thus do not interact or influence one another.

6.8.3. FUTURE RESEARCH

One of the useful advancements for AIRTRAC would ergo be to connect NO_x chemistry with aerosol microphysics, which can be accomplished by updating the tagging ratio in

[2] https://pace.oceansciences.org/home.htm

Eq. 6.2 according to the bimolecular reaction formulation [147, 156] applied to Reaction R25, thereby accounting for aviation-induced OH as a contributing factor. This updated approach, detailed in Eq. 6.23, establishes a framework for quantifying aviation's indirect effects on SO_2 through NO_x-driven OH production.

$$C_{SO_2}\big|_{avi} = \underbrace{C_{SO_2}(t=0)}_{\text{Emission}} - \underbrace{\frac{1}{2} \times \left(\frac{C_{SO_2}\big|_{avi}}{C_{SO_2}\big|_{avi} + C_{SO_2}\big|_{rem}} + \frac{C_{OH}\big|_{avi}}{C_{OH}\big|_{avi} + C_{OH}\big|_{rem}} \right)}_{\text{Revised tagging ratio}} \times \underbrace{\frac{M_{SO_2}}{M_{H_2SO_4}}}_{\text{Molar masses}} \times \underbrace{P_{H_2SO_4}}_{\text{Production rate}} \times \Delta t + \underbrace{R(C_{SO_2})}_{\text{Turbulence}} \tag{6.23}$$

Other significant technical advancements involve extending AIRTRAC to encompass the remaining seven aerosol modes and expanding its output to include the particle number concentration of SO_4. This parameter is crucial for accurately assessing aerosol-cloud interactions and their climatic implications.

Beyond further model development, a key next step is identifying the transport patterns most likely to result in aerosol-cloud interactions, as has been demonstrated as a proof of concept for two emission points in Section 6.7. Combining this analysis with the neuroscience-inspired clustering technique introduced in Chapter 5 could systematically and efficiently reveal the dominant SO_4 transport patterns for aviation. However, the clustering function (Eq. 5.1) may require further adaptation, such as replacing the perturbation RF with the total sulfate mixing ratio (sum of all nine modes). Additionally, exploring how sulfate transport pathways vary with weather patterns, as investigated by Frömming et al. [36] for other non-CO_2 climate forcers, and evaluating the non-linearity of aviation aerosol effects, akin to the NO_x-O_3 studies by Rosanka et al. [37] and Maruhashi et al. [13], are essential directions for future work. Finally, validation against another sulfate tagging scheme, similar to the approach used in Chapter 4 for NO_x-O_3, remains a critical step.

6.9. SUMMARY AND CONCLUSIONS

This chapter presents the new functionalities and technical implementation of the AIRTRAC 2.0 submodel within the EMAC framework, which now enables the estimation of mixing ratios for the soluble Aitken and accumulation modes of SO_4 stemming from aviation-induced SO_2 and H_2SO_4 emissions. To showcase AIRTRAC's capabilities in characterizing the transport patterns of aviation-related SO_x, two seasonal three-month simulation scenarios (winter and summer) were analyzed using the CMIP6 emissions inventory. Furthermore, ESA satellite data was integrated with AIRTRAC's output to illustrate how interactions between aviation-induced SO_4 and liquid clouds can be predicted. Given that AIRTRAC 2.0 is currently one of the few Lagrangian tagging models capable of tracking aviation's impact on SO_4, direct validation against other Lagrangian models remains challenging. As an initial assessment, additional perturbation-based simulations were conducted using a configuration similar to that of Righi et al. [160].

The transport patterns of SO_2 and SO_4 are primarily driven by atmospheric circulation, with certain vertical profiles aligning with tropospheric circulation patterns of the Hadley, Ferrel and Polar cells. Similar to interactions observed with NO_x-O_3 and other aviation-related non-CO_2 pollutants, SO_2 that is quickly transported to lower altitudes has a shorter atmospheric lifetime due to higher background OH concentrations, which accelerate its oxidation. Seasonal variations significantly affect SO_2 e-folding times: the median lifespan is approximately 22 days from January to March 2015 but decreases to 14 days during the summer months (July to September), reflecting a nearly 40% reduction. The production efficiencies of SO_4 also vary seasonally due to differences in solar radiation. In summer, increased sunlight enhances OH production, thereby boosting SO_4 formation. Between winter and summer, the median production efficiencies of SO_4ks and SO_4as increase by 41% and 174%, respectively. Regarding potential interactions with low-level liquid clouds, emissions in the Northern midlatitudes during summer (July) are less likely to reach the primary region of liquid cloud occurrence in the Southern tropics, as identified by ESA cloud satellite data, compared to emissions originating directly in the Southern tropics.

AIRTRAC 2.0 is a diagnostic tool that relies on the aerosol tendencies of MADE3, which have been validated by previous studies against observations from satellites and measurement stations (see Section 3.3.3). However, the validation of AIRTRAC itself is challenging, given its distinctive capability to quantify aviation-specific contributions to atmospheric SO_4. In theory, it should first be compared with a full tagging scheme, ideally within EMAC, as has been done in Chapter 4 for NO_x-O_3. Since EMAC does not currently have a sulfate tagging scheme, comparisons have been made with results from perturbation-based simulations using the EMAC model, which apply the same background emissions and many of the same submodels. Direct comparison of mixing ratios is not feasible given the fundamental methodological differences, with AIRTRAC modeling pulse emissions via a tagging approach while the perturbation simulations assume sustained emissions. Instead, the spatial distribution patterns of aviation-induced sulfate are assessed. For summer emissions, both approaches agree that SO_4as mixing ratios are strongest near the emission region, with enhanced downward transport between latitudes 20°-40°N. Yet, for the ks mode, AIRTRAC predicts the greatest mixing ratios around the emission region, whereas the perturbation method estimates these near the surface. These discrepancies likely arise from the inherent differences between pulse and sustained emission and between tagging versus perturbation methods.

Further validation of AIRTRAC 2.0 using models beyond EMAC is essential. While sulfate tagging models are relatively uncommon, a few do exist and could provide valuable reference points. Potential Eulerian benchmarks include the approach implemented in the CESM/CAM5 model by Yang et al. [236], the online SO_4 tagging model within NAQPMS used by Wu et al. [245], or the PSAT algorithm [247] integrated with the CAMx model as applied by Itahashi et al. [246]. A comparison with a Lagrangian tagging approach could involve using the HYSPLIT model, as seen in the inverse modeling study by Riccio et al. [248]. Validation against another tagging submodel within the EMAC framework would require extending the existing TAGGING submodel to include SO_4, similar to the comparison study in Chapter 4 involving NO_x and O_3. Beyond these validation efforts, the next critical steps for AIRTRAC's development include expanding its capabili-

ties to cover the remaining seven SO_4 modes, integrating NO_x-O_3 chemistry with its new SO_4 microphysics capabilities, and extending tagging to include aerosol particle number concentrations. These enhancements would not only deepen our understanding of aviation-induced SO_x climate effects, but also enable more robust assessments of aviation NO_x interactions with SO_4 and their subsequent influence on cloud interactions.

6.10. DATA AVAILABILITY STATEMENT

The simulation data produced and analyzed in this chapter are openly available in the following repository:
https://doi.org/10.4121/79bcd360-04fc-4efc-a908-09874b9703c5.

The code for AIRTRAC 2.0 is accessible upon reasonable request in the DKRZ Gitlab: https://gitlab.dkrz.de/MESSy/MESSy.

7

CONTRIBUTION TO CLIMATE-OPTIMAL ROUTING

A brief overview of the methodology behind the climate change functions is provided along with their significance in enabling climate-optimal routing. The datasets produced by AIRTRAC, as described in Chapters 4 and 5, have served as the computational foundation from which a lighter surrogate model for the estimation of short-term $NO_x - induced\ O_3$ warming impact has been developed. The application of this model to real flight trajectories is shown [154].

Parts of this chapter have been published in Rao et al. [154].

7.1. CLIMATE CHANGE FUNCTIONS (CCFS) AND CLIMATE-OPTIMAL ROUTING

AVIATION CO_2 emissions lead to climate effects that are largely independent of spatial factors, such as emission location, because of CO_2's significantly longer atmospheric lifetime, which extends over thousands of years—far longer than that of any other aviation-induced pollutant. In contrast, for non-CO_2 climate forcers, spatio-temporal factors like flight altitude and the season during which the flight occurs are critical. This presents an opportunity to mitigate aviation's non-CO_2 climate impact by avoiding climate-sensitive regions, a strategy known as climate-optimal routing. To implement this approach, the multidimensional climate change functions or CCFs are essential as they associate a climate impact per unit amount of emitted pollutant to a set of pre-defined locations on the globe. They rely on the selection of an appropriate climate metric that reflects both a reasonable time horizon within which to analyze the climate effects and the emission scenario, which underpins the assumed evolution of aviation technology over time [23, 261]. The climate metric used in Frömming et al. [36] for the development of the net NO_x, H_2O and contrail CCFs in the North Atlantic flight corridor is the average global temperature response over 20 years (ATR20) [23, 262]:

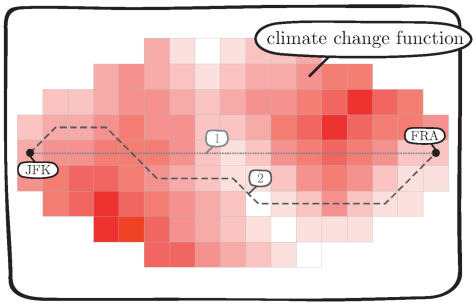
$$\text{ATR20} = \frac{1}{20}\int_{t_0}^{t_0+20} \Delta T(t)\,dt. \tag{7.1}$$

Choosing an appropriate climate metric depends on the specific research question. According to Grewe and Dahlmann [263], the effective choice of a climate metric is a multi-step process that involves carefully formulating a time-specific and quantifiable research question, setting a reference with which to compare an emission scenario (possibly in the future) and selecting an adequate time horizon. The choice of time horizon itself directly influences the value determined by a climate metric; shorter time horizons emphasize the impacts of short-lived climate forcers such as NO_x and contrails, whereas longer time horizons highlight the effects of longer-lived pollutants like CO_2 [264]. The original CCFs were developed to answer the question: "What is the short-term climate impact of a re-routing strategy?" Consequently, ATR20 was selected to focus on a short-term time horizon, using a 20-year period (in contrast, medium- to long-term scenarios might consider 50- or 100-year horizons). The climate impact is then measured in terms of the global mean change in Earth's surface temperature, or its average temperature response (ATR) [23].

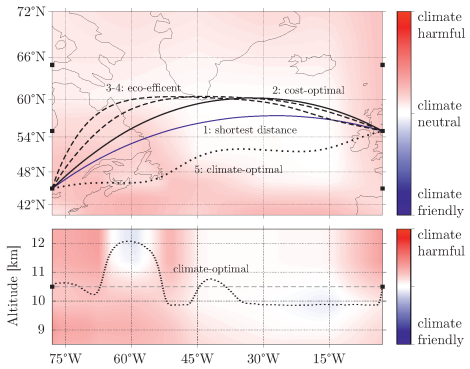
For short-term climate impact analyses, CCFs will depend on meteorological conditions in which the emission is introduced, in which case they are weather-dependent and ergo describe the spatial variation of the atmospheric effects of a pollutant within a specific weather pattern. Alternatively, they may be climatological, in which a longer-term climate response to a future scenario is assessed [18]. As a final step prior to determining green flight trajectories, the CCFs are fed into an air traffic optimization tool, like AIRTRAF [265] or Eurocontrol's System for traffic Assignment and Analysis at a Macroscopic level (SAAM) [266], to minimize the total climate impact predicted by CCFs throughout the flight trajectories.

The objective of climate-optimized trajectory planning using CCFs is conceptually

straightforward: to avoid regions where the values of a selected CCF—such as those representing contrails, net NO_x, or H_2O—are high. However, the practical implementation of this approach can be considerably more complex. Figure 7.1a shows two possible routes connecting New York (JFK) and Frankfurt (FRA). Trajectory 1 minimizes the distance between the two cities, whereas Trajectory 2 aims to reduce the total climate impact as estimated by CCFs. In this context, darker red regions indicate stronger climate effects. The optimization in Trajectory 2 may involve lateral deviations (in latitude and longitude) and/or altitudinal adjustments, as illustrated in Fig. 7.1b.



(a) Comparison between the shortest-distance path (Trajectory 1) and the climate-optimal route (Trajectory 2). The red hue indicates the climate impact predicted by the climate change function (CCF). Figure was reproduced from [157].



(b) A 3D climate-optimal route. The upper panel represents the optimal route in a latitude-longitude grid and the lower panel the optimal altitude as a function of longitude. Figure was reproduced from [267].

Figure 7.1: 2D and 3D climate-optimal trajectories based on the application of CCFs.

7

7.2. ALGORITHMIC CCFS (ACCFS)

Algorithmic CCFs or aCCFs were constructed with the objective of reducing the computational burden of calculating the climate impact for a given region with the traditional method of CCFs, since these require expensive large-scale simulations from complex climate models. In speeding up and simplifying this process, the possibility of making climate-optimized routing operational becomes more likely. Algorithmic CCFs have been developed for climate impacts arising from NO_x-O_3 chemistry, CH_4 and H_2O emissions by van Manen and Grewe [46]. This was accomplished by applying linear regression techniques to meteorological variables like the geopotential or the temperature of the atmosphere. They found that the potential vorticity was the most relevant parameter for H_2O aCCFs, for O_3 effects the temperature and geopotential were the most important and lastly the CH_4 aCCFs were derived as a function of the geopotential and the incoming solar flux at the top of the atmosphere. The validity of using aCCFs has been addressed, particularly by Rao et al. [268], in which they investigated how the climate impact could be reduced, even if, only the NO_x-O_3 aCCFs are considered. They found, despite certain discrepancies during the summer day, that such a method of climate-routing already shows promising results overall.

The aCCFs are a step in the direction of operationally enabling climate-optimal rout-

ing by quickly estimating the climate impact according to the most relevant meteorological factors for a certain climate forcer, they do however, bear three main limitations. The first is their reduced accuracy deriving from the application of a deterministic linear regression approach to represent highly non-linear phenomena[1], the second is the lack of an uncertainty quantification and ergo the inability to capture these at every estimated point and thirdly their domain of validity is confined to the North Atlantic Flight Corridor (see Fig. 3 in Grewe et al. [23]). Based on the adjusted regression coefficient R^2, which measures the goodness of fit between the aCCFs and the CCFs, the chosen regression models revealed low predictive skill, with a maximum value of 0.59 for H_2O aCCFs and a minimum of 0.17 for NO_x-induced CH_4 aCCFs [46]. Naturally, these R^2 values are proportional to the uncertainties already present in the CCFs, where the level of understanding is larger for H_2O direct effects than NO_x indirect effects [27]. Additionally, the computed R^2 values are likely to be lower given that no separation of the CCF input dataset into training and test data was performed (typically 80% of the data are used for the regression and the remaining 20% for its validation) [154].

7.3. PROBABILISTIC ACCFS (PACCFS)

The probablisitc aCCFs or paCCFs address the weaknesses mentioned in the previous section by adopting a Gaussian process (GP) regression approach as the underlying regression model to estimate the short-term iRF induced by aviation NO_x. Unlike the linear regression applied in van Manen and Grewe [46], the GP model developed by Rao et al. [154] produces a probability distribution for every estimated point based on a set of relevant features. For short-term NO_x-O_3 interactions, these were deemed to be the dry air temperature, the geopotential, solar irradiance, zonal wind velocity and the latitude of emissions according to the mutual information score. Two different types of GP models were produced for the paCCFs: the standard and the chained. The former is primarily characterized by homoskedasticity or constant variance and the latter by heteroskedasticity or changing variance. When comparing the performances of the aCCFs and the paCCFs in estimating the short-term iRF of NO_x-induced O_3, the latter displays superior predictive skill, with an R^2 of 0.42 for the former and 0.53 for the standard GP regression and 0.51 for the chained model.

Another advantage of the probabilistic approach over the aCCFs is the flexibility of the GP model given its non-parametric nature. This approach avoids constraining the underlying regression function to a predetermined form or fixed number of parameters, allowing for greater flexibility and fewer assumptions about its structure. As a result, it offers a more adaptable framework for extending the paCCFs to additional climate forcers by enabling the incorporation of new parameters or the removal of those that exhibit strong collinearity.

The chained GP model has been applied to estimate the O_3 iRF during cruise (Fig. 7.2 (a)) along three popular European flights between Amsterdam Schiphol airport and Madrid-Barajas airport (Fig. 7.2 (b)). Flights 1 and 2 departed in the morning (~10 UTC) while flight 3 departed in the late afternoon (~19 UTC). The iRF maximum for all three

[1] The product term of the potential temperature and geopotential is linearly regressed to account for non-linearities.

actual flights coincides at a latitude of approximately 45° N, the exact location is indicated by an orange parallelogram in Fig. 7.2 (b). Based solely on the short-term O_3 iRF, Fig. 7.2 (a) suggests that the flight trajectory with the largest O_3 climate impact at cruise is Flight 1 and the one with the smallest is Flight 2. When a more distinct flight path, like the theoretical great circle trajectory, is considered, the spatial variation of the O_3 iRF is also different, thereby confirming its sensitivity to the selected input features. Figure 7.2 (a) also reveals the uncertainty range that is provided throughout the trajectory. Their varying sizes indicate the heteroskedastic capability of the chained GP model. These intervals could be regarded as probabilities that an aircraft will induce a certain warming at cruise, where a narrower interval is desired as there is less uncertainty surrounding this estimate. The development of the paCCFs may therefore, in the future, contribute with the necessary uncertainty levels of certain aircraft manoeuvres in reducing the overall climate impact.

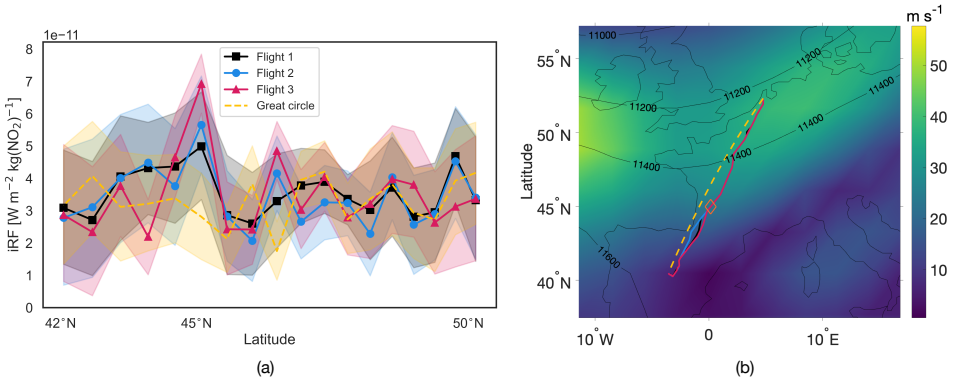


Figure 7.2: (a) Estimates for the climate impact according to the emission-scaled ozone instantaneous radiative forcing metric (iRF) in units of $Wm^{-2}kg(NO)^{-1}$ according to the chained GP model. The three solid lines represent real flight routes from the EUROCONTROL database [269] while the yellow dashed line depicts the great circle distance at cruise altitude. Each line has a corresponding shaded region that represents its 95% confidence interval about the mean. The markers along the mean iRFs denote specific points along the flight route at which the surrogate model was evaluated. The three flights exhibit maxima at 45° N. (b) Complete flight trajectories for the three real routes, including take-off and landing. The colormap and contour lines indicate the wind speed and geopotential height in ms^{-1} and m respectively at a pressure altitude of 216 hPa. The orange diamond represents the region of maximum climate impact for the three flights. Figure was reproduced from [154].

7.4. LIMITATIONS AND FURTHER RESEARCH

Despite the computational cost traditionally associated with constructing CCFs from global datasets of aviation climate impacts across various spatio-temporal conditions, AIRTRAC has markedly accelerated this process. By enabling simultaneous and independent emission scenarios to be calculated within a single simulation, AIRTRAC significantly enhances data generation efficiency. This leads to a greater volume of instantaneous radiative forcing estimates for different climate forcers across diverse conditions, which is crucial for the uncertainty quantification of reduced-order models like aCCFs

and paCCFs. In particular, the more flexible paCCFs benefit from a larger dataset to provide more coverage in its predictions. This dissertation has further developed AIRTRAC as the computational backbone for generating these surrogate models. Specific improvements include identifying correction factors to enhance the accuracy of short-term O_3 iRF predictions (see Chapter 3), as well as expanding the model's output from the North Atlantic flight corridor to a global scale (see Chapters 3 and 4). Additionally, AIRTRAC 2.0 provides preliminary analyses on the uncertain transport patterns of SO_4 aerosols (see Chapter 6). Figure 7.3 offers a concise overview of AIRTRAC's contributions to the evolution of CCFs, highlighting the benefits and limitations of each approach.

Despite these advancements in AIRTRAC, several steps remain before climate-optimal routing can be effectively implemented in the aviation industry. A notable limitation is related to the resolution dependency of AIRTRAC simulations. The simulations for aCCFs and paCCFs were conducted at a T42 resolution, introducing potential uncertainties if higher resolutions are used. Additionally, the current formulation of the paCCFs [154] does not incorporate the AIRTRAC correction factors identified in Chapter 4, however, these may be applied offline in subsequent paCCF studies. A more significant challenge lies in implementing the full range of non-CO_2 climate forcers for a comprehensive assessment of aviation's climate impact. Preliminary RF estimates suggest that the cooling impact of sulfate aerosols, particularly from their indirect effects, may be greater than aviation's largest warming contribution from contrails [226]. Thus, a robust routing strategy must carefully balance the trade-offs among various climate forcers. Moreover, the influence of plume-scale processes needs to be considered as well. For instance, the climate impact of NO_x emissions may currently be overestimated by approximately 20% [188–191], and the effects of plume-scale chemistry on more uncertain forcers, such as aerosol indirect effects, remain largely unknown. Addressing these gaps is critical for refining climate-optimal routing strategies and ensuring their efficacy in real-world applications.

In addition to these modeling challenges, several practical concerns have been raised regarding the implementation of climate-optimal routing, which may lead to resistance from some aviation stakeholders. For airlines, the primary concern is whether climate-friendlier routes would incur increased operating costs, as such routes might require deviations that extend flight duration. Grewe et al. [270], for instance, found that reducing the net climate impact (including CO_2, H_2O, contrails, and NO_x) by 25% and 100% on westbound Northern trans-Atlantic flights during a winter day would lead to additional time penalties of only 1.8 minutes and 35.4 minutes per flight, respectively. In terms of financial implications, reducing the climate impact by 25%, for instance, was found to increase economic costs (encompassing fuel, crew, and air traffic control expenses) by less than 0.5%. A companion study [271] examining Northern trans-Atlantic flights during both summer and winter seasons reported that a 10% reduction in aviation's climate impact could be achieved at an operational cost increase of only 1%. Notably, if market-based measures targeting non-CO_2 effects were introduced, operating costs could potentially decrease when adopting climate-optimal routes. A broader analysis conducted by Frias et al. [264], which included both domestic flights in the USA and international routes to East Asia, corroborated these results. The study demonstrated that reducing contrail-related climate effects by approximately 70% could be achieved with a minimal

increase of only 0.1% in additional fuel consumption. These findings have been further validated through a collaborative research initiative [272] between Google, Breakthrough Energy and American Airlines, where 70 real flights were optimized to avoid regions most sensitive to persistent contrail formation, as predicted by Google's AI-based models. Satellite observations indicated a 54% reduction in persistent contrail formation, albeit with a small 2% increase in fuel burn.

The added cost to passengers is projected to be negligible; a recent briefing by Transport and Environment [273] estimated that, on average, ticket prices would increase by approximately €1.60 for European flights and €4.30 for trans-Atlantic flights. From an air traffic management perspective, some argue that rerouting flights to avoid climate-sensitive areas could increase workload and complexity, particularly around congested regions [274]. However, a detailed simulation focusing on Northern trans-Atlantic flights indicated that the additional workload for air traffic controllers would be relatively small [18]. Moreover, if the objective is solely to mitigate contrail-induced warming, the impact on controller workload could be even less pronounced. According to Teoh et al. [275], only about 2% of flights are responsible for generating 80% of total annual contrail RF, suggesting that targeted rerouting efforts could yield substantial benefits with minimal disruption.

In summary, both modeling studies and real-world flight tests indicate that a significant portion of aviation's climate impact could be mitigated at a modest cost in terms of time, fuel, and economic cost. However, these conclusions are based on climate impact estimates that carry substantial uncertainties and do not fully account for all climate forcer effects, such as aerosol-cloud interactions—an area where the AIRTRAC model may offer valuable insights.

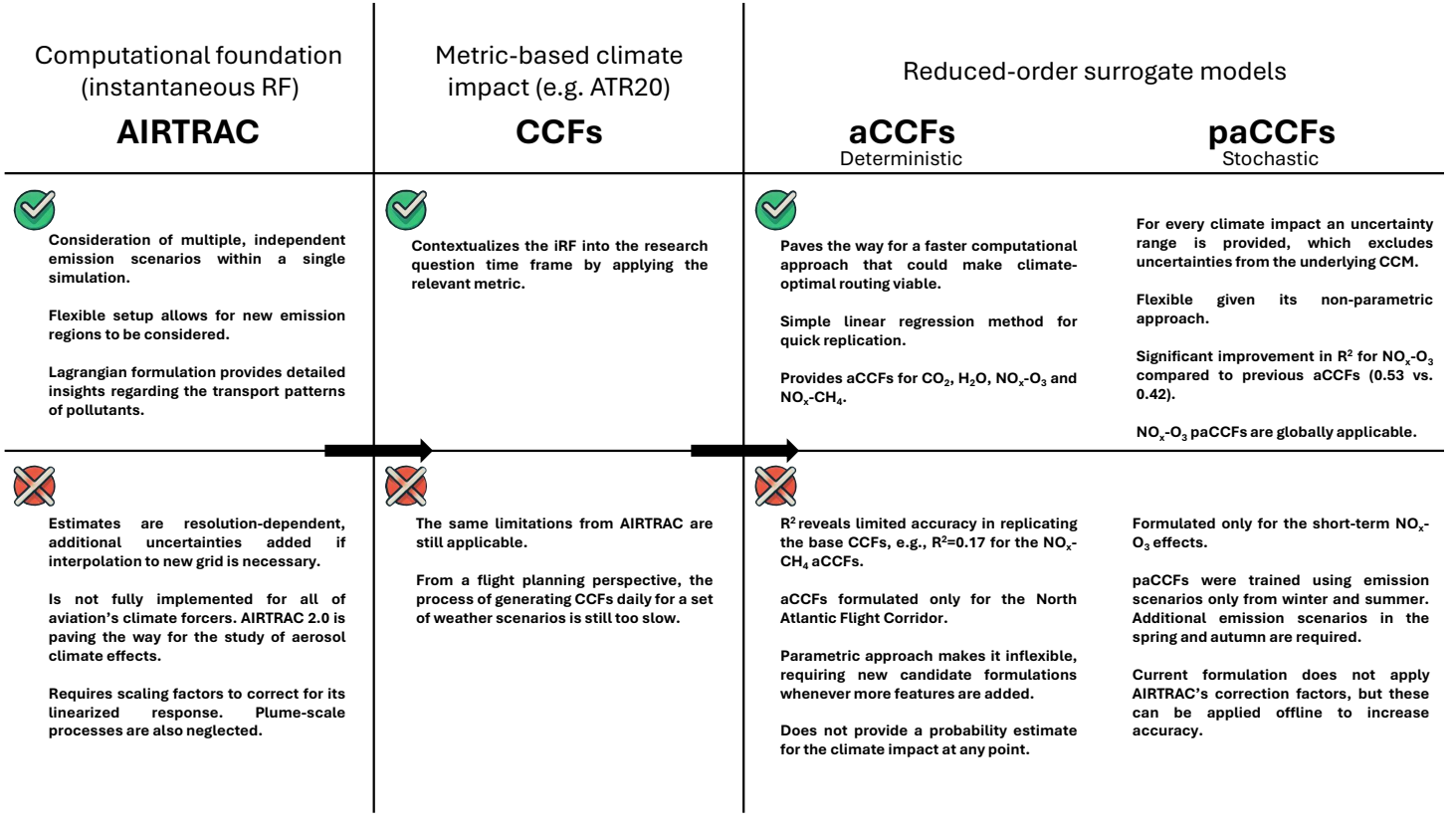


Figure 7.3: Summary of the strengths and limitations of AIRTRAC, climate change functions and associated surrogate models.

8

CONCLUSIONS AND OUTLOOK

The final chapter of this thesis offers a comprehensive overview of the key concepts discussed in the previous chapters. In Section 8.1, a detailed summary of the knowledge gained from each research objective, as outlined in Chapter 1, is provided. Additionally, Section 8.2 addresses the remaining limitations of the research and explores potential future directions that could expand on the findings presented here.

8.1. CONCLUSIONS

THE overarching goal of this dissertation has been to explore the transport patterns of non-CO_2 pollutants from aviation and their potential impact on climate. The research mainly focused on the short-term interactions between NO_x and O_3, along with the influence of SO_2 and H_2SO_4 emissions on SO_4 aerosols, given the significant uncertainties associated with these processes. The key findings related to each of the four research objectives, introduced in Section 1.3.1, are summarized in the sections that follow.

Research objective #1: Understand the spatio-temporal dependence of aviation short-term NO_x-O_3 climate effects on emission altitude, region, and season of emission, as well as how transport patterns play a role.

Chapter 5 has provided a detailed characterization of the global transport patterns of NO_x emissions and their influence on short-term O_3 production across two distinct seasons: summer and winter. This analysis was made possible by enhancing the scavenging mechanism of a Lagrangian tagging submodel, AIRTRAC, which is part of the EMAC climate-chemistry model. Lagrangian models such as AIRTRAC generate vast amounts of data by tracking the chemical evolution of pollutants along hundreds of thousands of air parcel trajectories. To efficiently distill insights from this extensive dataset, a clustering algorithm, originally developed for neuroscience applications, was incorporated into the post-processing workflow. This is the first time such an approach has been applied within the context of aviation climate effects, allowing for a systematic identification of the most probable transport pathways in each region.

The results demonstrated a strong dependence of transport patterns on both horizontal (meridional and zonal) and vertical wind components. Horizontally, aviation emissions are primarily guided by dominant westerlies in both the Northern and Southern Hemispheres. Vertically, emissions introduced in regions with strong downdrafts are rapidly transported to lower altitudes, where removal processes, on average, are more efficient and larger OH concentrations exist, resulting in shorter chemical lifetimes. In contrast, weak downdrafts or updrafts can lead to extended chemical lifetimes, as the upper layers of the atmosphere exhibit greater chemical and dynamic stability.

Seasonal variations were also observed. During the Northern summer, emissions at higher latitudes, particularly near the mid-latitudes, resulted in enhanced O_3 production due to more active photochemical processes. Conversely, O_3 production was lower during the winter months. On a regional scale, significant differences in O_3 production were attributed to local background NO_x levels. For instance, aviation emissions occurring in, or transported to, the Australasian region showed the highest O_3 production — almost by a factor of 3 compared to Eurasia during January — due to the lower background concentrations of NO. Furthermore, atmospheric transport patterns were found to play a critical role in carrying emissions to distant regions, effectively transforming them into non-local sources that drive climate impacts far from their point of origin—a phenomenon that becomes more pronounced for species with longer atmospheric lifetimes. For example, NO_x emitted near North America in July results in the largest short-

term O_3-induced RF over Europe, while NO_x emitted near South America in January has the largest impact on the Australasian region.

The findings from Chapter 4 largely align with previous studies, which suggest an almost linear relationship between changes in flight altitude and changes in climate impact (measured in terms of RF). Flying at higher altitudes during cruise is likely to exacerbate the warming effects from short-term NO_x-O_3 interactions, as the upper layers of the atmosphere are more stable and removal processes are less efficient. However, earlier conclusions were predominantly based on aviation emissions inventories heavily influenced by the higher flight density in the Northern trans-Atlantic corridor. While this assumption has been valid for the past few decades, it does not adequately reflect the substantial growth in flights in the Pacific region, which alters the flight patterns assumed in older studies. This dissertation addresses these gaps by analyzing regional sensitivities of aviation-induced NO_x-O_3 interactions with altitude (h) on a global scale, using a more balanced emissions distribution. In certain regions, the altitudinal sensitivity of these climate effects, represented by $\frac{dRF_{O_3}}{dh}$, increases significantly due to seasonal variations. For example, flying at higher altitudes during the summer can result in a much stronger warming effect compared to winter. In Eurasia, for instance, the altitudinal sensitivity of RF during summer is approximately twice as strong: $\left.\frac{\Delta RF_{O_3}}{\Delta h}\right|_{\text{summer}} \approx 2 \times \left.\frac{\Delta RF_{O_3}}{\Delta h}\right|_{\text{winter}}$.

Research objective #2: Quantify the differences between the tagging and perturbation methods in the context of short-term aviation NO_x-O_3 chemistry. Derive correction factors for a reduced-order Lagrangian tagging submodel (AIRTRAC) by comparing it to a high-fidelity tagging submodel so as to leverage its computational efficiency in sustainable decision-making.

Most assessments of aviation's climate effects rely on the perturbation approach, which is well-suited for quantifying the impact of changes in emissions. However, to accurately estimate the sectoral contribution to total radiative forcing, a tagging approach is required. A comprehensive evaluation of anthropogenic climate impacts should ideally incorporate both methods: the tagging approach to identify the sector with the greatest mitigation potential, and the perturbation approach to assess the effectiveness of mitigation measures. In Chapter 4, three methods for calculating the short-term O_3 warming effect from aviation NO_x emissions were compared: Lagrangian tagging, Eulerian tagging, and the perturbation method. The comparison between the more accurate Eulerian tagging method and the perturbation approach revealed differences in O_3 production efficiency, ranging from a factor of 1.16 to 2.55, with a mean value of 1.83. These results align with previous studies, which reported a factor of 1.6 for NO_x-induced O_3 warming [31, 41]. This dissertation has demonstrated, on a global scale, that the differences between these two approaches in the context of aviation's NO_x-O_3 effects are systematic. Specifically, the tagging method consistently yields values on average 60-80% higher than those derived from the perturbation method.

Despite AIRTRAC's computational efficiency, which allows for the analysis of multiple emission scenarios within a single simulation, it is limited by certain simplifications, such as a simplified chemistry mechanism and linearized reaction rates. In other words,

at each time step, aviation's contribution is linearized according to the non-linear background production and loss rates of the atmosphere. Specifically, at each time step, aviation's contribution is linearized relative to the emission amount, based on the non-linear background production and loss rates of the atmosphere. To enhance the accuracy of its Lagrangian tagging estimates, AIRTRAC was compared to a higher-fidelity tagging submodel, TAGGING. This comparison led to the derivation of global correction factors ranging from 1.7 to 5.9 for three cruise altitudes, which can be applied offline to adjust AIRTRAC's O_3 production efficiencies to more realistic values.

Research objective #3: Analyze how transport patterns influence SO_4 aerosol concentrations and identify conditions under which these aerosols are most likely to interact with low-level liquid clouds using the novel Lagrangian tagging submodel, AIRTRAC 2.0.

AIRTRAC has been expanded to account for the contributions of aviation-induced SO_2 and H_2SO_4 to the volume mixing ratios (VMR) of two key SO_4 aerosol mixing modes: the soluble Aitken and accumulation modes. To the best of the author's knowledge, this makes AIRTRAC one of the very few Lagrangian tagging submodels capable of tracking aviation-induced sulfate VMRs. As a proof of concept, Chapter 6 details two simulations in which SO_2 and H_2SO_4 emissions were released across 28 emission points, identified based on regions with the highest aviation SO_2 mass fluxes according to the CMIP6 aviation emissions inventory. Results demonstrated that aviation SO_2 is steadily depleted through oxidation by OH radicals, eventually forming H_2SO_4. Similar to NO_x and O_3, emissions that are transported to lower altitudes early on experience shorter SO_2 lifetimes due to more efficient removal processes but possibly also larger production efficiencies given the increased chemical activity in the lower troposphere. Seasonal variations also impact SO_2 lifetimes, with a median of 22 days in January and 14 days in July. This shorter SO_2 lifetime in summer translates to larger SO_4ks and as production efficiencies in summer relative to winter by 41% and 174%, respectively.

A cloud satellite dataset (AVHRR-AMv3) from ESA's Cloud_cci project was integrated with AIRTRAC's output to identify the emission conditions under which aviation-induced SO_4 is most likely to interact with low-level liquid clouds. Across both simulation periods, these clouds were predominantly concentrated in the Southern tropics (approximately 0°-30°S), with the largest liquid cloud fractions observed during the summer period (July–September, 2015). When comparing transport patterns arising from emissions in the Northern midlatitudes and the Southern tropics, both from a pressure altitude of about 240 hPa, emissions from the Southern tropics are more likely to interact with liquid clouds. This is due to their faster descent to lower altitudes, quickly reaching the region that most abounds with liquid clouds. Conversely, emissions in the Northern midlatitudes might linger near the emission altitude for over a week, resulting in lower SO_4 concentrations reaching lower altitudes.

The transport patterns produced from AIRTRAC 2.0 have been compared to those obtained from a perturbation approach. A fair comparison is difficult given their methodological differences and uniqueness of AIRTRAC 2.0, but results show certain agreement. The evolution of H_2SO_4 showed potential increases in VMR several days after emission

and in regions far displaced from the emission source, driven by the continued oxidation of SO_2 until its complete depletion. The transport patterns of both aviation-induced SO_2 and H_2SO_4 directly affect the VMR of SO_4 through various microphysical processes, including nucleation, coagulation, condensation, and growth. For the first time, this research derives tagging formulations for the coagulation of all nine SO_4 modes. This extension of AIRTRAC (version 2.0) has significant potential to reduce uncertainties surrounding aerosol-cloud interactions.

Research objective #4: Demonstrate how the datasets generated by this dissertation can power faster tools that can be trained to provide climate warming effects in a manner timely enough for climate-optimal routing.

The simulations conducted in Chapters 4 and 5 have resulted in the creation of one of the most comprehensive datasets for evaluating the short-term climate warming effects from aviation NO_x-induced O_3. This dataset has been instrumental in training the newly developed probabilistic-algorithmic climate change functions (paCCFs). Chapter 7 highlighted several key advantages of the paCCFs over their predecessor, the aCCFs. Among the most notable improvements are the heteroskedastic quantification of uncertainties for each mean estimate, enhanced accuracy with an R^2 of 0.53 compared to the R^2 of 0.42 of previous aCCFs, and the flexibility of the paCCFs, which allows for easy retraining with new data due to their non-parametric nature. As a proof of concept, the paCCFs were applied to three actual flights within the European airspace, demonstrating their potential for quantifying short-term warming from NO_x-induced O_3 at the level of individual flights. As AIRTRAC expands its coverage of aviation's various climate forcers, it holds significant promise for contributing to the enhancement of similar computational tools designed for operational use. These tools could eventually be integrated with climate-optimal designs, operations and market-based solutions.

8.2. OUTLOOK

The limitations and potential directions for future research are now discussed for each of the key topics explored in this dissertation.

TRANSPORT PATTERNS OF NO_X-O_3 AND THEIR CLIMATE EFFECTS

The research presented in Chapters 4 and 5 marks a significant advancement in visualizing the most probable global transport pathways of aviation NO_x emissions. Future simulations using finer vertical resolution could provide deeper insights into the advective and convective impacts along the trajectories across different regions. The datasets analyzed in this dissertation are based on a single emission time (06:00 UTC) and two specific days: January 1 and July 1, 2014. Expanding the analysis to include additional emission times (e.g., 00:00, 12:00 and 18:00 UTC) could help assess the influence of diurnal variations on O_3 production. Similarly, incorporating more sample days from the spring and autumn seasons would enable a more comprehensive, year-round analysis of seasonal cycles. Currently, the datasets focus solely on the short-term warming effects of O_3; however, other chemical interactions, such as reductions in CH_4 and stratospheric

water vapor (SWV), are also relevant to the net NO_x effect. To achieve a complete understanding of aviation's net NO_x impact, including the conditions under which this effect could potentially become negative, further simulations would be required.

A clustering algorithm called QuickBundles, originally developed for use in neuroscience, was applied to aviation NO_x emissions to enhance the efficiency of pattern recognition. Chapter 5 demonstrated the viability and advantages of this approach when applied to Lagrangian climate data. However, the robustness of the algorithm in determining the minimum number of required clusters still needs further evaluation, as some clusters contain only a single trajectory. One potential improvement to the algorithm would be to test an alternative distance function that incorporates weights for each of the three terms in Eq. 5.1. The optimal number of clusters was indirectly determined using a user-defined parameter θ, with values for each emission region based on the L-method [215]. It would be valuable to explore whether the same number of clusters could be achieved using alternative techniques, such as a combination of sum of squared errors (SSE) and silhouette coefficients, as demonstrated by Li et al. [208]. Additionally, it would be insightful to assess how extreme weather events, such as El Niño, might influence the clustering process, and to apply this technique to other pressure altitudes, such as 200 and 300 hPa.

THE FURTHER DEVELOPMENT OF AIRTRAC AND ITS EXTENSION TO SO_4 AEROSOLS

This dissertation presents significant advancements in the AIRTRAC submodel. One of the key improvements is the enhanced HNO_3 scavenging mechanism, which offers a more precise characterization of NO_x removal processes in the gaseous phase. Furthermore, AIRTRAC has been extended to study aerosols, particularly SO_4, and is one of the very few Lagrangian tagging submodels capable of providing deeper insights into aviation-induced aerosol transport patterns and of improving our understanding of aerosol-cloud interactions. Despite these advances, certain limitations persist in the gas-phase analysis of AIRTRAC. Chapters 4 and 5 highlight the simplified chemistry mechanism and linearized reaction rates as constraints compared to higher-fidelity submodels like TAGGING. Additionally, as discussed in Chapter 6, AIRTRAC 2.0 currently addresses only two of the nine possible mixing states of SO_4, with a complete formulation for all modes to be introduced in Maruhashi et al. [142]. The current implementation also includes certain simplifications in aerosol microphysics. For instance, the complete tagging formulation for coagulation, presented in Appendix E, has been simplified by linearizing the tagging ratio and excluding its dependence on the soluble mass fraction θ. While these simplifications reduce computational complexity, they may slightly compromise accuracy. Future work could explore how results might change if the full coagulation tagging formulations were applied. A major challenge remains in validating the results of AIRTRAC 2.0, as few models offer comparable aerosol tagging capabilities, and observational data for verification are limited. However, the recent launch of NASA's Plankton, Aerosol, Cloud, and ocean Ecosystem (PACE) satellite could provide new opportunities to better validate aerosol models such as AIRTRAC through global measurements of sulfate aerosol optical thickness. These data could be particularly valuable in future phases of AIRTRAC's application, especially when calculating radiative forcing from aerosol-cloud interactions.

Another promising direction for future research would be to enhance AIRTRAC by connecting its NO_x gas-phase and SO_4 aerosol capabilities. This would provide a more comprehensive understanding of how NO_x emissions might further enhance the cooling effect from SO_4 production by increasing atmospheric concentrations of hydroxyl radicals, a process that remains highly uncertain and is not currently addressed in Fig. 1.2 [27], but is discussed in Terrenoire et al. [120].

THE DEVELOPMENT OF NEXT-GENERATION CLIMATE IMPACT TOOLS

The NO_x-O_3 datasets generated by AIRTRAC have served as the computational backbone for training the paCCFs. While these functions demonstrate promising potential as computationally efficient tools for quantifying climate effects along individual flight routes, they inherit the same limitations previously discussed with regard to AIRTRAC. Specifically, the paCCFs are currently constrained to estimating only short-term warming effects from NO_x-induced O_3 and are based on data from just two emission days: January and July of 2014. To enhance the accuracy and applicability of the paCCFs moving forward, incorporating the correction factors derived in Chapter 4 will be essential.

Overall, this dissertation has made significant strides in advancing our understanding of the short-term O_3 warming impacts from aviation NO_x emissions by improving our comprehension of their atmospheric transport patterns. Through the enhancement and extension of the Lagrangian tagging submodel, AIRTRAC, a deeper understanding of the spatial and temporal dependencies of aviation emissions has been achieved. This work has also led to the development of the computationally efficient paCCFs, representing a key step toward more accurate and timely climate impact assessments—an essential component for the potential future implementation of climate-optimal solutions. Despite certain limitations, this research provides a solid foundation for future work to refine these models and broaden their applicability. Ultimately, the findings presented here offer promising pathways for mitigating aviation's climate impact and contribute to the broader goal of making air travel more environmentally sustainable in the near future.

A

APPENDIX A: FULL LIST OF APPLIED EMAC SUBMODELS

This appendix lists all of the EMAC submodels that were used across the simulations in this dissertation. A brief description as well as the corresponding source providing additional details are included. The complete list of submodels that have been developed to date by the MESSy Consortium may be consulted at https://messy-interface.org/.

Table A.1: EMAC submodels used in this work and their functionalities.

Submodel	Functionality	Source
AEROPT	Calculates aerosol optical properties	Dietmüller et al. [187]
AIRSEA	Computes exchange of chemical species between atmosphere and ocean	Pozzer et al. [276]
AIRTRAC	Calculates the contribution of a NO_x or H_2O emission to the atmospheric composition along air parcel trajectories. In version 2.0, the influence of SO_2 and H_2SO_4 on SO_4 may be studied.	Supplement of Grewe et al. [23], this work
ATTILA	Transport scheme for Lagrangian tracers. Accounts for turbulence, convection and advection of air parcels.	Brinkop et al. [169]
CLOUD	Calculates cloud cover, cloud scheme for ECHAM5.	Roeckner et al. [277]
CLOUDOPT	Calculates cloud optical properties.	Dietmüller et al. [187]
CONVECT	Calculates convection based on different parameterizations.	Tost et al. [168]
CVTRANS	Calculates transport of tracers due to convection.	Tost [278]
DDEP	Calculates dry deposition of gases and aerosols.	Kerkweg et al. [167]
E5VDIFF	Vertical diffusion for the ECHAM5 GCM.	MESSy Submodels [279]
GWAVE	Gravity wave parameterizations.	MESSy Submodels [279]
JVAL	Calculation of photolysis rates.	Sander et al. [280]
LGTMIX	Parameterization for Lagrangian air parcel mixing.	Brinkop and Jöckel [169]
LNOX	Parameterization for lightning NO_x.	Tost et al. [281]
MADE3	Calculation of aerosol microphysical processes.	Kaiser et al. [103], Beer et al. [282]
MECCA	Calculates tropospheric and stratospheric chemistry.	Sander et al. [155]
MSBM	Calculates heterogeneous reaction rates in the stratosphere for clouds and aerosols.	Jöckel et al. [151]
OFFEMIS	Prescribes offline emissions from inventories to grid-point and Lagrangian tracers.	Kerkweg et al. [283]
ONEMIS	Calculates 2D gas-phase emission fluxes during the simulation.	Kerkweg et al. [283]
ORBIT	Calculates parameters related to Earth's solar orbit.	Dietmüller et al. [187]
OROGW	Parameterization for orographic wave drag.	Roeckner et al. [149]
PTRAC	Tests for mass conservation and positive definiteness of grid-point and Lagrangian tracers.	Jöckel et al. [284]
RAD	ECHAM5 radiation scheme.	Dietmüller et al. [187]
SCAV	Wet scavenging process for gases and aerosols.	Tost et al. [168]
SEDI	Calculates sedimentation of aerosols.	Kerkweg et al. [167]
SURFACE	Calculates surface temperatures over land and ocean.	MESSy Submodels [279]
TNUDGE	Nudging of user-defined tracers.	Kerkweg et al. [283]
TREXP	Defines emission point sources for tracers.	Jöckel et al. [151]
TROPOP	Planetary boundary layer height setting and other diagnostics for the tropopause.	MESSy Submodels [279]
VISO	Vertically maps 3D fields in grid-point representation to iso-surfaces (i.e. tropopause layer) via linear interpolation.	Jöckel et al. [151]

B

APPENDIX B: COORDINATES OF EMISSION POINTS IN LAGRANGIAN SIMULATIONS

This appendix notes all emission points (in terms of latitude, longitude and altitude) used in the Lagrangian simulations performed in this thesis. Table B.1 specifies the coordinates at which NO is emitted (relevant for simulations from Chapters 4 and 5) while Table B.2 specifies the points at which SO_2 and H_2SO_4 are emitted (relevant for simulations from Chapter 6).

Table B.1: Geographic coordinates of all emission points at which 5×10^5 kg of NO is emitted on the first day of January and July in 2014. These coordinates are plotted in Fig. 4.1 for all pressure levels and only for the 250 hPa level in Fig. 5.1.

Location	Latitude (°N)	Longitude (°E)	Altitude (hPa)
North America	85,75,65,55,45,35,25	-115,-95,-75,-55	200, 250, 300
South America	10,0,-10,-20,-30,-40,-50	-90,-70,-50,-30	
Eurasia	60, 40	-10,0,10,20,30,40,50,60,70,80,90,100,110,120	
Africa	30,20,10,0,-10,-20,-30	-20,0,20,40	
Australasia	10,0,-10,-20,-30,-40,-50	90,110,130,150	

Table B.2: SO_2 and H_2SO_4 emission coordinates and amounts in kg. The contribution column is calculated according to Eq. E.1 and represents the relative contribution of a user-defined grid cell using the EP_selector Python tool [249]. The total amount of SO_2 and H_2SO_4 emitted across the 28 points equates to about 90% of the daily amount of globally produced SO_x [192]. The altitude is constant for all locations: 238.2 hPa.

EP	Latitude [deg. North]	Longitude [deg. East]	Contribution	Emission [kg(SO_2)]	Emission [kg(H_2SO_4)]
1	22.25	-155.25	0.9%	9.48E+03	2.96E+02
2	44.25	-142.25	1.4%	1.26E+04	3.93E+02
3	61.25	-155.25	2.6%	1.50E+04	4.69E+02
4	36.25	-112.25	6.8%	5.92E+04	1.85E+03
5	50.25	-100.25	2.5%	1.41E+04	4.40E+02
6	29.25	-81.25	3.1%	3.33E+04	1.04E+03
7	42.25	-71.25	11.0%	9.58E+04	2.99E+03
8	51.25	-61.25	2.0%	1.17E+04	3.65E+02
9	-20.25	-44.25	0.9%	9.37E+03	2.93E+02
10	-9.25	-37.25	1.0%	1.10E+04	3.43E+02
11	20.25	-20.25	1.1%	1.15E+04	3.59E+02
12	48.25	-58.25	3.0%	2.59E+04	8.09E+02
13	53.25	-36.25	4.9%	2.80E+04	8.75E+02
14	29.25	-14.25	1.5%	1.57E+04	4.90E+02
15	48.25	5.75	9.7%	8.48E+04	2.65E+03
16	52.25	-3.25	5.5%	3.12E+04	9.76E+02
17	27.25	53.75	1.4%	1.53E+04	4.79E+02
18	44.25	20.75	6.4%	5.58E+04	1.74E+03
19	53.25	20.75	3.2%	1.82E+04	5.67E+02
20	16.25	98.75	2.6%	2.78E+04	8.67E+02
21	43.25	66.75	2.4%	2.06E+04	6.43E+02
22	69.25	66.75	1.9%	1.09E+04	3.42E+02
23	3.25	105.75	1.7%	1.89E+04	5.91E+02
24	27.25	123.75	3.5%	3.79E+04	1.18E+03
25	42.25	135.75	4.5%	3.94E+04	1.23E+03
26	56.25	121.75	8.2%	7.11E+03	2.22E+02
27	38.25	142.75	3.4%	2.96E+04	9.24E+02
28	51.25	160.75	2.3%	1.33E+04	4.14E+02

C

APPENDIX C: SUPPLEMENTARY INFORMATION ON THE COMPARATIVE ANALYSIS BETWEEN CLIMATE IMPACT CALCULATION METHODS

This appendix provides additional information regarding the comparative assessment between three climate impact calculation approaches discussed in Chapter 4: Lagrangian tagging, Eulerian tagging and perturbation.

C

C.1. COMPLETE O_3 PRODUCTION EFFICIENCIES - JANUARY

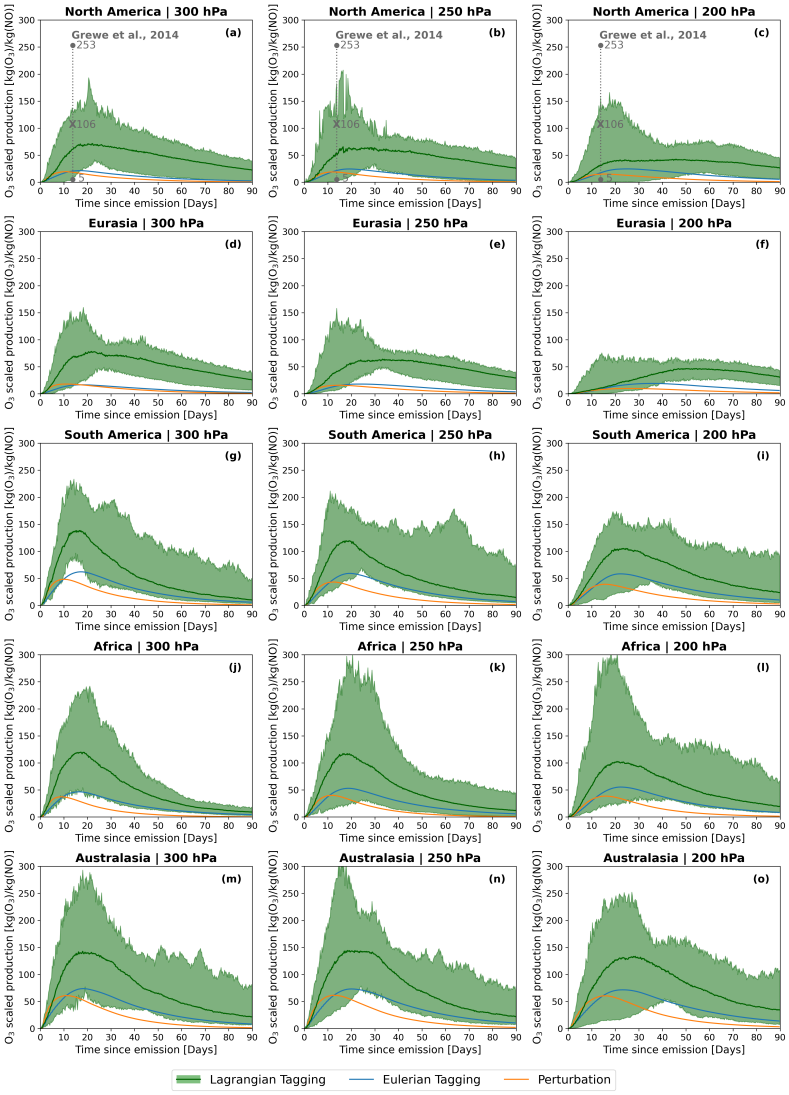


Figure C.1: Normalized NO_x-induced O_3 production. (a) to (o) Comparison between scaled O_3 mass curves (scaled by the amount 5×10^5 kg of NO per emission point) as estimated by the Lagrangian (green) and Eulerian (blue) tagging methods as well as the perturbation (orange) method for emissions in January. The shaded green area represents the range of possible O_3 estimates across the 28 independent emission scenarios for the Lagrangian method. The green line is the average of these 28 Lagrangian O_3 mass curves. NA represents North America, SA is South America, EU is Eurasia, AF is Africa and AU is Australasia. As an example, Figure (n) denotes the scenario in which NO is emitted at 250 hPa throughout the 28 emission points in Australasia. The dotted gray line in Figures (a) – (c) denotes the range of O_3 estimates (13.75 days after emission) obtained by Grewe et al. [23] using AIRTRAC to study 5×10^5 kg of NO released at 200, 250, 300 and 400 hPa during 06h00, 12h00 and 18h00 UTC in January. The gray "X" marks the mean value.

C.2. COMPLETE O_3 PRODUCTION EFFICIENCIES - JULY

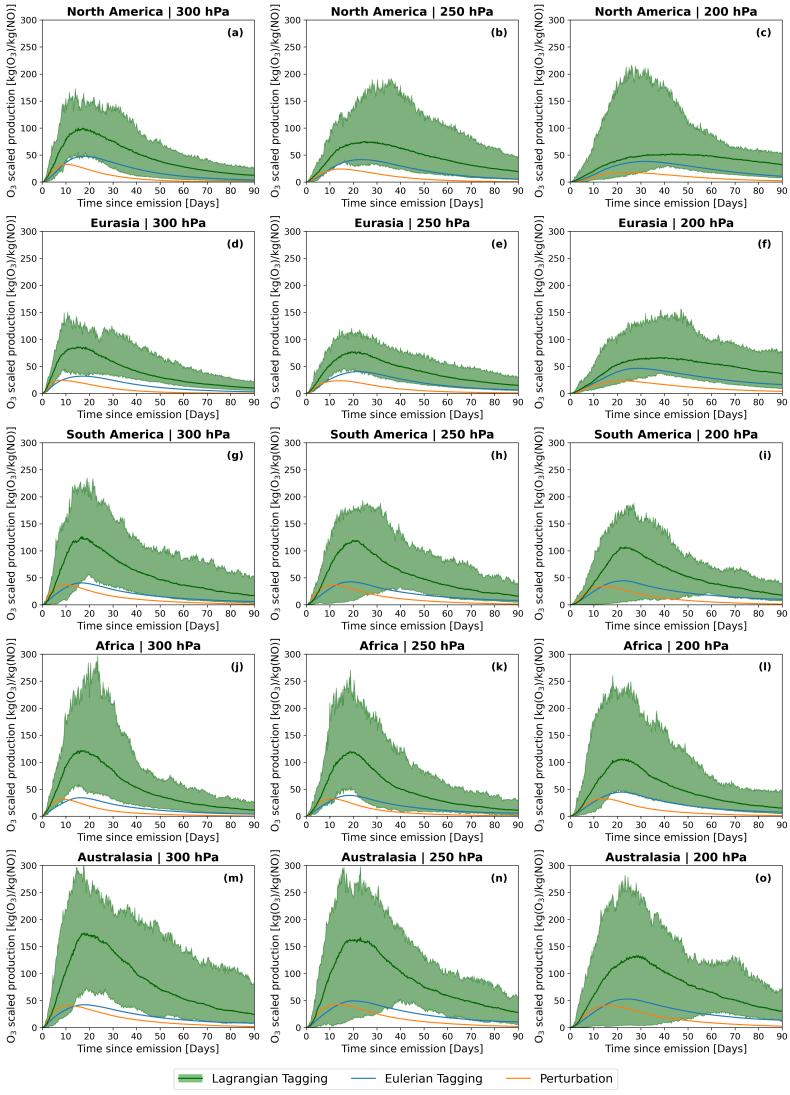


Figure C.2: Normalized NO_x-induced O_3 production. (a) to (o) Comparison between scaled O_3 mass curves (scaled by the amount 5×10^5 kg of NO per emission point) as estimated by the Lagrangian (green) and Eulerian (blue) tagging methods as well as the perturbation (orange) method for emissions in July. The shaded green area represents the range of possible O_3 estimates across the 28 independent emission scenarios for the Lagrangian method. The green line is the average of these 28 Lagrangian O_3 mass curves. NA represents North America, SA is South America, EU is Eurasia, AF is Africa and AU is Australasia. As an example, Figure (n) denotes the scenario in which NO is emitted at 250 hPa throughout the 28 emission points in Australasia.

C

C.3. KERNEL DENSITY ESTIMATOR (KDE) PLOTS FOR ALL SCENARIOS

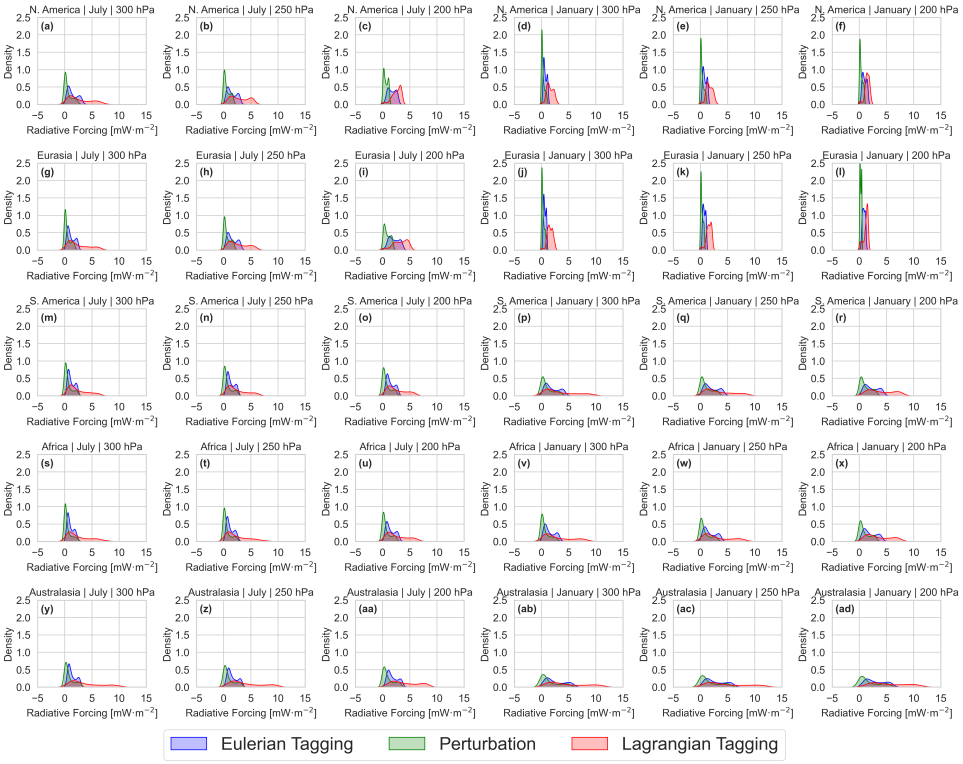


Figure C.3: Kernel density estimators (KDEs) (smoothing bandwidth determined by Scott's rule) for the radiative forcing of each calculation method (Lagrangian tagging, Eulerian tagging and perturbation), region (North (N.) America, Eurasia, South (S.) America, Africa and Australasia), emission time (January or July of 2014) and altitude (200, 250 and 300 hPa). The blue KDE represents Eulerian tagging, the green the perturbation approach and the red the Lagrangian tagging technique.

Bi-modal distributions are observed for most of the kernel density estimators (KDEs). The median values of the Lagrangian RF estimates in Fig. 4.5 in Chapter 4 are considerably smaller than the means in Fig. C.4, which further indicates that large positive values are raising the average point estimates. It is also clear from Fig. C.3 that the variance in AIRTRAC's RF estimates generally increases towards the troposphere, where there are more chemical processes occurring. This explains the lower mean obtained for North America at 200 hPa for July in Fig. C.4 (b) as the range of RF estimates deviates less from the mean towards larger values for an emission at 200 hPa (Fig. C.3 (c)) rather than at 300 hPa (Fig. C.3 (a)). In general, the Eulerian tagging and perturbation methods estimate RF with less uncertainty across the three pressure altitudes, given the narrower spread of their KDEs.

C.4. MEAN RADIATIVE FORCING FOR ALL SCENARIOS

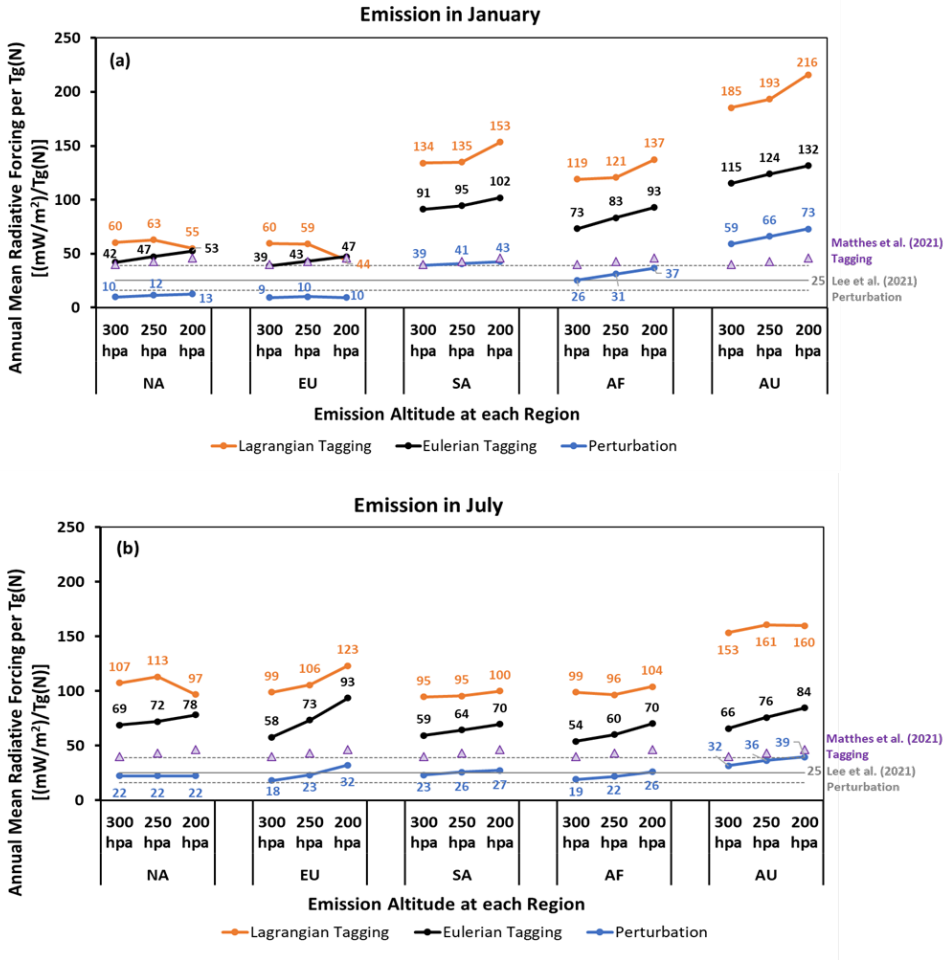


Figure C.4: Annualized, area-weighted mean radiative forcing point estimates from short-term NO_x-induced O_3 for emission altitudes of 300 hPa (~ 9.2 km), 250 hPa (~ 10.4 km) and 200 hPa (~ 11.8 km) across all five regions (North America (NA), South America (SA), Eurasia (EU), Africa (AF) and Australasia (AU)) during (a) 1 January and (b) 1 July of 2014. The solid gray line represents the corresponding mean RF estimate for short-term O_3 effects from Lee et al. [27] using a perturbation approach. The dotted gray lines demarcate the 90% confidence interval of the same study, where the 5% lower limit is 16 and 95% upper limit is 39 mWm^{-2}. The purple triangles depict the tagging estimates in mWm^{-2} of Matthes et al. [31], who calculated 43 for a base flight altitude (equated to 250 hPa in this thesis), 46 for a *flying higher* and 40 for a *flying lower* scenario, which were compared to my 200 and 300 hPa estimates, respectively. For clarity, these values are not labeled above. All RF estimates presented in (a) and (b) have been scaled to represent the equivalent value for a 1 Tg of nitrogen (N) emission.

C.5. VARIATION OF Δ RF BETWEEN LAGRANGIAN AND EULERIAN TAGGING

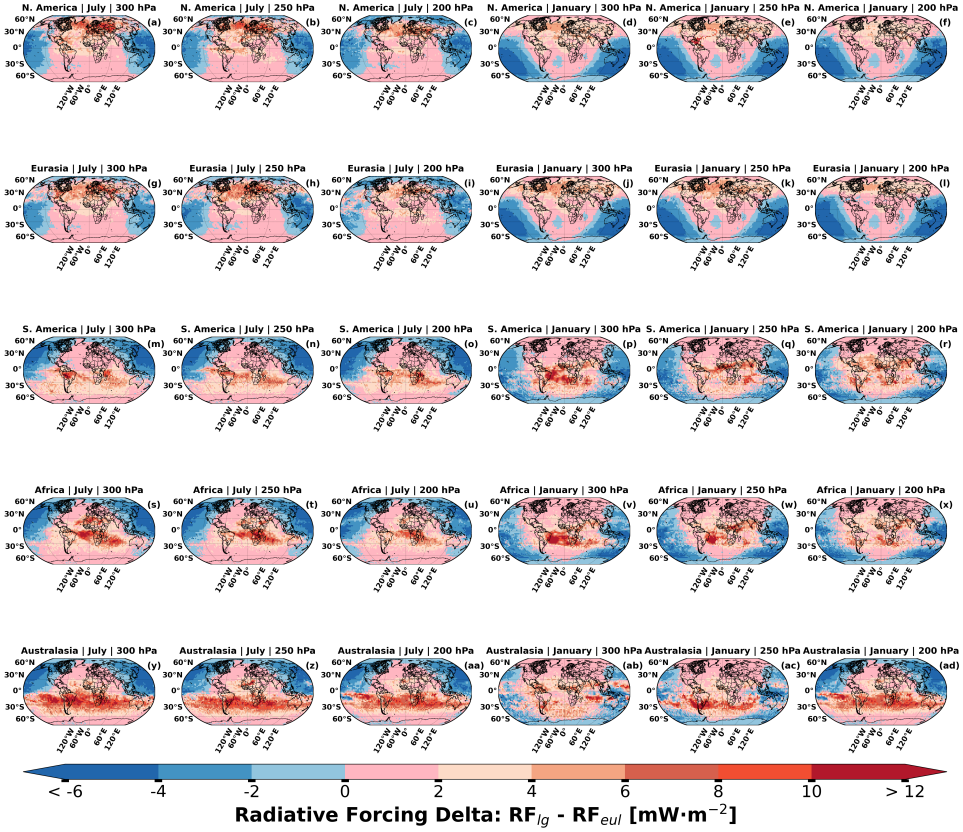


Figure C.5: Variation of the ΔRF ($RF_{lg} - RF_{eul}$) in mWm^{-2} between the Lagrangian and Eulerian tagging methods for all three pressure altitudes (200, 250 and 300 hPa), five regions (North (N.) America, Eurasia, South (S.) America, Africa and Australasia) and two emission times (January and July 1 of 2014).

Figure C.5 indicates that the Lagrangian tagging technique is mainly larger than the Eulerian submodel, especially in the vicinity of the emission and across the latitudinal band at which the dominant westerlies act. This is explained by Maruhashi et al. [13], where they show that the horizontal transport of an emitted substance is strongly dictated by the presence of westerlies (see their Figure C1). Eulerian tagging, on the other hand, exhibits consistently larger RF in Pacific regions relative to the Lagrangian submodel. For an emission in the Northern Hemisphere, for instance, Figures C.5 (a) - (l) show larger Eulerian estimates in the Southern Pacific. The opposite is true for an emission in the Southern Hemisphere, where Figures C.5 (m) - (ad) display larger values for the Eulerian submodel in the Northern Pacific region, as indicated in blue. We note that for NO emissions in January in Northern areas (i.e. North America and Eurasia), the Eulerian

approach calculates larger RF values relative to the Lagrangian submodel, particularly for Southern Pacific regions (Figs. C.5 (d) - (f) and (j) - (l)), which then globally reduces the differences between their median RFs for North America and Eurasia (Fig. 4.5 (a)). Similarly, for emissions in July in Southern regions (South America, Africa and Australasia), the Eulerian submodel is larger in the Northern Pacific regions (Figs. C.5 (m) - (o), (s) - (u) and (y) - (aa)). This then translates to having smaller differences between RF_{lg} and RF_{eul} for Southern emissions regions (Fig. 4.5 (b)).

C.6. SMALL SIGNAL CORRECTION TO THE TAGGING SUBMODEL

Originally, the TAGGING submodel was unable to accurately capture the climate response to small aviation emission signals in the order of 10^3 kg, which represents 1% of the usually emitted amount with a magnitude of 10^5 kg. This issue is illustrated in Figure C.6, where, before the correction, O_3 production was largely dominated by numerical noise after the peak production period, which occurs around 25 days, as shown by the red curve. The correction involved implementing additional thresholds to prevent the propagation of noise from sectors with minimal contributions. After applying these adjustments, the green curve in the figure demonstrates the expected behavior of NO_x-O_3 chemistry, with a significant reduction in noise and a more accurate representation of the system's response.

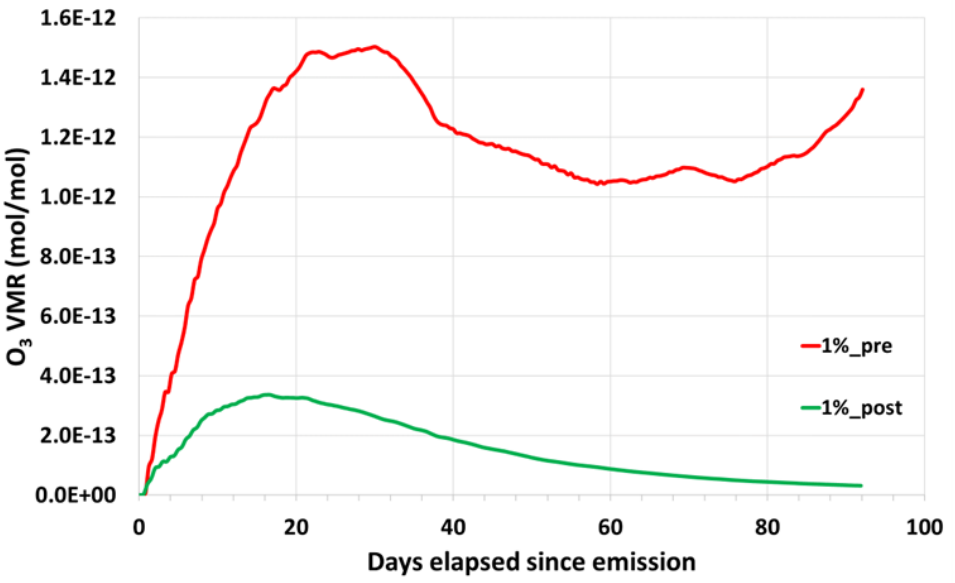


Figure C.6: The temporal evolution of the ozone volume mixing ratios (VMRs) estimated by the TAGGING submodel before the correction (red curve=1%_pre) and after the correction (green curve=1%_post) for an NO emission strength of 1% (5×10^3kg).

D

APPENDIX D: SUPPLEMENTARY INFORMATION ON THE ANALYSIS OF NO_X-O_3 TRANSPORT PATTERNS

This appendix provides additional information regarding the analysis of NO_x-O_3 transport patterns discussed in Chapter 5. The study of all regions and seasons is contained in the Supplement of Maruhashi et al. [13].

D.1. VERTICAL PROFILES OF MEDIAN AIR PARCEL TRAJECTORIES

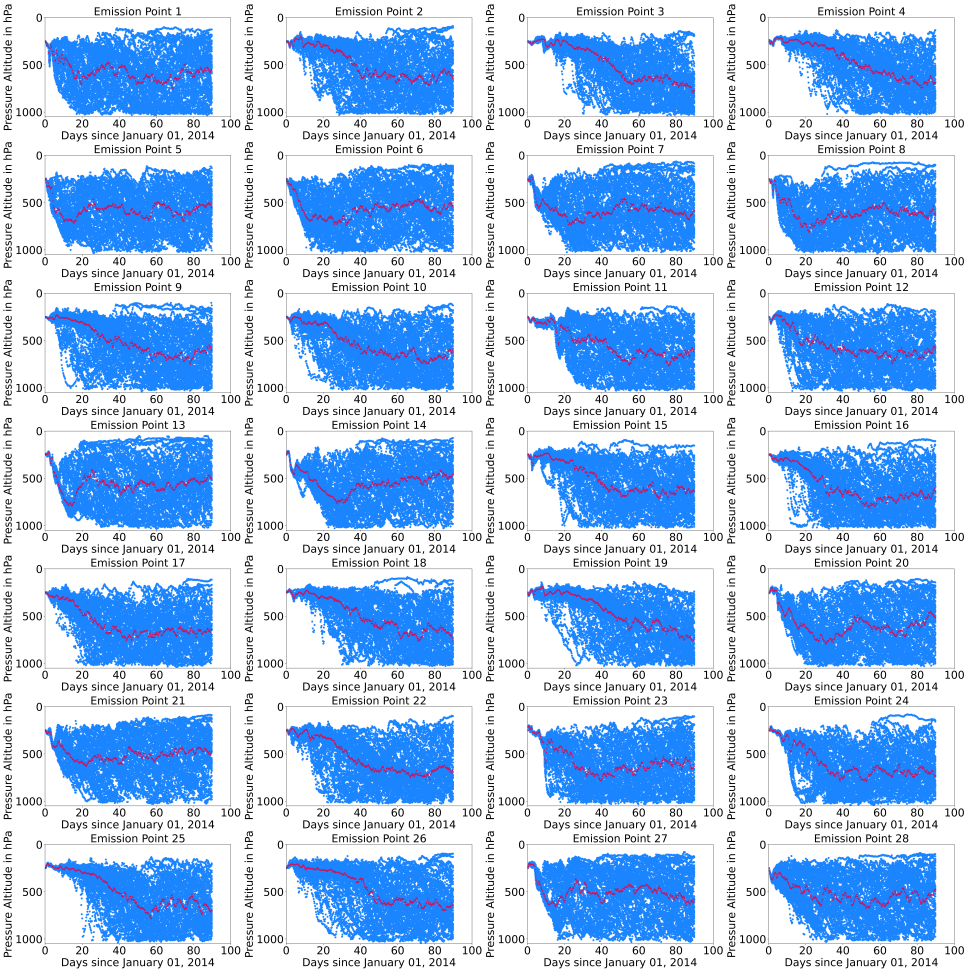


Figure D.1: Temporal evolution of the air parcel trajectory pressure altitude of median trajectories (red) based on 50 Lagrangian paths (blue) for all 28 emission points for North America for January - March 2014.

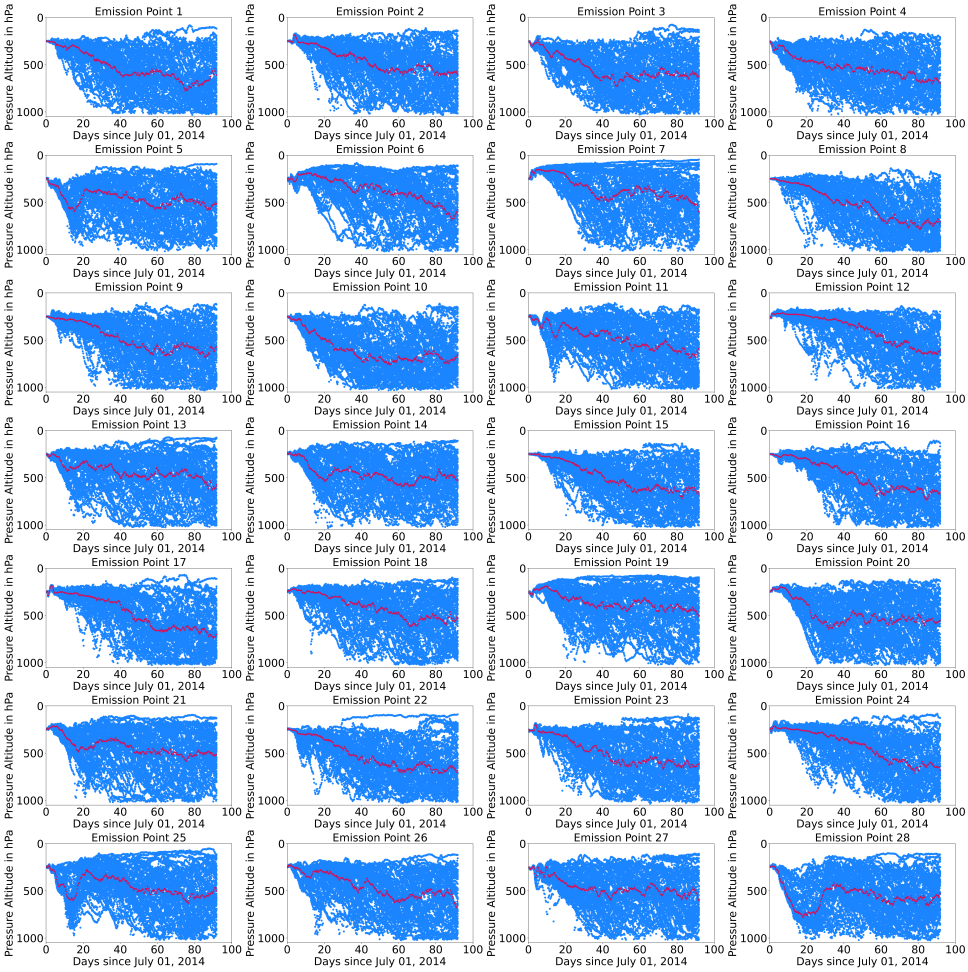


Figure D.2: Temporal evolution of the air parcel trajectory pressure altitude of median trajectories (red) based on 50 Lagrangian paths (blue) for all 28 emission points for North America for July - September 2014.

D.2. HORIZONTAL DISTRIBUTIONS OF MEDIAN AIR PARCELS

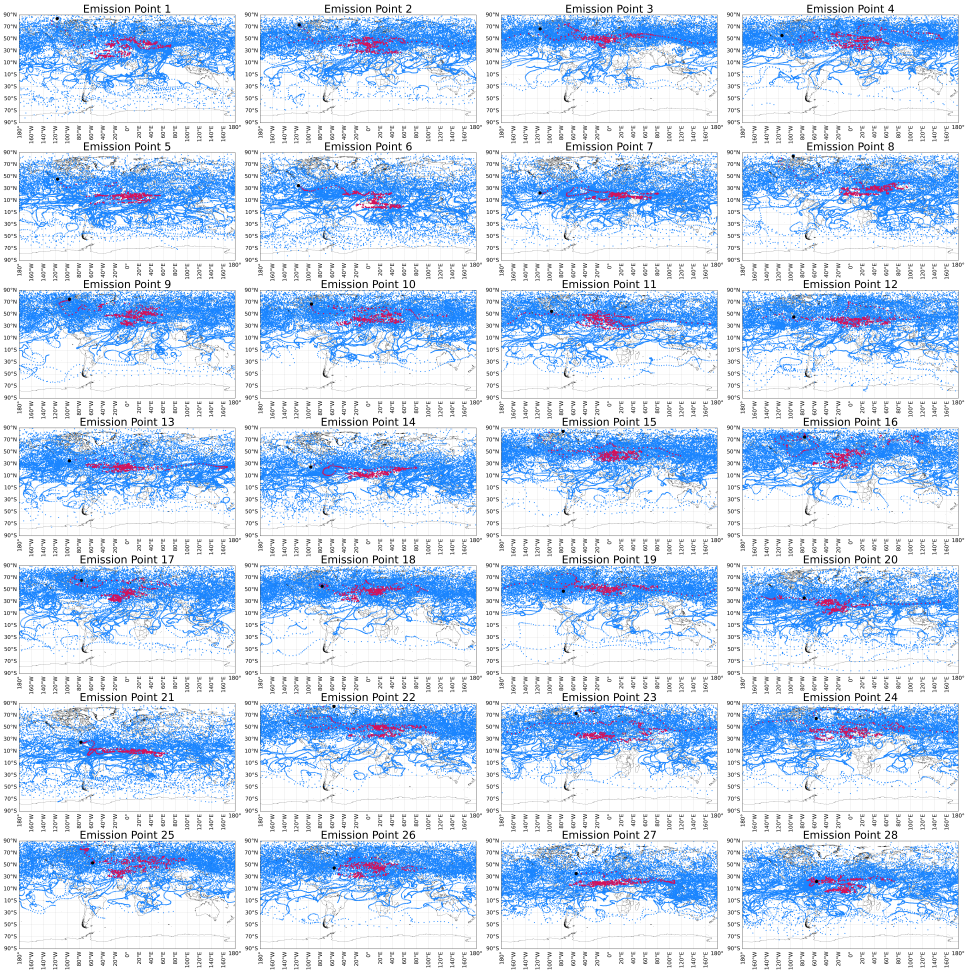


Figure D.3: Horizontal trajectories for air parcels released in North America during January 2014. The black dots denote the emission starting points. The red dots represent the median trajectory while the blue dots represent the 50 Lagrangian trajectories for each of the 28 emission points.

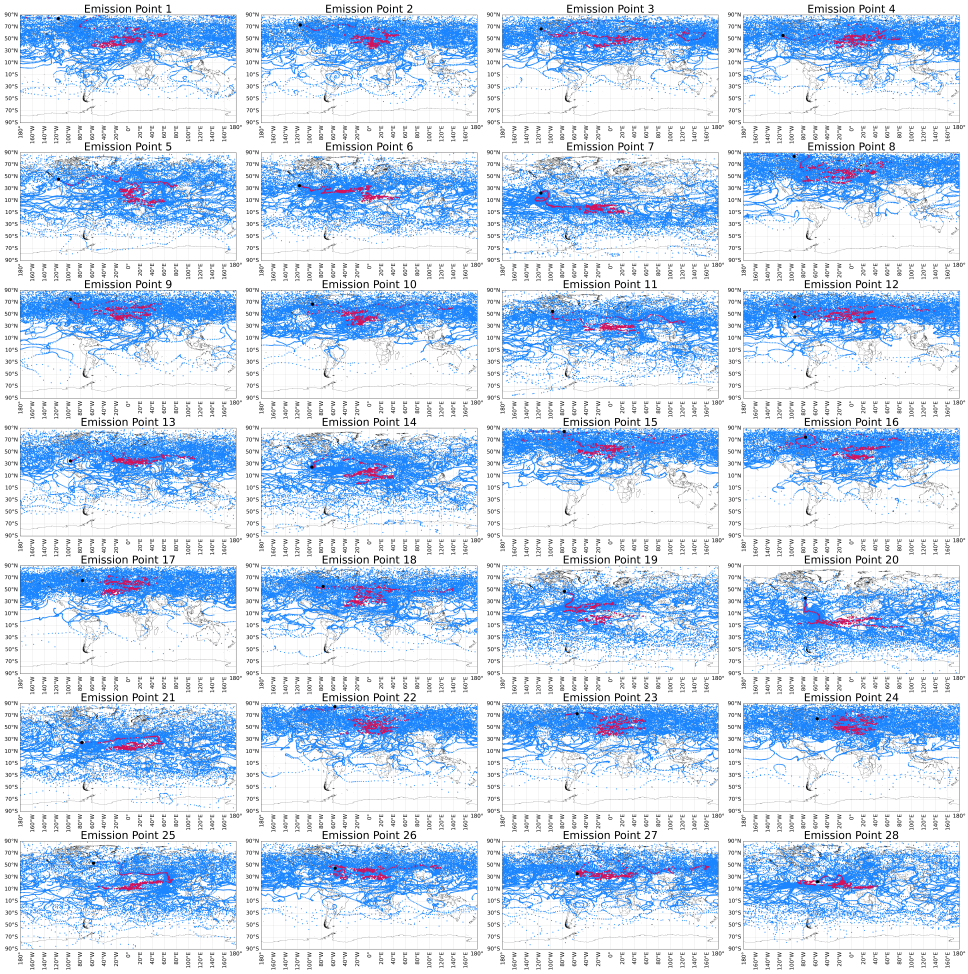


Figure D.4: Horizontal trajectories for air parcels released in North America during July 2014. The black dots denote the emission starting points. The red dots represent the median trajectory while the blue dots represent the 50 Lagrangian trajectories for each of the 28 emission points.

D.3. CALCULATION OF THE OPTIMAL NUMBERS

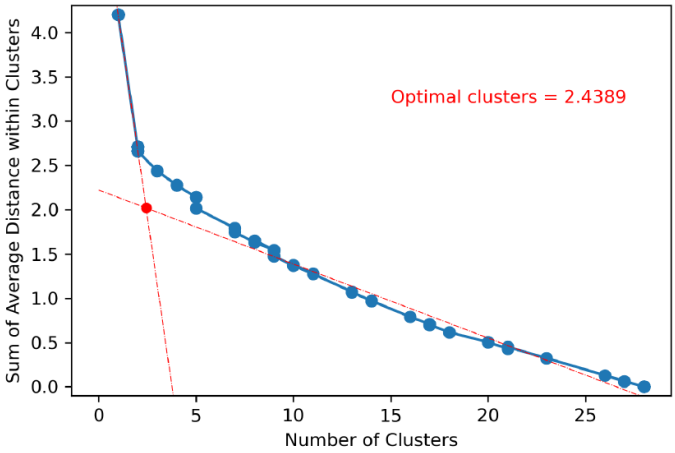


Figure D.5: Determination of optimal cluster threshold θ for North America during January - March 2014. Vertical axis is the sum of the averaged distance $E(\theta)$ (Eq. 5.2) as a function of the number of clusters (blue).

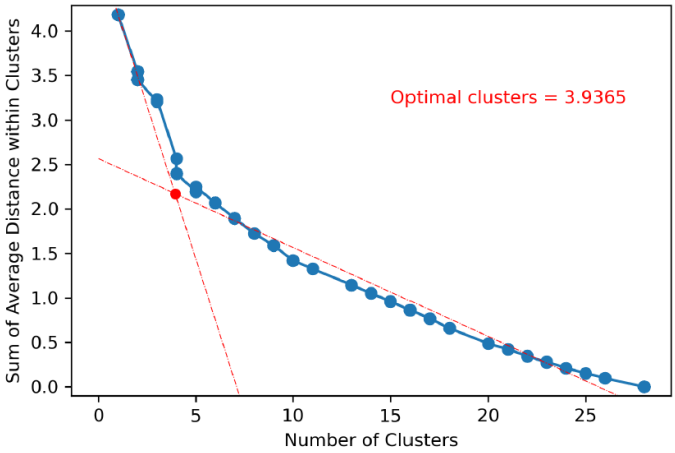


Figure D.6: Determination of optimal cluster threshold θ for North America during July - September 2014. Vertical axis is the sum of the averaged distance $E(\theta)$ (Eq. 5.2) as a function of the number of clusters (blue).

D.4. EMAC WIND FIELDS

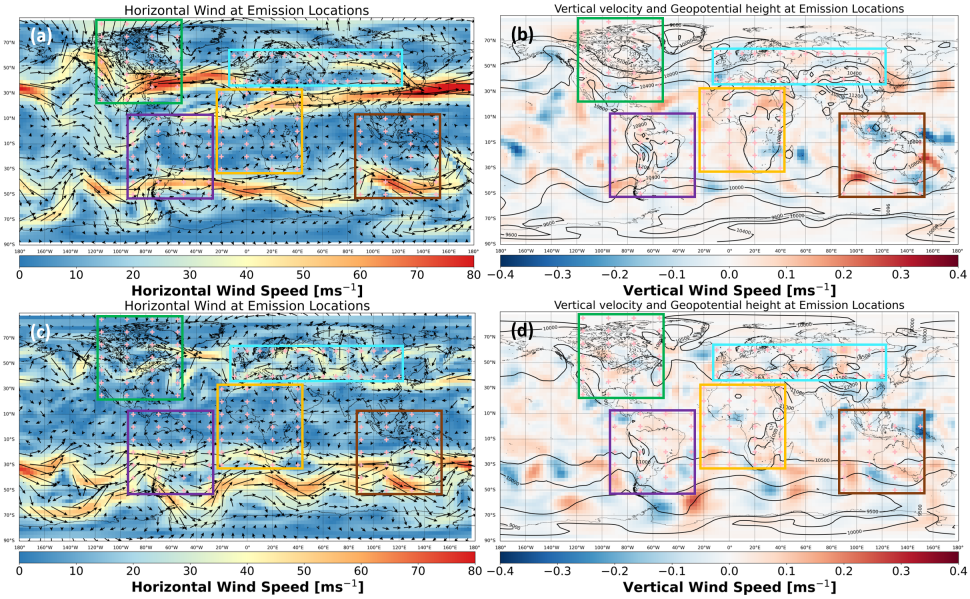


Figure D.7: Averaged horizontal and vertical wind fields at 250 hPa during January-March 2014 in panels (a) and (b). Same information is portrayed in panels (c) and (d) for July-September. Geopotential height contours in (b) and (d) are expressed in meters. The same emission points as in Fig. 5.1 are shown with '+' in each region. The colored boxes delineate the five emission regions.

D.5. VERTICAL TRANSPORT OF NO_X FOR EMISSION POINTS 8 AND 14 OF FIG. 5.9

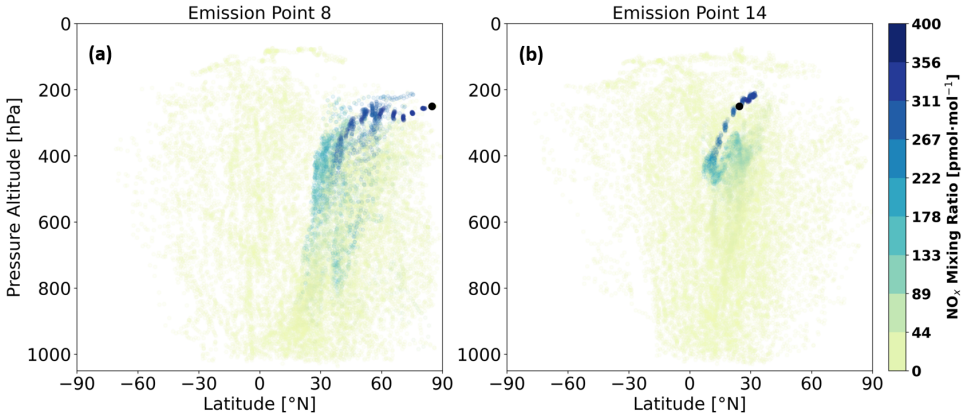


Figure D.8: Transport of emitted NO_X released in N. America during January 2014 at (a) emission point 8 within a meridional tilt and at (b) emission point 14 outside the tilt but within the northern westerly. The black dot denotes the emission point. The NO_X volume mixing ratio is expressed in picomoles per mole (pmol mol^{-1}).

D.6. MEAN RADIATIVE FORCING PER CLUSTER

Table D.1: Mean radiative forcing impact in mW m^{-2} normalized by trajectories per cluster during January-March 2014. The rows denotes the clusters in each region.

	N. America	S. America	Eurasia	Africa	Australasia
C1	0.0521 [0.0498, 0.0545]	0.0733 [0.0711, 0.0756]	0.0525 [0.0510, 0.0545]	0.0590 [0.0570, 0.0611]	0.0905 [0.0867, 0.0943]
C2	0.0529 [0.0513, 0.0545]	0.1061 [0.1025, 0.1098]	0.0529 [0.0512, 0.0545]	0.1185 [0.1139, 0.1230]	0.2253 [0.2093, 0.2413]
C3	–	0.1641 [0.1576, 0.1705]	–	0.0545 [0.0527, 0.0563]	0.1492 [0.1443, 0.1540]
C4	–	0.1745 [0.1671, 0.1820]	–	0.1130 [0.1090, 0.1170]	0.1720 [0.1650, 0.1790]
C5	–	–	–	–	0.1454 [0.1391, 0.1517]

Table D.2: Mean radiative forcing impact in mW m^{-2} normalized by trajectories per cluster during July-September 2014. The rows denotes the clusters in each region.

	N. America	S. America	Eurasia	Africa	Australasia
C1	0.1348 [0.1301, 0.1395]	0.0769 [0.0735, 0.0803]	0.0941 [0.0910, 0.0972]	0.0528 [0.0509, 0.0546]	0.1456 [0.1412, 0.1501]
C2	0.0672 [0.0654, 0.0690]	0.0615 [0.0594, 0.0637]	0.1180 [0.1141, 0.1219]	0.0685 [0.0658, 0.0712]	0.1070 [0.1032, 0.1107]
C3	0.1425 [0.1379, 0.1471]	0.0773 [0.0747, 0.0800]	0.0772 [0.0746, 0.0798]	0.0816 [0.0789, 0.0843]	0.1049 [0.1012, 0.1086]
C4	0.1138 [0.1098, 0.1178]	0.0299 [0.0285, 0.0313]	0.0984 [0.0953, 0.1015]	0.0534 [0.0502, 0.0566]	0.1162 [0.1119, 0.1205]

E

APPENDIX E: SUPPLEMENTARY INFORMATION ON THE ANALYSIS OF SO_4 AEROSOL TRANSPORT PATTERNS

This appendix provides additional information regarding the analysis of SO_4 transport patterns discussed in Chapter 6. Details regarding the EP_selector tool, its code and other supplementary analyses may be found in Maruhashi et al. [142] and in the accompanying data repository for this dissertation [249].

E.1. DETERMINATION OF SO_2 AND H_2SO_4 EMISSION LOCATIONS AND AMOUNTS

The coordinates of the 28 emission points in Fig. 6.2 are listed in Table B.2. These have been calculated by first identifying the pressure altitude for which the zonally averaged aviation SO_2 flux is the largest, as is shown in Fig. E.1. The distribution of latitude-longitude coordinates (see Fig. E.2) is obtained by selecting the coordinates of the maximum SO_2 fluxes from the 28 grid cells with the largest flux contributions (see Eq. E.1). The EP_selector tool [249] has been designed to systematically store the coordinates of these locations by first computing flux contributions across all user-defined grid cells. For those with the largest contributions, the coordinates of the maxima are recorded. As the EP_selector tool possesses several adjustable inputs like the latitudinal and longitudinal spacing for each grid cell as well as the number of grid cells in which to search for the n largest values, it is necessary to select an appropriate combination for these parameters. The chosen combination is based on maximizing the total grid cells while ensuring that the total flux contribution is above 90%.

The SO_2 flux concentration per grid cell i, $\Gamma_i^{SO_2}$, is given by Eq. E.1:

$$\Gamma_i^{SO_2} = \frac{A_i \times SO_{2,i}}{\sum_j^T A_j \times SO_{2,j}} \times 100\%. \tag{E.1}$$

The total number of grid cells is given by $T = \frac{180^\circ}{\Delta lat} \times \frac{360^\circ}{\Delta lon}$, $SO_{2,i}$ is the total flux within a grid cell i and the area of a grid cell A_i is calculated according to Kelly and Šavrič [194]:

$$A_i = R_\oplus^2 \times \Delta lat \times \Delta lon \times \cos\overline{lat_l}, \tag{E.2}$$

where $\overline{lat_l}$ is the average between the bounding latitudes of grid cell i. The amount of SO_2 mass emitted per grid cell at an emission point, $SO'_{2,i}$, is then found by the product $SO'_{2,i} = 0.98 \times \Gamma_i^{SO_2} \times SO_{2,Total}$, where $SO_{2,Total}$ is approximately the total amount of SO_2 mass produced globally by aviation within a day. The amount of H_2SO_4 is found by assuming that aviation's sulphur-based emissions are 98% SO_2 and 2% H_2SO_4. This means that the amount of H_2SO_4 mass emitted per grid cell, $H_2SO'_{4,i}$, may be found in terms of $SO'_{2,i}$, according to Eq. E.3:

$$\frac{SO'_{2,i}}{SO'_{2,i} + \frac{M_{SO_2}}{M_{H_2SO_4}} \times H_2SO'_{4,i}} = 0.98 \Rightarrow H_2SO'_{4,i} = \frac{0.02}{0.98} \times \frac{M_{H_2SO_4}}{M_{SO_2}} \times SO'_{2,i}. \tag{E.3}$$

The molecular masses for SO_2 and H_2SO_4 are denoted by M_{SO_2} and $M_{H_2SO_4}$ respectively.

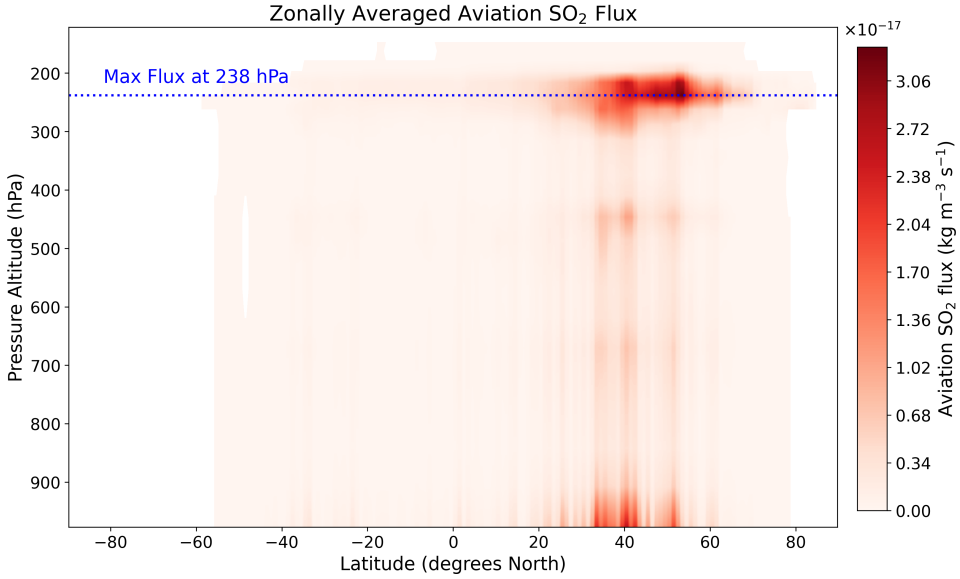


Figure E.1: Variation of the zonally averaged aviation SO_2 mass flux with pressure altitude from the CMIP6 emissions inventory. The blue dotted line represents the pressure altitude of 238.2 hPa (~240 hPa or 10.6 km) at which the maximum flux occurs.

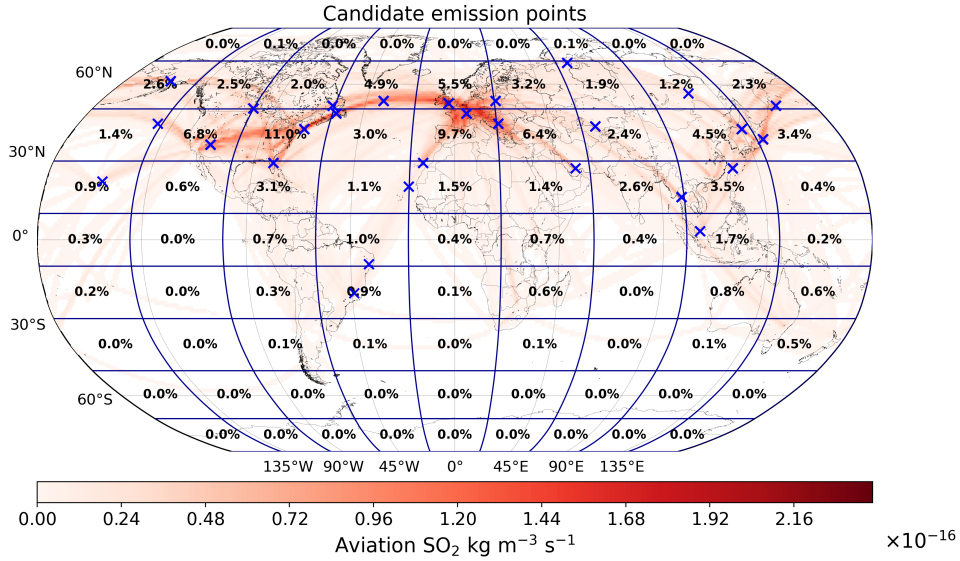


Figure E.2: Horizontal distribution of the 28 emission points (blue 'x' marks) determined by the EP_selector tool. The continuous blue lines indicate the coarser mesh produced from spacings of 20° and 40° in the latitudinal and longitudinal directions respectively. The color bar depicts the spatial variation of aviation's SO_2 mass flux according to the CMIP6 emissions inventory. The percentages represent the fractional contribution of a grid cell towards the total SO_2 flux.

E.2. MATHEMATICAL FORMULATIONS FOR THE TAGGING OF THE MADE3 COAGULATION TENDENCY

The tagging formulations for the remaining eight aerosol modes are derived by applying Eq. 3.3 to Eq. 3.16. For each mode, the same procedure applied in Chapter 6 to derive Eq. 6.12 is followed. Each tendency is formulated as a function of the soluble mass fraction θ relative to water. Each derivation fulfills the tagging additivity requirement of Eq. 3.4. As a reminder from Chapter 6, it is important to note that $x_i = x_i^{avi} + x_i^{rem}$ and that $C_p = C_{NH_4,p} + C_{NO_3,p} + C_{Na,p} + C_{Cl,p} + C_{POM,p} + C_{BC,p} + C_{DU,p} + C_{H_2O,p}$ where p is one of the nine aerosol modes.

AITKEN MIXED (KM) MODE

$$\left.\frac{\partial x_2}{\partial t}\right|_{coag} = F_2(\mathbf{x}) = \begin{cases} 0 & ; \theta = 1 \\ A\frac{x_1}{x_1+C_1} - B\frac{x_2}{x_2+C_2} + C\frac{x_3}{x_3+C_3} & ; \theta \in [0.1, 1[\\ -B'\frac{x_2}{x_2+C_2} & ; \theta \in [0, 0.1[\end{cases} \tag{E.4}$$

Where the terms A, B, B' and C are defined as:

$$A = \rho_1 \frac{\pi}{6}\left[f_{1,2} + f_{1,3}\right],$$

$$B = \rho_2 \frac{\pi}{6}\left[f_{2,4} + f_{2,5} + f_{2,6} + f_{2,7} + f_{2,8}\right],$$

$$B' = \rho_2 \frac{\pi}{6}\left[f_{2,3} + f_{2,6} + f_{2,9}\right],$$

$$C = \rho_3 \frac{\pi}{6} f'_{2,3}.$$

Aviation's contribution is then given by:

$$\left.\frac{\partial x_2^{avi}}{\partial t}\right|_{coag} = \begin{cases} 0;\ \theta = 1 \\ F_2(\mathbf{x})\dfrac{AC_1\frac{x_1^{avi}}{(x_1+C_1)^2} - BC_2\frac{x_2^{avi}}{(x_2+C_2)^2} + CC_3\frac{x_3^{avi}}{(x_3+C_3)^2}}{AC_1\frac{x_1}{(x_1+C_1)^2} - BC_2\frac{x_2}{(x_2+C_2)^2} + CC_3\frac{x_3}{(x_3+C_3)^2}};\ \theta \in [0.1, 1[\\ F_2(\mathbf{x})\frac{x_2^{avi}}{x_2};\ \theta \in [0, 0.1[. \end{cases} \tag{E.5}$$

It is interesting to note that when $\theta = 1$ in Eq. E.4 the coagulation tendency is zero as there is no collision event that produces a final particle in the soluble state when one of the colliding particles is in the km mode. This is consistent with Table 3.2 in which all collision events are specified.

AITKEN INSOLUBLE (KI) MODE

$$\left.\frac{\partial x_3}{\partial t}\right|_{coag} = F_3(\mathbf{x}) = \begin{cases} 0;\ \theta = 1 \\ -C\frac{x_3}{x_3+C_3};\ \theta \in [0.1, 1[\\ A'\frac{x_1}{x_1+C_1} + B'\frac{x_2}{x_2+C_2} - C'\frac{x_3}{x_3+C_3} + D'\frac{x_4}{x_4+C_4} + E'\frac{x_5}{x_5+C_5};\ \theta \in [0, 0.1[\end{cases} \tag{E.6}$$

Where the terms A', B', C', C, D' and E' are defined as:

$$A' = \rho_1 \frac{\pi}{6} f_{1,3},$$

$$B' = \rho_2 \frac{\pi}{6} f_{2,3},$$

$$C' = \rho_3 \frac{\pi}{6} \left[f_{3,6} + f_{3,9} \right],$$

$$C = \rho_3 \frac{\pi}{6} \left[f'_{1,3} + f'_{2,3} + f_{3,4} + f_{3,5} + f_{3,7} + f_{3,8} \right],$$

$$D' = \rho_4 \frac{\pi}{6} f'_{3,4},$$

$$E' = \rho_5 \frac{\pi}{6} f'_{3,5}.$$

Aviation's contribution is given by:

$$\left.\frac{\partial x_3^{avi}}{\partial t}\right|_{coag} = \begin{cases} 0;\ \theta = 1 \\ F_3(\mathbf{x})\frac{x_3^{avi}}{x_3};\ \theta \in [0.1, 1[\\ F_3(\mathbf{x})\frac{A'C_1\frac{x_1^{avi}}{(x_1+C_1)^2} + B'C_2\frac{x_2^{avi}}{(x_2+C_2)^2} - C'C_3\frac{x_3^{avi}}{(x_3+C_3)^2} + D'C_4\frac{x_4^{avi}}{(x_4+C_4)^2} + E'C_5\frac{x_5^{avi}}{(x_5+C_5)^2}}{A'C_1\frac{x_1}{(x_1+C_1)^2} + B'C_2\frac{x_2}{(x_2+C_2)^2} - C'C_3\frac{x_3}{(x_3+C_3)^2} + D'C_4\frac{x_4}{(x_4+C_4)^2} + E'C_5\frac{x_5}{(x_5+C_5)^2}};\ \theta \in [0, 0.1[. \end{cases} \tag{E.7}$$

ACCUMULATION SOLUBLE (AS) MODE

$$\left.\frac{\partial x_4}{\partial t}\right|_{coag} = F_4(\mathbf{x}) = \begin{cases} A\frac{x_1}{x_1+C_1} - D\frac{x_4}{x_4+C_4};\ \theta = 1 \\ -D'\frac{x_4}{x_4+C_4};\ \theta \in [0.1, 1[\\ -D''\frac{x_4}{x_4+C_4};\ \theta \in [0, 0.1[\end{cases} \tag{E.8}$$

Where the terms A, D, D' and D" are defined as:

$$A = \rho_1 \frac{\pi}{6} f_{1,4},$$

$$D = \rho_4 \frac{\pi}{6} f_{4,7},$$

$$D' = \rho_4 \frac{\pi}{6} \left[f'_{2,4} + f'_{3,4} + f_{4,5} + f_{4,6} + f_{4,8} + f_{4,9} \right],$$

$$D'' = \rho_4 \frac{\pi}{6} \left[f'_{3,4} + f_{4,6} + f_{4,9} \right].$$

Aviation's contribution is given by:

$$\left.\frac{\partial x_4^{avi}}{\partial t}\right|_{coag} = \begin{cases} F_4(\mathbf{x}) \dfrac{AC_1 \frac{x_1^{avi}}{(x_1+C_1)^2} - DC_4 \frac{x_4^{avi}}{(x_4+C_4)^2}}{AC_1 \frac{x_1}{(x_1+C_1)^2} - DC_4 \frac{x_4}{(x_4+C_4)^2}}; \theta = 1 \\ F_4(\mathbf{x}) \frac{x_4^{avi}}{x_4}; \theta \in [0.1, 1[\\ F_4(\mathbf{x}) \frac{x_4^{avi}}{x_4}; \theta \in [0, 0.1[. \end{cases} \tag{E.9}$$

ACCUMULATION MIXED (AM) MODE

$$\left.\frac{\partial x_5}{\partial t}\right|_{coag} = F_5(\mathbf{x}) = \begin{cases} 0; \theta = 1 \\ A' \frac{x_1}{x_1+C_1} + B' \frac{x_2}{x_2+C_2} + C' \frac{x_3}{x_3+C_3} + D' \frac{x_4}{x_4+C_4} - E' \frac{x_5}{x_5+C_5} + F' \frac{x_6}{x_6+C_6}; \theta \in [0.1, 1[\\ -E'' \frac{x_5}{x_5+C_5}; \theta \in [0, 0.1[\end{cases} \tag{E.10}$$

Where the terms A', B', C', D', E', E" and F' are defined as:

$$A' = \rho_1 \frac{\pi}{6} \left[f_{1,5} + f_{1,6} \right],$$

$$B' = \rho_2 \frac{\pi}{6} \left[f_{2,4} + f_{2,5} + f_{2,6} \right],$$

$$C' = \rho_3 \frac{\pi}{6} \left[f_{3,4} + f_{3,5} \right],$$

$$D' = \rho_4 \frac{\pi}{6} \left[f'_{2,4} + f'_{3,4} + f_{4,5} + f_{4,6} \right],$$

$$E' = \rho_5 \frac{\pi}{6} \left[f_{5,7} + f_{5,8} + f_{5,9} \right],$$

$$E'' = \rho_5 \frac{\pi}{6} \left[f'_{3,5} + f_{5,6} + f_{5,9} \right],$$

$$F' = \rho_6 \frac{\pi}{6} \left[f'_{1,6} + f'_{2,6} + f'_{4,6} + f'_{5,6} \right].$$

Aviation's contribution is given by:

$$\left.\frac{\partial x_5^{avi}}{\partial t}\right|_{coag} = \begin{cases} 0;\ \theta = 1 \\ F_5(\mathbf{x}) \dfrac{A'C_1 \frac{x_1^{avi}}{(x_1+C_1)^2} + B'C_2 \frac{x_2^{avi}}{(x_2+C_2)^2} + C'C_3 \frac{x_3^{avi}}{(x_3+C_3)^2} + D'C_4 \frac{x_4^{avi}}{(x_4+C_4)^2} - E'C_5 \frac{x_5^{avi}}{(x_5+C_5)^2} + F'C_6 \frac{x_6^{avi}}{(x_6+C_6)^2}}{A'C_1 \frac{x_1}{(x_1+C_1)^2} + B'C_2 \frac{x_2}{(x_2+C_2)^2} + C'C_3 \frac{x_3}{(x_3+C_3)^2} + D'C_4 \frac{x_4}{(x_4+C_4)^2} - E'C_5 \frac{x_5}{(x_5+C_5)^2} + F'C_6 \frac{x_6}{(x_6+C_6)^2}};\ \theta \in [0.1, 1[\\ F_5(\mathbf{x}) \dfrac{x_5^{avi}}{x_5};\ \theta \in [0, 0.1[. \end{cases} \tag{E.11}$$

ACCUMULATION INSOLUBLE (AI) MODE

$$\left.\frac{\partial x_6}{\partial t}\right|_{coag} = F_6(\mathbf{x}) = \begin{cases} 0;\ \theta = 1 \\ -F \frac{x_6}{x_6+C_6};\ \theta \in [0.1, 1[\\ A' \dfrac{x_1}{x_1+C_1} + B' \dfrac{x_2}{x_2+C_2} + C' \dfrac{x_3}{x_3+C_3} + D' \dfrac{x_4}{x_4+C_4} + E' \dfrac{x_5}{x_5+C_5} \\ \quad - F' \dfrac{x_6}{x_6+C_6} + G' \dfrac{x_7}{x_7+C_7} + H' \dfrac{x_8}{x_8+C_8};\ \theta \in [0, 0.1[\end{cases} \tag{E.12}$$

Where the terms A', B', C', D', E', F', F, G' and H' are defined as:

$$A' = \rho_1 \frac{\pi}{6} f_{1,6},$$

$$B' = \rho_2 \frac{\pi}{6} f_{2,6},$$

$$C' = \rho_3 \frac{\pi}{6} f_{3,6},$$

$$D' = \rho_4 \frac{\pi}{6} f_{4,6},$$

$$E' = \rho_5 \frac{\pi}{6} f_{5,6},$$

$$F = \rho_6 \frac{\pi}{6} \left[f'_{1,6} + f_{2,6} + f'_{4,6} + f'_{5,6} + f_{6,7} + f_{6,8} \right],$$

$$F' = \rho_6 \frac{\pi}{6} f_{6,9},$$

$$G' = \rho_7 \frac{\pi}{6} f'_{6,7},$$

$$H' = \rho_8 \frac{\pi}{6} f'_{6,8}.$$

Aviation's contribution is given by:

$$\left.\frac{\partial x_6^{avi}}{\partial t}\right|_{coag} = \begin{cases} 0;\ \theta = 1 \\ F_6(\mathbf{x})\frac{x_6^{avi}}{x_6};\ \theta \in [0.1, 1[\\ F_6(\mathbf{x})\frac{A'C_1\frac{x_1^{avi}}{(x_1+C_1)^2}+B'C_2\frac{x_2^{avi}}{(x_2+C_2)^2}+C'C_3\frac{x_3^{avi}}{(x_3+C_3)^2}+D'C_4\frac{x_4^{avi}}{(x_4+C_4)^2}+E'C_5\frac{x_5^{avi}}{(x_5+C_5)^2}-F'C_6\frac{x_6^{avi}}{(x_6+C_6)^2}+G'C_7\frac{x_7^{avi}}{(x_7+C_7)^2}+H'C_8\frac{x_8^{avi}}{(x_8+C_8)^2}}{A'C_1\frac{x_1}{(x_1+C_1)^2}+B'C_2\frac{x_2}{(x_2+C_2)^2}+C'C_3\frac{x_3}{(x_3+C_3)^2}+D'C_4\frac{x_4}{(x_4+C_4)^2}+E'C_5\frac{x_5}{(x_5+C_5)^2}-F'C_6\frac{x_6}{(x_6+C_6)^2}+G'C_7\frac{x_7}{(x_7+C_7)^2}+H'C_8\frac{x_8}{(x_8+C_8)^2}};\ \theta \in [0, 0.1[. \end{cases} \tag{E.13}$$

Coarse Soluble (cs) mode

$$\left.\frac{\partial x_7}{\partial t}\right|_{coag} = F_7(\mathbf{x}) = \begin{cases} A\frac{x_1}{x_1+C_1} + D\frac{x_4}{x_4+C_4};\ \theta = 1 \\ -G'\frac{x_7}{x_7+C_7};\ \theta \in [0.1, 1[\\ -G''\frac{x_7}{x_7+C_7};\ \theta \in [0, 0.1[\end{cases} \tag{E.14}$$

Where the terms A, D, G' and G" are defined as:

$$A = \rho_1 \frac{\pi}{6} f_{1,7},$$

$$D = \rho_4 \frac{\pi}{6} f_{4,7},$$

$$G' = \rho_7 \frac{\pi}{6} \left[f'_{2,7} + f'_{3,7} + f'_{5,7} + f'_{6,7} + f_{7,8} + f_{7,9}\right],$$

$$G'' = \rho_7 \frac{\pi}{6} \left[f'_{6,7} + f_{7,9}\right].$$

Aviation's contribution is given by:

$$\left.\frac{\partial x_7^{avi}}{\partial t}\right|_{coag} = \begin{cases} F_7(\mathbf{x}) \dfrac{AC_1 \frac{x_1^{avi}}{(x_1+C_1)^2} + DC_4 \frac{x_4^{avi}}{(x_4+C_4)^2}}{AC_1 \frac{x_1}{(x_1+C_1)^2} + DC_4 \frac{x_4}{(x_4+C_4)^2}}; \ \theta = 1 \\ F_7(\mathbf{x}) \frac{x_7^{avi}}{x_7}; \ \theta \in [0.1, 1[\\ F_7(\mathbf{x}) \frac{x_7^{avi}}{x_7}; \ \theta \in [0, 0.1[. \end{cases} \tag{E.15}$$

COARSE MIXED (CM) MODE

$$\left.\frac{\partial x_8}{\partial t}\right|_{coag} = F_8(\mathbf{x}) = \begin{cases} 0; \ \theta = 1 \\ A' \dfrac{x_1}{x_1+C_1} + B' \dfrac{x_2}{x_2+C_2} + C' \dfrac{x_3}{x_3+C_3} + D' \dfrac{x_4}{x_4+C_4} + E' \dfrac{x_5}{x_5+C_5} \\ + F' \dfrac{x_6}{x_6+C_6} + G' \dfrac{x_7}{x_7+C_7} + I' \dfrac{x_9}{x_9+C_9}; \ \theta \in [0.1, 1[\\ -H'' \frac{x_8}{x_8+C_8}; \ \theta \in [0, 0.1[\end{cases} \tag{E.16}$$

Where the terms A', B', C', D', E' F', G', H" and I' are defined as:

$$A' = \rho_1 \frac{\pi}{6} f_{1,8},$$

$$B' = \rho_2 \frac{\pi}{6} \left[f_{2,7} + f_{2,8} \right],$$

$$C' = \rho_3 \frac{\pi}{6} \left[f_{3,7} + f_{3,8} \right],$$

$$D' = \rho_4 \frac{\pi}{6} \left[f_{4,8} + f_{4,9} \right],$$

$$E' = \rho_5 \frac{\pi}{6} \left[f_{5,7} + f_{5,8} + f_{5,9} \right],$$

$$F' = \rho_6 \frac{\pi}{6} \left[f_{6,7} + f_{6,8} \right],$$

$$G' = \rho_7 \frac{\pi}{6} \left[f'_{2,7} + f'_{3,7} + f'_{5,7} + f'_{6,7} + f_{7,8} + f_{7,9} \right],$$

$$H'' = \rho_8 \frac{\pi}{6} \left[f'_{6,8} + f_{8,9} \right],$$

$$I' = \rho_9 \frac{\pi}{6} \left[f'_{4,9} + f'_{5,9} + f'_{7,9} + f'_{8,9} \right].$$

Aviation's contribution is given by:

$$\left.\frac{\partial x_8^{avi}}{\partial t}\right|_{coag} = \begin{cases} 0;\ \theta = 1 \\ F_8(\mathbf{x})\dfrac{A'C_1\frac{x_1^{avi}}{(x_1+C_1)^2}+B'C_2\frac{x_2^{avi}}{(x_2+C_2)^2}+C'C_3\frac{x_3^{avi}}{(x_3+C_3)^2}+D'C_4\frac{x_4^{avi}}{(x_4+C_4)^2}+E'C_5\frac{x_5^{avi}}{(x_5+C_5)^2}+F'C_6\frac{x_6^{avi}}{(x_6+C_6)^2}+G'C_7\frac{x_7^{avi}}{(x_7+C_7)^2}+I'C_9\frac{x_9^{avi}}{(x_9+C_9)^2}}{A'C_1\frac{x_1}{(x_1+C_1)^2}+B'C_2\frac{x_2}{(x_2+C_2)^2}+C'C_3\frac{x_3}{(x_3+C_3)^2}+D'C_4\frac{x_4}{(x_4+C_4)^2}+E'C_5\frac{x_5}{(x_5+C_5)^2}+F'C_6\frac{x_6}{(x_6+C_6)^2}+G'C_7\frac{x_7}{(x_7+C_7)^2}+I'C_9\frac{x_9}{(x_9+C_9)^2}};\ \theta \in [0.1,1[\\ F_8(\mathbf{x})\dfrac{x_8^{avi}}{x_8};\ \theta \in [0,0.1[. \end{cases} \tag{E.17}$$

COARSE INSOLUBLE (CI) MODE

$$\left.\frac{\partial x_9}{\partial t}\right|_{coag} = F_9(\mathbf{x}) = \begin{cases} 0;\ \theta = 1 \\ -I'\frac{x_9}{x_9+C_9};\ \theta \in [0.1,1[\\ A''\dfrac{x_1}{x_1+C_1}+B''\dfrac{x_2}{x_2+C_2}+C''\dfrac{x_3}{x_3+C_3}+D''\dfrac{x_4}{x_4+C_4}+E''\dfrac{x_5}{x_5+C_5} \\ +F''\dfrac{x_6}{x_6+C_6}+G''\dfrac{x_7}{x_7+C_7}+H''\dfrac{x_8}{x_8+C_8};\ \theta \in [0,0.1[\end{cases} \tag{E.18}$$

Where the terms A", B", C", D", E", F", G", H" and I' are defined as:

$$A'' = \rho_1 \frac{\pi}{6} f_{1,9},$$

$$B'' = \rho_2 \frac{\pi}{6} f_{2,9},$$

$$C'' = \rho_3 \frac{\pi}{6} f_{3,9},$$

$$D'' = \rho_4 \frac{\pi}{6} f_{4,9},$$

$$E'' = \rho_5 \frac{\pi}{6} f_{5,9},$$

$$F'' = \rho_6 \frac{\pi}{6} f_{6,9},$$

$$G'' = \rho_7 \frac{\pi}{6} f_{7,9},$$

$$H'' = \rho_8 \frac{\pi}{6} f_{8,9},$$

$$I' = \rho_9 \frac{\pi}{6} \left[f'_{4,9} + f'_{5,9} + f'_{7,9} + f'_{8,9} \right].$$

Aviation's contribution is given by:

$$\left.\frac{\partial x_9^{avi}}{\partial t}\right|_{coag} = \begin{cases} 0;\ \theta = 1 \\ F_9(\mathbf{x})\frac{x_9^{avi}}{x_9};\ \theta \in [0.1, 1[\\ F_9(\mathbf{x})\frac{A''C_1\frac{x_1^{avi}}{(x_1+C_1)^2}+B''C_2\frac{x_2^{avi}}{(x_2+C_2)^2}+C''C_3\frac{x_3^{avi}}{(x_3+C_3)^2}+D''C_4\frac{x_4^{avi}}{(x_4+C_4)^2}+E''C_5\frac{x_5^{avi}}{(x_5+C_5)^2}+F''C_6\frac{x_6^{avi}}{(x_6+C_6)^2}+G''C_7\frac{x_7^{avi}}{(x_7+C_7)^2}+H''C_8\frac{x_8^{avi}}{(x_8+C_8)^2}}{A''C_1\frac{x_1}{(x_1+C_1)^2}+B''C_2\frac{x_2}{(x_2+C_2)^2}+C''C_3\frac{x_3}{(x_3+C_3)^2}+D''C_4\frac{x_4}{(x_4+C_4)^2}+E''C_5\frac{x_5}{(x_5+C_5)^2}+F''C_6\frac{x_6}{(x_6+C_6)^2}+G''C_7\frac{x_7}{(x_7+C_7)^2}+H''C_8\frac{x_8}{(x_8+C_8)^2}};\ \theta \in [0, 0.1[. \end{cases} \tag{E.19}$$

E.3. SPATIO-TEMPORAL EVOLUTION OF AVIATION SO_2

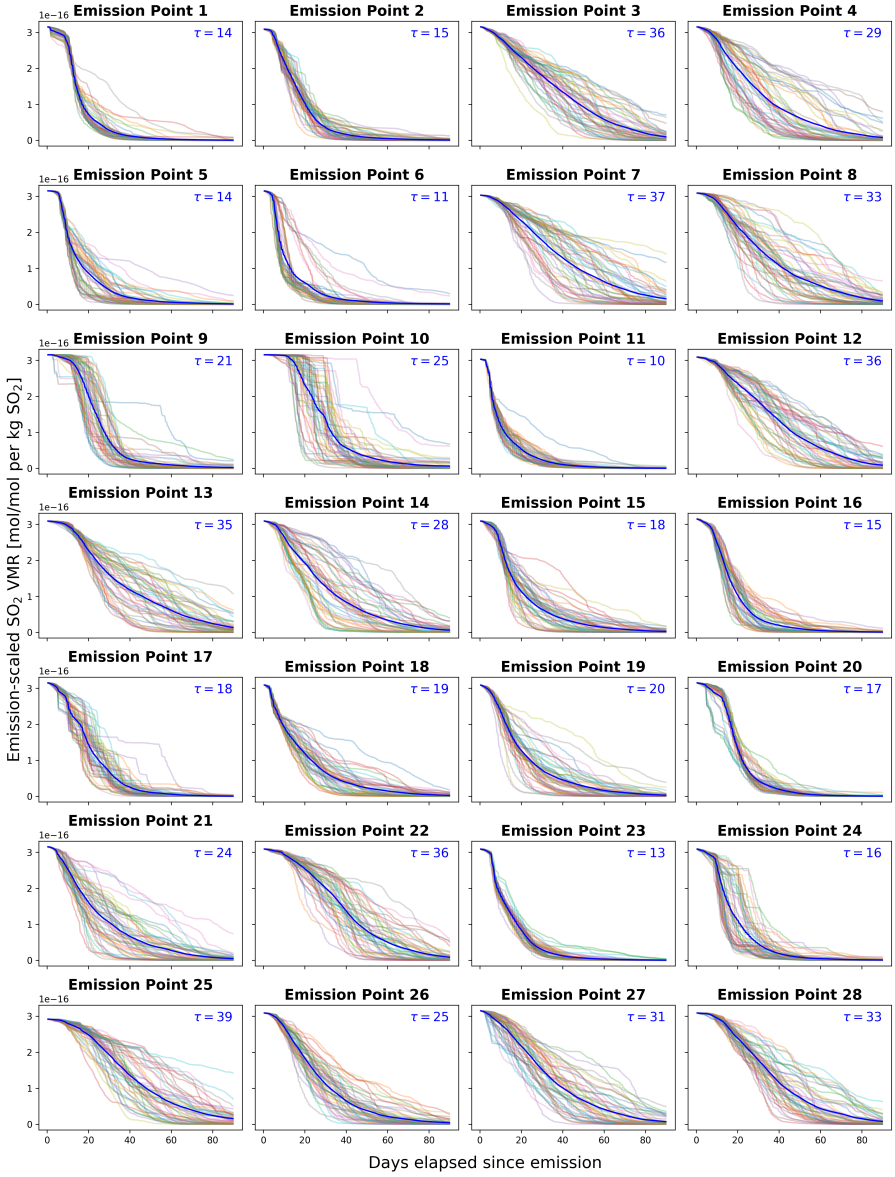


Figure E.3: SO_2 time series for the period January - March 2015. The vertical axis represents the volume mixing ratio of SO_2 scaled by the corresponding SO_2 emission amount detailed in Table B.2, i.e. the production efficiency. The horizontal axis denotes the days elapsed since the emission. The multi-colored curves track the SO_2 production efficiency across 50 air parcel trajectories per emission point and the thicker dark blue line is their mean. The value of τ in each sub-plot represents the e-folding time of the mean curve. The locations of the 28 emission points are shown in Fig. 6.2.

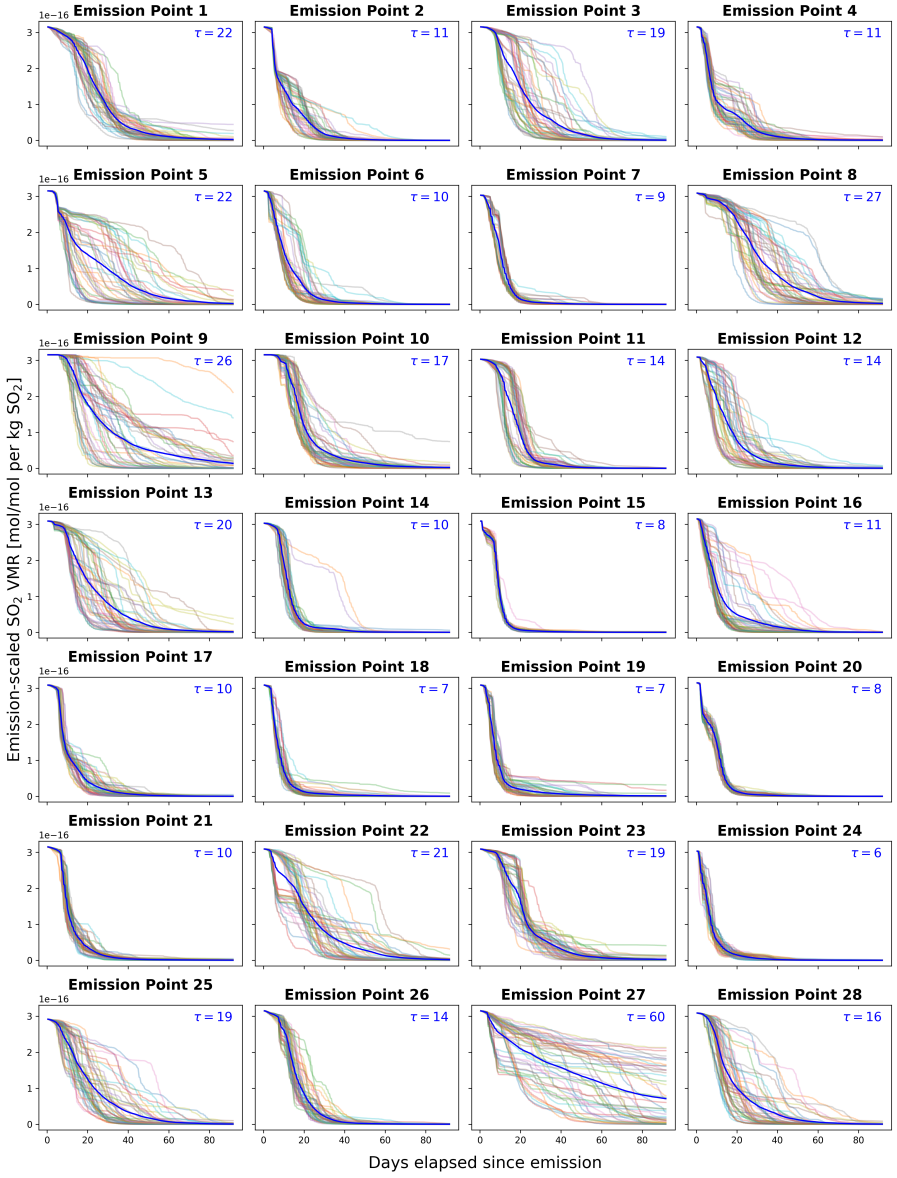


Figure E.4: SO_2 time series for the period July - September 2015. The vertical axis represents the volume mixing ratio of SO_2 scaled by the corresponding SO_2 emission amount detailed in Table B.2, i.e. the production efficiency. The horizontal axis denotes the days elapsed since the emission. The multi-colored curves track the SO_2 production efficiency across 50 air parcel trajectories per emission point and the thicker dark blue line is their mean. The value of τ on each sub-plot represents the e-folding time of the mean curve. The locations of the 28 emission points are shown in Fig. 6.2.

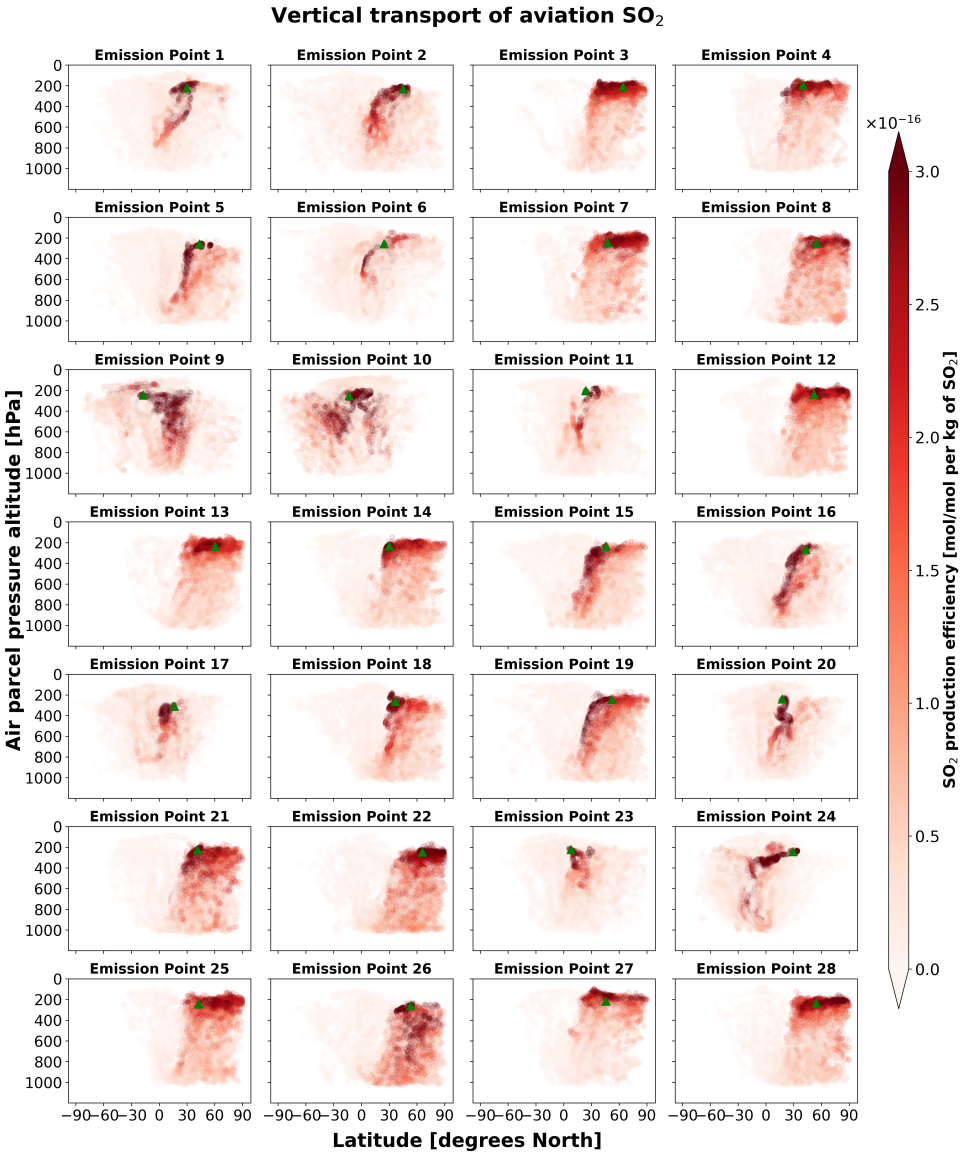


Figure E.5: SO_2 vertical profiles for the period January - March 2015. The vertical axis represents an air parcel's pressure altitude while the horizontal axis denotes its latitude. The color bar measures the SO_2 production efficiency across 50 air parcel trajectories in each emission point. The locations of the 28 emission points are shown in Fig. 6.2 and emitted amounts of SO_2 in Table B.2.

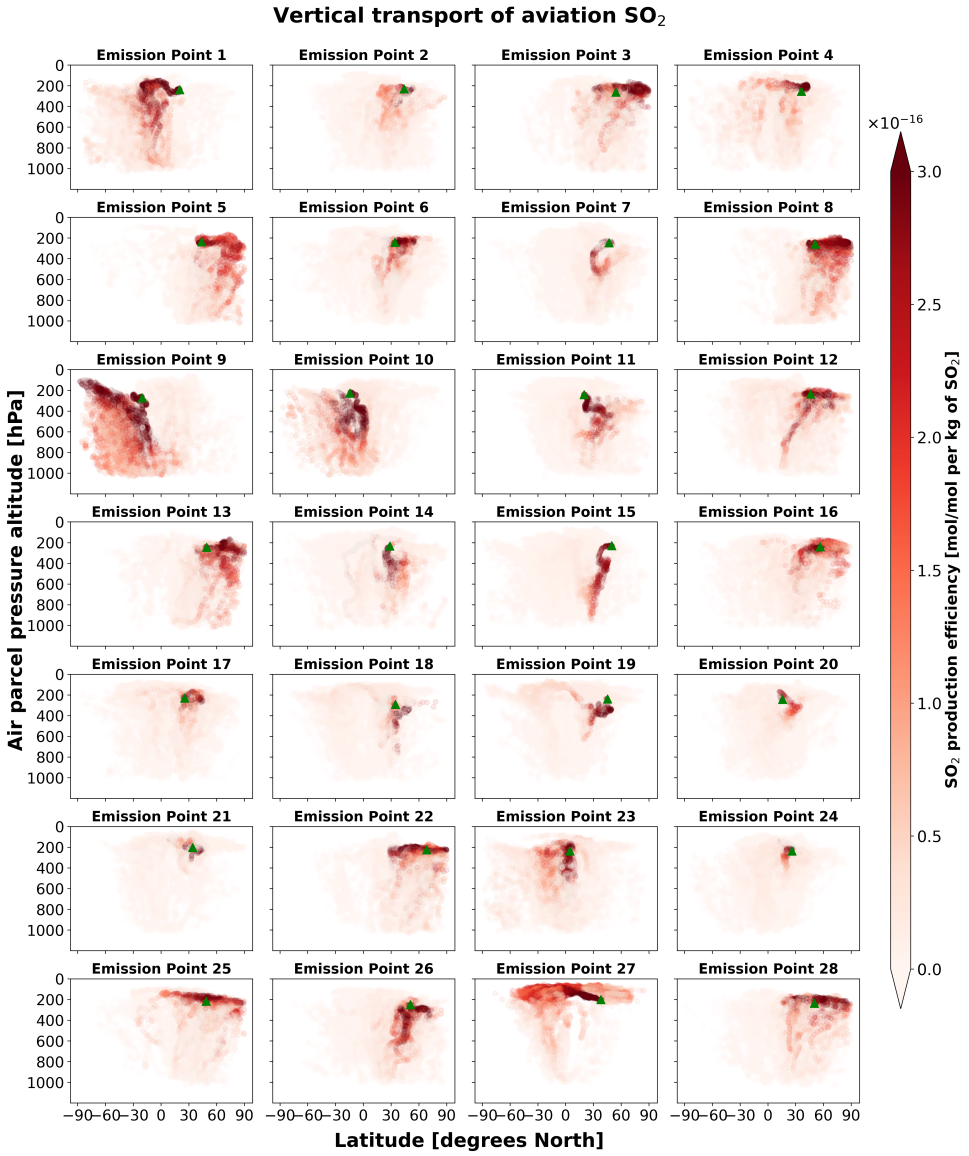


Figure E.6: SO_2 vertical profiles for the period July - September 2015. The vertical axis represents an air parcel's pressure altitude while the horizontal axis denotes its latitude. The color bar measures the SO_2 production efficiency across 50 air parcel trajectories in each emission point. The locations of the 28 emission points are shown in Fig. 6.2 and emitted amounts of SO_2 in Table B.2.

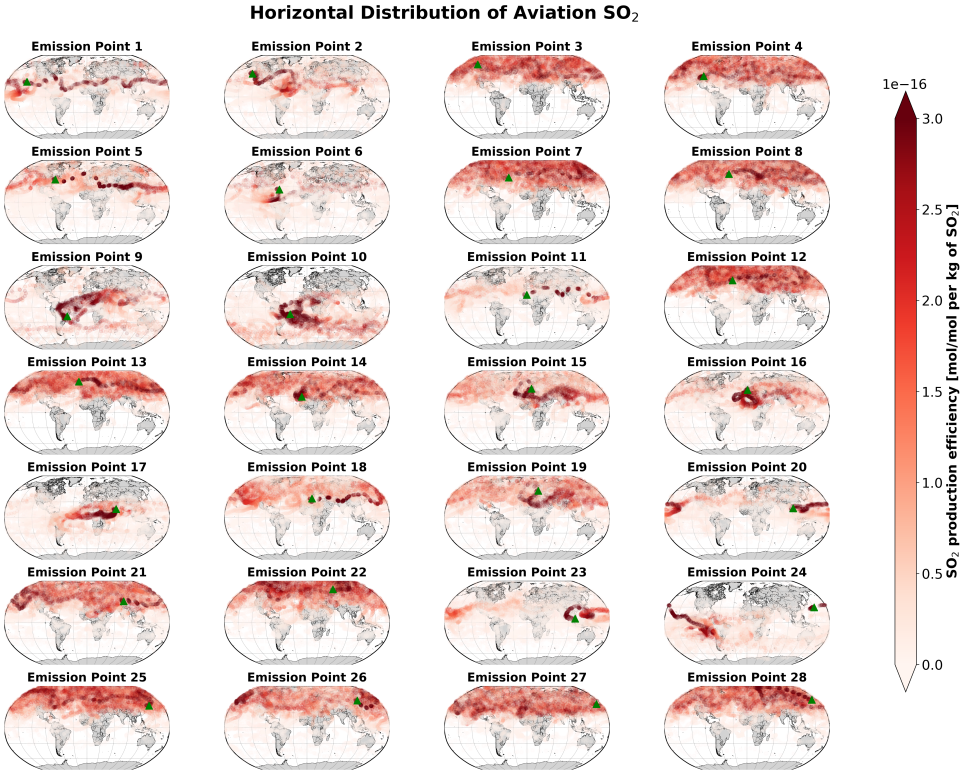


Figure E.7: SO_2 horizontal distributions for the period January - March 2015. The color bar measures the SO_2 production efficiency across 50 air parcel trajectories in each emission point. The locations of the 28 emission points are shown in Fig. 6.2 and emitted amounts of SO_2 in Table B.2.

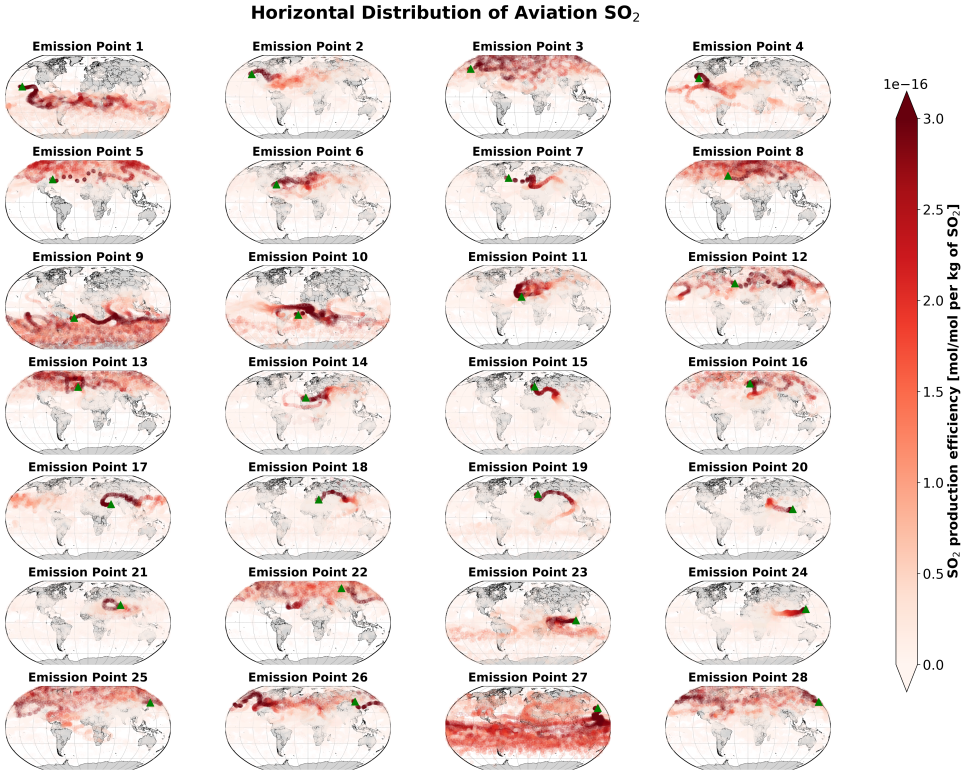


Figure E.8: SO_2 horizontal distributions for the period July - September 2015. The color bar measures the SO_2 production efficiency across 50 air parcel trajectories in each emission point. The locations of the 28 emission points are shown in Fig. 6.2 and emitted amounts of SO_2 in Table B.2.

E.4. SPATIO-TEMPORAL EVOLUTION OF AVIATION H_2SO_4

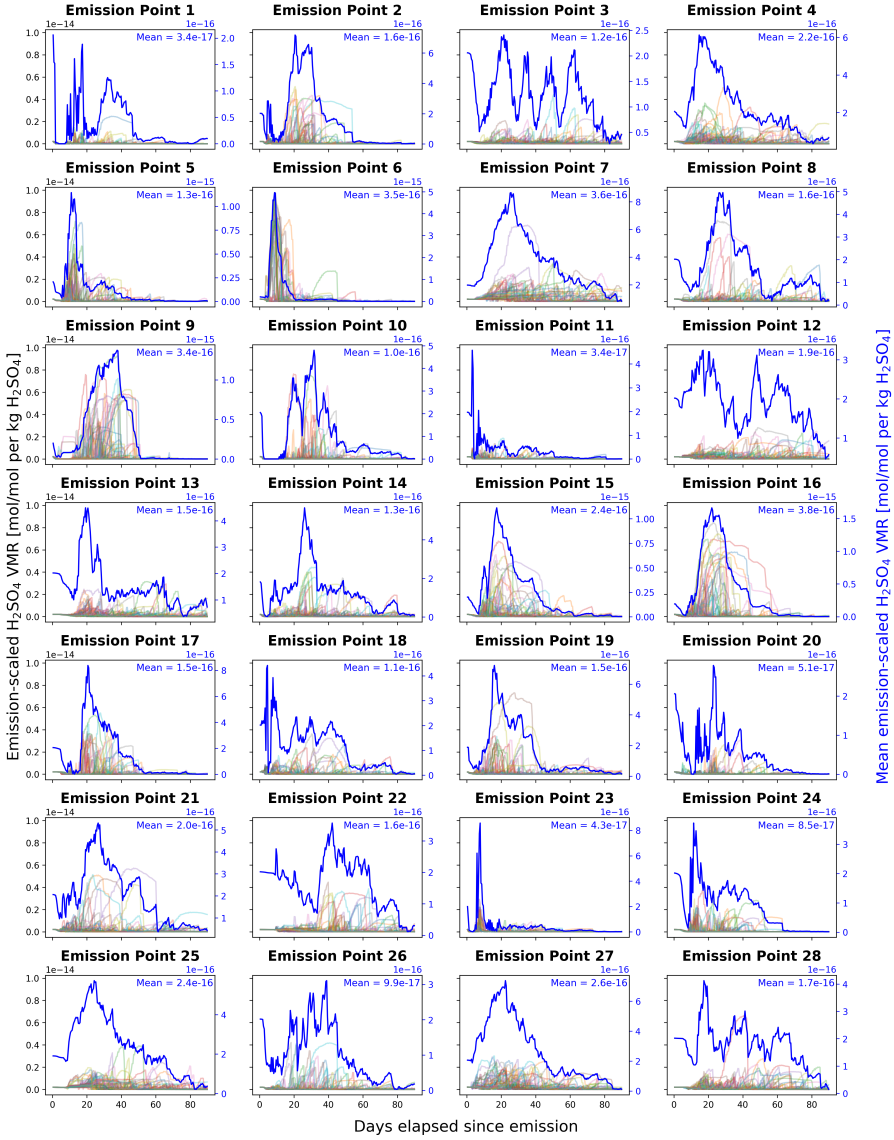


Figure E.9: H_2SO_4 time series for the period January - March 2015. The vertical axis represents the volume mixing ratio of H_2SO_4 scaled by the corresponding emission amount detailed in Table B.2, i.e. the production efficiency. The horizontal axis denotes the days elapsed since the emission. The multi-colored curves track the H_2SO_4 production efficiency across 50 air parcel trajectories in each emission point and the thicker dark blue line is their mean. The mean value of this mean curve is shown for each emission point. The locations of the 28 emission points are shown in Fig. 6.2.

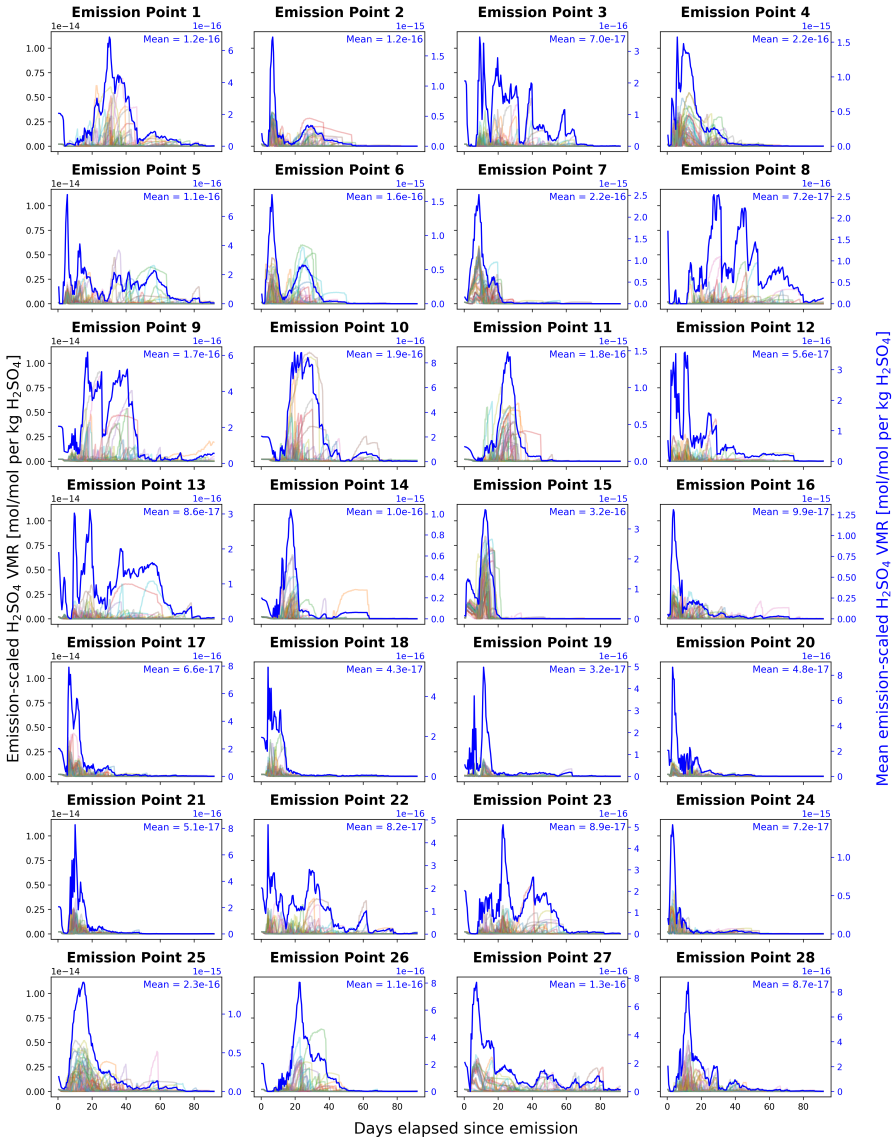


Figure E.10: H_2SO_4 time series for the period July - September 2015. The vertical axis represents the volume mixing ratio of H_2SO_4 scaled by the corresponding emission amount detailed in Table B.2, i.e. the production efficiency. The horizontal axis denotes the days elapsed since the emission. The multi-colored curves track the H_2SO_4 production efficiency across 50 air parcel trajectories in each emission point and the thicker dark blue line is their mean. The mean value of this mean curve is shown for each emission point. The locations of the 28 emission points are shown in Fig. 6.2.

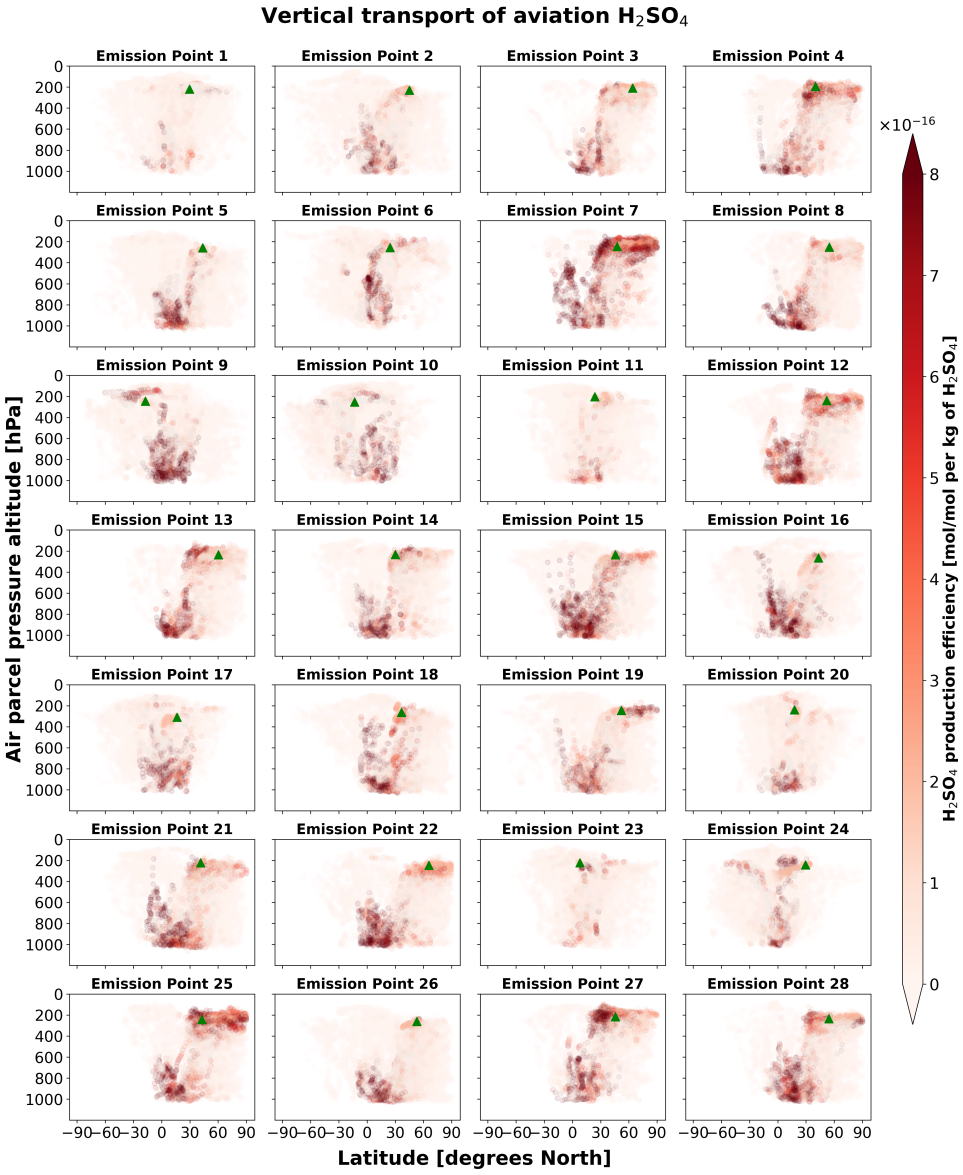


Figure E.11: H_2SO_4 vertical profiles for the period January - March 2015. The vertical axis represents an air parcel's pressure altitude while the horizontal axis denotes its latitude. The color bar measures the H_2SO_4 production efficiency across 50 air parcel trajectories in each emission point. The locations of the 28 emission points are shown in Fig. 6.2 and emitted amounts of H_2SO_4 in Table B.2.

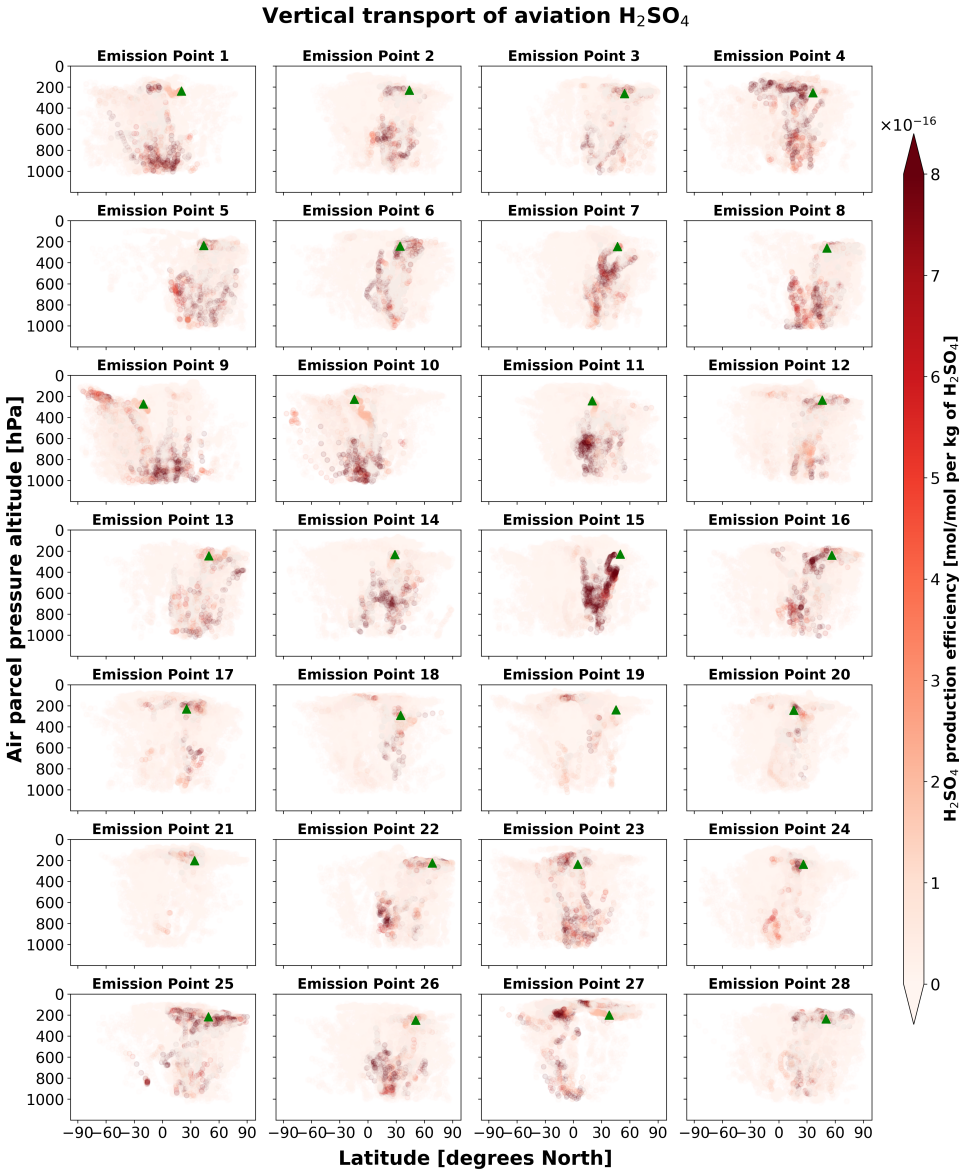


Figure E.12: H_2SO_4 vertical profiles for the period July - September 2015. The vertical axis represents an air parcel's pressure altitude while the horizontal axis denotes its latitude. The color bar measures the H_2SO_4 production efficiency across 50 air parcel trajectories. The locations of the 28 emission points are shown in Fig. 6.2 and emitted amounts of H_2SO_4 in Table B.2.

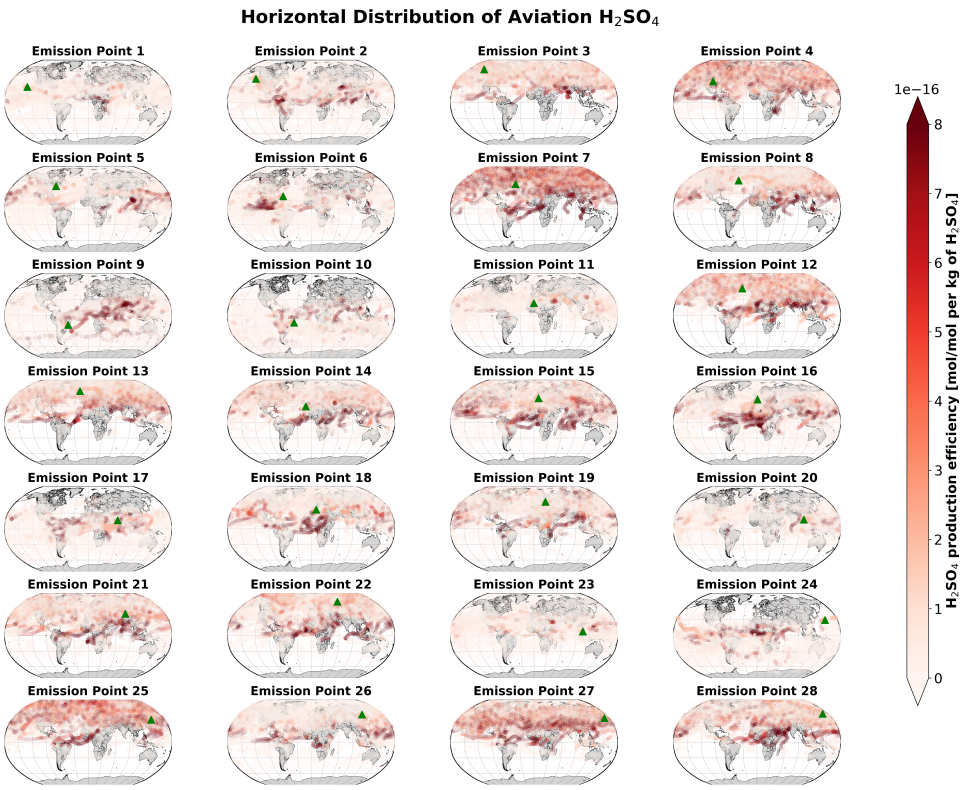


Figure E.13: H_2SO_4 horizontal distributions for the period January - March 2015. The color bar measures the H_2SO_4 production efficiency across 50 air parcel trajectories. The locations of the 28 emission points are shown in Fig. 6.2 and emitted amounts of H_2SO_4 in Table B.2.

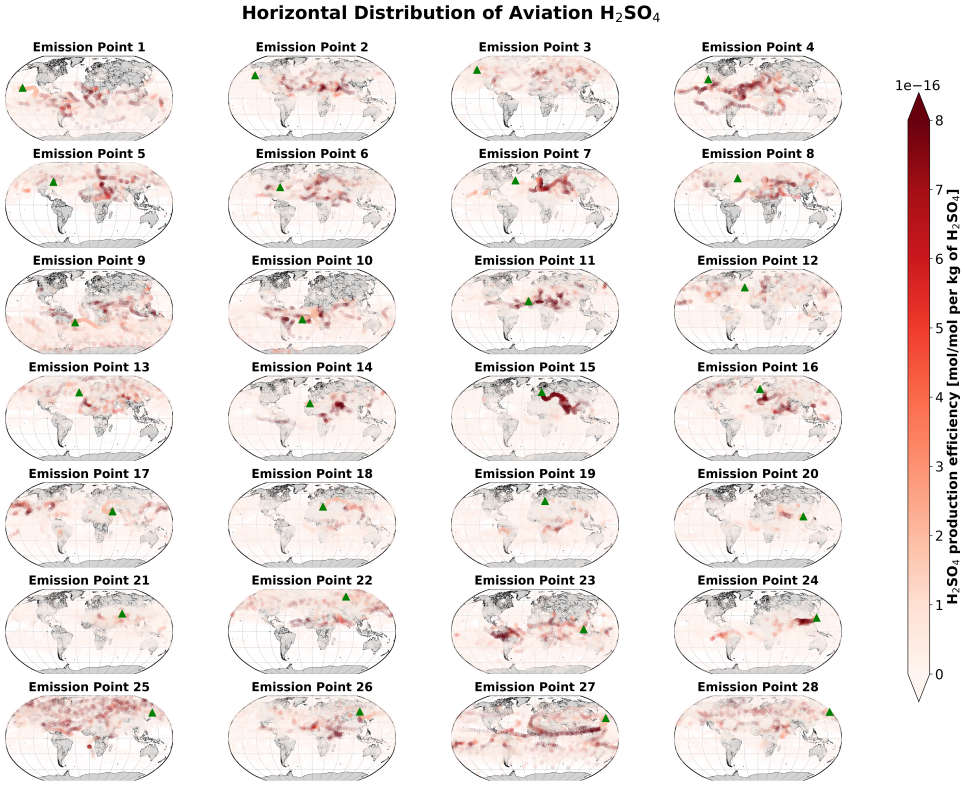


Figure E.14: H_2SO_4 horizontal distributions for the period July - September 2015. The color bar measures the H_2SO_4 production efficiency across 50 air parcel trajectories. The locations of the 28 emission points are shown in Fig. 6.2 and emitted amounts of H_2SO_4 in Table B.2.

E.5. SPATIO-TEMPORAL EVOLUTION OF AVIATION SO_4KS

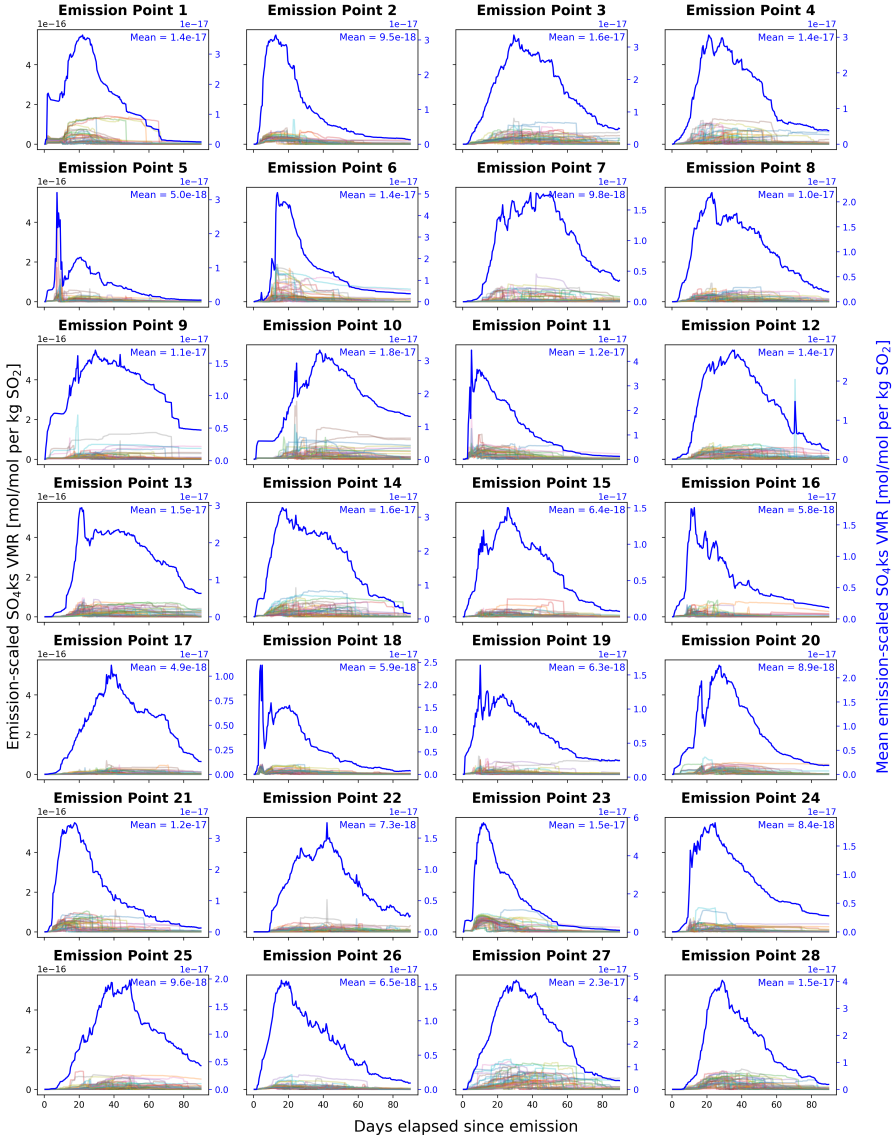


Figure E.15: SO_4ks time series for the period January - March 2015. The vertical axis represents the volume mixing ratio of SO_4ks scaled by the amount of emitted SO_2 detailed in Table B.2, i.e. the production efficiency. The horizontal axis denotes the days elapsed since the emission. The multi-colored curves track the SO_4ks production efficiency across 50 air parcel trajectories in each emission point and the thicker dark blue line is their mean. The mean value of this mean curve is shown for each emission point. The locations of the 28 emission points are shown in Fig. 6.2.

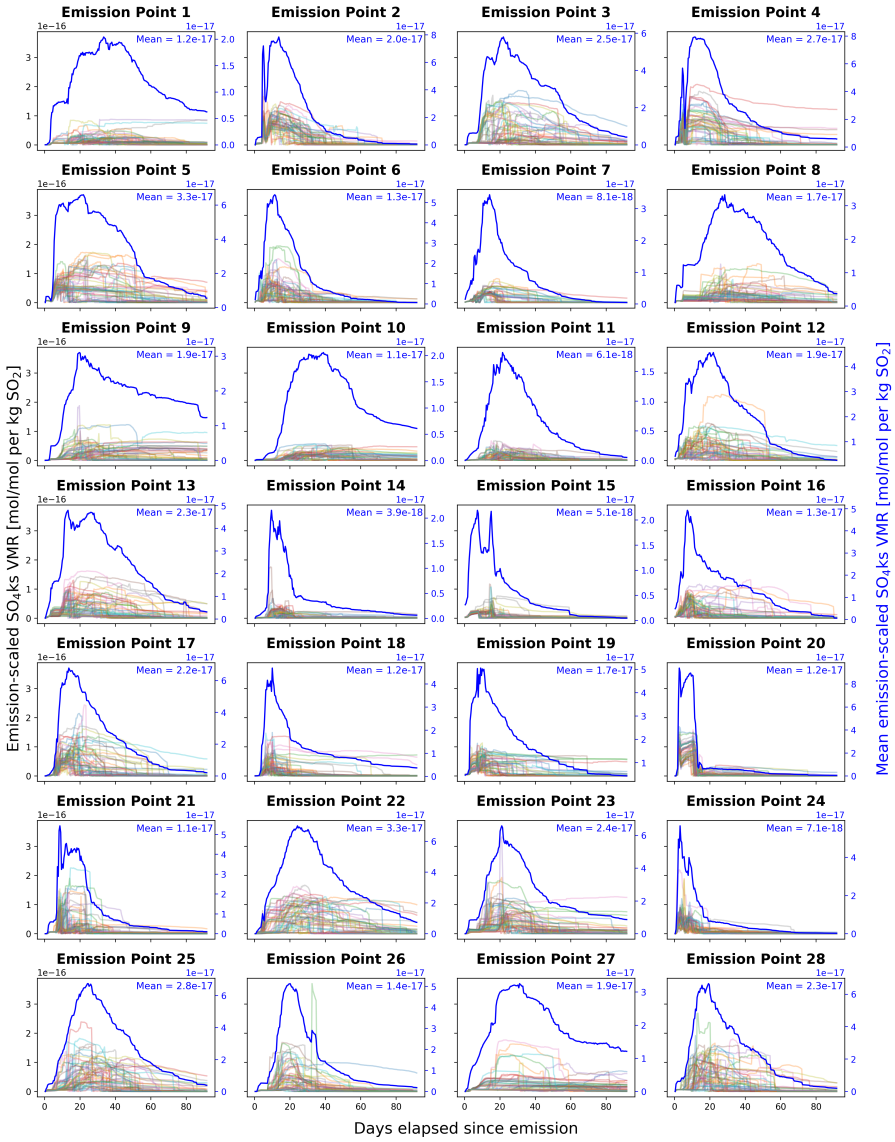


Figure E.16: SO_4ks time series for the period July - September 2015. The vertical axis represents the volume mixing ratio of SO_4ks scaled by the amount of emitted SO_2 detailed in Table B.2, i.e. the production efficiency. The horizontal axis denotes the days elapsed since the emission. The multi-colored curves track the SO_4ks production efficiency across 50 air parcel trajectories in each emission point and the thicker dark blue line is their mean. The mean value of this mean curve is shown for each emission point. The locations of the 28 emission points are shown in Fig. 6.2.

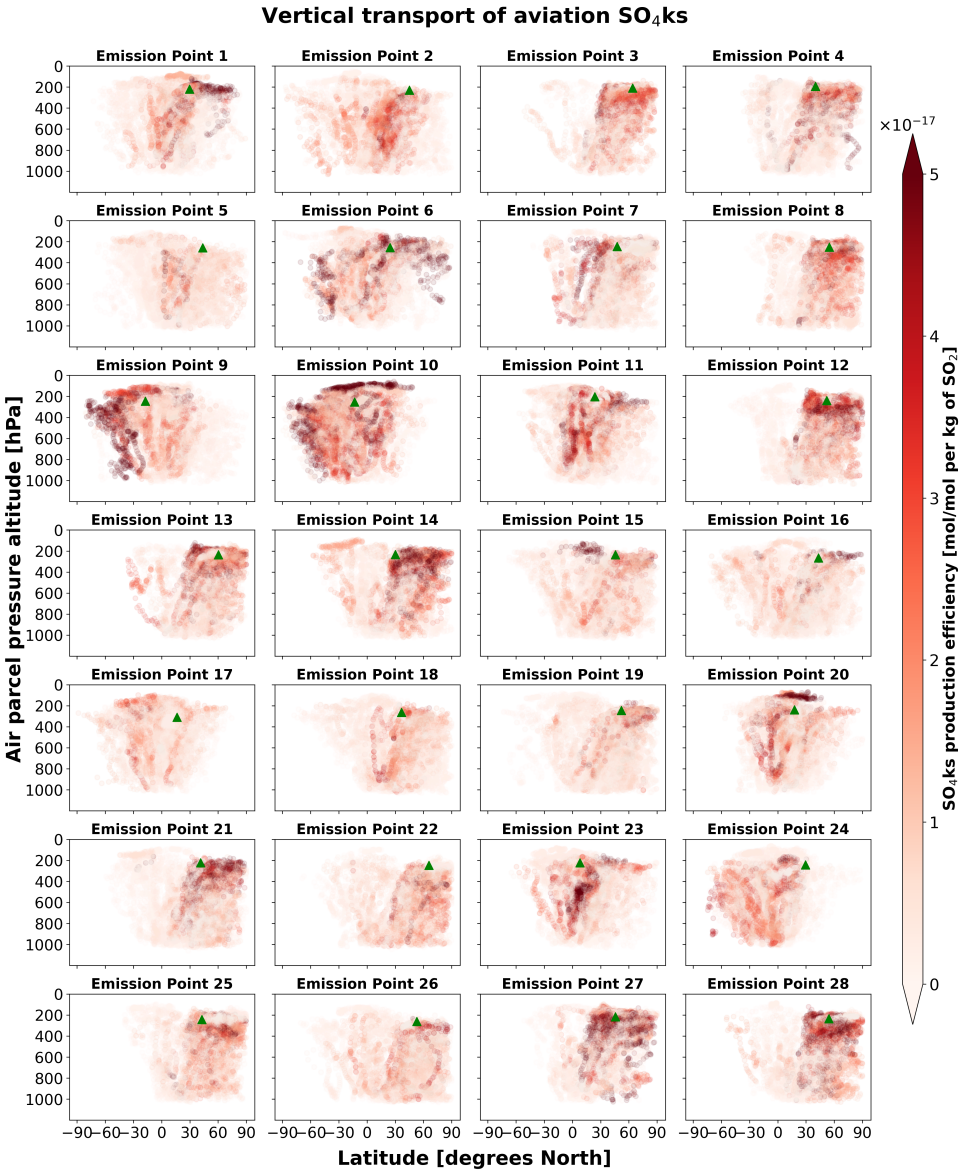


Figure E.17: SO_4ks vertical profiles for the period January - March 2015. The vertical axis represents an air parcel's pressure altitude while the horizontal axis denotes its latitude. The color bar measures the SO_4ks production efficiency per kg of emitted SO_2 across 50 air parcel trajectories. The locations of the 28 emission points are shown in Fig. 6.2 and emitted amounts in Table B.2.

E

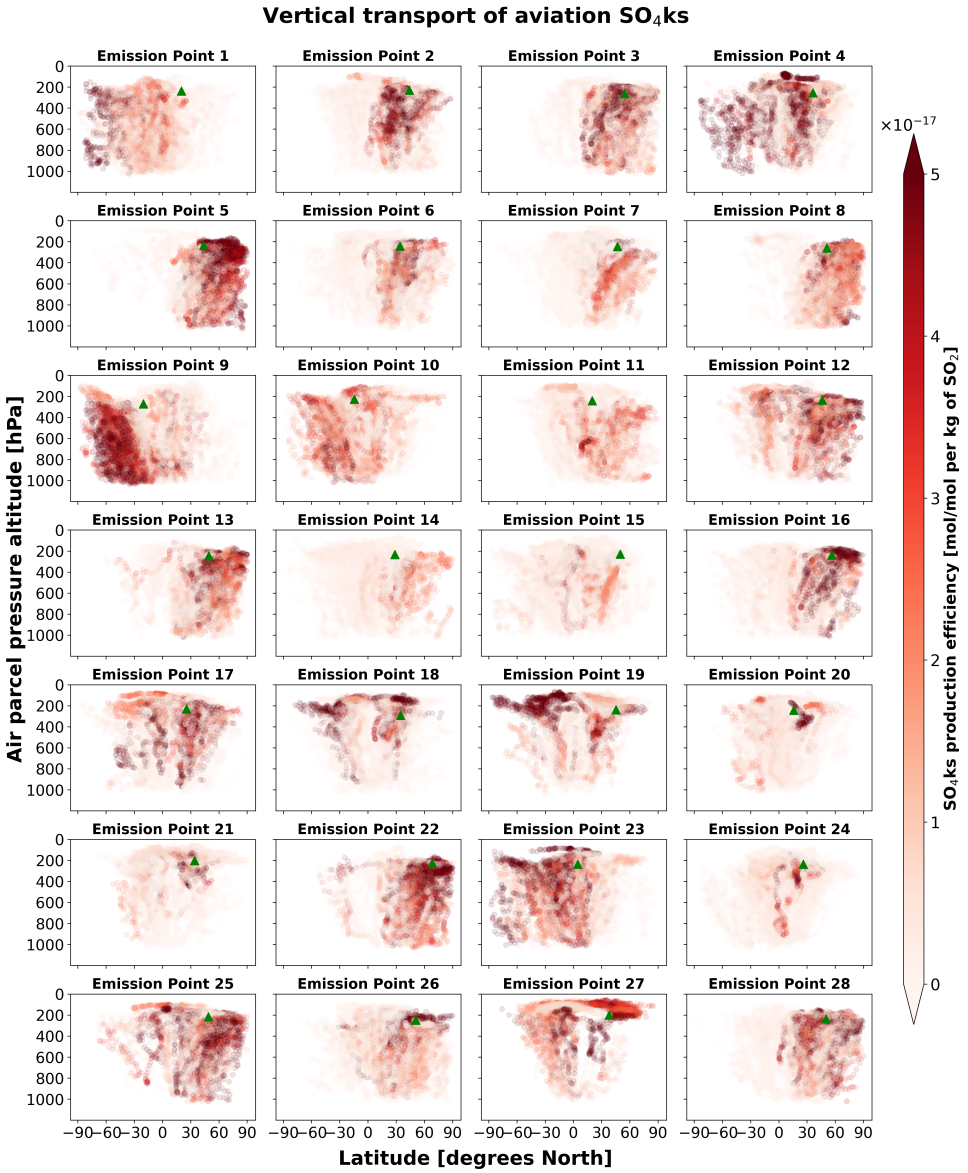


Figure E.18: SO_4ks vertical profiles for the period July - September 2015. The vertical axis represents an air parcel's pressure altitude while the horizontal axis denotes its latitude. The color bar measures the SO_4ks production efficiency per kg of emitted SO_2 across 50 air parcel trajectories. The locations of the 28 emission points are shown in Fig. 6.2 and emitted amounts in Table B.2.

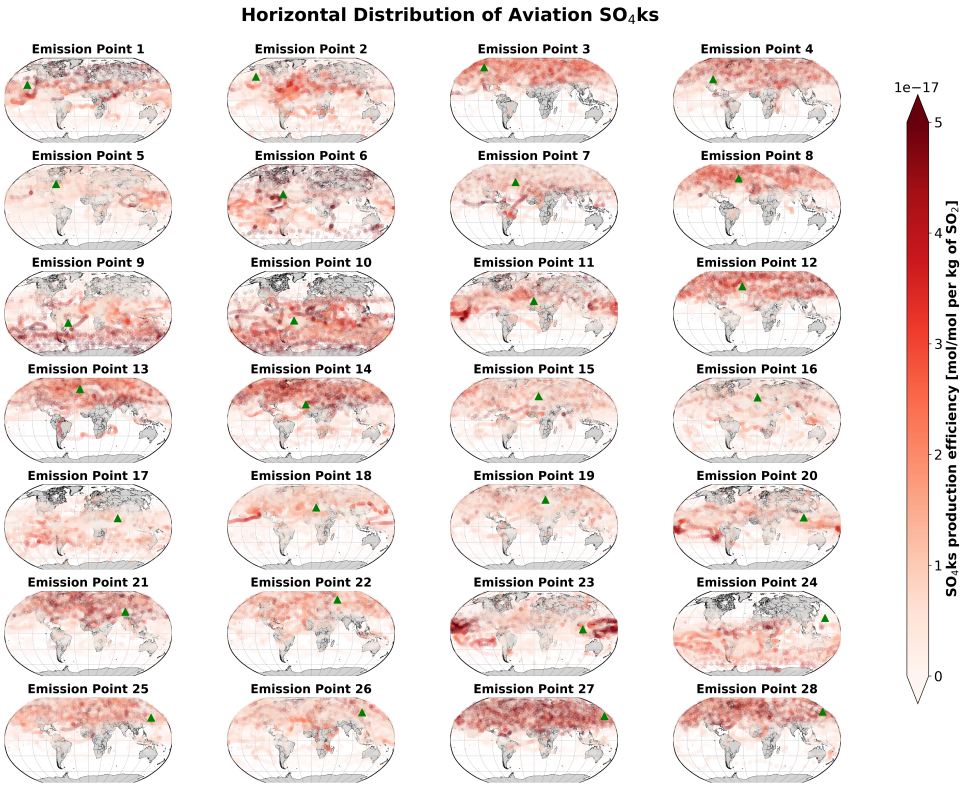


Figure E.19: SO_4ks horizontal distributions for the period January - March 2015. The color bar measures the SO_4ks production efficiency per kg of emitted SO_2 across 50 air parcel trajectories. The locations of the 28 emission points are shown in Fig. 6.2 and emitted amounts in Table B.2.

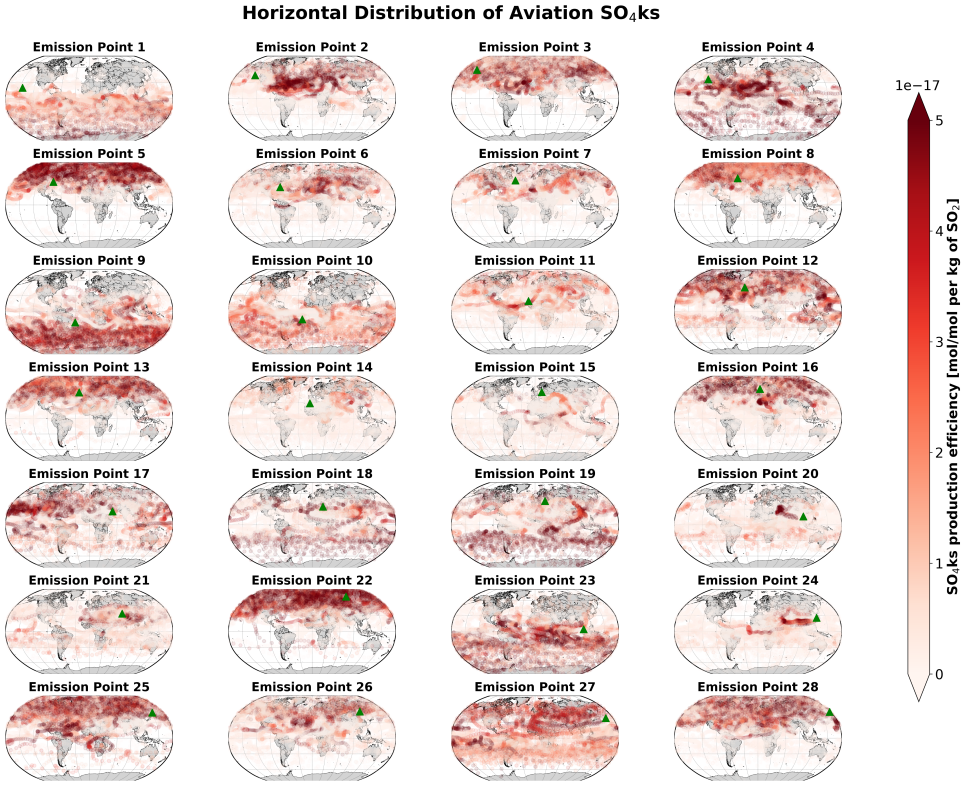


Figure E.20: SO_4ks horizontal distributions for the period July - September 2015. The color bar measures the SO_4ks production efficiency per kg of emitted SO_2 across 50 air parcel trajectories. The locations of the 28 emission points are shown in Fig. 6.2 and emitted amounts in Table B.2.

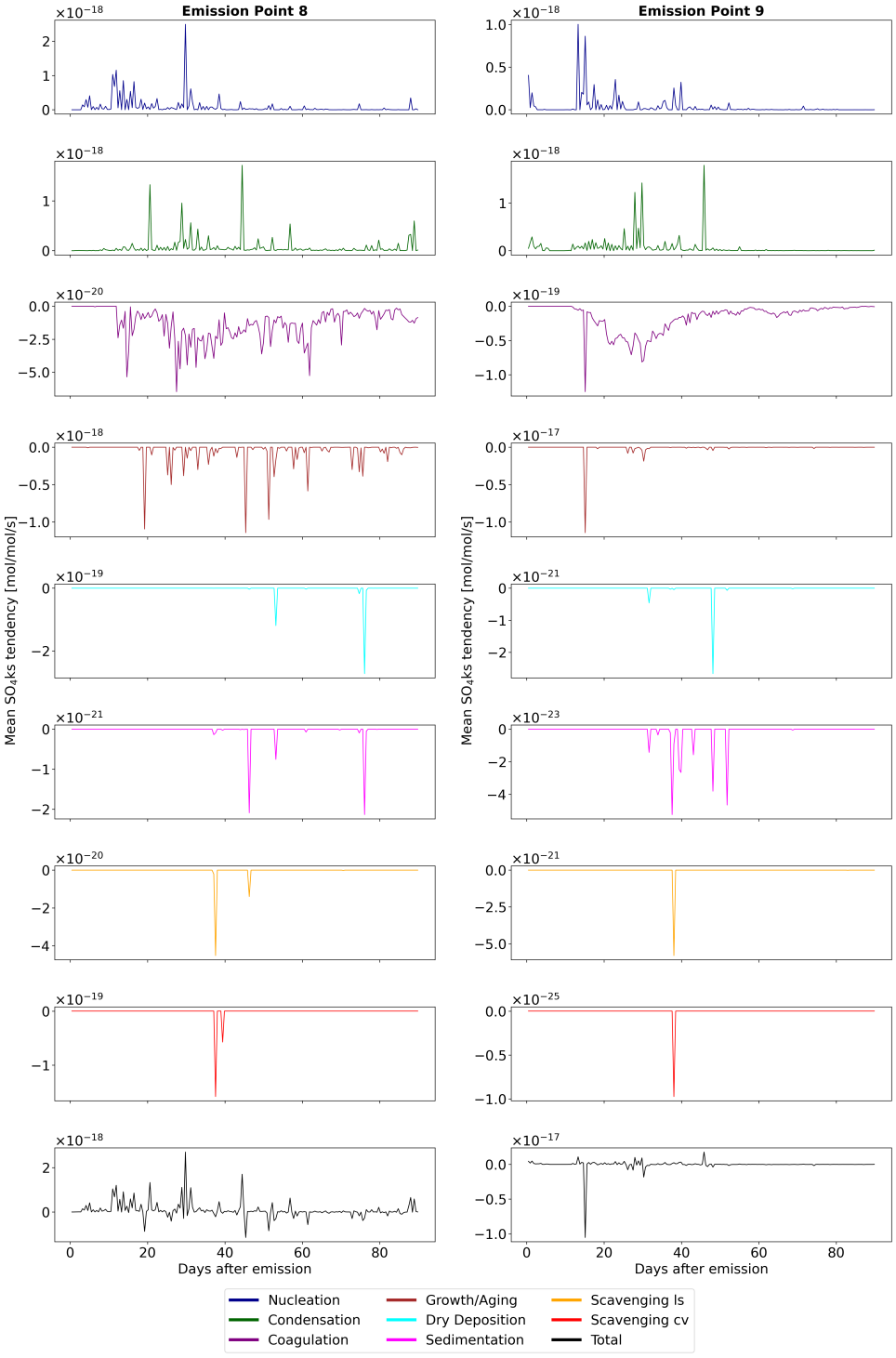


Figure E.21: Summary of process contributions to the total SO_4ks tendency for the period January - March 2015.

E.6. SPATIO-TEMPORAL EVOLUTION OF AVIATION SO_4AS

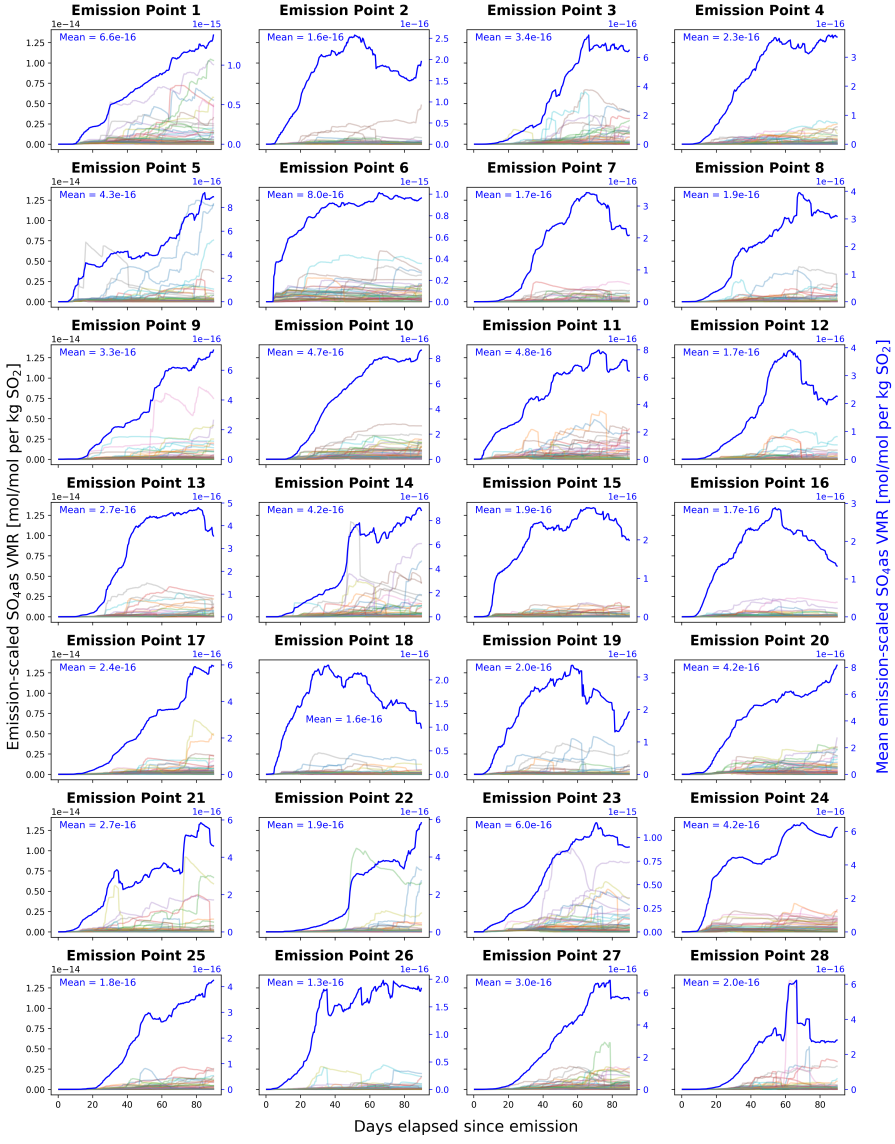


Figure E.22: SO_4as time series for the period January - March 2015. The vertical axis represents the volume mixing ratio of SO_4as scaled by the amount of emitted SO_2 detailed in Table B.2, i.e. the production efficiency. The horizontal axis denotes the days elapsed since the emission. The multi-colored curves track the SO_4as production efficiency across 50 air parcel trajectories in each emission point and the thicker dark blue line is their mean. The mean value of this mean curve is shown for each emission point. The locations of the 28 emission points are shown in Fig. 6.2.

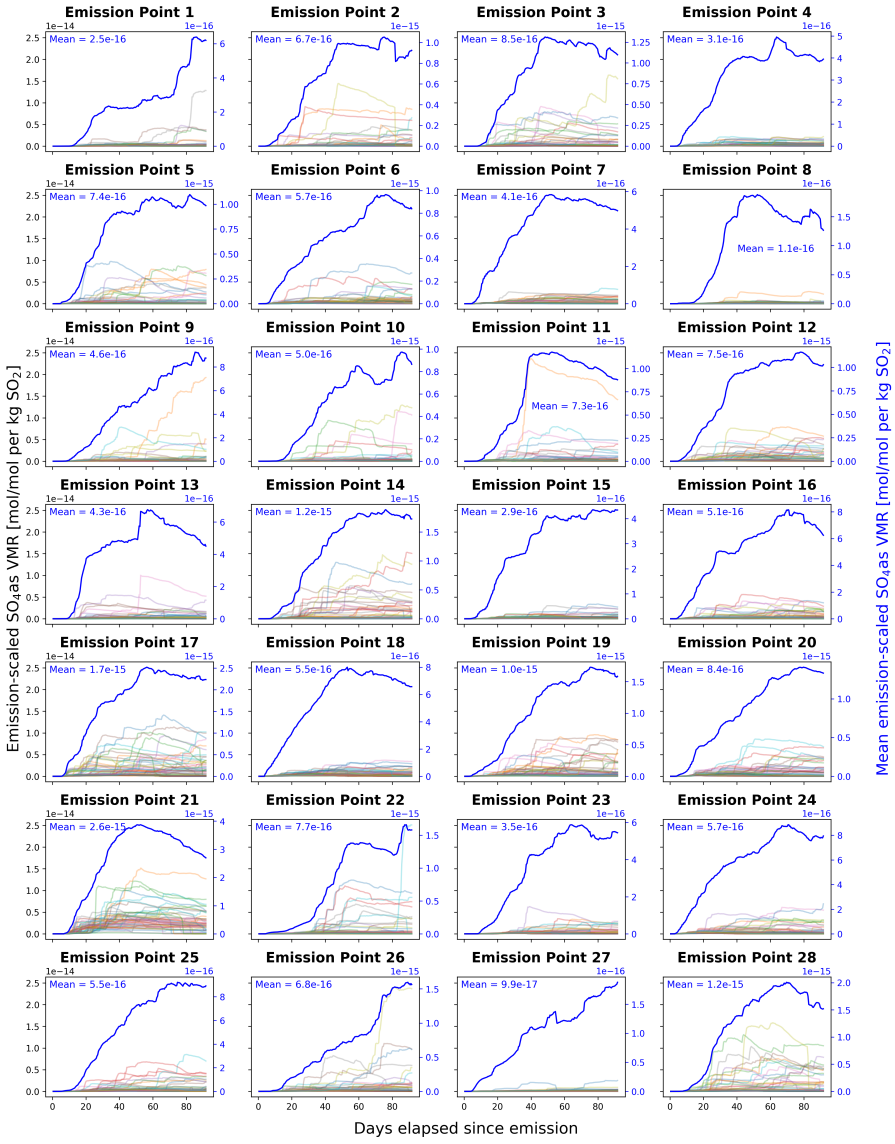


Figure E.23: SO_4as time series for the period July - September 2015. The vertical axis represents the volume mixing ratio of SO_4as scaled by the amount of emitted SO_2 detailed in Table B.2, i.e. the production efficiency. The horizontal axis denotes the days elapsed since the emission. The multi-colored curves track the SO_4as production efficiency across 50 air parcel trajectories in each emission point and the thicker dark blue line is their mean. The mean value of this mean curve is shown for each emission point. The locations of the 28 emission points are shown in Fig. 6.2.

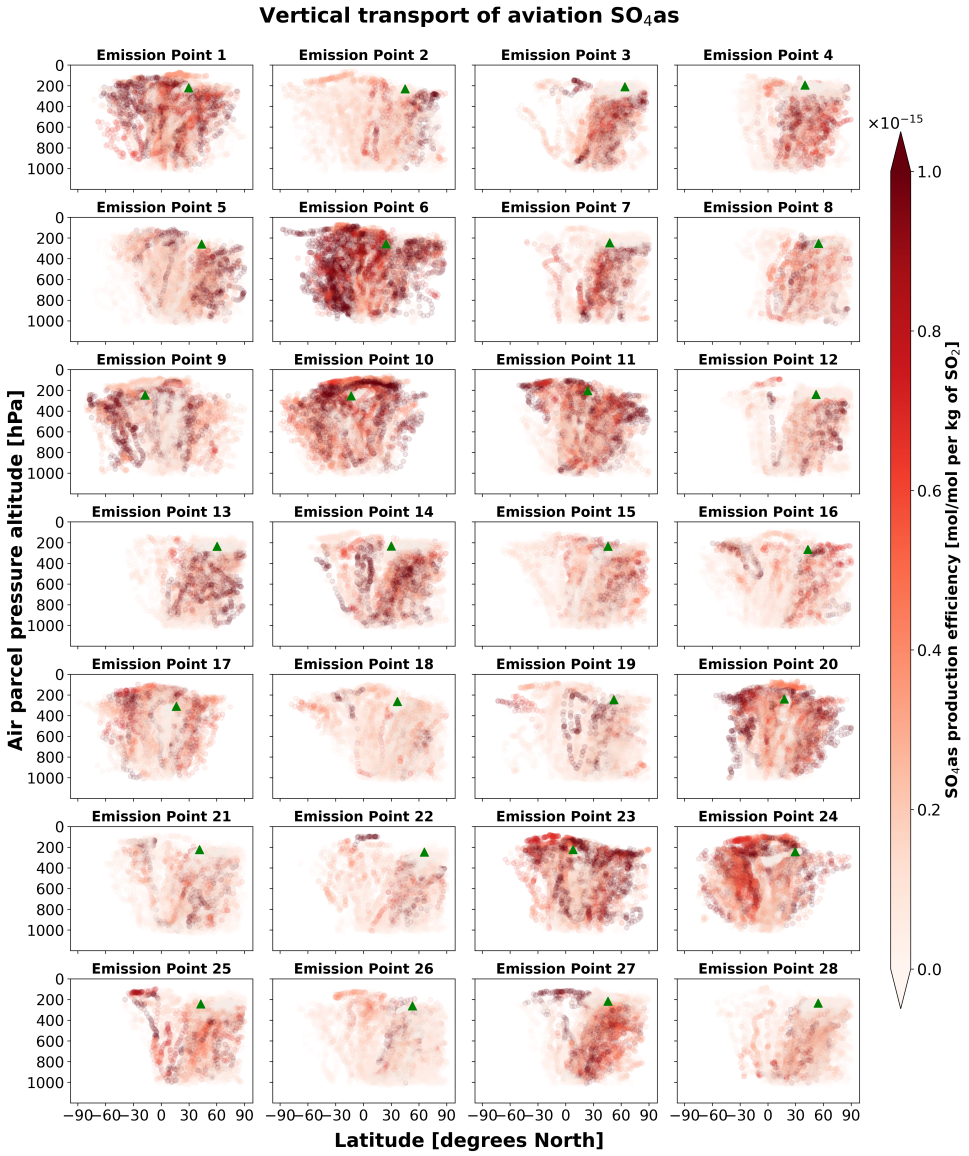


Figure E.24: SO_4as vertical profiles for the period January - March 2015. The vertical axis represents an air parcel's pressure altitude while the horizontal axis denotes its latitude. The color bar measures the SO_4as production efficiency per kg of emitted SO_2 across 50 air parcel trajectories. The locations of the 28 emission points are shown in Fig. 6.2 and emitted amounts in Table B.2.

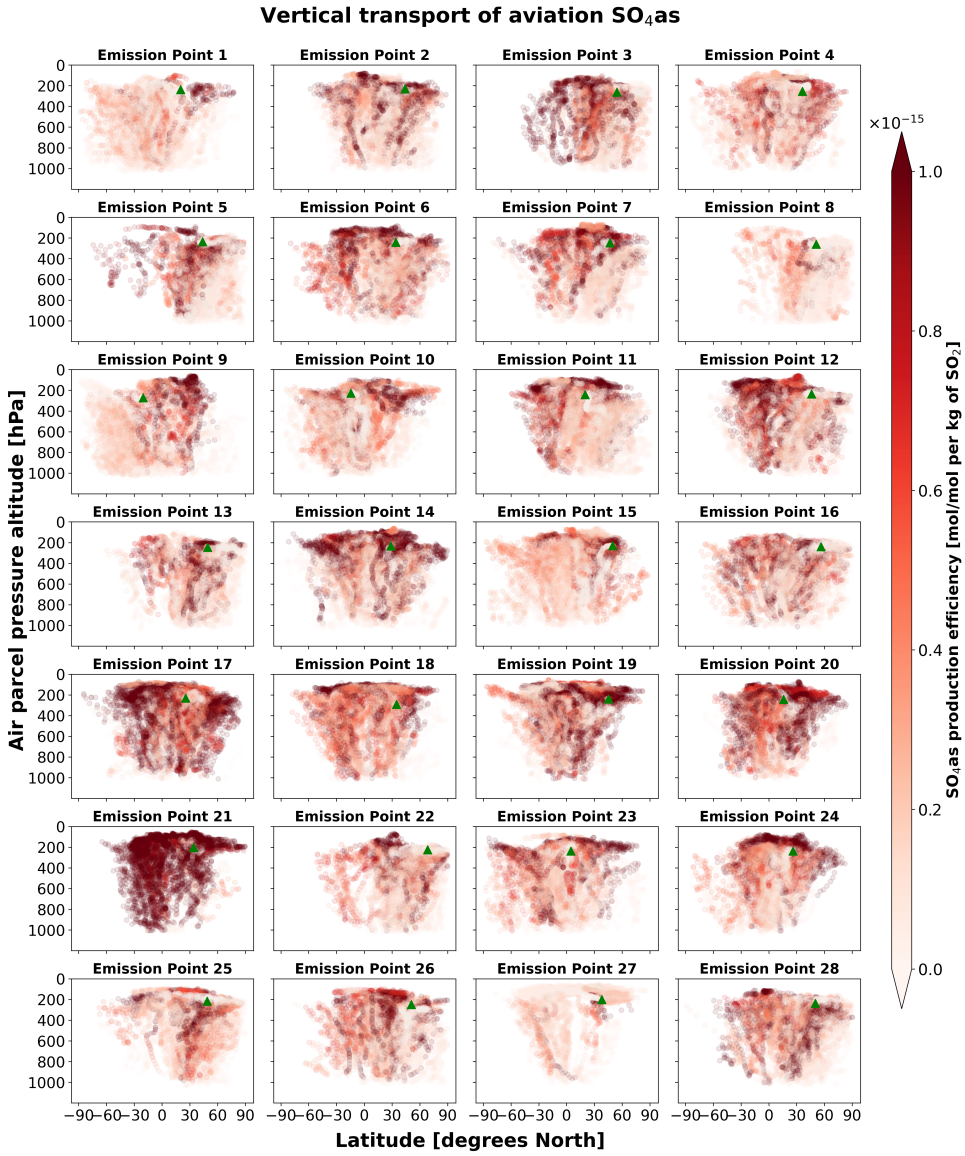


Figure E.25: SO_4as vertical profiles for the period July - September 2015. The vertical axis represents an air parcel's pressure altitude while the horizontal axis denotes its latitude. The color bar measures the SO_4as production efficiency per kg of emitted SO_2 across 50 air parcel trajectories. The locations of the 28 emission points are shown in Fig. 6.2 and emitted amounts in Table B.2.

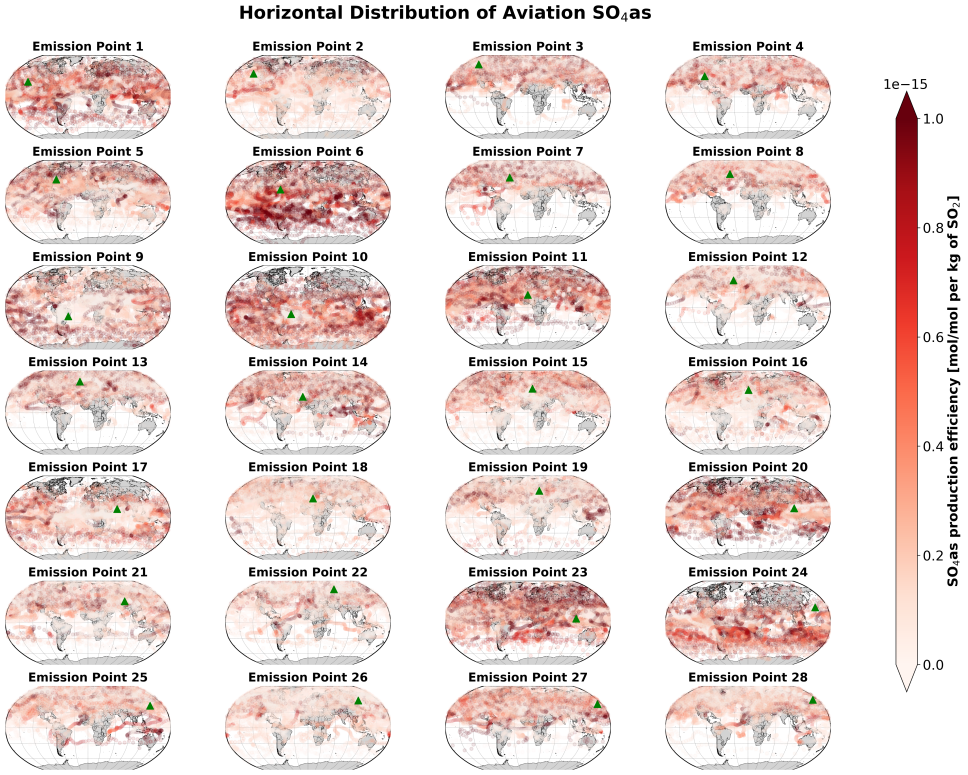


Figure E.26: SO_4as horizontal distributions for the period January - March 2015. The color bar measures the SO_4as production efficiency per kg of emitted SO_2 across 50 air parcel trajectories. The locations of the 28 emission points are shown in Fig. 6.2 and emitted amounts in Table B.2.

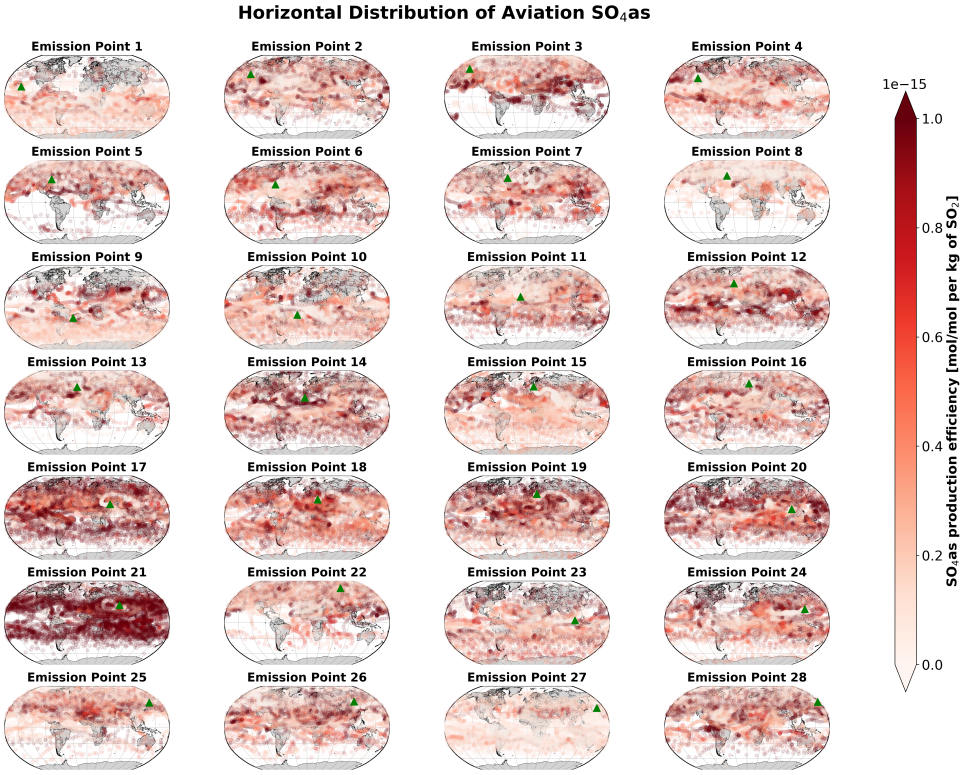


Figure E.27: SO_4as horizontal distributions for the period July - September 2015. The color bar measures the SO_4as production efficiency per kg of emitted SO_2 across 50 air parcel trajectories. The locations of the 28 emission points are shown in Fig. 6.2 and emitted amounts in Table B.2.

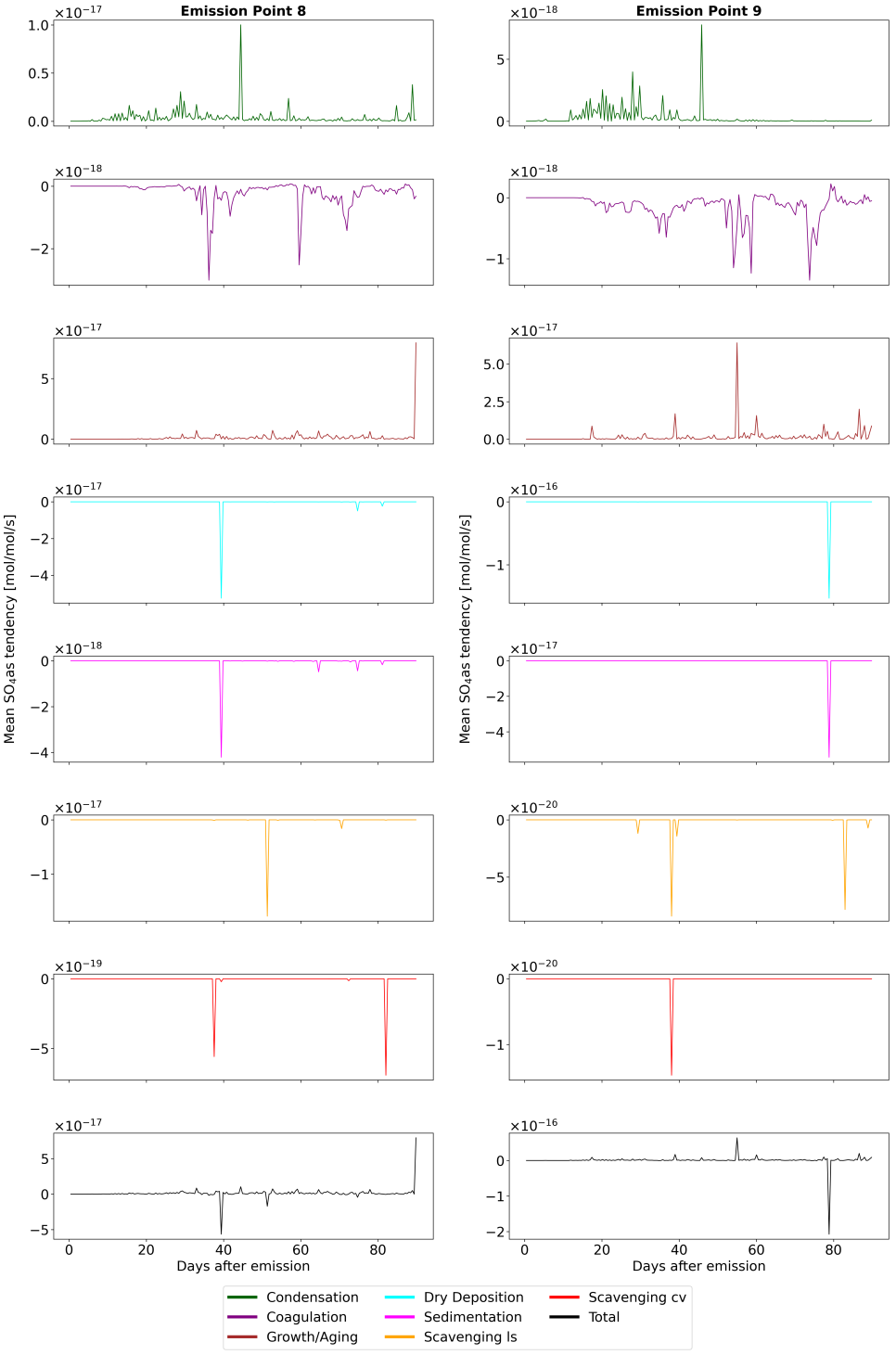
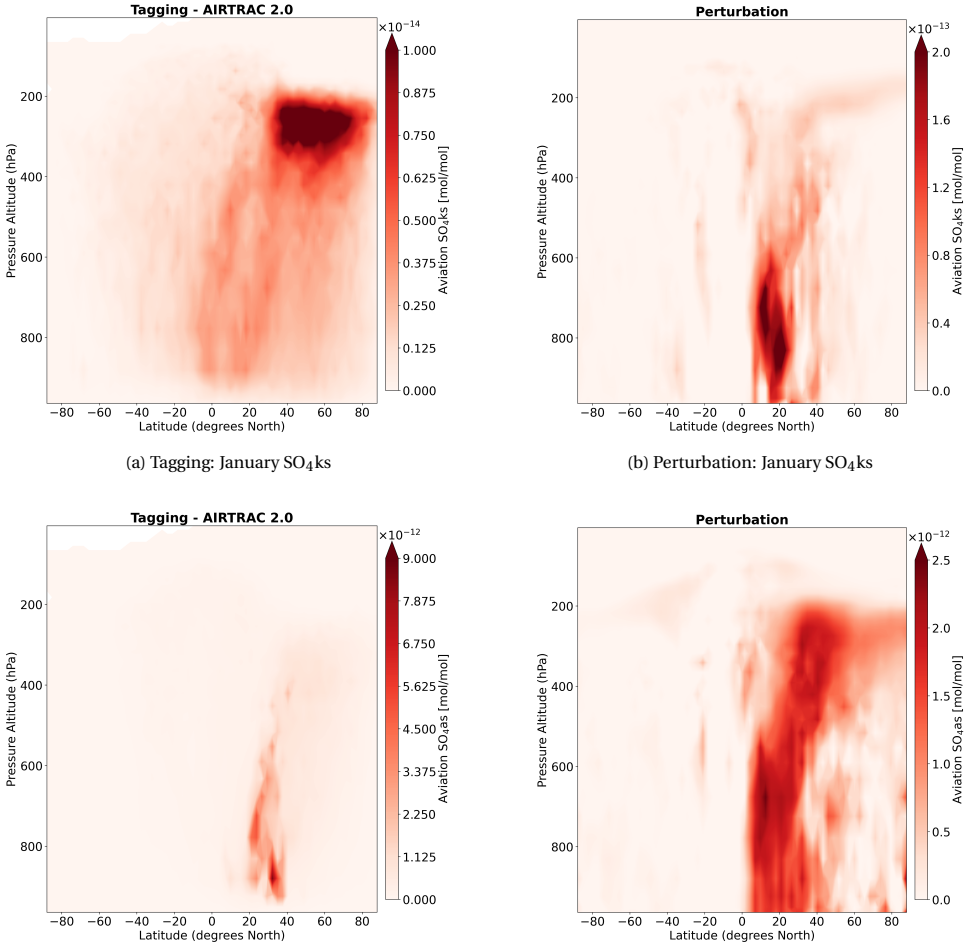


Figure E.28: Summary of process contributions to the total SO_4as tendency for the period January - March 2015.

E.7. EVALUATION OF AIRTRAC 2.0: JANUARY - MARCH 2015



(a) Tagging: January SO_4ks

(b) Perturbation: January SO_4ks

(c) Tagging: January SO_4as

(d) Perturbation: January SO_4as

Figure E.29: Comparison of AIRTRAC's tagging estimates with the perturbation method using a modeling setup similar to Righi et al. [160] for SO_4ks and SO_4as during the period January - March 2015.

E.8. SENSITIVITY OF SO_4 MIXING RATIO WITH LGTMIX MIXING PARAMETER D

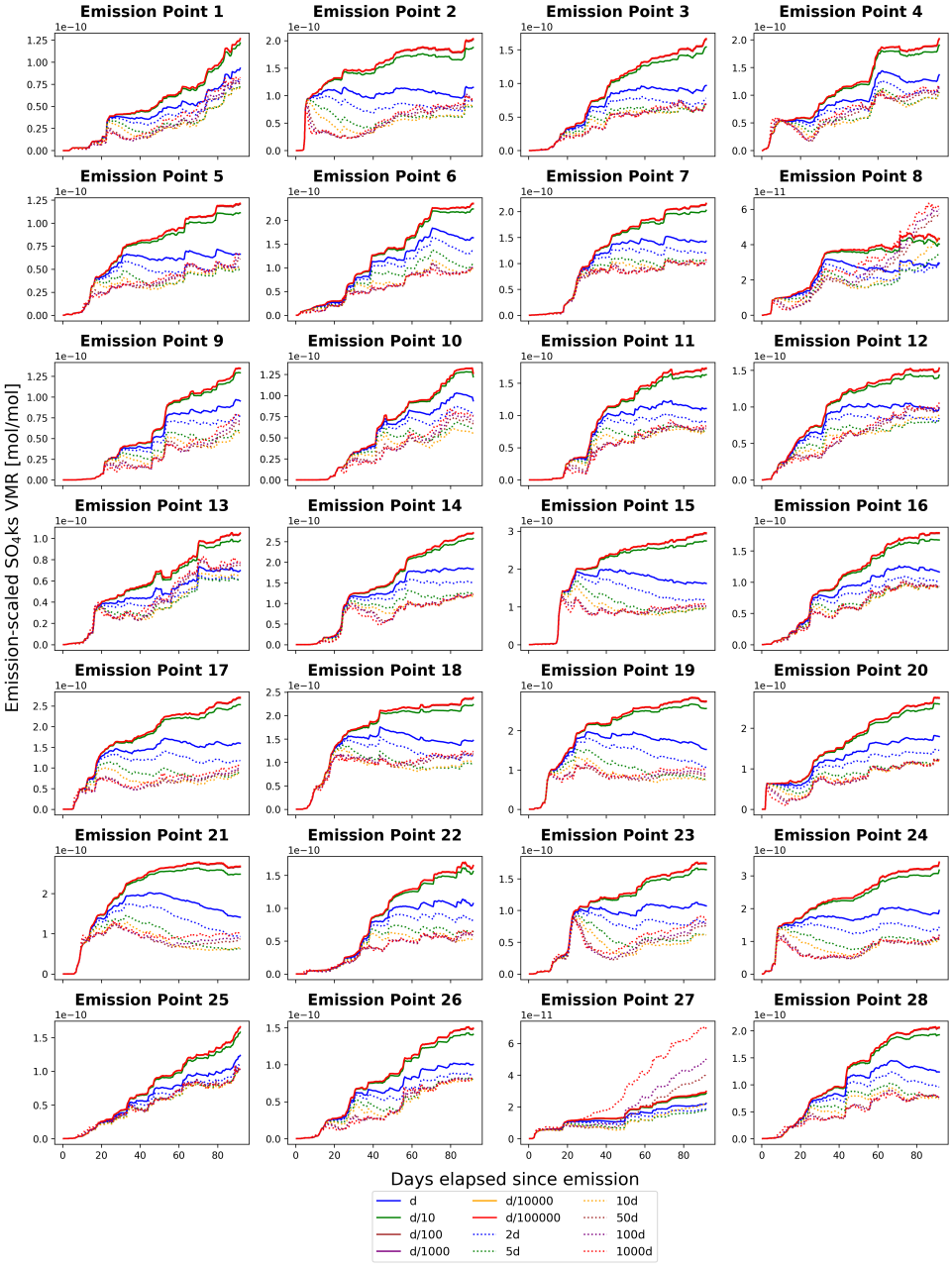


Figure E.30: Sensitivity of the SO_4ks volume mixing ratio with the mixing parameter d from the LGTMIX submodel. The simulation that uses a mixing parameter d corresponds to the original values used for gas-phase chemistry. A range of mixing parameters from $d/10^5$ to $1000d$ is considered.

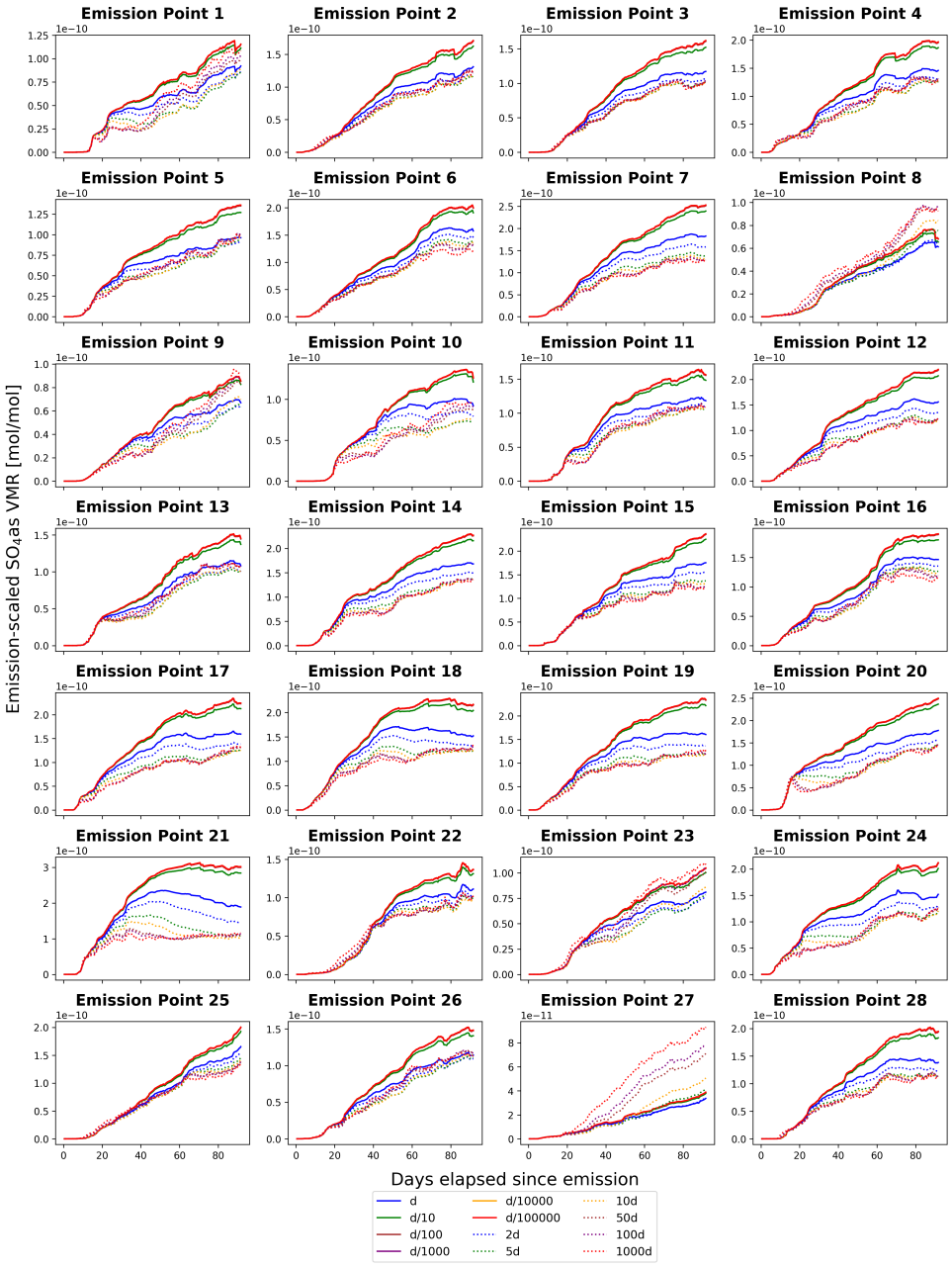


Figure E.31: Sensitivity of the SO_4as volume mixing ratio with the mixing parameter d from the LGTMIX submodel. The simulation that uses a mixing parameter d corresponds to the original values used for gas-phase chemistry. A range of mixing parameters from $d/10^5$ to $1000d$ is considered.

BIBLIOGRAPHY

[1] J. A. Stoop and J. P. Kahan. “Flying is the Safest Way to Travel: How Aviation was a Pioneer in Independent Accident Investigation”. In: *European Journal of Transport and Infrastructure Research* 5.2 (2005). DOI: 10.18757/ejtir.2005.5.2.4392.

[2] D. S. Lee, D. W. Fahey, P. M. Forster, P. J. Newton, R. C. Wit, L. L. Lim, B. Owen, and R. Sausen. “Aviation and global climate change in the 21st century”. In: *Atmospheric Environment* 43.22-23 (2009), pp. 3520–3537. DOI: 10.1016/j.atmosenv.2009.04.024.

[3] International Air Transport Association. *State of the Region: Europe*. IATA Economic Report. 2018. URL: https://www.iata.org/en/iata-repository/publications/economic-reports/regional-briefing---europe---december-2018/.

[4] S. Morrell, R. Taylor, and D. Lyle. “A review of health effects of aircraft noise”. In: *Australian and New Zealand Journal of Public Health* 21.2 (1997), pp. 221–236. DOI: 10.1111/j.1467-842X.1997.tb01690.x.

[5] M. Kaltenbach, C. Maschke, and R. Klinke. “Health consequences of aircraft noise”. In: *Dtsch Arztebl Int* 105.31-32 (2008), pp. 548–556. DOI: 10.3238/arztebl.2008.0548.

[6] A. A. Faiyetole and J. T. Sivowaku. “The effects of aircraft noise on psychosocial health”. In: *Journal of Transport & Health* 22 (2021), p. 101230. DOI: 10.1016/j.jth.2021.101230.

[7] S. H. L. Yim, G. L. Lee, I. H. Lee, F. Allroggen, A. Ashok, F. Caiazzo, S. D. Eastham, R. Malina, and S. R. H. Barrett. “Global, regional and local health impacts of civil aviation emissions”. In: *Environmental Research Letters* 10.3 (2015), p. 034001. DOI: 10.1088/1748-9326/10/3/034001.

[8] V. Grewe, A. G. Rao, T. Grönstedt, C. Xisto, F. Linke, J. Melkert, J. Middel, B. Ohlenforst, S. Blakey, S. Christie, S. Matthes, and K. Dahlmann. “Evaluating the climate impact of aviation emission scenarios towards the Paris agreement including COVID-19 effects”. In: *Nature Communications* 12 (2021), p. 3841. DOI: 10.1038/s41467-021-24091-y.

[9] R. B. Skeie, J. Fuglestvedt, T. Berntsen, M. T. Lund, G. Myhre, and K. Rypdal. “Global temperature change from the transport sectors: Historical development and future scenarios”. In: *Atmospheric Environment* 43.39 (2009), pp. 6260–6270. DOI: 10.1016/j.atmosenv.2009.05.025.

[10] Ø. Hodnebrog, T. K. Berntsen, O. Dessens, M. Gauss, V. Grewe, I. S. A. Isaksen, B. Koffi, G. Myhre, D. Olivié, M. J. Prather, J. A. Pyle, F. Stordal, S. Szopa, Q. Tang, P. van Velthoven, J. E. Williams, and K. Ødemark. "Future impact of non-land based traffic emissions on atmospheric ozone and OH – an optimistic scenario and a possible mitigation strategy". In: *Atmos. Chem. Phys.* 11 (2011), pp. 11293–11317. DOI: 10.5194/acp-11-11293-2011.

[11] K. Dahlmann, V. Grewe, M. Ponater, and S. Matthes. "Quantifying the contributions of individual NOx sources to the trend in ozone radiative forcing". In: *Atmospheric Environment* 45 (2011), pp. 2860–2868. DOI: 10.1016/j.atmosenv.2011.02.071.

[12] F.D.A. Quadros, M. Snellen, and I.C. Dedoussi. "Regional sensitivities of air quality and human health impacts to aviation emissions". In: *Environmental Research Letters* 15.10 (2020), p. 105013. DOI: 10.1088/1748-9326/abb2c5.

[13] J. Maruhashi, V. Grewe, C. Frömming, P. Jöckel, and I. C. Dedoussi. "Transport patterns of global aviation NOx and their short-term O3 radiative forcing – a machine learning approach". In: *Atmos. Chem. Phys.* 22 (2022), pp. 14253–14282. DOI: 10.5194/acp-22-14253-2022.

[14] Airbus. *First ZEROe engine fuel cell successfully powers on*. 2024. URL: https://www.airbus.com/en/newsroom/stories/2024-01-first-zeroe-engine-fuel-cell-successfully-powers-on (visited on 04/22/2024).

[15] Tim Hepher, Reuters. *Airbus postpones development of new hydrogen aircraft*. 2025. URL: https://www.reuters.com/business/aerospace-defense/airbus-postpones-development-new-hydrogen-aircraft-2025-02-07/ (visited on 02/07/2025).

[16] H. Carvalho, R. A. Gomes, and M. Caetano. "Technological aircraft evolution and aviation emissions: an environmental progress case for the A320 family in Brazil". In: *Int. J. Environ. Sci. Technol.* 21 (2024), pp. 1–12. DOI: 10.1007/s13762-023-04952-3.

[17] Delft University of Technology. *Flying-V: Flying long distances energy-efficiently*. URL: https://www.tudelft.nl/en/ae/flying-v (visited on 04/22/2024).

[18] V. Grewe, K. Dahlmann, J. Flink, C. Frömming, R. Ghosh, K. Gierens, R. Heller, J. Hendricks, P. Jöckel, S. Kaufmann, K. Kölker, F. Linke, T. Luchkova, B. Lührs, J. Van Manen, S. Matthes, A. Minikin, M. Niklaß, M. Plohr, M. Righi, S. Rosanka, A. Schmitt, U. Schumann, I. Terekhov, S. Unterstrasser, M. Vázquez-Navarro, C. Voigt, K. Wicke, H. Yamashita, A. Zahn, and H. Ziereis. "Mitigating the Climate Impact from Aviation: Achievements and Results of the DLR WeCare Project". In: *Aerospace* 4.3 (2017). ISSN: 2226-4310. DOI: 10.3390/aerospace4030034.

[19] M. J. Watson, P. G. Machado, A. V. da Silva, Y. Saltar, C. O. Ribeiro, C. A. O. Nascimento, and A. W. Dowling. "Sustainable aviation fuel technologies, costs, emissions, policies, and markets: A critical review". In: *Journal of Cleaner Production* 449 (2024), p. 141472. ISSN: 0959-6526. DOI: 10.1016/j.jclepro.2024.141472.

[20] *Kyoto Protocol*. UNFCCC. 1997. URL: https://unfccc.int/kyoto_protocol (visited on 04/27/2024).

[21] J. Scheelhaase, W. Grimme, and S. Maertens. “EU trilogue results for the aviation sector – key issues and expected impacts”. In: *Transportation Research Procedia* 78 (2024), pp. 206–214. DOI: 10.1016/j.trpro.2024.02.027.

[22] M. Efthymiou and A. Papatheodorou. “EU Emissions Trading scheme in aviation: Policy analysis and suggestions”. In: *Journal of Cleaner Production* 237 (2019), p. 117734. ISSN: 0959-6526. DOI: 10.1016/j.jclepro.2019.117734.

[23] V. Grewe, C. Frömming, S. Matthes, S. Brinkop, M. Ponater, S. Dietmüller, P. Jöckel, H. Garny, E. Tsati, K. Dahlmann, O. A. Søvde, J. Fuglestvedt, T. K. Berntsen, K. P. Shine, E. A. Irvine, T. Champougny, and P. Hullah. “Aircraft routing with minimal climate impact: the REACT4C climate cost function modelling approach (V1.0)”. In: *Geosci. Model Dev.* 7 (2014), pp. 175–201. DOI: 10.5194/gmd-7-175-2014.

[24] International Air Transport Association (IATA) Economics. *Air Passenger Market Analysis: February 2024*. 2024. URL: https://www.iata.org/en/iata-repository/publications/economic-reports/air-passenger-market-analysis-february-2024/ (visited on 04/15/2024).

[25] R. Meerkötter and M. Vázquez-Navarro. “Earth’s Radiation Budget: The Driver for Weather and Climate”. In: *Atmospheric Physics*. Ed. by U. Schumann. Research Topics in Aerospace. Berlin, Heidelberg: Springer, 2012. DOI: 10.1007/978-3-642-30183-4_4.

[26] G. Myhre, D. Shindell, F.-M. Bréon, W. Collins, J. Fuglestvedt, J. Huang, D. Koch, J.-F. Lamarque, D. Lee, B. Mendoza, T. Nakajima, A. Robock, G. Stephens, T. Takemura, and H. Zhang. “Anthropogenic and Natural Radiative Forcing”. In: *Climate Change 2013: The Physical Science Basis. Contribution of Working Group I to the Fifth Assessment Report of the Intergovernmental Panel on Climate Change*. Ed. by T.F. Stocker, D. Qin, G.-K. Plattner, M. Tignor, S.K. Allen, J. Boschung, A. Nauels, Y. Xia, V. Bex, and P.M. Midgley. Cambridge, United Kingdom and New York, NY, USA: Cambridge University Press, 2013.

[27] D. S. Lee, D. W. Fahey, A. Skowron, M. R. Allen, U. Burkhardt, Q. Chen, S. J. Doherty, S. Freeman, P. M. Forster, J. Fuglestvedt, A. Gettelman, R. R. De León, L. L. Lim, M. T. Lund, R. J. Millar, B. Owen, J. E. Penner, G. Pitari, M. J. Prather, R. Sausen, and L. J. Wilcox. “The contribution of global aviation to anthropogenic climate forcing for 2000 to 2018”. In: *Atmospheric Environment* 244.117834 (2021). DOI: 10.1016/j.atmosenv.2020.117834.

[28] M. Klöwer, M. R. Allen, D. S. Lee, S. R. Proud, L. Gallagher, and A. Skowron. “Quantifying aviation’s contribution to global warming”. In: *Environmental Research Letters* 16.10 (2021), p. 104027. DOI: 10.1088/1748-9326/ac286e.

[29] J. E. Penner, D. H. Lister, D. J. Griggs, D. J. Dokken, and M. McFarland. *Aviation and the Global Atmosphere: A Special Report in Collaboration with the Scientific Assessment Panel to the Montreal Protocol on Substances that Deplete the Ozone Layer*. Cambridge, UK: Cambridge University Press, 1999.

[30] C. Frömming, M. Ponater, K. Dahlmann, V. Grewe, D. S. Lee, and R. Sausen. "Aviation-Induced Radiative Forcing and Surface Temperature Change in Dependency of the Emission Altitude". In: *Journal of Geophysical Research: Atmospheres* 117 (2012), p. D19104. DOI: 10.1029/2012JD018204.

[31] S. Matthes, L. Lim, U. Burkhardt, K. Dahlmann, S. Dietmüller, V. Grewe, A. S. Haslerud, J. Hendricks, B. Owen, G. Pitari, M. Righi, and A. Skowron. "Mitigation of Non-CO2 Aviation's Climate Impact by Changing Cruise Altitudes". In: *Aerospace* 8 (2021), p. 36. DOI: 10.3390/aerospace8020036.

[32] D. S. Stevenson and R. G. Derwent. "Does the Location of Aircraft Nitrogen Oxide Emissions Affect Their Climate Impact?" In: *Geophysical Research Letters* 36 (2009), p. L17810. DOI: 10.1029/2009GL039422.

[33] M. O. Köhler, G. Rädel, K. P. Shine, H. L. Rogers, and J. A. Pyle. "Latitudinal Variation of the Effect of Aviation NOx Emissions on Atmospheric Ozone and Methane and Related Climate Metrics". In: *Atmospheric Environment* 64 (2013), pp. 1–9. DOI: 10.1016/j.atmosenv.2012.09.013.

[34] C. K. Gilmore, S. R. H. Barrett, J. Koo, and Q. Wang. "Temporal and spatial variability in the aviation NOx-related O_3 impact". In: *Environmental Research Letters* 8 (2013), p. 034027. DOI: 10.1088/1748-9326/8/3/034027.

[35] D. S. Stevenson, R. M. Doherty, M. G. Sanderson, W. J. Collins, C. E. Johnson, and R. G. Derwent. "Radiative forcing from aircraft NOx emissions: Mechanisms and seasonal dependence". In: *Journal of Geophysical Research* 109 (2004), p. D17307. DOI: 10.1029/2004JD004759.

[36] C. Frömming, V. Grewe, S. Brinkop, P. Jöckel, A. S. Haslerud, S. Rosanka, J. van Manen, and S. Matthes. "Influence of weather situation on non-CO2 aviation climate effects: the REACT4C climate change functions". In: *Atmos. Chem. Phys.* 21 (2021), pp. 9151–9172. DOI: 10.5194/acp-21-9151-2021.

[37] S. Rosanka, C. Frömming, and V. Grewe. "The impact of weather patterns and related transport processes on aviation's contribution to ozone and methane concentrations from NOx emissions". In: *Atmospheric Chemistry and Physics* 20 (2020), pp. 12347–12361. DOI: 10.5194/acp-20-12347-2020.

[38] M. Gauss, I. S. A. Isaksen, D. S. Lee, and O. A. Søvde. "Impact of Aircraft NOx Emissions on the Atmosphere—Tradeoffs to Reduce the Impact". In: *Atmospheric Chemistry and Physics* 6 (2006), pp. 1529–1548. DOI: 10.5194/acp-6-1529-2006.

[39] A. Skowron, D. S. Lee, and R. R. de León. "The Assessment of the Impact of Aviation NOx on Ozone and Other Radiative Forcing Responses—The Importance of Representing Cruise Altitudes Accurately". In: *Atmospheric Environment* 74 (2013), pp. 159–168. DOI: 10.1016/j.atmosenv.2013.03.034.

[40] O. A. Søvde, S. Matthes, A. Skowron, D. Iachetti, L. L. Lim, B. Owen, Ø. Hodnebrog, G. Di Genova, G. Pitari, and D. S. Lee. "Aircraft Emission Mitigation by Changing Route Altitude: A Multi-Model Estimate of Aircraft NOx Emission Impact on O_3 Photochemistry". In: *Atmospheric Environment* 95 (2014), pp. 468–479. DOI: 10.1016/j.atmosenv.2014.06.049.

[41] V. Grewe, S. Matthes, and K. Dahlmann. “The contribution of aviation NOx emissions to climate change: are we ignoring methodological flaws?” In: *Environmental Research Letters* 14 (2019), p. 121003. DOI: 10.1088/1748-9326/ab5dd7.

[42] J. E. Kristjánsson. “Studies of the aerosol indirect effect from sulfate and black carbon aerosols”. In: *Journal of Geophysical Research* 107 (2002). DOI: 10.1029/2001JD000887.

[43] L. A. Barrie, Y. Yi, W. R. Leaitch, U. Lohmann, P. Kasibhatla, G. J. Roelofs, J. Wilson, F. McGovern, C. Benkovitz, M. A. Melieres, K. Law, J. Prospero, M. Kritz, D. Bergmann, C. Bridgeman, M. Chin, J. Christensen, R. Easter, J. Feichter, C. Land, A. Jeuken, E. Kjellstrom, D. Koch, and P. Rasch. “A comparison of large-scale atmospheric sulphate aerosol models (COSAM): overview and highlights”. In: *Tellus B* 53 (2001), pp. 615–645. DOI: 10.3402/tellusb.v53i5.16642.

[44] B. Weinzierl, A. Ansmann, J. Prospero, D. Althausen, N. Benker, F. Chouza, M. Dollner, D. Farrell, W. Fomba, V. Freudenthaler, J. Gasteiger, S. Groß, M. Haarig, B. Heinold, K. Kandler, T. Kristensen, O. Mayol-Bracero, T. Müller, O. Reitebuch, D. Sauer, A. Schäfler, K. Schepanski, A. Spanu, I. Tegen, C. Toledano, and A. Walser. “The Saharan Aerosol Long-range Transport and Aerosol-Cloud Interaction Experiment (SALTRACE): overview and selected highlights”. In: *Bulletin of the American Meteorological Society* 98 (2017), pp. 1427–1451. DOI: 10.1175/BAMS-D-15-00142.1.

[45] V. Grewe and A. Stenke. “AirClim: an efficient tool for climate evaluation of aircraft technology”. In: *Atmospheric Chemistry and Physics* 8 (2008), pp. 4621–4639. DOI: 10.5194/acp-8-4621-2008.

[46] J. Van Manen and V. Grewe. “Algorithmic climate change functions for the use in eco-efficient flight planning”. In: *Transportation Research Part D: Transport and Environment* 67 (2019), pp. 388–405. DOI: 10.1016/j.trd.2018.12.016.

[47] S. Gössling and A. Humpe. “The global scale, distribution and growth of aviation: Implications for climate change”. In: *Global Environmental Change* 65 (2020), p. 102194. DOI: 10.1016/j.gloenvcha.2020.102194.

[48] K. E. Trenberth and C. J. Guillemot. “The total mass of the atmosphere”. In: *J. Geophys. Res.* 99.D11 (1994), pp. 23079–23088. DOI: 10.1029/94JD02043.

[49] G. P. Brasseur and D. J. Jacob. “Atmospheric Structure and Dynamics”. In: *Modeling of Atmospheric Chemistry*. Cambridge University Press, 2017, pp. 21–53.

[50] J. H. Seinfeld. *Atmospheric Chemistry and Physics: From Air Pollution to Climate Change*. Newark: John Wiley & Sons, Incorporated, 2016.

[51] T. Kaluza, D. Kunkel, and P. Hoor. “On the occurrence of strong vertical wind shear in the tropopause region: a 10-year ERA5 northern hemispheric study”. In: *Weather Clim. Dynam.* 2 (2021), pp. 631–651. DOI: 10.5194/wcd-2-631-2021.

[52] N. E. Daidzic. “On Atmospheric Lapse Rates”. In: *International Journal of Aviation, Aeronautics, and Aerospace* 6.4 (2019). DOI: 10.15394/ijaaa.2019.1374.

[53] H. Ritchie, L. Rodés-Guirao, and M. Roser. “Ozone Layer”. In: *Our World in Data* (2023). URL: https://ourworldindata.org/ozone-layer.

[54] M. McElroy, S. Wofsy, J. Penner, and J. McConnell. “Atmospheric Ozone: Possible Impact of Stratospheric Aviation”. In: *Journal of the Atmospheric Sciences* 31.1 (1974), pp. 287–304. DOI: 10.1175/1520-0469(1974)031<0287:AOPIOS>2.0.CO;2.

[55] National Oceanic and Atmospheric Administration (NOAA). *Layers of the Atmosphere*. Accessed on May 6, 2024. URL: https://www.noaa.gov/jetstream/atmosphere/layers-of-atmosphere.

[56] E. Aguado and J.E. Burt. *Understanding Weather and Climate*. 6th. Harlow: Pearson Education, 2013.

[57] National Weather Service. *Geopotential Height*. Accessed May 6, 2024. URL: https://www.weather.gov/source/zhu/ZHU_Training_Page/Miscellaneous/Heights_Thicknesses/thickness_temperature.htm.

[58] S. J. Colucci. “Anticyclones”. In: *Encyclopedia of Atmospheric Sciences*. Ed. by G. R. North, J. Pyle, and F. Zhang. Second. Academic Press, 2015, pp. 273–279. ISBN: 9780123822253. DOI: 10.1016/B978-0-12-382225-3.00071-2.

[59] A.H. Lynch and J.J. Cassano. “Epilogue: The General Circulation”. In: *Applied Atmospheric Dynamics*. Hoboken, NJ: John Wiley & Sons, 2006. Chap. 15.

[60] C. A. Gueymard. “The sun’s total and spectral irradiance for solar energy applications and solar radiation models”. In: *Solar Energy* 76.4 (2004), pp. 423–453. ISSN: 0038-092X. DOI: 10.1016/j.solener.2003.08.039.

[61] R. T. Pierrehumbert. “Infrared radiation and planetary temperature”. In: *Physics Today* 64.1 (2011), pp. 33–38. DOI: 10.1063/1.3541943.

[62] K. Trenberth, J. Fasullo, and J. Kiehl. “Earth’s Global Energy Budget”. In: *Bulletin of the American Meteorological Society* 90.3 (2009), pp. 311–324. DOI: 10.1175/2008BAMS2634.1.

[63] I. N. James. *Introduction to Circulating Atmospheres*. Cambridge Atmospheric and Space Science Series. Cambridge University Press, 1994. DOI: 10.1017/CBO9780511622977.

[64] P. Rudolph, ed. *Handbook of Crystal Growth*. Second. Elsevier, 2015. DOI: 10.1016/C2013-0-09791-5.

[65] G. Kirchhoff. “Ueber das Verhältniss zwischen dem Emissionsvermögen und dem Absorptionsvermögen der Körper für Wärme und Licht”. In: *Ann. Phys.* 185 (1860), pp. 275–301. DOI: 10.1002/andp.18601850205.

[66] D. Staley and G. Jurica. “Effective Atmospheric Emissivity under Clear Skies”. In: *Journal of Applied Meteorology and Climatology* 11.2 (1972), pp. 349–356. DOI: 10.1175/1520-0450(1972)011<0349:EAEUCS>2.0.CO;2.

[67] National Aeronautics and Space Administration (NASA) Jet Propulsion Laboratory (JPL). *Joint Emissivity Database Initiative (JEDI)*. Accessed 2024-05-15. URL: https://emissivity.jpl.nasa.gov/.

[68] G. L. Stephens, D. O’Brien, P. J. Webster, P. Pilewskie, S. Kato, and J. Li. “The Albedo of Earth”. In: *Reviews of Geophysics* 53.1 (2015), pp. 141–163. DOI: 10.1002/2014RG000449.

[69] M. Ponater, S. Pechtl, R. Sausen, U. Schumann, and G. Huttig. “Potential of the cryoplane technology to reduce aircraft climate impact: A state-of-the-art assessment”. In: *Atmospheric Environment* 40 (2006), pp. 6928–6944. DOI: 10.1016/j.atmosenv.2006.06.036.

[70] V. Grewe, A. Stenke, M. Ponater, R. Sausen, G. Pitari, D. Iachetti, H. Rogers, O. Dessens, J. Pyle, I. S. A. Isaksen, L. Gulstad, O. A. Søvde, C. Marizy, and E. Pascuillo. “Climate impact of supersonic air traffic: an approach to optimize a potential future supersonic fleet – results from the EU-project SCENIC”. In: *Atmospheric Chemistry and Physics* 7 (2007), pp. 5129–5145. DOI: 10.5194/acp-7-5129-2007.

[71] T. Birner, S. M. Davis, and D. J. Seidel. “The changing width of Earth’s tropical belt”. In: *Physics Today* 67.12 (2014), pp. 38–44. DOI: 10.1063/PT.3.2620.

[72] I. M. Dima and J. M. Wallace. “On the Seasonality of the Hadley Cell”. In: *Journal of the Atmospheric Sciences* 60.12 (2003), pp. 1522–1527. DOI: 10.1175/1520-0469(2003)060<1522:OTSOTH>2.0.CO;2.

[73] M. Pidwirny. *Fundamentals of Physical Geography*. 2nd. Physicalgeography.net, 2006.

[74] A.H. Lynch and J.J. Cassano. “Fundamental Forces”. In: *Applied Atmospheric Dynamics*. Hoboken, NJ: John Wiley & Sons, 2006. Chap. 4.

[75] The Information Architects of Encyclopaedia Britannica. *Hadley cell*. Accessed: 2024-05-17. URL: https://www.britannica.com/facts/Hadley-cell.

[76] Met Office. *Global circulation patterns*. Accessed: 2024-10-29. 2024. URL: https://www.metoffice.gov.uk/weather/learn-about/weather/atmosphere/global-circulation-patterns (visited on 10/29/2024).

[77] F. Ploeger, M. Diallo, E. Charlesworth, P. Konopka, B. Legras, J. C. Laube, J.-U. Grooß, G. Günther, A. Engel, and M. Riese. “The stratospheric Brewer–Dobson circulation inferred from age of air in the ERA5 reanalysis”. In: *Atmospheric Chemistry and Physics* 21 (2021), pp. 8393–8412. DOI: 10.5194/acp-21-8393-2021.

[78] N. Butchart. “The Brewer-Dobson circulation”. In: *Reviews of Geophysics* 52 (2014). DOI: 10.1002/2013RG000448.

[79] M. Abalos, N. Calvo, S. Benito-Barca, H. Garny, S. C. Hardiman, P. Lin, M. B. Andrews, N. Butchart, R. Garcia, C. Orbe, D. Saint-Martin, S. Watanabe, and K. Yoshida. “The Brewer–Dobson circulation in CMIP6”. In: *Atmospheric Chemistry and Physics* 21 (2021), pp. 13571–13591. DOI: 10.5194/acp-21-13571-2021.

[80] W. J. Collins, R. G. Derwent, B. Garnier, C. E. Johnson, M. G. Sanderson, and D. S. Stevenson. “Effect of stratosphere-troposphere exchange on the future tropospheric ozone trend”. In: *Journal of Geophysical Research* 108.D12 (2003), p. 8528. DOI: 10.1029/2002JD002617.

[81] G. Zeng and J. A. Pyle. “Changes in tropospheric ozone between 2000 and 2100 modeled in a chemistry-climate model”. In: *Geophysical Research Letters* 30.7 (2003), p. 1392. DOI: 10.1029/2002GL016708.

[82] H. Bönisch, A. Engel, Th. Birner, P. Hoor, D. W. Tarasick, and E. A. Ray. "On the structural changes in the Brewer-Dobson circulation after 2000". In: *Atmospheric Chemistry and Physics* 11 (2011), pp. 3937–3948. DOI: 10.5194/acp-11-3937-2011.

[83] G. Brasseur, J. J. Orlando, and G. S. Tyndall, eds. *Atmospheric Chemistry and Global Change*. New York: Oxford University Press, 1999.

[84] R. Atkinson. "Atmospheric chemistry of VOCs and NOx". In: *Atmospheric Environment* 34.12-14 (2000), pp. 2063–2101. ISSN: 1352-2310. DOI: 10.1016/S1352-2310(99)00460-4.

[85] G. P. Brasseur and D. J. Jacob. "Chemical Processes in the Atmosphere". In: *Modeling of Atmospheric Chemistry*. Cambridge University Press, 2017, pp. 54–83.

[86] K. Riedel and K. Lassey. "Detergent of the atmosphere". In: *Water & Atmosphere* 16.2 (2008). URL: https://niwa.co.nz/sites/default/files/import/attachments/detergent.pdf.

[87] L. Jaeglé, D. J. Jacob, W. H. Brune, and P. O. Wennberg. "Chemistry of HOx radicals in the upper troposphere". In: *Atmospheric Environment* 35.3 (2001), pp. 469–489. ISSN: 1352-2310. DOI: 10.1016/S1352-2310(00)00376-9.

[88] S. Depayras, T. Kondakova, H. J. Heipieper, M. G. J. Feuilloley, N. Orange, and C. Duclairoir-Poc. "The Hidden Face of Nitrogen Oxides Species: From Toxic Effects to Potential Cure?" In: *Emerging Pollutants - Some Strategies for the Quality Preservation of Our Environment*. InTech, 2018. DOI: 10.5772/intechopen.75822.

[89] D. W. Bond, S. Steiger, R. Zhang, X. Tie, and R. E. Orville. "The importance of NOx production by lightning in the tropics". In: *Atmospheric Environment* 36.9 (2002), pp. 1509–1519. ISSN: 1352-2310. DOI: 10.1016/S1352-2310(01)00553-2.

[90] Y. Zeldovich and N. Semenov. "Kinetics of Chemical Reactions in Flames". In: *Journal of Experimental and Theoretical Physics* 10.NACA-TM-1084 (1946). URL: https://ntrs.nasa.gov/citations/20050031118.

[91] M. A. Galbiati, A. Cavigiolo, A. Effuggi, D. Gelosa, and R. Rota. "MILD Combustion for Fuel-NO_x Reduction". In: *Combustion Science and Technology* 176.7 (2004), pp. 1035–1054. DOI: 10.1080/00102200490426424.

[92] M. Masiol and R. M. Harrison. "Aircraft engine exhaust emissions and other airport-related contributions to ambient air pollution: A review". In: *Atmospheric Environment* 95 (2014), pp. 409–455. DOI: 10.1016/j.atmosenv.2014.05.070.

[93] T. H. Karakoc, C. O. Colpan, S. Ekici, and O. Yetik. "Promising fuels and green energy technologies for aviation". In: *International Journal of Green Energy* 1 (2022). DOI: 10.1080/15435075.2022.2082253.

[94] S. Wu, L. J. Mickley, D. J. Jacob, J. A. Logan, R. M. Yantosca, and D. Rind. "Why are there large differences between models in global budgets of tropospheric ozone?" In: *Journal of Geophysical Research: Atmospheres* 112.D5 (2007), p. D05302. DOI: 10.1029/2006JD007801.

[95] L. T. Murray, L. J. Mickley, J. O. Kaplan, E. D. Sofen, M. Pfeiffer, and B. Alexander. "Factors controlling variability in the oxidative capacity of the troposphere since the Last Glacial Maximum". In: *Atmospheric Chemistry and Physics* 14 (2014), pp. 3589–3622. DOI: 10.5194/acp-14-3589-2014.

[96] National Research Council. *Rethinking the Ozone Problem in Urban and Regional Air Pollution*. Washington, DC: The National Academies Press, 1991. DOI: 10.17226/1889.

[97] A. Petzold and B. Kärcher. "Aerosols in the Atmosphere". In: *Atmospheric Physics*. Ed. by U. Schumann. Research Topics in Aerospace. Berlin, Heidelberg: Springer, 2012, pp. 25–96. DOI: 10.1007/978-3-642-30183-4_3.

[98] J. L. Mauderly and J. C. Chow. "Health Effects of Organic Aerosols". In: *Inhalation Toxicology* 20.3 (2008), pp. 257–288. DOI: 10.1080/08958370701866008.

[99] M.J. Berg, Y.W. Heinson, O. Kemppinen, and S. Holler. "Solving the inverse problem for coarse-mode aerosol particle morphology with digital holography". In: *Scientific Reports* 7 (2017), p. 9400. DOI: 10.1038/s41598-017-09957-w.

[100] J. C. Kaiser, J. Hendricks, M. Righi, N. Riemer, R. A. Zaveri, S. Metzger, and V. Aquila. "The MESSy aerosol submodel MADE3 (v2.0b): description and a box model test". In: *Geosci. Model Dev.* 7 (2014), pp. 1137–1157. DOI: 10.5194/gmd-7-1137-2014.

[101] V. Aquila, J. Hendricks, A. Lauer, N. Riemer, H. Vogel, D. Baumgardner, A. Minikin, A. Petzold, J. P. Schwarz, J. R. Spackman, B. Weinzierl, M. Righi, and M. Dall'Amico. "MADE-in: a new aerosol microphysics submodel for global simulation of insoluble particles and their mixing state". In: *Geosci. Model Dev.* 4 (2011), pp. 325–355. DOI: 10.5194/gmd-4-325-2011.

[102] W. C. Hinds. *Aerosol Technology: Properties, Behavior, and Measurement of Airborne Particles*. Wiley Interscience, 1999.

[103] J. C. Kaiser, J. Hendricks, M. Righi, P. Jöckel, H. Tost, K. Kandler, B. Weinzierl, D. Sauer, K. Heimerl, J. P. Schwarz, A. E. Perring, and T. Popp. "Global aerosol modeling with MADE3 (v3.0) in EMAC (based on v2.53): model description and evaluation". In: *Geosci. Model Dev.* 12 (2019), pp. 541–579. DOI: 10.5194/gmd-12-541-2019.

[104] Z. Tan. "Properties of Aerosol Particles". In: *Air Pollution and Greenhouse Gases*. Green Energy and Technology. Singapore: Springer, 2014. DOI: 10.1007/978-981-287-212-8_1.

[105] J. D. Anderson. *Fundamentals of Aerodynamics (SI Units)*. McGraw-Hill Education, 2011.

[106] R. Clift, J. R. Grace, and M. E. Weber. *Bubbles, Drops, and Particles*. Dover Publications, 2013.

[107] B. E. Rapp. "Chapter 9 - Fluids". In: *Microfluidics: Modelling, Mechanics and Mathematics*. Ed. by B. E. Rapp. Micro and Nano Technologies. Oxford: Elsevier, 2017, pp. 243–263. ISBN: 978-1-4557-3141-1. DOI: https://doi.org/10.1016/B978-1-4557-3141-1.50009-5.

[108] M. D. Allen and O. G. Raabe. “Slip Correction Measurements of Spherical Solid Aerosol Particles in an Improved Millikan Apparatus”. In: *Aerosol Science and Technology* 4.3 (1985), pp. 269–286. DOI: 10.1080/02786828508959055.

[109] H. Pruppacher and J. Klett. *Microphysics of Clouds and Precipitation*. 2nd. Dordrecht: Kluwer Academic Publishers, 1997, p. 954.

[110] G. P. Brasseur and D. J. Jacob. “Formulations of Radiative, Chemical, and Aerosol Rates”. In: *Modeling of Atmospheric Chemistry*. Cambridge: Cambridge University Press, 2017, pp. 205–252.

[111] H. Vehkamäki, M. Kulmala, I. Napari, K. E. J. Lehtinen, C. Timmreck, M. Noppel, and A. Laaksonen. “An improved parameterization for sulfuric acid-water nucleation rates for tropospheric and stratospheric conditions”. In: *Journal of Geophysical Research* 107 (2002), pp. 4622–4631. DOI: 10.1029/2002JD002184.

[112] Z. Erdélyi, Z. Balogh, and D. L. Beke. “Kinetic critical radius in nucleation and growth processes–Trapping effect”. In: *Acta Materialia* 58.17 (2010), pp. 5639–5645. DOI: 10.1016/j.actamat.2010.06.037.

[113] J. Hendricks, M. Righi, and V. Aquila. “Global Atmospheric Aerosol Modeling”. In: *Atmospheric Physics*. Ed. by U. Schumann. Research Topics in Aerospace. Berlin, Heidelberg: Springer, 2012, pp. 671–686. DOI: 10.1007/978-3-642-30183-4_34.

[114] P. E. Wagner. “Aerosol Growth by Condensation”. In: *Aerosol Microphysics II*. Ed. by W. H. Marlow. Vol. 29. Topics in Current Physics. Berlin, Heidelberg: Springer, 1982, pp. 85–172. DOI: 10.1007/978-3-642-81805-9_5.

[115] S. R. Turns. *An Introduction to Combustion: Concepts and Applications*. New York: McGraw-Hill, 1996, pp. 291–297.

[116] F. Joos, R. Roth, J. S. Fuglestvedt, G. P. Peters, I. G. Enting, W. von Bloh, V. Brovkin, E. J. Burke, M. Eby, N. R. Edwards, T. Friedrich, T. L. Frölicher, P. R. Halloran, P. B. Holden, C. Jones, T. Kleinen, F. T. Mackenzie, K. Matsumoto, M. Meinshausen, G.-K. Plattner, A. Reisinger, J. Segschneider, G. Shaffer, M. Steinacher, K. Strassmann, K. Tanaka, A. Timmermann, and A. J. Weaver. “Carbon dioxide and climate impulse response functions for the computation of greenhouse gas metrics: a multi-model analysis”. In: *Atmospheric Chemistry and Physics* 13 (2013), pp. 2793–2825. DOI: 10.5194/acp-13-2793-2013.

[117] P. Ciais, C. Sabine, G. Bala, L. Bopp, V. Brovkin, J. Canadell, A. Chhabra, R. DeFries, J. Galloway, M. Heimann, C. Jones, C. Le Quéré, R.B. Myneni, S. Piao, and P. Thornton. “Carbon and Other Biogeochemical Cycles”. In: *Climate Change 2013: The Physical Science Basis. Contribution of Working Group I to the Fifth Assessment Report of the Intergovernmental Panel on Climate Change*. Ed. by T.F. Stocker, D. Qin, G.-K. Plattner, M. Tignor, S.K. Allen, J. Boschung, A. Nauels, Y. Xia, V. Bex, and P.M. Midgley. Cambridge, United Kingdom and New York, NY, USA: Cambridge University Press, 2013.

[118] S. Noël, K. Weigel, K. Bramstedt, A. Rozanov, M. Weber, H. Bovensmann, and J. P. Burrows. "Water vapour and methane coupling in the stratosphere observed using SCIAMACHY solar occultation measurements". In: *Atmospheric Chemistry and Physics* 18 (2018), pp. 4463–4476. DOI: 10.5194/acp-18-4463-2018.

[119] C. D. Holmes, Q. Tang, and M. J. Prather. "Uncertainties in Climate Assessment for the Case of Aviation NO". In: *Proc. Natl. Acad. Sci. USA* 108 (2011), pp. 10997–11002. DOI: 10.1073/pnas.1101458108.

[120] E. Terrenoire, D. A. Hauglustaine, Y. Cohen, A. Cozic, R. Valorso, F. Lefèvre, and S. Matthes. "Impact of Present and Future Aircraft NOx and Aerosol Emissions on Atmospheric Composition and Associated Direct Radiative Forcing of Climate". In: *Atmos. Chem. Phys.* 22 (2022), pp. 11987–12023. DOI: 10.5194/acp-22-11987-2022.

[121] M. Etminan, G. Myhre, E. J. Highwood, and K. P. Shine. "Radiative forcing of carbon dioxide, methane, and nitrous oxide: A significant revision of the methane radiative forcing". In: *Geophysical Research Letters* 43.24 (2016), pp. 12614–12623. DOI: 10.1002/2016GL071930.

[122] D. S. Lee, M. R. Allen, N. Cumpsty, B. Owen, K. P. Shine, and A. Skowron. "Uncertainties in mitigating aviation non-CO2 emissions for climate and air quality using hydrocarbon fuels". In: *Environmental Science: Atmospheres* 3 (2023), pp. 1693–1740. DOI: 10.1039/D3EA00091E.

[123] M. Gauss, I. S. A. Isaksen, S. Wong, and W.-C. Wang. "Impact of H2O emissions from cryoplanes and kerosene aircraft on the atmosphere". In: *Journal of Geophysical Research* 108.D10 (2003), p. 4304. DOI: 10.1029/2002JD002623.

[124] J. Pletzer, D. Hauglustaine, Y. Cohen, P. Jöckel, and V. Grewe. "The climate impact of hydrogen-powered hypersonic transport". In: *Atmos. Chem. Phys.* 22 (2022), pp. 14323–14354. DOI: 10.5194/acp-22-14323-2022.

[125] J. Pletzer and V. Grewe. "Sensitivities of atmospheric composition and climate to altitude and latitude of hypersonic aircraft emissions". In: *Atmospheric Chemistry and Physics* 24 (2024), pp. 1743–1775. DOI: 10.5194/acp-24-1743-2024.

[126] U. Schumann. "Formation, properties and climatic effects of contrails". In: *Comptes Rendus Physique* 6.4-5 (2005), pp. 549–565. DOI: 10.1016/j.crhy.2005.05.002.

[127] B. Kärcher, U. Burkhardt, A. Bier, L. Bock, and I. J. Ford. "The microphysical pathway to contrail formation". In: *J. Geophys. Res. Atmos.* 120 (2015), pp. 7893–7927. DOI: 10.1002/2015JD023491.

[128] B. Kärcher. "Formation and radiative forcing of contrail cirrus". In: *Nature Communications* 9 (2018), p. 1824. DOI: 10.1038/s41467-018-04068-0.

[129] R. Teoh, U. Schumann, and M. E. J. Stettler. "Beyond Contrail Avoidance: Efficacy of Flight Altitude Changes to Minimise Contrail Climate Forcing". In: *Aerospace* 7 (2020), p. 121. DOI: 10.3390/aerospace7090121.

[130] J. M. Haywood and K. P. Shine. “The effect of anthropogenic sulfate and soot aerosol on the clear sky planetary radiation budget”. In: *Geophys. Res. Lett.* 22.5 (1995), pp. 603–606. DOI: 10.1029/95GL00075.

[131] S. Twomey. “The influence of pollution on the shortwave albedo of clouds”. In: *Journal of Atmospheric Sciences* 34 (1977), pp. 1149–1152. DOI: 10.1175/1520-0469(1977)034<1149:TIOPOT>2.0.CO;2.

[132] U. Lohmann and J. Feichter. “Impact of sulfate aerosols on albedo and lifetime of clouds: A sensitivity study with the ECHAM GCM”. In: *Journal of Geophysical Research* 102 (1997), pp. 13685–13700. DOI: 10.1029/97JD00631.

[133] R. Sausen, K. Gierens, V. Eyring, J. Hendricks, and M. Righi. “Climate Impact of Transport”. In: *Atmospheric Physics*. Ed. by U. Schumann. Research Topics in Aerospace. Berlin, Heidelberg: Springer, 2012. DOI: 10.1007/978-3-642-30183-4_43.

[134] B. Albrecht. “Aerosols, cloud microphysics, and fractional cloudiness”. In: *Science* 245 (1989), pp. 1227–1230. DOI: 10.1126/science.245.4923.1227.

[135] U. Lohmann and J. Feichter. “Global indirect aerosol effects: a review”. In: *Atmospheric Chemistry and Physics* 5 (2005), pp. 715–737. DOI: 10.5194/acp-5-715-2005.

[136] J. Langner, H. Rodhe, P. J. Crutzen, and P. Zimmermann. “Anthropogenic influence on the distribution of tropospheric sulphate aerosol”. In: *Nature* 359.6397 (1992), pp. 712–716. URL: https://doi.org/10.3402/tellusa.v24i5.10658.

[137] D. K. Farmer, E. K. Boedicker, and H. M. DeBolt. “Dry Deposition of Atmospheric Aerosols: Approaches, Observations, and Mechanisms”. In: *Ann. Rev. Phys. Chem.* 72 (2021), pp. 16.1–16.23. DOI: 10.1146/annurev-physchem-090519-034936.

[138] H. Rodhe and J. Grandell. “On the removal time of aerosol particles from the atmosphere by precipitation scavenging”. In: *Tellus* 24 (1972), pp. 442–454. DOI: 10.3402/tellusa.v24i5.10658.

[139] M. Y. Danilin, D. W. Fahey, U. Schumann, M. J. Prather, J. E. Penner, M. K. W. Ko, D. K. Weisenstein, C. H. Jackman, G. Pitari, I. Köhler, R. Sausen, C. J. Weaver, A. R. Douglass, P. S. Connell, D. E. Kinnison, F. J. Dentener, E. L. Fleming, T. K. Berntsen, I. S. A. Isaksen, J. M. Haywood, and B. Kärcher. “Aviation Fuel Tracer Simulation: Model Intercomparison and Implications”. In: *Geophysical Research Letters* 25.20 (1998), pp. 3947–3950. DOI: 10.1029/1998GL900058.

[140] M. R. Schoeberl and G. A. Morris. “A Lagrangian simulation of supersonic and subsonic aircraft exhaust emissions”. In: *Journal of Geophysical Research: Atmospheres* 105 (2000), pp. 11833–11839. DOI: 10.1029/1999JD901151.

[141] V. Grewe, C. Reithmeier, and D. T. Shindell. “Dynamic-chemical coupling of the upper troposphere and lower stratosphere region”. In: *Chemosphere* 47.8 (2002), pp. 851–861. DOI: 10.1016/S0045-6535(02)00038-3.

[142] J. Maruhashi, M. Righi, M. Sharma, J. Hendricks, J. Jöckel, V. Grewe, and I.C. Dedoussi. “AIRTRAC 2.0: a Lagrangian aerosol tagging sub-model for the analysis of aviation SO_4 transport patterns”. In preparation.

[143] J. Maruhashi, M. Mertens, V. Grewe, and I. C. Dedoussi. "A multi-method assessment of the regional sensitivities between flight altitude and short-term O_3 climate warming from aircraft NO_x emissions". In: *Environmental Research Letters* 19.5 (2024), p. 054007. DOI: 10.1088/1748-9326/ad376a.

[144] G. P. Brasseur and D. J. Jacob. "The Concept of Model". In: *Modeling of Atmospheric Chemistry*. Cambridge University Press, 2017, pp. 1–20.

[145] U. Burkhardt and I. Sölch. "Cirrus Clouds and Their Representation in Models". In: *Atmospheric Physics*. Ed. by U. Schumann. Research Topics in Aerospace. Springer, Berlin, Heidelberg, 2012. DOI: 10.1007/978-3-642-30183-4_42.

[146] A. Clappier, C. A. Belis, D. Pernigotti, and P. Thunis. "Source apportionment and sensitivity analysis: two methodologies with two different purposes". In: *Geosci. Model Dev.* 10 (2017), pp. 4245–4256. DOI: 10.5194/gmd-10-4245-2017.

[147] V. Grewe, E. Tsati, and P. Hoor. "On the attribution of contributions of atmospheric trace gases to emissions in atmospheric model applications". In: *Geosci. Model Dev.* 3 (2010), pp. 487–499. DOI: 10.5194/gmd-3-487-2010.

[148] L.K. Emmons, P.G. Hess, J.F. Lamarque, and G.G. Pfister. "Tagged ozone mechanism for MOZART-4, CAM-chem and other chemical transport models". In: *Geoscientific Model Development* 5.6 (2012), pp. 1531–1542. DOI: 10.5194/gmd-5-1531-2012.

[149] E. Roeckner, G. Bäuml, L. Bonaventura, R. Brokopf, M. Esch, M. Giorgetta, S. Hagemann, I. Kirchner, L. Kornblueh, E. Manzini, U. Schlese, and U. Schulzweida. *The atmospheric general circulation model ECHAM 5. PART I: Model description*. Tech. rep. 349. Max-Planck-Institut für Meteorologie, 2003. URL: https://hdl.handle.net/21.11116/0000-0005-A14B-1.

[150] P. Jöckel, A. Kerkweg, A. Pozzer, R. Sander, H. Tost, H. Riede, A. Baumgaertner, S. Gromov, and B. Kern. "Development cycle 2 of the modular Earth submodel system (MESSy2)". In: *Geosci. Model Dev.* 3 (2010), pp. 717–752. DOI: https://doi.org/10.5194/gmd-3-717-2010.

[151] P. Jöckel, A. Kerkweg, A. Pozzer, R. Sander, H. Tost, H. Riede, A. Baumgaertner, S. Gromov, and B. Kern. "Development cycle 2 of the Modular Earth Submodel System (MESSy2)". In: *Geosci. Model Dev.* 3 (2010), pp. 717–752. DOI: 10.5194/gmd-3-717-2010.

[152] F. Haenel, W. Woiwode, J. Buchmüller, F. Friedl-Vallon, M. Höpfner, S. Johansson, F. Khosrawi, O. Kirner, A. Kleinert, H. Oelhaf, J. Orphal, R. Ruhnke, B.-M. Sinnhuber, J. Ungermann, M. Weimer, and P. Braesicke. "Challenge of modelling GLORIA observations of upper troposphere–lowermost stratosphere trace gas and cloud distributions at high latitudes: a case study with state-of-the-art models". In: *Atmospheric Chemistry and Physics* 22 (2022), pp. 2843–2870. DOI: 10.5194/acp-22-2843-2022.

[153] A. Kerkweg and P. Jöckel. "The 1-way on-line coupled atmospheric chemistry model system MECO(n) – Part 1: Description of the limited-area atmospheric chemistry model COSMO/MESSy". In: *Geosci. Model Dev.* 5 (2012), pp. 87–110. DOI: 10.5194/gmd-5-87-2012.

[154] P. Rao, R. Dwight, D. Singh, J. Maruhashi, I.C. Dedoussi, V. Grewe, and C. Frömming. "The ozone radiative forcing of nitrogen oxide emissions from aviation can be estimated using a probabilistic approach". In: *Communications Earth & Environment* 5.558 (2024). DOI: 10.1038/s43247-024-01691-2.

[155] R. Sander, A. Baumgaertner, D. Cabrera-Perez, F. Frank, S. Gromov, J.-U. Grooß, H. Harder, V. Huijnen, P. Jöckel, V. A. Karydis, K. E. Niemeyer, A. Pozzer, H. Riede, M. G. Schultz, D. Taraborrelli, and S. Tauer. "The community atmospheric chemistry box model CAABA/MECCA-4.0". In: *Geosci. Model Dev.* 12 (2019), pp. 1365–1385. DOI: 10.5194/gmd-12-1365-2019.

[156] V. Grewe. "A generalized tagging method". In: *Geosci. Model Dev.* 6 (2013), pp. 247–253. DOI: 10.5194/gmd-6-247-2013.

[157] V. Grewe, E. Tsati, M. Mertens, C. Frömming, and P. Jöckel. "Contribution of emissions to concentrations: the TAGGING 1.0 submodel based on the Modular Earth Submodel System (MESSy 2.52)". In: *Geoscientific Model Development* 10 (2017), pp. 2615–2633. DOI: 10.5194/gmd-10-2615-2017.

[158] V. S. Rieger, M. Mertens, and V. Grewe. "An advanced method of contributing emissions to short-lived chemical species (OH and HO2): the TAGGING 1.1 submodel based on the Modular Earth Submodel System (MESSy 2.53)". In: *Geoscientific Model Development* 11 (2018), pp. 2049–2066. DOI: 10.5194/gmd-11-2049-2018.

[159] I. J. Ackermann, H. Hass, M. Memmesheimer, A. Ebel, F. S. Binkowski, and U. Shankar. "Modal aerosol dynamics model for Europe: development and first applications". In: *Atmospheric Environment* 32 (1998), pp. 2981–2999. DOI: 10.1016/S1352-2310(98)00006-5.

[160] M. Righi, J. Hendricks, and S. Brinkop. "The global impact of the transport sectors on the atmospheric aerosol and the resulting climate effects under the Shared Socioeconomic Pathways (SSPs)". In: *Earth System Dynamics* 14 (2023), pp. 835–859. DOI: 10.5194/esd-14-835-2023.

[161] E. Weingartner, H. Burtscher, and H. Baltensperger. "Hygroscopic properties of carbon and diesel soot particles". In: *Atmospheric Environment* 31 (1997), pp. 2311–2327. DOI: 10.1016/S1352-2310(97)00023-X.

[162] A. F. Khalizov, R. Zhang, D. Zhang, H. Xue, J. Pagels, and P. H. McMurry. "Formation of highly hygroscopic soot aerosols upon internal mixing with sulfuric acid vapor". In: *Journal of Geophysical Research* 114 (2009), p. D05208. DOI: 10.1029/2008JD010595.

[163] F. S. Binkowski and S. J. Roselle. "Models-3 community multiscale air quality (CMAQ) model aerosol component – 1. Model description". In: *Journal of Geophysical Research: Atmospheres* 108 (2003), p. 4183. DOI: 10.1029/2001JD001409.

[164] R. L. Modini, Z. D. Ristovski, G. R. Johnson, C. He, N. Surawski, L. Morawska, T. Suni, and M. Kulmala. "New particle formation and growth at a remote, subtropical coastal location". In: *Atmospheric Chemistry and Physics* 9 (2009), pp. 7607–7621. DOI: 10.5194/acp-9-7607-2009.

[165] S. Ueda, K. Miura, R. Kawata, H. Furutani, M. Uematsu, Y. Omori, and H. Tanimoto. "Number–size distribution of aerosol particles and new particle formation events in tropical and subtropical Pacific Oceans". In: *Atmospheric Environment* 142 (2016), pp. 324–339. DOI: 10.1016/j.atmosenv.2016.07.055.

[166] E. R. Whitby, P. McMurray, U. Shankar, and F. Binkowski. *Modal Aerosol Dynamics Modeling*. Tech. Rep. 600/3-91/020. Available as NTIS PB91-161729/AS. Research Triangle Park: Atmospheric Research and Exposure Assessment Lab., US Environmental Protection Agency, 1991.

[167] A. Kerkweg, J. Buchholz, L. Ganzeveld, A. Pozzer, H. Tost, and P. Jöckel. "Technical Note: An implementation of the dry removal processes DRY DEPosition and SEDImentation in the Modular Earth Submodel System (MESSy)". In: *Atmos. Chem. Phys.* 6 (2006), pp. 4617–4632. DOI: 10.5194/acp-6-4617-2006.

[168] H. Tost, P. Jöckel, A. Kerkweg, R. Sander, and J. Lelieveld. "Technical note: A new comprehensive SCAVenging submodel for global atmospheric chemistry modelling". In: *Atmos. Chem. Phys.* 6 (2006), pp. 565–574. DOI: 10.5194/acp-6-565-2006.

[169] S. Brinkop and P. Jöckel. "ATTILA 4.0: Lagrangian advective and convective transport of passive tracers within the ECHAM5/MESSy (2.53.0) chemistry–climate model". In: *Geosci. Model Dev.* 12 (2019), pp. 1991–2008. DOI: 10.5194/gmd-12-1991-2019.

[170] C. Reithmeier and R. Sausen. "ATTILA: Atmospheric Tracer Transport in a Lagrangian Model". In: *Tellus B: Chemical and Physical Meteorology* 54.3 (2002), pp. 278–299. DOI: 10.3402/tellusb.v54i3.16666.

[171] B. A. Hamilton. *Alternative Jet Fuels Emissions, Quantification Methods Creation and Validation Report*. Final Report. McLean, Virginia: ACRP Project 02-80, 2019, p. 122.

[172] C. J. Miller, P. Prashanth, F. Allroggen, C. Grobler, J. S. Sabnis, R. L. Speth, and S. R. Barrett. "An Environmental Cost Basis for Regulating Aviation NOx Emissions". In: *Environmental Research Communications* 4.5 (2022), p. 055002. DOI: 10.1088/2515-7620/ac6938.

[173] F. D. A. Quadros, M. Snellen, and I. C. Dedoussi. "Recent and Projected Trends in Global Civil Aviation Fleet Average NOx Emissions Indices". In: *AIAA SCITECH 2022 Forum*. 2022, pp. 2022–51.

[174] V. Grewe, M. Dameris, C. Fichter, and D. S. Lee. "Impact of Aircraft NOx Emissions. Part 2: Effects of Lowering the Flight Altitude". In: *Meteorologische Zeitschrift* 11 (2002), pp. 197–205.

[175] C. Fichter, S. Marquart, R. Sausen, and D. S. Lee. "The Impact of Cruise Altitude on Contrails and Related Radiative Forcing". In: *Meteorologische Zeitschrift* 14 (2005), pp. 563–572.

[176] Airbus. *Global Market Forecast 2023–2042*. https://www.airbus.com/en/products-services/commercial-aircraft/market/global-market-forecast. Accessed: 25 August 2023. 2023.

[177] M. Mertens, V. Grewe, V. S. Rieger, and P. Jöckel. “Revisiting the Contribution of Land Transport and Shipping Emissions to Tropospheric Ozone”. In: *Atmospheric Chemistry and Physics* 18 (2018), pp. 5567–5588. DOI: 10.5194/acp-18-5567-2018.

[178] P. Thunis, A. Clappier, L. Tarrason, C. Cuvelier, A. Monteiro, E. Pisoni, J. Wesseling, C. A. Belis, G. Pirovano, S. Janssen, C. Guerreiro, and E. Peduzzi. “Source Apportionment to Support Air Quality Planning: Strengths and Weaknesses of Existing Approaches”. In: *Environment International* 130 (2019), p. 104825. DOI: 10.1016/j.envint.2019.05.019.

[179] Z. S. Wang, C. J. Chien, and G. S. Tonnesen. “Development of a Tagged Species Source Apportionment Algorithm to Characterize Three-Dimensional Transport and Transformation of Precursors and Secondary Pollutants”. In: *Journal of Geophysical Research: Atmospheres* 114 (2009), p. D21206. DOI: 10.1029/2008JD010846.

[180] C. L. Blanchard. “Methods for Attributing Ambient Air Pollutants to Emission Sources”. In: *Annual Review of Environment and Resources* 24 (1999), pp. 329–365. DOI: 10.1146/annurev.energy.24.1.329.

[181] D. S. Cohan, A. Hakami, Y. Hu, and A. G. Russell. “Nonlinear Response of Ozone to Emissions: Source Apportionment and Sensitivity Analysis”. In: *Environmental Science & Technology* 39 (2005), pp. 6739–6748. DOI: 10.1021/es048664m.

[182] V. Grewe, K. Dahlmann, S. Matthes, and W. Steinbrecht. “Attributing Ozone to NOx Emissions: Implications for Climate Mitigation Measures”. In: *Atmospheric Environment* 59 (2012), pp. 102–107. DOI: 10.1016/j.atmosenv.2012.05.002.

[183] R. Kranenburg, A. J. Segers, C. Hendriks, and M. Schaap. “Source Apportionment Using LOTOS-EUROS: Module Description and Evaluation”. In: *Geoscientific Model Development* 6 (2013), pp. 721–733. DOI: 10.5194/gmd-6-721-2013.

[184] I. C. Dedoussi, S. D. Eastham, E. Monier, and S. R. H. Barrett. “Premature Mortality Related to United States Cross-State Air Pollution”. In: *Nature* 578 (2020), pp. 261–265. DOI: 10.1038/s41586-020-1983-8.

[185] J. Maruhashi, M. Mertens, V. Grewe, and I. C. Dedoussi. *Supplementary Dataset for "A Multi-Method Assessment of the Regional Sensitivities Between Flight Altitude and Short-Term O3 Climate Warming from Aircraft NOx Emissions"*. 4TU ResearchData. 2024. DOI: 10.4121/56327667-69f1-4340-be45-9f9a6bd80584.v1.

[186] R. Sander, A. Baumgaertner, S. Gromov, H. Harder, P. Jöckel, A. Kerkweg, D. Kubistin, E. Regelin, H. Riede, A. Sandu, D. Taraborrelli, H. Tost, and Z.-Q. Xie. “The Atmospheric Chemistry Box Model CAABA/MECCA-3.0”. In: *Geoscientific Model Development* 4 (2011), pp. 373–380. DOI: 10.5194/gmd-4-373-2011.

[187] S. Dietmüller, P. Jöckel, H. Tost, M. Kunze, C. Gellhorn, S. Brinkop, C. Frömming, M. Ponater, B. Steil, A. Lauer, and J. Hendricks. “A new radiation infrastructure for the Modular Earth Submodel System (MESSy, based on version 2.51)”. In: *Geosci. Model Dev.* 9 (2016), pp. 2209–2222. DOI: 10.5194/gmd-9-2209-2016.

[188] E. W. Meijer, P. F. Van Velthoven, W. M. Wauben, J. P. Beck, and G. J. Velders. "The Effects of the Conversion of Nitrogen Oxides in Aircraft Exhaust Plumes in Global Models". In: *Geophysical Research Letters* 24 (1997), pp. 3013–3016. DOI: 10.1029/97GL53156.

[189] A. G. Kraabøl and F. Stordal. "Modelling Chemistry in Aircraft Plumes 2: The Chemical Conversion of NOx to Reservoir Species under Different Conditions". In: *Atmospheric Environment* 34 (2000), pp. 3951–3962. DOI: 10.1016/S1352-2310(00)00155-2.

[190] M. A. Cameron, M. Z. Jacobson, A. D. Naiman, and S. K. Lele. "Effects of Plume-Scale Versus Grid-Scale Treatment of Aircraft Exhaust Photochemistry". In: *Geophysical Research Letters* 40 (2013), pp. 5815–5820. DOI: 10.1002/2013GL057665.

[191] T. M. Fritz, S. D. Eastham, R. L. Speth, and S. R. H. Barrett. "The Role of Plume-Scale Processes in Long-Term Impacts of Aircraft Emissions". In: *Atmospheric Chemistry and Physics* 20 (2020), pp. 5697–5727. DOI: 10.5194/acp-20-5697-2020.

[192] F. D. A. Quadros, M. Snellen, J. Sun, and I. C. Dedoussi. "Global Civil Aviation Emissions Estimates for 2017–2020 Using ADS-B Data". In: *Journal of Aircraft* 59 (2022), pp. 1394–1405. DOI: 10.2514/1.C036763.

[193] P. Jöckel, H. Tost, A. Pozzer, M. Kunze, O. Kirner, C. A. M. Brenninkmeijer, S. Brinkop, D. S. Cai, C. Dyroff, J. Eckstein, F. Frank, H. Garny, K.-D. Gottschaldt, P. Graf, V. Grewe, A. Kerkweg, B. Kern, S. Matthes, M. Mertens, S. Meul, M. Neumaier, M. Nützel, S. Oberländer-Hayn, R. Ruhnke, T. Runde, R. Sander, D. Scharffe, and A. Zahn. "Earth System Chemistry integrated Modelling (ESCiMo) with the Modular Earth Submodel System (MESSy) version 2.51". In: *Geosci. Model Dev.* 9 (2016), pp. 1153–1200. DOI: 10.5194/gmd-9-1153-2016.

[194] K. Kelly and B. Šavrič. "Area and volume computation of longitude–latitude grids and three-dimensional meshes". In: *Transactions in GIS* 25 (2021), pp. 6–24. DOI: 10.1111/tgis.12636.

[195] M. O. Köhler, G. Rädel, O. Dessens, K. P. Shine, H. L. Rogers, O. Wild, and J. A. Pyle. "Impact of perturbations to nitrogen oxide emissions from global aviation". In: *Journal of Geophysical Research* 113 (2008), p. D11305. DOI: 10.1029/2007JD009140.

[196] A. Skowron, D. S. Lee, and R. R. De León. "Variation of radiative forcings and global warming potentials from regional aviation NOx emissions". In: *Atmospheric Environment* 104 (2015), pp. 69–78. DOI: 10.1016/j.atmosenv.2014.12.043.

[197] M. A. Cameron, M. Z. Jacobson, S. R. H. Barrett, H. Bian, C. C. Chen, S. D. Eastham, A. Gettelman, A. Khodayari, Q. Liang, H. B. Selkirk, N. Unger, D. J. Wuebbles, and X. Yue. "An intercomparative study of the effects of aircraft emissions on surface air quality". In: *Journal of Geophysical Research: Atmospheres* 122 (2017), pp. 8325–8344. DOI: 10.1002/2016JD025594.

[198] P. Prashanth, S. D. Eastham, R. L. Speth, and S. R. H. Barrett. "Aerosol formation pathways from aviation emissions". In: *Environmental Research Communications* 4 (2022), p. 021002. DOI: 10.1088/2515-7620/ac5229.

[199] T. M. Fritz, I. C. Dedoussi, S. D. Eastham, R. L. Speth, D. K. Henze, and S. R. H. Barrett. "Identifying the ozone-neutral aircraft cruise altitude". In: *Atmospheric Environment* 276 (2022), p. 119057. DOI: 10.1016/j.atmosenv.2022.119057.

[200] G. Myhre, J. S. Nilsen, L. Gulstad, K. P. Shine, B. Rognerud, and I. S. A. Isaksen. "Radiative forcing due to stratospheric water vapour from CH_4 oxidation". In: *Geophysical Research Letters* 34 (2007), p. L01807. DOI: 10.1029/2006GL027472.

[201] G. Brasseur, R. Cox, D. Hauglustaine, I. Isaksen, J. Lelieveld, D. H. Lister, R. Sausen, U. Schumann, A. Wahner, and P. Wiesen. "European scientific assessment of the atmospheric effects of aircraft emissions". In: *Atmospheric Environment* 32 (1998), pp. 2329–2418. DOI: 10.1016/S1352-2310(97)00486-X.

[202] R. Melssen. "Real-World Complexity of Central Trajectories". Master's Thesis. Universiteit Utrecht, 2020.

[203] J. Lee, J. Han, and K. Whang. "Trajectory Clustering: A Partition-and-Group Framework". In: *SIGMOD '07: Proceedings of the 2007 ACM SIGMOD International Conference on Management of Data*. June 2007, pp. 593–604. DOI: 10.1145/1247480.1247546.

[204] S. J. Corrado, T. G. Puranik, O. J. Pinon, and D. N. Mavris. "Trajectory Clustering within the Terminal Airspace Utilizing a Weighted Distance Function". In: *Proceedings*. Vol. 59. 2020, p. 7. DOI: 10.3390/proceedings2020059007.

[205] L. Basora, J. Morio, and C. Mailhot. "A Trajectory Clustering Framework to Analyse Air Traffic Flows". In: *Proceedings of the 7th SESAR Innovation Days*. Last accessed: 29 October 2022. Belgrade, Serbia: SESAR Joint Undertaking, 2017. URL: https://www.sesarju.eu/sites/default/files/documents/sid/2017/SIDs_2017_paper_45.pdf.

[206] X. Olive and L. Basora. "A Python Toolbox for Processing Air Traffic Data: A Use Case with Trajectory Clustering". In: *7th OpenSky Workshop 2019*. Zurich, Switzerland, Nov. 2019, pp. 73–60. DOI: 10.29007/sf1f.

[207] X. Olive and J. Morio. "Trajectory clustering of air traffic flows around airports". In: *Aerospace Science and Technology* 84 (2019), pp. 776–781. DOI: 10.1016/j.ast.2018.11.031.

[208] J. Li, J. Hendricks, M. Righi, and C. G. Beer. "An aerosol classification scheme for global simulations using the K-means machine learning method". In: *Geoscientific Model Development* 15 (2022), pp. 509–533. DOI: 10.5194/gmd-15-509-2022.

[209] P. Kassomenos, S. Vardoulakis, R. Borge, J. Lumbreras, C. Papaloukas, and S. Karakitsios. "Comparison of statistical clustering techniques for the classification of modelled atmospheric trajectories". In: *Theoretical and Applied Climatology* 102 (2010), pp. 1–12. DOI: 10.1007/s00704-009-0233-7.

[210] O. A. Tarasova, C. A. M. Brenninkmeijer, P. Jöckel, A. M. Zvyagintsev, and G. I. Kuznetsov. "A climatology of surface ozone in the extra tropics: cluster analysis of observations and model results". In: *Atmospheric Chemistry and Physics* 7 (2007), pp. 6099–6117. DOI: 10.5194/acp-7-6099-2007.

[211] C. Grobler, P. J. Wolfe, K. Dasadhikari, I. C. Dedoussi, F. Allroggen, R. L. Speth, S. D. Eastham, A. Agarwal, M. D. Staples, and J. Sabnis. "Marginal climate and air quality costs of aviation emissions". In: *Environmental Research Letters* 14 (2019), p. 114031. DOI: 10.1088/1748-9326/ab4942.

[212] E. Garyfallidis, M. Brett, M. M. Correia, G. B. Williams, and I. Nimmo-Smith. "QuickBundles, a Method for Tractography Simplification". In: *Frontiers in Neuroscience* 6 (2012), p. 175. DOI: 10.3389/fnins.2012.00175.

[213] T. Edwards, C. Jones, and P. Corcoran. "Extracting Geometric Representations of Trajectories Using Topological Data Analysis". In: *Proceedings of GeoComputation 2019: 15th International Conference*. University of Otago, University of Auckland, University of Canterbury, and Victoria University of Wellington. Queenstown, New Zealand: The University of Auckland, 2019. DOI: 10.17608/k6.auckland.9869063.v2.

[214] J. H. Hartigan and M. A. Wong. "A K-Means Clustering Algorithm". In: *Applied Statistics* 28 (1979), pp. 100–108.

[215] S. Salvador and P. Chan. "Learning States and Rules for Detecting Anomalies in Time Series". In: *Applied Intelligence* 23 (2005), pp. 241–255.

[216] N. Najibi and N. Devineni. "Recent trends in the frequency and duration of global floods". In: *Earth System Dynamics* 9 (2018), pp. 757–783. DOI: 10.5194/esd-9-757-2018.

[217] V. Grewe, C. Reithmeier, and D. T. Shindell. "Dynamic-chemical coupling of the upper troposphere and lower stratosphere region". In: *Chemosphere: Global Change Science* 47 (2002), pp. 851–861.

[218] A. F. Z. Levine and M. J. McPhaden. "How the July 2014 easterly wind burst gave the 2015–2016 El Niño a head start". In: *Geophysical Research Letters* 43.12 (2016), pp. 6503–6510. DOI: 10.1002/2016GL069204.

[219] S. R. H. Barrett, R. E. Britter, and I. Waitz. "Global mortality attributable to aircraft cruise emissions". In: *Environmental Science & Technology* 44.20 (2010), pp. 7736–7742. DOI: 10.1021/es101325r.

[220] R. G. Derwent, M. Dosa, M. A. H. Khan, R. Holland, and D. E. Shallcross. "Atmospheric chemistry regimes in intercontinental air traffic corridors: Ozone versus NO_x sensitivity". In: *Atmospheric Environment* 328 (2024), p. 120521. DOI: 10.1016/j.atmosenv.2024.120521.

[221] P. Jöckel, H. Tost, A. Pozzer, C. Brühl, J. Buchholz, L. Ganzeveld, P. Hoor, A. Kerkweg, M. G. Lawrence, R. Sander, B. Steil, G. Stiller, M. Tanarhte, D. Taraborrelli, J. van Aardenne, and J. Lelieveld. "The atmospheric chemistry general circulation model ECHAM5/MESSy1: consistent simulation of ozone from the surface to the mesosphere". In: *Atmospheric Chemistry and Physics* 6 (2006), pp. 5067–5104. DOI: 10.5194/acp-6-5067-2006.

[222] L. K. Emmons, D. A. Hauglustaine, J.-F. Muller, M. A. Carroll, G. P. Brasseur, D. Brunner, J. Staehelin, V. Thouret, and A. Marenco. “Data composites of airborne observation of tropospheric ozone and its precursor”. In: *Journal of Geophysical Research* 105 (2000), pp. 20497–20538. DOI: 10.1029/2000JD900232.

[223] A. Pozzer, P. Jöckel, H. Tost, R. Sander, L. Ganzeveld, A. Kerkweg, and J. Lelieveld. “Simulating organic species with the global atmospheric chemistry general circulation model ECHAM5/MESSy1: a comparison of model results with observations”. In: *Atmospheric Chemistry and Physics* 7 (2007), pp. 2527–2550. DOI: 10.5194/acp-7-2527-2007.

[224] E. Garyfallidis, M. Brett, B. Amirbekian, A. Rokem, S. Van Der Walt, M. Descoteaux, I. Nimmo-Smith, and DIPY contributors. “DIPY, a library for the analysis of diffusion MRI data”. In: *Frontiers in Neuroinformatics* 8 (2014). last access: 29 October 2022, p. 8. URL: https://dipy.org.

[225] M. Righi, J. Hendricks, and R. Sausen. “The global impact of the transport sectors on atmospheric aerosol: simulations for year 2000 emissions”. In: *Atmospheric Chemistry and Physics* 13 (2013), pp. 9939–9970. DOI: 10.5194/acp-13-9939-2013.

[226] A. Gettelman and C. Chen. “The Climate Impact of Aviation Aerosols”. In: *Geophysical Research Letters* 40 (2013), pp. 2785–2789. DOI: 10.1002/grl.50520.

[227] B. Kärcher, O. Möhler, P. J. DeMott, S. Pechtl, and F. Yu. “Insights into the role of soot aerosols in cirrus cloud formation”. In: *Atmospheric Chemistry and Physics* 7 (2007), pp. 4203–4227. DOI: 10.5194/acp-7-4203-2007.

[228] A. Petzold, M. Gysel, X. Vancassel, R. Hitzenberger, H. Puxbaum, S. Vrochticky, E. Weingartner, U. Baltensperger, and P. Mirabel. “On the effects of organic matter and sulphur-containing compounds on the CCN activation of combustion particles”. In: *Atmospheric Chemistry and Physics* 5 (2005), pp. 3187–3203. DOI: 10.5194/acp-5-3187-2005.

[229] T. Jurkat, C. Voigt, F. Arnold, H. Schlager, J. Kleffmann, H. Aufmhoff, D. Schäuble, M. Schaefer, and U. Schumann. “Measurements of HONO, NO, NOy and SO2 in aircraft exhaust plumes at cruise”. In: *Geophysical Research Letters* 38 (2011), p. L10807. DOI: 10.1029/2011GL046884.

[230] B. Owen, J.G. Anet, N. Bertier, S. Christie, M. Cremaschi, S. Dellaert, J. Edebeli, U. Janicke, J. Kuenen, L. Lim, and E. Terrenoire. “Review: Particulate Matter Emissions from Aircraft”. In: *Atmosphere* 13 (2022), p. 1230. DOI: 10.3390/atmos13081230.

[231] S. Mikkonen, S. Romakkaniemi, J. N. Smith, H. Korhonen, T. Petäjä, C. Plass-Duelmer, M. Boy, P. H. McMurry, K. E. J. Lehtinen, J. Joutsensaari, A. Hamed, R. L. Mauldin III, W. Birmili, G. Spindler, F. Arnold, M. Kulmala, and A. Laaksonen. “A statistical proxy for sulphuric acid concentration”. In: *Atmos. Chem. Phys.* 11 (2011), pp. 11319–11334. DOI: 10.5194/acp-11-11319-2011.

[232] E. R. Whitby and P. McMurry. “Modal aerosol dynamics modeling”. In: *Aerosol Sci. Technol.* 27 (1997), pp. 673–688. DOI: 10.1080/02786829708965504.

[233] A. Laaksonen, L. Pirjola, M. Kulmala, K.-H. Wohlfrom, F. Arnold, and F. Raes. "Upper tropospheric SO_2 conversion into sulphuric acid aerosols and cloud condensation nuclei". In: *J. Geophys. Res.* 105 (2000), pp. 1459–1468. DOI: 10.1029/1999JD900933.

[234] M. I. Khoder. "Atmospheric conversion of sulfur dioxide to particulate sulfate and nitrogen dioxide to particulate nitrate and gaseous nitric acid in an urban area". In: *Chemosphere* 49 (2002), pp. 675–684. DOI: 10.1016/S0045-6535(02)00391-0.

[235] L. R. Martin and D. E. Damschen. "Aqueous oxidation of sulfur dioxide by hydrogen peroxide at low pH". In: *Atmospheric Environment (1967)* 15.9 (1981), pp. 1615–1621. DOI: 10.1016/0004-6981(81)90146-3.

[236] Y. Yang, H. Wang, S. J. Smith, R. Easter, P.-L. Ma, Y. Qian, H. Yu, C. Li, and P. J. Rasch. "Global source attribution of sulfate concentration and direct and indirect radiative forcing". In: *Atmospheric Chemistry and Physics* 17 (2017), pp. 8903–8922. DOI: 10.5194/acp-17-8903-2017.

[237] A. Kirkevåg, T. Iversen, and A. Dahlback. "On radiative effects of black carbon and sulphate aerosols". In: *Atmospheric Environment* 33 (1999), pp. 2621–2635.

[238] J. E. Penner, M. Andreae, H. Annegarn, L. Barrie, J. Feichter, D. Hegg, A. Jayaraman, R. Leaitch, D. Murphy, J. Nganga, G. Pitari, et al. "Aerosols, their Direct and Indirect Effects". In: *Climate Change 2001: The Scientific Basis, Contribution of Working Group I to the Third Assessment Report of the Intergovernmental Panel on Climate Change (IPCC)*. Ed. by J. T. Houghton, Y. Ding, D. J. Griggs, M. Noguer, P. J. van der Linden, and D. Xiaosu. Cambridge: Cambridge University Press, 2001. Chap. 5, pp. 289–348.

[239] J. Haywood and O. Boucher. "Estimates of the direct and indirect radiative forcing due to tropospheric aerosols: A review". In: *Reviews of Geophysics* 38.4 (2000), pp. 513–543. DOI: 10.1029/1999RG000078.

[240] Z. Z. Kapadia, D. V. Spracklen, S. R. Arnold, D. J. Borman, G. W. Mann, K. J. Pringle, S. A. Monks, C. L. Reddington, F. Benduhn, A. Rap, C. E. Scott, E. W. Butt, and M. Yoshioka. "Impacts of aviation fuel sulfur content on climate and human health". In: *Atmospheric Chemistry and Physics* 16 (2016), pp. 10521–10541. DOI: 10.5194/acp-16-10521-2016.

[241] L. Feng, S. J. Smith, C. Braun, M. Crippa, M. J. Gidden, R. Hoesly, Z. Klimont, M. van Marle, M. van den Berg, and G. R. van der Werf. "The generation of gridded emissions data for CMIP6". In: *Geoscientific Model Development* 13 (2020), pp. 461–482. DOI: 10.5194/gmd-13-461-2020.

[242] J.-F. Lamarque, T. C. Bond, V. Eyring, C. Granier, A. Heil, Z. Klimont, D. Lee, C. Liousse, A. Mieville, B. Owen, M. G. Schultz, D. Shindell, S. J. Smith, E. Stehfest, J. Van Aardenne, O. R. Cooper, M. Kainuma, N. Mahowald, J. R. McConnell, V. Naik, K. Riahi, and D. P. van Vuuren. "Historical (1850–2000) gridded anthropogenic and biomass burning emissions of reactive gases and aerosols: methodology and application". In: *Atmospheric Chemistry and Physics* 10 (2010), pp. 7017–7039. DOI: 10.5194/acp-10-7017-2010.

[243] O. Fricko, P. Havlik, J. Rogelj, Z. Klimont, M. Gusti, N. Johnson, P. Kolp, M. Strubegger, H. Valin, M. Amann, T. Ermolieva, N. Forsell, M. Herrero, C. Heyes, G. Kindermann, V. Krey, D. L. McCollum, M. Obersteiner, S. Pachauri, S. Rao, E. Schmid, W. Schoepp, and K. Riahi. "The marker quantification of the Shared Socioeconomic Pathway 2: A middle-of-the-road scenario for the 21st century". In: *Global Environmental Change* 42 (2017), pp. 251–267. DOI: 10.1016/j.gloenvcha.2016.06.004.

[244] D. S. Lee, G. Pitari, V. Grewe, K. Gierens, J. E. Penner, A. Petzold, M. J. Prather, U. Schumann, A. Bais, T. Berntsen, and D. Iachetti. "Transport impacts on atmosphere and climate: Aviation". In: *Atmospheric Environment* 44.37 (2010), pp. 4678–4734. DOI: 10.1016/j.atmosenv.2009.06.005.

[245] J. B. Wu, Z. Wang, Q. Wang, J. Li, J. Xu, H. Chen, B. Ge, G. Zhou, and L. Chang. "Development of an on-line source-tagged model for sulfate, nitrate and ammonium: A modeling study for highly polluted periods in Shanghai, China". In: *Environmental Pollution* 221 (2017), pp. 168–179. DOI: https://doi.org/10.1016/j.envpol.2016.11.061.

[246] S. Itahashi, H. Hayami, K. Yumimoto, and I. Uno. "Chinese province-scale source apportionments for sulfate aerosol in 2005 evaluated by the tagged tracer method". In: *Environmental Pollution* 220 (2017), pp. 1366–1375. DOI: https://doi.org/10.1016/j.envpol.2016.10.098.

[247] K. M. Wagstrom, S. N. Pandis, G. Yarwood, G. M. Wilson, and R. E. Morris. "Development and application of a computationally efficient particulate matter apportionment algorithm in a three-dimensional chemical transport model". In: *Atmospheric Environment* 42.22 (2008), pp. 5650–5659. DOI: https://doi.org/10.1016/j.atmosenv.2008.03.012.

[248] A. Riccio, E. Chianese, G. Agrillo, C. Esposito, and G. Tirimberio. "Source apportion of atmospheric particulate matter: a joint Eulerian/Lagrangian approach". In: *Environmental Science and Pollution Research* 21 (2014), pp. 13160–13168. DOI: 10.1007/s11356-013-2367-5.

[249] J. Maruhashi. *Supplementary dataset for the PhD dissertation entitled "Characterizing the transport patterns and climate effects of aviation NOx and SO4 emissions using a novel Lagrangian tagging method"*. 4TU.ResearchData, 2024. DOI: 10.4121/79bcd360-04fc-4efc-a908-09874b9703c5.

[250] I. Bulatovic, A. L. Igel, C. Leck, J. Heintzenberg, I. Riipinen, and A. M. L. Ekman. "The importance of Aitken mode aerosol particles for cloud sustenance in the summertime high Arctic – a simulation study supported by observational data". In: *Atmospheric Chemistry and Physics* 21 (2021), pp. 3871–3897. DOI: 10.5194/acp-21-3871-2021.

[251] M. L. Pöhlker, M. Zhang, R. Campos Braga, O. O. Krüger, U. Pöschl, and B. Ervens. "Aitken mode particles as CCN in aerosol- and updraft-sensitive regimes of cloud droplet formation". In: *Atmospheric Chemistry and Physics* 21 (2021), pp. 11723–11740. DOI: 10.5194/acp-21-11723-2021.

[252] S. Shostak, K. Kim, Y. Horbatenko, and C. H. Choi. "Sulfuric Acid Formation via H_2SO_3 Oxidation by H_2O_2 in the Atmosphere". In: *The Journal of Physical Chemistry A* 123 (2019), pp. 8385–8390. DOI: 10.1021/acs.jpca.9b05444.

[253] F. Sheng, L. Jingjing, C. Yu, T. Fu-Ming, D. Xuemei, and L. Jing-Yao. "Theoretical study of the oxidation reactions of sulfurous acid/sulfite with ozone to produce sulfuric acid/sulfate with atmospheric implications". In: *RSC Advances* 8 (2018), pp. 7988–7996. DOI: 10.1039/C8RA00411K.

[254] M. Stengel, O. Sus, S. Stapelberg, S. Finkensieper, B. Würzler, D. Philipp, R. Hollmann, and C. Poulsen. *ESA Cloud Climate Change Initiative (ESA Cloud_cci) data: Cloud_cci AVHRR-AM L3C/L3U CLD_PRODUCTS v3.0*. 2019. DOI: 10.5676/DWD/ESA_Cloud_cci/AVHRR-AM/V003.

[255] M. Stengel, O. Sus, S. Stapelberg, S. Finkensieper, B. Würzler, D. Philipp, R. Hollmann, and C.A. Poulsen. *ESA Cloud Climate Change Initiative (Cloud CCI): AVHRR-AM monthly gridded cloud properties, version 3.0*. Accessed on: November 17, 2024. 2020. URL: https://tinyurl.com/AVHRR-AM.

[256] M. Stengel, S. Stapelberg, O. Sus, C. Schlundt, C. Poulsen, G. Thomas, M. Christensen, C. Carbajal Henken, R. Preusker, J. Fischer, A. Devasthale, U. Willén, K.-G. Karlsson, G. R. McGarragh, S. Proud, A. C. Povey, R. G. Grainger, J. F. Meirink, A. Feofilov, R. Bennartz, J. S. Bojanowski, and R. Hollmann. "Cloud property datasets retrieved from AVHRR, MODIS, AATSR and MERIS in the framework of the Cloud_cci project". In: *Earth System Science Data* 9 (2017), pp. 881–904. DOI: 10.5194/essd-9-881-2017.

[257] M. Stengel, S. Stapelberg, O. Sus, S. Finkensieper, B. Würzler, D. Philipp, R. Hollmann, C. Poulsen, M. Christensen, and G. McGarragh. "Cloud_cci Advanced Very High Resolution Radiometer post meridiem (AVHRR-PM) dataset version 3: 35-year climatology of global cloud and radiation properties". In: *Earth System Science Data* 12 (2020), pp. 41–60. DOI: 10.5194/essd-12-41-2020.

[258] A. Lauer, V. Eyring, J. Hendricks, P. Jöckel, and U. Lohmann. "Global model simulations of the impact of ocean-going ships on aerosols, clouds, and the radiation budget". In: *Atmos. Chem. Phys.* 7 (2007), pp. 5061–5079. DOI: 10.5194/acp-7-5061-2007.

[259] A. van Donkelaar, R. V. Martin, W. R. Leaitch, A. M. Macdonald, T. W. Walker, D. G. Streets, Q. Zhang, E. J. Dunlea, J. L. Jimenez, J. E. Dibb, L. G. Huey, R. Weber, and M. O. Andreae. "Analysis of aircraft and satellite measurements from the Intercontinental Chemical Transport Experiment (INTEX-B) to quantify long-range transport of East Asian sulfur to Canada". In: *Atmospheric Chemistry and Physics* 8 (2008), pp. 2999–3014. DOI: 10.5194/acp-8-2999-2008.

[260] S. Tiwari, M. J. Pekris, and J. J. Doherty. "A review of liquid hydrogen aircraft and propulsion technologies". In: *International Journal of Hydrogen Energy* 57 (2024), pp. 1174–1196. DOI: 10.1016/j.ijhydene.2023.12.263.

[261] A. Simorgh, M. Soler, D. González-Arribas, S. Matthes, V. Grewe, S. Dietmüller, S. Baumann, H. Yamashita, F. Yin, F. Castino, F. Linke, B. Lührs, and M. M. Meuser. "A Comprehensive Survey on Climate Optimal Aircraft Trajectory Planning". In: *Aerospace* 9.3 (2022), p. 146. DOI: 10.3390/aerospace9030146.

[262] E. S. Dallara, I. M. Kroo, and I. A. Waitz. "Metric for Comparing Lifetime Average Climate Impact of Aircraft". In: *AIAA Journal* 49.8 (2011), pp. 1600–1613. DOI: 10.2514/1.J050763.

[263] V. Grewe and K. Dahlmann. "How ambiguous are climate metrics? And are we prepared to assess and compare the climate impact of new air traffic technologies?" In: *Atmospheric Environment* 106 (2015), pp. 373–374. DOI: 10.1016/j.atmosenv.2015.02.039.

[264] A.M. Frias, M.L. Shapiro, Z. Engberg, R. Zopp, M. Soler, and M.E.J. Stettler. "Feasibility of contrail avoidance in a commercial flight planning system: an operational analysis". In: *Environmental Research: Infrastructure and Sustainability* 4.1 (2024), p. 015013. DOI: 10.1088/2634-4505/ad310c.

[265] H. Yamashita, F. Yin, V. Grewe, P. Jöckel, S. Matthes, B. Kern, K. Dahlmann, and C. Frömming. "Newly developed aircraft routing options for air traffic simulation in the chemistry–climate model EMAC 2.53: AirTraf 2.0". In: *Geosci. Model Dev.* 13 (2020), pp. 4869–4890. DOI: 10.5194/gmd-13-4869-2020.

[266] Eurocontrol. *SAAM Reference Manual 4.2.0 Beta*. Ed. by Eurocontrol. Version 21-12-2012, p. 434. 2012.

[267] B. Lührs, M. Niklass, C. Frömming, V. Grewe, and V. Gollnick. "Cost-Benefit Assessment of 2D and 3D Climate And Weather Optimized Trajectories". In: *16th AIAA Aviation Technology, Integration, and Operations Conference*. AIAA 2016-3758. AIAA, 2016. DOI: 10.2514/6.2016-3758.

[268] P. Rao, F. Yin, V. Grewe, H. Yamashita, P. Jöckel, S. Matthes, M. Mertens, and C. Frömming. "Case Study for Testing the Validity of NOx-Ozone Algorithmic Climate Change Functions for Optimising Flight Trajectories". In: *Aerospace* 9.5 (2022), p. 231. DOI: 10.3390/aerospace9050231.

[269] Eurocontrol. *Aviation data for research*. Accessed on 26 September 2023. 2023. URL: https://www.eurocontrol.int/dashboard/rnd-data-archive.

[270] V. Grewe, T. Champougny, S. Matthes, C. Frömming, S. Brinkop, O. A. Søvde, E. A. Irvine, and L. Halscheidt. "Reduction of the air traffic's contribution to climate change: A REACT4C case study". In: *Atmospheric Environment* 94 (2014), pp. 616–625. DOI: 10.1016/j.atmosenv.2014.05.059.

[271] V. Grewe, S. Matthes, C. Frömming, S. Brinkop, P. Jöckel, K. Gierens, T. Champougny, J. Fuglestvedt, A. Haslerud, E. Irvine, and K. Shine. "Feasibility of climate-optimized air traffic routing for trans-Atlantic flights". In: *Environmental Research Letters* 12.3 (2017), p. 034003. DOI: 10.1088/1748-9326/aa5ba0.

[272] C. Elkin and D. Sanekommu. *How AI Is Helping Airlines Mitigate the Climate Impact of Contrails*. Accessed: 2024-11-16. Google Blog. Nov. 2023. URL: https://blog.google/technology/ai/ai-airlines-contrails-climate-change/.

[273] Transport and Environment. *Contrail avoidance: aviation's climate opportunity of the decade*. Accessed: 2024-11-16. 2024. URL: https://www.transportenvironment.org/articles/contrail-avoidance.

[274] F. Baneshi, M. Soler, and A. Simorgh. "Conflict assessment and resolution of climate-optimal aircraft trajectories at network scale". In: *Transportation Research Part D: Transport and Environment* 115 (2023), p. 103592. DOI: 10.1016/j.trd.2022.103592.

[275] R. Teoh, Z. Engberg, U. Schumann, C. Voigt, M. Shapiro, S. Rohs, and M. E. J. Stettler. "Global aviation contrail climate effects from 2019 to 2021". In: *Atmospheric Chemistry and Physics* 24 (2024), pp. 6071–6093. DOI: 10.5194/acp-24-6071-2024.

[276] A. Pozzer, P. Jöckel, R. Sander, J. Williams, L. Ganzeveld, and J. Lelieveld. "Technical Note: The MESSy-submodel AIRSEA calculating the air-sea exchange of chemical species". In: *Atmos. Chem. Phys.* 6 (2006), pp. 5435–5444. DOI: 10.5194/acp-6-5435-2006.

[277] E. Roeckner, R. Brokopf, M. Esch, M. Giorgetta, S. Hagemann, L. Kornblueh, E. Manzini, U. Schlese, and U. Schulzweida. "Sensitivity of Simulated Climate to Horizontal and Vertical Resolution in the ECHAM5 Atmosphere Model". In: *J. Climate* 19 (2006), pp. 3771–3791. DOI: 10.1175/jcli3824.1.

[278] H. Tost. *CVTRANS*. Johannes Gutenberg University of Mainz, Germany, available at: https://envmodel.ipa.uni-mainz.de/submodels-cvtrans (last access on 21 June 2024). 2019.

[279] MESSy Submodels. *The MESSy Submodels and Submodel licenses*. https://messy-interface.org/messy/submodels/. Accessed: 21 June 2024.

[280] R. Sander, P. Jöckel, O. Kirner, A. T. Kunert, J. Landgraf, and A. Pozzer. "The photolysis module JVAL-14, compatible with the MESSy standard, and the JVal PreProcessor (JVPP)". In: *Geosci. Model Dev.* 7 (2014), pp. 2653–2662. DOI: 10.5194/gmd-7-2653-2014.

[281] H. Tost, P. Jöckel, and J. Lelieveld. "Lightning and convection parameterisations – uncertainties in global modelling". In: *Atmos. Chem. Phys.* 7 (2007), pp. 4553–4568. DOI: 10.5194/acp-7-4553-2007.

[282] C. G. Beer, J. Hendricks, M. Righi, B. Heinold, I. Tegen, S. Groß, D. Sauer, A. Walser, and B. Weinzierl. "Modelling mineral dust emissions and atmospheric dispersion with MADE3 in EMAC v2.54". In: *Geosci. Model Dev.* 13 (2020), pp. 4287–4303. DOI: 10.5194/gmd-13-4287-2020.

[283] A. Kerkweg, R. Sander, H. Tost, and P. Jöckel. "Technical note: Implementation of prescribed (OFFLEM), calculated (ONLEM), and pseudo-emissions (TNUDGE) of chemical species in the Modular Earth Submodel System (MESSy)". In: *Atmos. Chem. Phys.* 6 (2006), pp. 3603–3609. DOI: 10.5194/acp-6-3603-2006.

[284] P. Jöckel, A. Kerkweg, J. Buchholz-Dietsch, H. Tost, R. Sander, and A. Pozzer. "Technical Note: Coupling of chemical processes with the Modular Earth Submodel System (MESSy) submodel TRACER". In: *Atmos. Chem. Phys.* 8 (2008), pp. 1677–1687. DOI: 10.5194/acp-8-1677-2008.

ACKNOWLEDGMENTS

There would be no “Maruhashi et al.” without the incredible support of the so-called “et al.”—a rather cold and crude term for generalizing the many amazing people from whom I’ve learned and drawn inspiration. This section is for all of you who have helped bring this dissertation to life, whether directly or indirectly, in big ways or small. Your contributions have meant the world to me and I am forever grateful. Now, because I am in my thirties and my memory isn’t what it used to be, I might forget to acknowledge some people. For that, I truly apologize in advance.

I’ll start with my supervisory team: Volker and Irene. I am incredibly honored to have been entrusted with such a challenging research topic and to have been given the scientific freedom to explore solutions that may have, at times, seemed out of the ordinary. Your continued confidence in my abilities throughout these years has been instrumental, especially in moments when I wasn’t sure how to tackle a tough problem. Volker, I very much enjoyed our long discussions regarding the formulation of the aerosol tagging equations, and of talking about differential equations in general. You have been an outstanding mentor and I have learned a great deal from you. Irene, your attention to detail, brilliant ideas and optimistic outlook have always made our meetings productive and fun. I am very grateful that you took the time to organize sessions where we had the opportunity to practice upcoming conference presentations and pitches and receive useful feedback. Your unwavering support has truly made all the difference and has made me a much stronger researcher and presenter. I can confidently say that completing a PhD demands immense effort from the candidate, but it also requires a bit of luck — choosing a great topic doesn’t guarantee having great mentors like Volker and Irene. I was lucky enough to get both.

I also had the privilege of learning a lot from several researchers at DLR. I am grateful to the great Patrick Jöckel, who initially helped me set up a complex climate-chemistry model on a supercomputer, something I had never done. His vast knowledge of all things EMAC was key to understanding the intricacies of its many submodels. For AIRTRAC 1.0, I want to thank Christine Frömming, who generously shared her knowledge of the model’s assumptions, provided post-processing tools, and helped me interpret the output. For ATTILA, I appreciated the insightful discussions with Sabine Brinkop, and I’m also thankful to Mariano Mertens for helping expand my understanding of the tagging methodology. I was fortunate to co-author a paper with him and I am grateful for the many Eulerian tagging simulations he ran. When it comes to aerosols, I owe thanks to Johannes Hendricks and Mattia Righi, who provided a great introduction to the complexities of aerosol microphysics. A special shoutout to Mattia for patiently answering all my questions about the MADE3 submodel, he has played a key role in the construction of AIRTRAC 2.0. And of course, thanks to Monica Sharma for the helpful discussions on her contributions to MADE3 as well.

My kind and talented colleagues from the former ANCE section also made this PhD

journey more enjoyable and inspiring. Thanks to Lisette, who kindly showed me around the Aerospace Faculty on my very first day. To Bieke, my original officemate, for helping me settle in and feel welcome in a new country. To Pratik, who added value to my datasets by creating a really cool surrogate model, introduced me to some excellent Indian restaurants (you're welcome for the Japanese ones!), and also treated me to some amazing home-cooked Indian food. To Flávio, whose comprehensive aviation emissions inventory was helpful throughout my research. To Federica, for our engaging chat on the differences between the tagging and perturbation methods as well as your very useful pasta recommendations. To Jurriaan, for keeping us updated on all things Snellius. To Irina, for your humor and friendly nature. To Roberto, for the jokes that always landed. To Jeff, my cheesecake co-chef in the 2022 ANCE Baking Competition, for proving that with teamwork, even my highly questionable culinary *mistalents* could somehow result in an edible cheesecake. To Luccas, for presenting very interesting concepts regarding aircraft plume modeling. To Amy, for lifting the office mood with your energy. To Harjot, for your friendly nature and flavorful lemon rice. To Hugo, for our Portuguese chats that reminded me of home. To Marloes, for your lightning-fast help with contracts and anything bureaucratic. I also want to thank the two awesome groups of BSc students (from the DSE Project and the Test, Analysis and Simulation course) I had the pleasure of co-mentoring. You reminded me that the best way to learn something is to try and teach it. Your creativity and enthusiasm were truly impressive. Special thanks also go to the partners of the ACACIA EU Project, and in particular to Nicolas Bellouin, for organizing several workshops that gave me the valuable opportunity to present my research to a wide audience of well-established researchers. Finally, a big thanks to Merel Engelsman for the incredible talent in translating my research into an engaging and easy-to-understand story for the TU Delft website.

I owe a great deal to my family, including my grandparents, aunts, and uncles, for their unconditional support and over-the-top faith in my potential. To my mom, whose passion for flight inspired me to take on this wild path called Aerospace Engineering. Your love and unwavering belief in me have propelled me higher than any jet ever could! To my dad, for always encouraging me to follow my dreams and choose joy over salary. To my sister, whose confidence in me is so strong it actually made me believe I could pull this off. And to Bilson, my loyal canine companion who kept me warm by curling up behind my chair throughout my BSc, both MSc degrees, and part of this PhD — your fluffy support was tireless, and your absence is deeply felt.

Finally, to Eline, my fun and loving partner who's been by my side since the early days of this PhD. You are a balancing force that ensures I am not overwhelmed with the challenges of life. Your cozy cooking is a loving constant that always helps to counter the bitterness of daily stress. Truth be told, the Salmon Wellington you made was a huge help to get me through the anxiety of the GNG meeting. It still puzzles me how an amateur vegetarian chef was able to execute this difficult dish to perfection on the very first try. I might not always understand your British accent, but your love is loud and clear, needing no translation. Thank you for your patience, your humor, your endless support and for the Dutch translation of this abstract!

Jin Maruhashi
Lisbon, April 2025

CURRICULUM VITÆ

Jin MARUHASHI

28-03-1993 Born in Brasília, Brazil.

EDUCATION

2009–2011 Secondary education
Carlucci American International School of Lisbon
International Baccalaureate Bilingual Diploma
Lisbon, Portugal

2011–2014 Bachelor of Science (BSc) in Aerospace Engineering
University of Lisbon (Instituto Superior Técnico)
Lisbon, Portugal

2015–2017 Master of Science (MSc) in Finance
NOVA School of Business and Economics (NOVA SBE)
Lisbon, Portugal

2017–2019 Master of Science (MSc) in Aerospace Engineering
University of Lisbon (Instituto Superior Técnico)
Lisbon, Portugal

2020–2024 Doctor of Philosophy (PhD) in Aerospace Engineering
Delft University of Technology (TU Delft)
Thesis: Characterizing the transport patterns and climate effects of aviation emissions using a novel Lagrangian tagging method
Promotors: Prof. dr. V. Grewe and dr. I.C. Dedoussi

AWARDS

2022 Best Climate Action Paper of 2022

Awarded by TU Delft for the article: "Transport patterns of global aviation NO_x and their short-term O_3 radiative forcing - a machine learning approach"
https://tinyurl.com/w9k3k6pz

2022 Best Climate Science Paper of 2022

Awarded by TU Delft for the article: "Transport patterns of global aviation NO_x and their short-term O_3 radiative forcing - a machine learning approach"
https://tinyurl.com/mr3ne7bn

PROFESSIONAL EXPERIENCE

2016 IoT (Internet of Things) Summer Intern
Vodafone Portugal
Lisbon, Portugal

2017 VBA (Visual Basic for Applications) Specialist
CTT Correios de Portugal
Lisbon, Portugal

2018–2019 Aeronautical Meteorology Intern
Portuguese Institute for Sea and Atmosphere (IPMA)
Lisbon, Portugal

2019–2020 Data Analytics Expert
Vodafone Portugal
Lisbon, Portugal

2024 Postdoctoral Researcher
Delft University of Technology
Delft, Netherlands

LIST OF PUBLICATIONS

PEER-REVIEWED JOURNAL ARTICLES

6. **J. Maruhashi**, M. Righi, M. Sharma, J. Hendricks, P. Jöckel, V. Grewe and I.C. Dedoussi. *AIRTRAC 2.0: a Lagrangian aerosol tagging sub-model for the analysis of aviation SO_4 transport patterns*, Manuscript in preparation.

5. N. Bellouin, M. Bickel, U. Burkhardt, Y. Cohen, I.C. Dedoussi, M. Dollner, J. Fuglestvedt, A. Gettelman, K. Gierens, V. Grewe, J. Hahofer, D. Hauglustaine, J. Hendricks, Z. Kanji, B. Kärcher, M. Krämer, D. Lee, R.R. de Leon, Y. Li, U. Lohmann, M. Lund, **J. Maruhashi**, S. Matthes, R. Paoli, J. Penner, A. Petzold, J. Quaas, F. Quadros, M. Righi, B. Samset, A. Skowron, E. Terrenoire, M. Tesche, S. Unterstrasser, C. Voigt and B. Weinzierl. *Assessment of the uncertainty in the effective radiative forcing of aviation: nitrogen oxide emissions, contrail cirrus formation, and aerosol-cloud interactions*, Manuscript in preparation.

4. P. Rao, R. Dwight, D. Singh, **J. Maruhashi**, I.C. Dedoussi, V. Grewe and C. Frömming. *The ozone radiative forcing of nitrogen oxide emissions from aviation can be estimated using a probabilistic approach*, Commun Earth Environ 5, 558, 2024.

3. **J. Maruhashi**, M. Mertens, V. Grewe and I.C. Dedoussi. *A multi-method assessment of the regional sensitivities between flight altitude and short-term O_3 climate warming from aircraft NO_x emissions*, Environmental Research Letters, 19, 054007, 2024.

2. **J. Maruhashi**, V. Grewe, C. Frömming, P. Jöckel and I.C. Dedoussi. *Transport patterns of global aviation NO_x and their short-term O_3 radiative forcing - a machine learning approach*, Atmospheric Chemistry and Physics, 22, 14253-14282, 2022.

1. **J. Maruhashi**, P. Serrão and M. Belo-Pereira. *Analysis of mountain wave effects on a hard landing incident in Pico aerodrome using the AROME model and airborne observations*, Atmosphere, 10(7), 350, 2019.

CONFERENCE PRESENTATIONS

6. **J. Maruhashi**, M. Mertens, V. Grewe and I.C. Dedoussi. *The impact of flight altitude on short-term NO_x-O_3 climate effects - a global multi-method assessment*, 4th ECATS Conference 2023, Delft, Netherlands, 24-26 October 2023.

5. **J. Maruhashi**, M. Mertens, V. Grewe and I.C. Dedoussi. *Assessing the appropriateness of different climate modelling approaches for the estimation of aviation NO_x climate effects*, EGU General Assembly 2023, Vienna, Austria, 24-28 April 2023, EGU23-9246.

4. P. Rao, R. Dwight, **J. Maruhashi**, I.C. Dedoussi, V. Grewe and C. Frömming. *Towards a new surrogate model for predicting short-term NO_x-O_3 effects from aviation using Gaussian processes*, EGU General Assembly 2023, Vienna, Austria, 24-28 April 2023, EGU23-4337.

3. **J. Maruhashi**, V. Grewe, C. Frömming, P. Jöckel and I.C. Dedoussi. *A Lagrangian study of globally emitted aviation NO_x and associated short-term O_3 radiative forcing effects*, EGU General Assembly 2022, Vienna, Austria, 23-27 May 2022, EGU22-6646.

2. **J. Maruhashi**, V. Grewe, and I.C. Dedoussi. *Clustering of ATTILA Trajectories using a Neuroscience Algorithm (QuickBundles) for the Characterization of Emission Transport Pathways*, 10th Annual EMAC Symposium 2021, Online, 31 May - June 2, 2021.

1. M. Belo-Pereira, **J. Maruhashi** and P. Serrão. *Mountain wave turbulence in the vicinity of Pico aerodrome*, X Technical Conference on Meteorology, Lisbon, Portugal, 20-21 November 2019.

EUROPEAN COMMISSION (EC) TECHNICAL REPORTS

2. **J. Maruhashi**, V. Grewe, I.C. Dedoussi, J. Hendricks and M. Righi. *Deliverable 1.3: Quantification and evaluation of the importance of the aviation aerosol interactions with low-level clouds*, ACACIA EU project deliverable, February 29, 2024.

1. **J. Maruhashi**, V. Grewe, I.C. Dedoussi, J. Hendricks and M. Righi. *Deliverable 5.2: Synthesis of operational solutions envisaged for reducing aviation emissions*, ACACIA EU project deliverable, June 30, 2022.

INTERVIEWS

1. **J. Maruhashi**. *Jin Maruhashi over Groener Vliegen en stikstofoxiden*, Omroep Delft, Delft, Netherlands, 30 March 2023.


TU Delft